

**Quantum systems in restricted geometries  
coupled to bosonic fields**

Inauguraldissertation

zur

Erlangung des akademischen Grades eines

Doktors der Naturwissenschaften

der

Mathematisch-Naturwissenschaftlichen Fakultät

der

Ernst-Moritz-Arndt-Universität Greifswald

vorgelegt von

Thomas Koch

geboren am 6. April 1984

in Stralsund

Greifswald, September 30, 2016



Dekan: Prof. Dr. Werner Weitschies

1. Gutachter: Prof. Dr. Holger Fehske

2. Gutachter: .....

Tag der Promotion: .....



# Contents

<b>1</b>	<b>Exposé</b>	<b>1</b>
1.1	Introduction . . . . .	1
1.2	Phonon-assisted transport through Molecular Junctions . . . . .	4
1.3	Luminescence of trapped semiconductor excitons . . . . .	16
<b>2</b>	<b>Thesis Articles</b>	<b>27</b>
2.1	Article I — Nonequilibrium transport through molecular junctions in the quantum regime . . . . .	29
2.2	Article II — Phonon-affected steady-state transport through molecular quantum dots . . . . .	45
2.3	Article III — Thermoelectric effects in molecular quantum dots with contacts . . . . .	55
2.4	Article IV — Interacting multicomponent exciton gases in a potential trap: Phase separation and Bose-Einstein condensation . . . . .	67
2.5	Article V — Phase separation of multicomponent excitonic Bose-Einstein condensates . . . . .	75
2.6	Article VI — Condensation of excitons in $\text{Cu}_2\text{O}$ at ultracold temperatures: experiment and theory . . . . .	79
2.7	Article VII — Theory of zero-phonon decay luminescence of semiconductor excitons . . . . .	117
	<b>Bibliography</b>	<b>130</b>
	<b>Scientific Contributions</b>	<b>131</b>
	<b>Declaration</b>	<b>135</b>
	<b>Curriculum Vitae</b>	<b>137</b>
	<b>Acknowledgement</b>	<b>139</b>



# 1 Exposé

## 1.1 Introduction

Recent advances in nanoengineering and laser optics allow for the fabrication of a wide range of systems that subject fermionic particles to geometric restrictions. This may happen, e.g., through the reduction of dimensionality, as in mesoscopic junctions [1] and quantum wells [2], or through the creation of trapping potentials, as in optical lattices [3]. Such systems provide a highly controllable environment for the investigation of many-body interactions. A significant factor is the coupling of the fermions to internal or external bosonic fields. For instance, quasi one-dimensional systems are prone to metal-insulator transitions that are induced by the interaction with quantized lattice vibrations, i.e., phonons [4]. Also, restricted semiconductor geometries permit long lifetimes and high densities of excitons and exciton-polaritons, allowing the investigation of light-matter interaction and quantum-condensation. In addition, the fine tuning of electrical and optical characteristics suggests practical applications, such as the construction of novel electronic and thermoelectric devices using spintronics and molecular transistors, or the simulation of other many-body systems [3]

This thesis considers two of these systems, specifically the thermoelectric transport through a molecular junction, and the Bose-Einstein condensation and luminescence of several species of trapped semiconductor excitons. While the systems are discussed in more detail in Secs. 1.2 and 1.3, respectively, their main characteristics are given in Fig. 1.

A molecular junction consists of a small organic molecule that is contacted by two metallic leads. Under voltage or temperature bias, molecular junctions show non-linear transport characteristics, such as hysteresis, switching and negative-differential conductance. They are, therefore, considered a promising candidate in the search for further miniaturization and new functionality of electronic devices. When being occupied by charge carriers, the molecule may undergo structural changes, rotations or vibrations. These processes correspond to the interaction of passing electrons with local phonon modes of considerable energy. They can be observed as vibrational signatures in the current-voltage characteristics of the device [5–8]. The situation resembles the coupling of electronic excitations to lattice vibrations in an infinite molecular crystal, which has been studied extensively by means of the Holstein model [9–11]. For strong electron-phonon coupling, this model predicts the formation of small polarons, i.e., electrons dragging a phonon cloud through the lattice, thereby greatly reducing their mobility [11–13]. In the case of molecular junctions, translational symmetry is broken and the electron-phonon

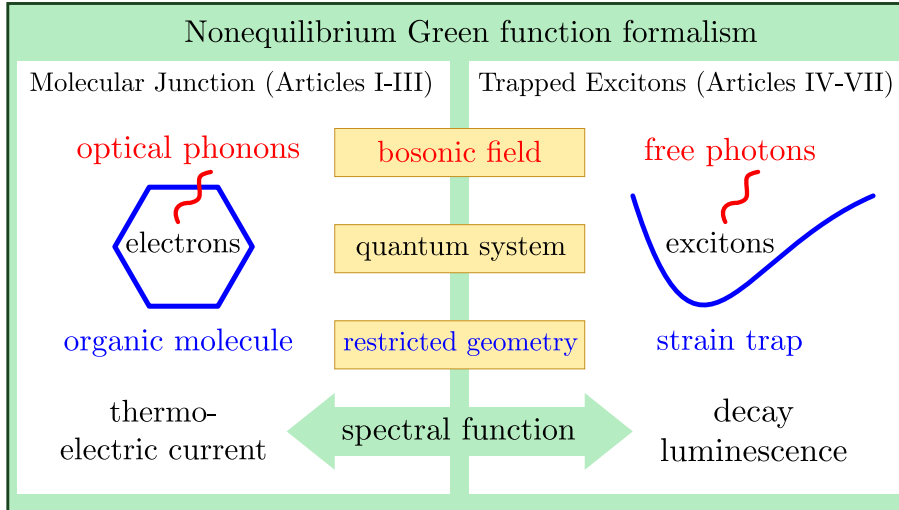


**Fig. 1:** Illustration of the common characteristics of the molecular junction and the system of trapped semiconductor excitons.

interaction is restricted to a small area and few, well separated levels. [14–18]. Transport through the junction will, therefore, strongly depend on the ratio of electron-phonon and molecule-lead coupling strengths. The question arises how quasiparticle renormalization accounts for the vibrational signatures in the current-voltage and thermopower characteristics of the junction, and whether the formation of a transient, polaron-like state at the molecule is a possible explanation for the observed non-linear phenomena [19].

The junction can be described as a quantum dot, i.e., as a quantum system of finite size and reduced dimensionality, that interacts with macroscopic charge and heat reservoirs. According to the formula by Meir and Wingreen [20], the charge current between the reservoirs is determined by the interacting electronic spectral function of the dot, the calculation of which is the central task of our work. A basic model for a deformable junction results from adding local Holstein coupling to a Fano-Anderson-impurity model. Previous approaches, that were based on a Lang-Firsov shift transformation, found that strong electron-phonon coupling reduces the effective coupling to the leads, but may also facilitate transport by lowering the tunneling barrier and permitting phonon-assisted, quasi-elastic transmission [21–24]. In the works presented here, we follow an approach previously developed for the Holstein molecular crystal model [9–11]: We account for polaronic effects away from the strong-coupling antiadiabatic limit by using a variational form of the Lang-Firsov transformation. In this way, we are able to interpolate between the regime of weak scattering, quasi-coherent lead-to-lead tunneling and incoherent hopping transport via a polaron-like dot state.

The second system considered here is a mixture of several species of excitons in a small semiconductor crystal that are spatially restricted by a stress induced potential trap. As with phonons, excitons are an elementary excitation of a solid body



system. They consist of a bound pair of excited electrons and holes. For strong Coulomb interaction the overlap of electron and hole wave functions creates, to first order, a composite boson. As such, excitons have long been considered ideal candidates for the observation of Bose-Einstein condensation, due to their small mass and because high densities are achievable via laser excitation [25–29]. Our work is motivated by recent experiments by Stolz *et al.* on the Bose-Einstein condensation of para- and orthoexcitons in cuprous oxide ( $\text{Cu}_2\text{O}$ ) [30]. At ultracold temperatures, the excitons are created via laser excitation and confined to the trap to counter diffusion processes and achieve critical densities.

Small, long living trapped excitons can be described as weakly interacting Bose gases in external potentials, the thermodynamics of which has been investigated extensively in the theory of one-component atomic gases [31–34], and has been applied to excitons [35, 36]. Given the generalisations to multi-component atomic gases [37–41] and spinor polaritons [42, 43], this thesis describes a generalisation to a multi-component gas of interacting para- and orthoexcitons. We derive coupled equations of motion for the condensate wave functions and the field operators of non-condensed excitons. Applying a mean-field approximation to the inter- and intra-species coupling, as well as a Bogoliubov-transformation we obtain and numerically evaluate self-consistent expressions for the spatially dependent exciton densities and dispersions in the trap.

In the experiment, however, the exciton density distribution is not directly accessible. Yet, excitons are only quasi-stable and decay via the emission of photons, which provides the primary method of detection. Then the question is, what are the footprints of a possible exciton condensate in the decay luminescence signal. In the articles IV-VI, we consider this problem based on the formula by Shi and Verechaka [44], according to which the luminescence intensity of the direct paraexciton and phonon-assisted orthoexciton decay is given by the respective excitonic spectral functions. In the article VII, we extend the theory of paraexciton decay by including anomalous processes in the exciton-photon interaction Hamiltonian. The resulting luminescence formula is dependent on the photonic correlation function.

For both systems considered in this work, the calculation of the experimentally relevant signal — the thermoelectric junction current and the excitonic decay luminescence, respectively — requires us to derive suitable interacting correlation and spectral functions at finite temperatures. In doing so, we suppose a steady-state situation: At the quantum dot, the charge current is driven by differing, fixed chemical potentials or temperatures in the leads. Similarly, for the extended exciton luminescence theory we suppose that the excitons achieve quasi-equilibrium before recombination, so that they act as a constant reservoir for the creation of photons. We work with the non-equilibrium Green function technique, that was formulated differently yet equivalently by Kadanoff and Baym [45], and Keldysh [46]. It is based on generalized Green functions that are defined on a contour running along the imaginary time axis (Kadanoff-Baym) or from the time the disturbance was switched on to the present and back again (Keldysh). Upon the contour, the Dyson equations or perturbation series are structurally equivalent to the equilibrium the-

ory. Neglecting initial correlations, the wanted correlation functions result from analytical continuation to the real time axis.

## 1.2 Phonon-assisted transport through Molecular Junctions

Molecular junctions are electronic devices where the functional element is a single organic molecule contacted by a number of metallic electrodes or leads. Such systems may feature single aromatic rings, molecular wires [47], C<sub>60</sub> fullerene molecules [8,48] or suspended carbon nanotubes [49,50]. The position of the molecular levels can be tuned with the help of a gate electrode [51,52], while their broadening is given by the dot-lead coupling strength, which depends, e.g., on the lead distance or the metal-molecule anchoring group [53]. Due to their highly energy-dependent and tunable transmission, molecular junctions may also constitute small and efficient power generators or heat pumps. Their theoretical efficiency has been shown to approach the Carnot value in the weak dot-lead coupling limit. [54] However, since moderate level broadening is needed for useful power output, the regime of comparable electronic and phononic time scales becomes interesting.

**Quantum dot model** We consider the well-known Anderson-Holstein model, which is sketched in Fig. 2 and is given by the following Hamiltonian ( $\hbar = 1$ ):

$$H = (\Delta - \mu)d^\dagger d - g\omega_0 d^\dagger d(b^\dagger + b) + \omega_0 b^\dagger b + \sum_{k,a} (\varepsilon_{ka} - \mu)c_{ka}^\dagger c_{ka} - \frac{1}{\sqrt{N}} \sum_{k,a} \left( t_{ka} d^\dagger c_{ka} + t_{ka}^* c_{ka}^\dagger d \right). \quad (1)$$

The organic molecule is represented by a single dot level  $\Delta$  with the fermionic operators  $d^{(\dagger)}$ . Its vibrational degrees of freedom are subsumed into the interaction ( $\propto g\omega_0$ ) with a single optical phonon mode with operators  $b^{(\dagger)}$  and energy  $\omega_0$ . Moreover, the dot level is coupled to the left and right leads ( $\propto t_{ka}$  with  $a = L, R$ ), which are modeled as two continuous sets of free fermion states, with energies  $\varepsilon_{ka}$  and operators  $c_{ka}^{(\dagger)}$ . In equilibrium, the system is characterized by a common chemical potential  $\mu$ . In the nonequilibrium situation, each lead is held at its own thermal equilibrium with the chemical potentials  $\mu_a = \mu - U_a$  [55]. The application of the voltage bias  $\Phi = (U_L - U_R)/e$  is described by adding to (1) the term

$$H_{\text{int}} = \sum_a U_a \sum_k c_{ka}^\dagger c_{ka}, \quad (2)$$

with the electron charge  $e < 0$ . For a given lead density of states  $\Gamma^{(0)}(\omega)$ , the electron current  $J$  through the dot is calculated using the Meir-Wingreen formula [20]

$$J = \frac{e}{2} \int_{-\infty}^{\infty} \frac{d\omega}{2\pi} \Gamma^{(0)}(\omega + \mu) \tilde{A}(\omega; U) [f_L(\omega + U_L) - f_R(\omega + U_R)]. \quad (3)$$

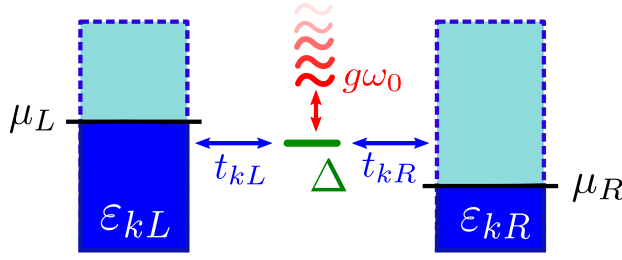


**Fig. 2:** Sketch of the quantum dot model. A single electronic level  $\Delta$  is coupled to two macroscopic leads, each in its own thermal equilibrium with the chemical potentials  $\mu_{L,R}$ . The dot electrons interact with an optical phonon mode of energy  $\omega_0$ .

In the above expression,  $\tilde{A}$  is the electronic dot spectral function, which contains all the effects of the electron-phonon (EP) and dot-lead (DL) interactions at the dot. Its calculation is the central task of the work presented in the following sections.

**Variational ansatz** If we set the DL coupling  $t_{ka} = 0$  in Eq. (1), the Hamiltonian represents an isolated vibrating dot and can be diagonalized via a canonical Lang-Firsov shift transformation [12]. In the corresponding ground state, an electron at the dot is accompanied by a finite number of phonons, in analogy to polarons. In contrast, for vanishing EP coupling  $g = 0$  the Hamiltonian in Eq. (1) reduces to that of a rigid tunneling impurity, and is readily solved in the Green functions formalism [56]. To account for the competition between polaron localization and coherent tunneling in the *full* model, we apply to Eq. (1) two variational shift transformations [19, 57–59], introducing the parameter  $\gamma \in [0, 1]$ :

$$S_1(\gamma) = \exp\{\gamma g(b^\dagger - b)d^\dagger d\}, \quad S_2(\gamma) = \exp\{(1 - \gamma)g(b^\dagger - b)n_d\}. \quad (4)$$

The transformation  $S_2(\gamma)$  models the adiabatic regime, where the equilibrium position of the oscillator is shifted according to the mean occupation  $n_d = \langle d^\dagger d \rangle$  of the dot level. The transformation  $S_1(\gamma)$  describes the antiadiabatic regime, in which the dot deformation adjusts quickly to the presence of an electron. For  $\gamma \rightarrow 1$ , it coincides with the Lang-Firsov transformation. Thus, the parameter  $\gamma$  can be understood as a measure of the polaronic character of the dot state. The transformed Hamiltonian  $\tilde{H} = S_1 S_2 H S_2 S_1$  reads

$$\begin{aligned} \tilde{H} = & (\tilde{\Delta} - \mu) d^\dagger d - C_d(d^\dagger d - n_d) + \omega_0 b^\dagger b + \varepsilon_p(1 - \gamma)^2 n_d^2 \\ & + \sum_{k,a} (\varepsilon_{ka} - \mu) c_{ka}^\dagger c_{ka} - \sum_{k,a} \left( C_{ka} d^\dagger c_{ka} + C_{ka}^\dagger c_{ka}^\dagger d \right), \end{aligned} \quad (5)$$

with so-called polaron binding energy  $\varepsilon_p = g^2 \omega_0$  (which will be used as a measure of the EP coupling strength) and the renormalized dot level and interaction parameters

$$\tilde{\Delta} = \Delta - \varepsilon_p \gamma (2 - \gamma) - 2\varepsilon_p (1 - \gamma)^2 n_d, \quad (6)$$

$$C_{ka} = \frac{t_{ka}}{\sqrt{N}} e^{-\gamma g(b^\dagger - b)}, \quad C_d = g\omega_0 (1 - \gamma)(b^\dagger + b). \quad (7)$$

For finite  $\gamma$ , the transformations reduce the effective EP coupling in  $C_d$  at the cost of an exponential suppression of the effective DL coupling in  $C_{ka}$ . Note that the

transformed Hamiltonian is written in the polaronic picture, i.e., the operators  $d$  and  $b$  in Eq. (5) now represent dressed electrons and the excitations of a shifted oscillator. The original electron and phonon operators read  $\tilde{d} = e^{\gamma g(b^\dagger - b)}d$  and  $\tilde{b} = b + \gamma g d^\dagger d + (1 - \gamma)g n_d$ .

**Polaronic spectral function** To find the electronic spectral function  $\tilde{A}$  needed for the current formula (3), we first factorize the electronic Green function  $\tilde{G}_{dd}$  into polaronic and phononic parts [22–24]:

$$\tilde{G}_{dd}(t_1, t_2; U, t_0) \approx G_{dd}(t_1, t_2; U, t_0) \langle \mathcal{T}_\tau e^{\gamma g(b^\dagger(t_1) - b(t_1))} e^{-\gamma g(b(t_2)^\dagger - b(t_2))} \rangle. \quad (8)$$

The phononic average in Eq. (8) is evaluated assuming an independent Einstein-oscillator. The resulting relations between the electronic ( $\tilde{A}$ ) and polaronic ( $A$ ) spectral functions is given in Eqs. (89) of article I. The polaronic Green function in Eq. (8) is defined as

$$G_{dd}(t_1, t_2; U, t_0) = -\frac{i}{\langle S \rangle} \langle \mathcal{T}_t d(t_1) d^\dagger(t_2) S \rangle, \quad (9)$$

and is a function of complex times  $t \in [t_0, t_0 - i\beta]$ , whereby  $t_0$  is the switch on time of the disturbance  $H_{\text{int}}$  and  $\beta = 1/k_B T$ . The average  $\langle \dots \rangle$  and the time dependence of the operators  $d^{(\dagger)}$  are determined by  $\tilde{H}$  while the external disturbance  $H_{\text{int}}$  is separated in the time-ordered exponential operator

$$S = \mathcal{T}_t \exp \left\{ -i \int_{t_0}^{t_0 - i\beta} dt H_{\text{int}}(t) \right\}. \quad (10)$$

As is shown in detail in Secs. B and C of article I, we write the function  $G_{dd}$  as a functional of a polaronic self-energy  $\Sigma_{dd}$  and use it to derive the equations of motion of the real-time response functions  $g_{dd}^{\gtrless}$ . After a Fourier transformation, the formal solution of the steady-state equations can be written as  $g_{dd}^<(\omega; U) = A(\omega; U) \bar{f}(\omega; U)$  and  $g_{dd}^>(\omega; U) = A(\omega; U)(1 - \bar{f}(\omega; U))$ , with the polaronic dot spectral function

$$A(\omega; U) = \frac{\Gamma(\omega; U)}{\left[ \omega - \tilde{\Delta} + \mu - \mathcal{P} \int \frac{d\omega'}{2\pi} \frac{\Gamma(\omega'; U)}{\omega - \omega'} \right]^2 + \left[ \frac{\Gamma(\omega; U)}{2} \right]^2}, \quad (11)$$

the dot occupation  $\bar{f}(\omega; U) = \Sigma_{dd}^<(\omega; U)/\Gamma(\omega; U)$ , and the damping function  $\Gamma(\omega; U) = \Sigma_{dd}^>(\omega; U) + \Sigma_{dd}^<(\omega; U)$ .

In Sec. D of article I, we derive an approximation to  $\Sigma_{dd}^{\gtrless}$  by adding to  $H_{\text{int}}$  the interaction with fictitious external fields  $\{V\}$ , expressing the equation of motion of  $G_{dd}$  in terms of functional derivatives  $\delta \Sigma_{dd}/\delta V$  and solving it iteratively up to second order in  $C_{ka}$  and  $C_d$ . Letting  $\{V\} \rightarrow 0$ , the Fourier transform of the polaronic self-energy reads

$$\begin{aligned} \Sigma_{dd}^<(\omega; U) &= \Sigma_{dd}^{(1)<}(\omega; U) \\ &+ [(1 - \gamma)g\omega_0]^2 \left[ A(\omega - \omega_0; U) n_B(\omega_0) \bar{f}(\omega - \omega_0; U) \right. \\ &\left. + A(\omega + \omega_0; U) (n_B(\omega_0) + 1) \bar{f}(\omega + \omega_0; U) \right], \end{aligned} \quad (12)$$

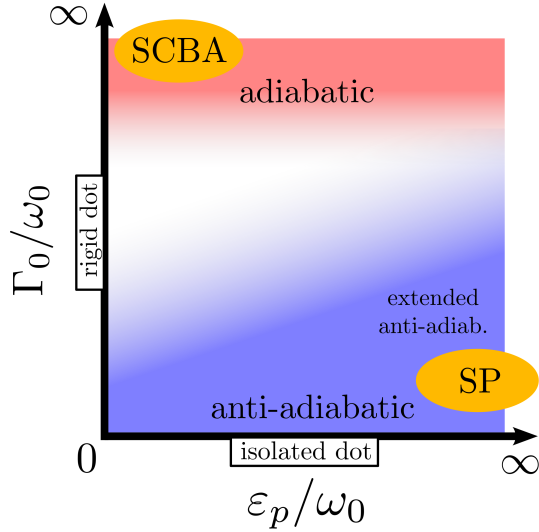


**Fig. 3:** Illustration of the dot-lead and electron-phonon coupling strength regimes given by the relative magnitudes of the tunneling rate  $\Gamma_0$  and the polaron binding energy  $\varepsilon_p$ . The self-consistent Born-approximation (SCBA) and the small polaron approach (SP) are applicable in the adiabatic, weak coupling regime and the (extended) antiadiabatic, strong coupling regime, respectively. The variational calculation allows the investigation of the crossover regime with comparable coupling strengths.

with the result after the first iteration step,

$$\begin{aligned} \Sigma_{dd}^{(1)<}(\omega; U) = & e^{-\gamma^2 g^2 \coth \theta} \sum_a \left\{ I_0(\kappa) \Gamma_a^{(0)}(\omega + \mu) f_a(\omega + U_a) + \sum_{s \geq 1} I_s(\kappa) 2 \sinh(s\theta) \right. \\ & \times \left[ \Gamma_a^{(0)}(\omega + \mu - s\omega_0) n_B(s\omega_0) f_a(\omega + U_a - s\omega_0) \right. \\ & \left. \left. + \Gamma_a^{(0)}(\omega + \mu + s\omega_0) (n_B(s\omega_0) + 1) f_a(\omega + U_a + s\omega_0) \right] \right\}, \end{aligned} \quad (13)$$

and  $\theta = \beta\omega_0/2$  and  $\kappa = \gamma^2 g^2 / \sinh \theta$ . The function  $\Sigma_{dd}^{>}$  follows from Eq. (12) by interchanging  $n_B \leftrightarrow (1 + n_B)$ ,  $f_a \leftrightarrow (1 - f_a)$ , and  $\bar{f} \leftrightarrow (1 - \bar{f})$ .

The self-consistent set of Eqs. (6), (11) and (12) is the central result of our theory and the basis for the numerical calculation of the nonequilibrium dot spectrum and the junction current. The functions  $\Sigma_{dd}^{\geq}$  describe the damping of the dot state resulting from the in- and out-scattering of polaron-like quasiparticles. They account for inelastic (quasielastic) dot-lead transport involving the emission and absorption of an unequal (equal) number of phonons. The corresponding dot spectral function includes terms of arbitrarily high order in  $g$ , through the explicit summation over  $s$  in Eq. (13) and the iteration of the self-consistent equations (11) and (12).

Our result is dependent on the variational parameter  $\gamma$ , which allows for the investigation of the vibrating quantum dot system in a wide range of EP and DL coupling strengths. This is depicted in Fig. 3, whereby we suppose identical leads with  $\Gamma_a^{(0)}(\omega) = \text{const} = \Gamma_0$ . For  $\gamma \rightarrow 0$ , our result corresponds to the self-consistent Born-approximation (SCBA), which starts from the rigid dot and expands the electronic self-energy to second order in  $g\omega_0$  [56]. This approximation is applicable to the adiabatic regime  $\Gamma_0 \gg \omega_0$  with small EP coupling. For  $\gamma \rightarrow 1$ , our approximation is comparable to approaches based on the complete Lang-Firsov transformation [21–24], which are applicable to the strong coupling, antiadiabatic regime  $\Gamma_0 \ll \omega_0$ . Eidelstein *et al.* [60] argued that this regime can be extended to  $\Gamma_0 \lesssim \omega_0$  if the exponential renormaliation of the effective DL coupling is so strong that  $\Gamma_0 e^{-g^2} \ll \omega_0$ . Only when  $\Gamma_0 e^{-g^2}$  approaches  $\omega_0$  the system crosses over to the

adiabatic regime, whereby  $\gamma$  provides a measure of the polaronic character of the dot state.

We determine the optimal parameter,  $\gamma_{\min}$ , by minimizing the thermodynamical potential, which can be derived for  $\Delta T = 0$  using the famous “ $\lambda$ -trick” [61], and reads

$$\Omega = -\frac{1}{\beta} \ln(1 + e^{-\beta(\tilde{\Delta}-\mu)}) + \varepsilon_p(1 - \gamma)^2 n_d^2 - \int \frac{d\omega}{\pi} \bar{f}^{(1)}(\omega) \left\{ \frac{\tilde{\Delta} - \mu - \omega}{|\tilde{\Delta} - \mu - \omega|} + \arctan \left( \frac{\omega - \tilde{\Delta} + \mu - \mathcal{P} \int \frac{d\omega'}{2\pi} \frac{\Gamma^{(1)}(\omega')}{\omega - \omega'}}{\Gamma^{(1)}(\omega)/2} \right) \right\}, \quad (14)$$

with  $\Gamma^{(1)} = \Sigma_{dd}^{(1)>} + \Sigma_{dd}^{(1)<}$  and  $\bar{f}^{(1)} = \Sigma_{dd}^{(1)<}/\Gamma^{(1)}$ .

In the following, we give an overview over our numerical results for the dot spectrum and the linear and nonlinear conductance in different DL and EP coupling regimes. We compare our variational calculation to the appropriate limits, i.e., to the SCBA with  $\gamma = 0$  and the small polaron picture with  $\gamma = 1$ . Thereby we use  $\omega_0 = 1$  as the energy unit and set  $\mu = 0$ . If not otherwise noted, we keep  $T = 0.01$ .

**Results I: Electronic spectral function** Fig. 4(a) presents our results for the adiabatic regime with  $\Gamma_0 = 10$ . The  $\gamma = 0$  spectrum is a single Lorentzian with a width of  $\Gamma_0$ , signaling the hybridization of the dot level with the lead states. Even for strong EP coupling  $\varepsilon_p = 5$ , only small dips and peaks at  $\omega = \pm\omega_0$  suggest a phononic influence [62]. The variational calculation yields  $\gamma_{\min} = 0.28$ . Now the spectrum shows several prominent phononic features at integer multiples of  $\omega_0$  due to logarithmic singularities in the denominator of Eq. (11). Here, incoming high energy particles scatter to lower states via the emission of phonons. Most notably,  $\tilde{A}(0)$  is diminished, meaning transport through the dot remains coherent, but with a lower tunneling amplitude than predicted by the SCBA calculation.

In Fig. 4(b) we consider the antiadiabatic system with  $\Gamma_0 = 0.1$  and moderate EP coupling  $\varepsilon_p = 1$ . The half width of the central Lorentzian peak is now given by  $\tilde{\Gamma}_0 \approx \Gamma_0 e^{-\gamma^2 g^2}$ . Around the central resonance peak at  $\omega = \tilde{\Delta} = 0$ , the dot density of states is exponentially suppressed, which is the hallmark of the so-called Franck-Condon blockade [63]. We find several pronounced side bands separated from the main peak by integers of  $\omega_0$ . They are weighted according to a Poisson distribution with the mean  $\gamma^2 g^2$ , suggesting that incoherent hopping transport takes place via an intermediate polaronic dot state. The variational calculation yields  $\gamma_{\min} = 0.81$ , which, compared to the small polaron case  $\gamma = 1$ , shifts spectral weight from the sidebands back to the main peak.

Lastly, Fig. 4(c) exhibits the dot spectrum in the regime of comparable electronic and phononic time scales with  $\Gamma_0 = 1$  and intermediate EP coupling  $\varepsilon_p = 2$ . We find  $\gamma_{\min} \approx 0.5$  and a dot state that shows characteristics of both limiting cases: A central zero-phonon peak and few phonon sidebands with a width of the order of their spacing, clearly separated by the logarithmic suppression effect. Due to Pauli-blocking, for low temperatures the sidebands are always offset by  $\omega_0$  from the

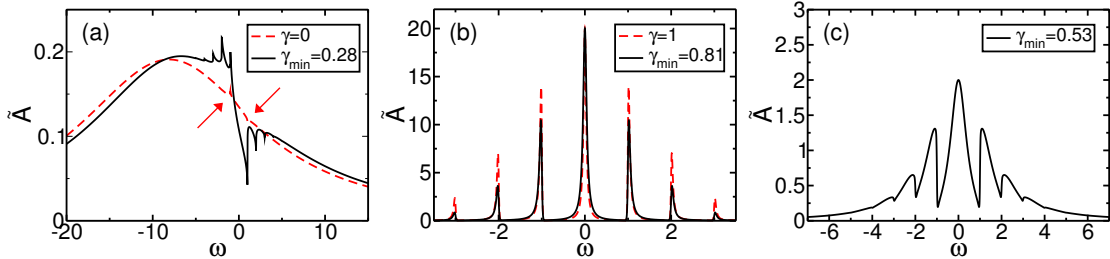


**Fig. 4:** Electronic equilibrium spectral function. Panel (a): Adiabatic regime with  $\Gamma_0 = 10$ ,  $\varepsilon_p = 5$ ,  $\Delta = 0$ . The variational result with  $\gamma_{\min} = 0.28$  is compared to the SCBA with  $\gamma = 0$ . Arrows mark the phononic features. Panel (b): Antiadiabatic regime with  $\Gamma_0 = 0.1$ ,  $\varepsilon_p = 1$ ,  $\Delta = 1$ , and  $\gamma_{\min} = 0.81$ , compared to the small polaron picture with  $\gamma = 1$ . Panel (c): Crossover regime with  $\Gamma_0 = 1$ ,  $\varepsilon_p = 2$ ,  $\Delta = 2$ , and  $\gamma_{\min} = 0.53$ . Adapted from article I.

Fermi level, irrespective of  $\Delta$ . This “floating” [16] of the side bands is missed by single particle approaches [22, 23].

**Results II: Charging transition and linear response** Fig. 5(a) shows how in the intermediate regime with  $\Gamma_0 = 1$  the dot charges as the bare dot level  $\Delta$  is lowered. For growing EP coupling the transition shifts, becomes steeper and even discontinuous. Here the system switches between two stable solutions  $n_d$ , the effective dot level  $\tilde{\Delta}$  skips the Fermi energy, and there is no particle-hole symmetric situation. The parameter  $\gamma_{\min}$  slightly grows with  $\varepsilon_p$ , but is roughly constant as a function of  $\Delta$ .

For vanishing voltage bias  $\Phi \rightarrow 0$ , we express the current as  $J = -L\Phi$ , with the linear conductance

$$L = \lim_{\Phi \rightarrow 0} \{-J/\Phi\} = \frac{e^2 \Gamma_0}{2} \int_{-\infty}^{\infty} \frac{d\omega}{2\pi} [-f'(\omega)] \tilde{A}(\omega). \quad (15)$$

As Fig. 5(b) documents, the linear conductance of the vibrating dot has a maximum at  $\Delta = \varepsilon_p$ , when  $\tilde{\Delta}$  crosses the Fermi energy and resonant tunneling is possible. The signals width decreases with growing  $\varepsilon_p$ , due to the Franck-Condon blockade. This result coincides with the findings of Entin-Wohlmann *et al.* [62] and contradicts the broadening of the resonance shown in the work of Mitra *et al.* [16]. In the discontinuous case the resonance is skipped altogether and the signals maximum decreases. Yet even for strong EP coupling, due to the floating of the phonon side bands we find no signatures that would directly indicate the vibrational structure of the dot state.

If we increase the global temperature to  $T \approx \omega_0$  (cf. Fig. 5(c)), the conductance resonance spreads, since for thermally excited lead electrons the injection gap is reduced. Now, free dot phonons may be absorbed by incident electrons. Our ansatz accounts for this with  $\gamma_{\min}$  approaching one near the resonance. In contrast to the low temperature result, we now find three peaks in the conductance signal: The floating condition is relaxed and phonon side bands contribute. More importantly,

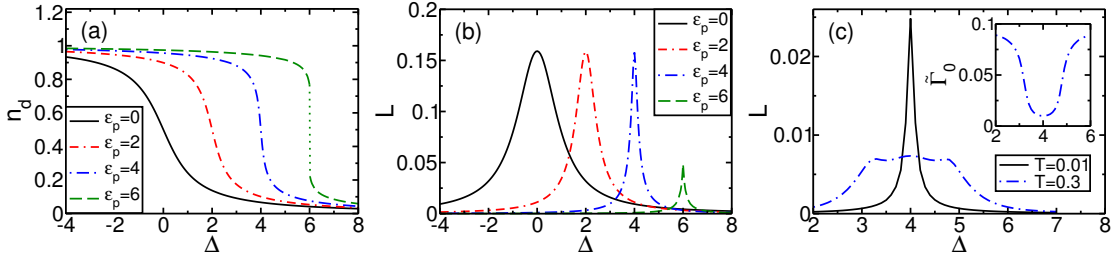


**Fig. 5:** Panels (a) and (b): Equilibrium dot occupation and linear conductance as functions of the bare dot level for  $\Gamma_0 = 1$ ,  $T = 0.01$  and several  $\varepsilon_p$ . Panel (c): Linear conductance as a function of the bare dot level for  $\Gamma_0 = 0.3$ ,  $\varepsilon_p = 4$ , and  $T = 0.3$  compared to the low temperature case. Inset: renormalized DL coupling strength. Adapted from article I.

when the polaron forms, the effective DL coupling reduces by one order of magnitude (see inset), causing dips in the conductance. That is why the side peaks in  $L$  are not situated a full  $\omega_0$  away from the main resonance.

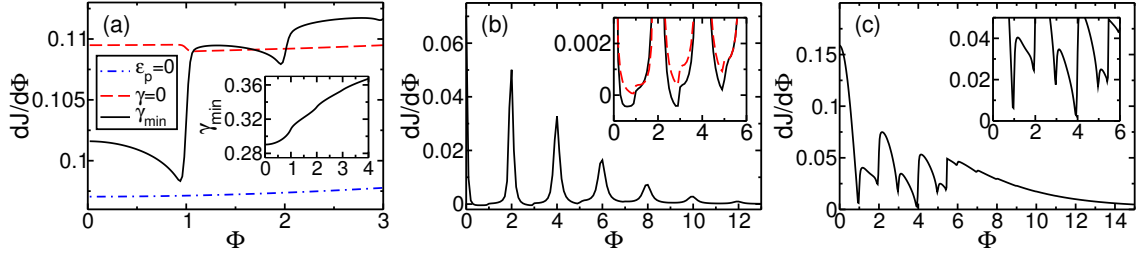
**Results III: Differential conductance** When we increase the voltage bias  $\Phi$  between the leads, the nonequilibrium spectral functions of different adiabaticity and coupling regimes retain the essential features of their equilibrium counterparts in Fig. 4 (cf. Figs. 4, 5, and 6 in article I) We now examine the influence of these features on the differential conductance  $dJ/d\Phi$  of the quantum dot system.

Figure 6(a) presents our results for the adiabatic, off-resonant tunneling regime ( $\Gamma_0 = 10$ ,  $\Delta = 8$ ,  $\varepsilon_p = 2$ ). Compared to the rigid dot, the  $\gamma = 0$  calculation predicts an increase in the low voltage conductance due to the lowering of the effective dot level. For finite  $\gamma_{\min}$  (see inset) this positive contribution is countered by the reduction of the effective DL coupling. This effect strengthens as the voltage grows and causes a pronounced dip in the differential conductance. At  $\Phi = \omega_0 = 1$ , phonon emission by incident electrons becomes possible and opens up a new, inelastic transport channel. This is typically signalled by a step in the conductance signal. For  $\gamma = 0$ , we find a single small downward step, while for finite  $\gamma_{\min}$ , there are several large upward steps, which are followed by the DL renormalization dip.

In the antiadiabatic, resonant tunneling regime ( $\Gamma_0 = 0.1$ ,  $\Delta = \varepsilon_p = 2$ ), the conductance signal presented in Figs. 6(b) show pronounced peaks whenever the voltage equals multiple integers of  $2\omega_0$ . They indicate resonant transport through the polaronic side bands in  $\tilde{A}$ , i.e., via a transient polaronic dot state. Between these peaks, due to the Franck-Condon blockade, the differential conductance approaches zero. For  $\gamma = 1$  it stays strictly positive. In the variational calculation, where the polaronic renormalization grows stronger with increasing voltage bias, the differential conductance becomes negative. At  $\Phi = 1$  and  $\Phi = 3$ , positive inelastic conductance steps (as we have seen in the adiabatic case) render the differential conductance positive again.

Fig. 6(c) shows the conductance signal in the resonant, intermediate coupling regime ( $\Gamma_0 = 1$ ,  $\Delta = \varepsilon_p = 2$ ). As the voltage grows, the polaron effect strength-





**Fig. 6:** Differential conductance as a function of the voltage bias. Panel (a): Adiabatic, off-resonant regime with  $\Gamma_0 = 10$ ,  $\Delta = 8$ , and  $\varepsilon_p = 2$ . The variational result ( $\gamma_{\min}$  given in inset) is compared to the SCBA with  $\gamma = 0$  and the rigid dot with  $\varepsilon_p = 0$ . Panel (b): Antiadiabatic regime with  $\Gamma_0 = 0.1$ ,  $\Delta = 2$ , and  $\varepsilon_p = 2$ . Inset: Zoom on the low-voltage region and comparison with the small polaron picture with  $\gamma = 1$ . Panel (c): Crossover regime with  $\Gamma_0 = 1$ ,  $\Delta = 2$ , and  $\varepsilon_p = 2$ . Inset: Zoom on the low-voltage region. Adapted from articles I and II.

ens whenever a new inelastic channel is accessible, as is shown by means of the renormalized DL coupling  $\tilde{\Gamma}_0 = \Gamma_0 e^{-\gamma^2 g^2}$  in the inset. The vibrational features in the conductance signal overlap, have comparable spectral weight and are heavily modulated by the voltage dependent polaronic renormalization. There is no clear distinction between quasielastic peaks and inelastic steps. Moreover, the differential conductance approaches zero between the broad conductance peaks, but remains strictly positive. In their work, La Magna and Deretzis [19] suggested the variationally determined renormalization of the dot-lead coupling as a possible mechanism for the observed nonlinear behavior of the differential conductance. We conclude that for the antiadiabatic regime, this remains true within our approximation. In the intermediate regime however, the occurrence of negative differential conductance is suppressed when multi-phonon transport processes are taken into account.

**Results IV: Sticking effect** In the previous section, the conductance features of the system have mainly been explained through the voltage dependent renormalization of the DL coupling. In Fig. 7 we present another interesting consequence of the variational polaron formation, concerning the effective dot level. For weak to intermediate EP coupling  $\varepsilon_p = 0.11 \dots 0.33$ , our result for  $\gamma = 0$  is in good agreement with the work of Entin-Wohlman *et al.* [62]. However, for  $\varepsilon_p = 0.33$  the variational calculation shows an additional peak-like feature atop the broad conductance resonance. This can be understood from Fig. 7(b): With growing voltage bias the variational parameter increases, so that the level  $\tilde{\Delta}$  shifts upwards until at  $\Phi = 0.62$  it equals the chemical potential of the right lead. For  $0.65 < \Phi < 0.8$ , the variational parameter decreases in such a way that  $\tilde{\Delta}$  stays in resonance with the sinking lead chemical potential, simultaneously relaxing the renormalization of the DL coupling. Thereby, the system maximizes the tunneling current, forming the new conductance peak. For strong EP coupling, this “sticking” of the polaronic dot level to the lead chemical potentials may occur in conjunction with negative differential conductance, as Fig. 6 of article II shows.

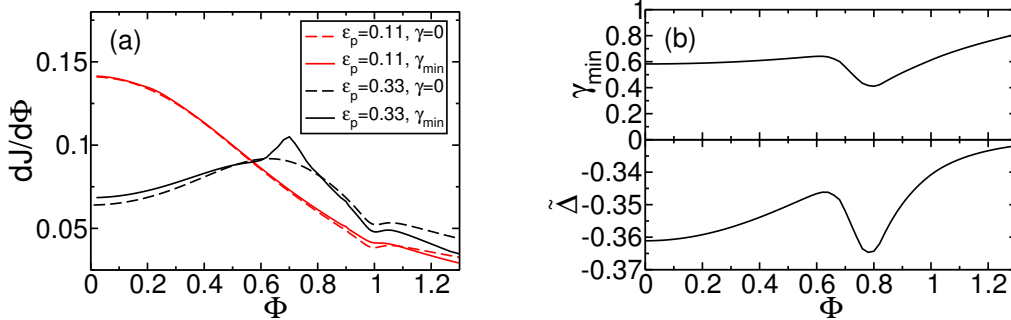


**Fig. 7:** Panel (a): Differential conductance as a function of the voltage for  $\Gamma_0 = 0.33$ ,  $\Delta = 0$  and different  $\epsilon_p$ . The variational calculation is compared to the SCBA with  $\gamma = 0$ . Panel (b): Optimal variational parameter  $\gamma_{\min}$  and renormalized dot-level  $\tilde{\Delta}$  as functions of the voltage for  $\epsilon_p = 0.33$ . Adapted from article II.

**Thermoelectric transport** In article III we extend the theory presented above to incorporate a finite temperature bias between the leads. In addition to the chemical potentials  $\mu_a$ , the leads are now characterized by the temperatures  $T_a$ . The dot oscillator is supposed to be strongly coupled to a heat bath of temperature  $T_P$ .

In this situation the effective electron temperature at the dot is not generally known. In Sec. B of article III we argue in detail how the Kadanoff-Baym formalism can, nevertheless, be applied to this situation. In short, we note that the formalism does not refer to some special properties of the statistical ensemble. We therefore generalize the definitions (9) and (10) to time variables in the interval  $[t_0, t_0 - i\sigma]$ , replacing the usual  $\beta = 1/k_B T$  with a time ordering parameter  $\sigma$  that has no physical meaning. We neglect initial correlations and assume that before the disturbance  $H_{\text{int}}$  was turned on, the system was in a steady state with the temperatures  $T_a$  and  $T_P$ . The function  $G_{dd}$  defined in this way serves purely as a functional of the time ordered operators determining  $g_{dd}^{\geq}$ . As a result, the solution of the steady-state equations is formally equivalent to the result in Eq. (11). We concentrate on the effect of the DL coupling renormalization and use the self-energy function after the first iteration step, i.e., Eq. (13). The different temperatures enter the self-energy through the Bose function  $n_B$  of the phonon bath and the Fermi functions  $f_a$  of the leads. Lastly, we suppose the parameter  $\gamma_{\min}$  to be mainly determined by the EP and DL interaction and assume the equilibrium thermodynamic potential of the system to be a reasonable approximation for the variational function.

**Results V: Thermocurrent and thermovoltage** In the following, we consider the particle current through the junction resulting from a finite temperature difference  $\Delta T$  between the leads. Thereby we suppose  $T_L = T + \Delta T$  and  $T_P = T_R = T$  with  $T = 0.01$ . Figures 8 and 9 present our results in the regime of intermediate DL and EP coupling. For small  $\Delta T$ , it is instructive to consider the thermoelectrical

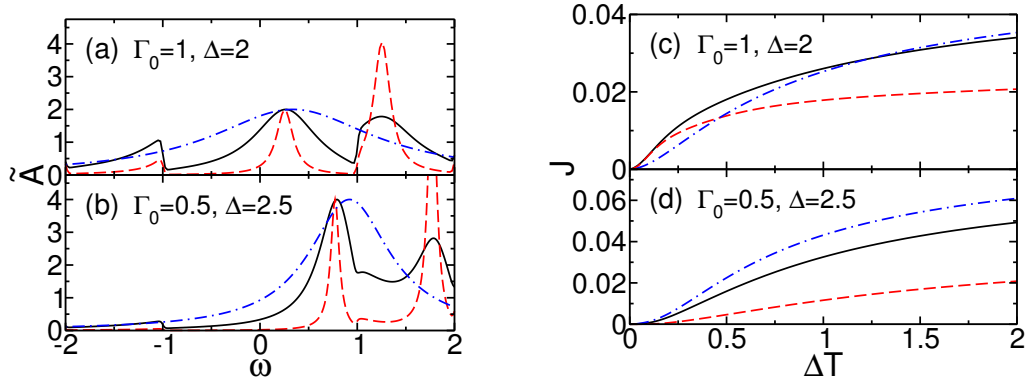


**Fig. 8:** Panel (a): Equilibrium electronic spectral function near resonance with  $\Gamma_0 = 1$ ,  $\Delta = 2$ , and  $\varepsilon_p = 2$ . The variational calculation (black line) is compared to the small polaron limit  $\gamma = 1$  (red dashed line) and to the result for  $\varepsilon_p = 0$  (blue dot-dashed line). In the latter two cases  $\Delta$  is set in such a way that  $\tilde{\Delta}$  is the same as in the variational calculation. Panel (b): Same as (a), but for  $\Gamma_0 = 0.5$ ,  $\Delta = 2.5$ ,  $\varepsilon_p = 2$ . Panels (c) and (d): Junction current as a function of the temperature bias for the same parameters as in (a) and (b), respectively. Adapted from article III.

conductance defined as

$$X = \lim_{\Delta T \rightarrow 0} \{TJ/\Delta T\} = \frac{e\Gamma_0}{2}\beta \int_{-\infty}^{\infty} \frac{d\omega}{2\pi} \omega f'(\omega) \tilde{A}(\omega). \quad (16)$$

It implies that the net linear thermoelectric current is determined by the flow and counterflow of hot and cold charge carriers near the Fermi level. In the particle-hole symmetric case with  $\tilde{\Delta} = 0$  these flows cancel exactly. Near resonance ( $0 < |\tilde{\Delta}| < \tilde{\Gamma}_0$ ), finite EP interaction increases the slope of  $\tilde{A}$  around the Fermi level, as can be seen in Fig. 8(a). Now the quantum dot acts as a more effective energy filter and the linear thermoelectric response increases compared to the noninteracting case, as can be seen in Fig. 8(c). In contrast, in the tunneling regime ( $|\tilde{\Delta}| > \tilde{\Gamma}_0$ ) the value and slope of  $\tilde{A}$  at the Fermi surface is strongly diminished due to the Franck-Condon blockade. Hence, the linear thermocurrent decreases compared to the rigid dot, as is verified in Figs. 8(b) and (d). We find however, that the maximum current through the vibrating molecule is always smaller than for the rigid dot, since considerable spectral weight is shifted to the floating phonon side bands. Even for large  $\Delta T$ , their contribution is exponentially small.

In a typical experiment, the strength of the thermoelectric effect is measured via the thermovoltage  $\Phi_0$ , i.e., the voltage bias necessary to cancel the thermally induced current. In the off-resonant situation considered in Fig. 8(b), the Franck-Condon blockade reduces the electrical conductance. Consequently, the voltage bias  $\Phi_0$  required to compensate the thermally induced current grows compared to the rigid dot, as Figures 9(a) shows. For large temperature differences, we find a maximum value  $\Phi_0 = 1.5$ . Here one of the lead chemical potentials crosses the zero-phonon peak at  $\omega = \Phi_0/2$  in the spectrum (cf. Fig. 8(b)). The systems conductance grows considerably and any thermally induced current can easily be compensated

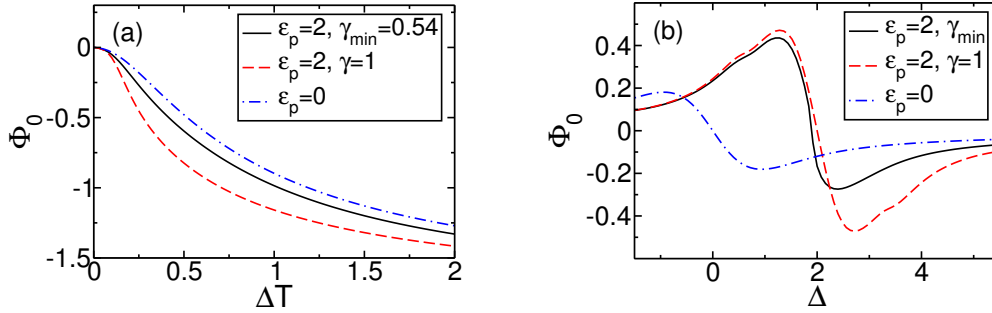


**Fig. 9:** Panel (a): Thermovoltage as a function of the temperature bias for  $\Gamma_0 = 0.5$ ,  $\varepsilon_p = 2$ , and  $\Delta = 2.5$ . Panel (b): Thermovoltage as a function of the bare dot level for  $\Gamma_0 = 0.5$ ,  $\varepsilon_p = 2$ , and  $\Delta T = 0.25$ . Adapted from article III.

by a slight growth in  $\Phi$ . That is why for fixed  $\tilde{\Delta}$ , we find no phononic features in  $\Phi_0(\Delta T)$ .

Lastly, in Fig. 9(b) we fix the temperature bias  $\Delta T = 0.25$  and vary the dot level. The thermovoltage signal runs linearly through zero, resembling the tooth-like thermopower predicted in Ref. [64] and measured in Ref. [51]. For temperature differences of the order of the phonon energy, the floating condition of the phonon side bands is relaxed. When the side bands cross the Fermi surface, we find slight drops in the thermovoltage, that hint at the polaron-like character of the dot state.

**Summary and outlook** In the work presented here, we have investigated the steady-state thermoelectric transport through a contacted organic molecule. Based on the Anderson-Holstein model for a vibrating quantum dot, we calculated the systems interacting spectral function and self-energy within the nonequilibrium Green function formalism. To account for the polaronic character of the dot state we applied a variational Lang-Firsov transformation and determined the optimal variational parameter self-consistently by minimizing the thermodynamic potential. This allowed a detailed study of the dot spectrum for small-to-large DL coupling and weak-to-strong EP interaction and an investigation of the polaronic signatures in the transport properties of the system.

In the adiabatic regime, our variational calculation shifts spectral weight from elastic to inelastic transport processes. Though transport remains overall coherent, inelastic scattering causes pronounced upward steps in the differential conductance. In the extended antiadiabatic regime, prominent conductance peaks signal incoherent transport through a transient polaronic dot state. Between these peaks, the growing polaron effect causes negative differential conductance. In the intermediate regime, our results confirm that the  $\Delta$ -dependent linear conductance signal narrows with growing EP interaction due to the Franck Condon blockade effect. Only for temperatures comparable to the phonon energy, secondary resonances arise, since now the polaron effect grows stronger when the dot level approaches resonance. When the renormalized DL coupling becomes larger than the phonon energy, the occurrence of negative differential conductance is prevented by the onset of inelastic

transport. The step- and peak-like signatures of inelastic and quasi-elastic transport have comparable weight. In the off-resonant situation, the polaronic level sticks to the shifting lead chemical potentials, thereby creating a new, peak-like conductance feature.

The influence of polaron formation on the thermoelectric effect is strongly dependent on the relative position of the dot level to the lead Fermi-surfaces. Near resonance, the Franck-Condon blockade increases the imbalance between the streams of hot and cold carriers, thereby boosting the induced current. As a function of  $\Delta T$ , the thermo-voltage shows no polaronic features, since the thermocurrent is small and is easily compensated by zero-phonon transport. As a function of the dot level, however, weak polaronic sidebands arise when  $\Delta T$  is of the order of  $\omega_0$  and the floating condition is relaxed.

A possible extension of our work concerns the inclusion of Coulomb interaction effects: For a combined Holstein-Hubbard quantum dot model strong EP coupling may result in a net attractive Coulomb interaction. [65] Andergassen *et al.* [66] argued that for the negative- $U$  Anderson model the charge Kondo effect enhances the thermoelectric response due to a highly asymmetric dot spectral function. Our variational ansatz might account for the competition of a repulsive dot potential with the negative polaronic level shift and, therefore, interpolate between the positive- $U$  Holstein-Hubbard dot model and an effective anisotropic Kondo regime.

Moreover, we have not yet considered energy transport through the junction. Energy deposition, i.e., heating or cooling of the molecule should strongly depend on the renormalized electron-phonon interaction given by the variational parameter. Preferably, such a calculation would also account for the dynamics of the phonon subsystem by means of nonequilibrium phonon Green functions. The resulting effective temperature of the dot electrons could to be determined numerically [67]. In this way, the nonlinear behaviour of the variational parameter, which was responsible for the negative differential conductance, could be carried over to the discussion of thermoelectric transport.

While the local Holstein coupling captures the molecules vibrations, the deformation of the dot-lead anchoring groups could be modeled by introducing phonon-affected dot-lead hopping, in analogy to the Edwards fermion-boson model [68–71]. The latter describes a particle distorting an ordered background medium. Unrestricted electron hopping is amended by a term that creates (destroys) a boson at the site the particle leaves (enters). Then particle mobility is governed by the relaxation rate of the resulting string of background fluctuations. It would be interesting to investigate this “string effect” when it is restricted to few sites at the quantum dot.

Lastly, in the light of recent advances in the fabrication of nanostructures, new geometries should be considered, like multi-terminal junctions or a molecule placed on an Aharonov-Bohm ring.

### 1.3 Luminescence of trapped semiconductor excitons

The theoretical work presented here was motivated by recent experiments on natural cuprous oxide crystals performed by Stolz *et al.*, which are sketched in Fig. 10 and described in detail in article VI. Excitons of the so-called yellow series in cuprous oxide ( $\text{Cu}_2\text{O}$ ) have a large binding energy of 150 meV and a Mott density of  $3 \cdot 10^{18} \text{ cm}^{-3}$  at cryogenic temperatures [72, 73]. Due to the doubly degenerate valence and conduction bands, the ground state of this series splits into the triply degenerate orthoexciton and the nondegenerate paraexciton. The orthoexciton is only weakly optically allowed while the paraexciton is optically forbidden in all orders. Their lifetime is of the order of microseconds, so that thermodynamic quasi-equilibrium may be reached. In the experiment, excitons are created via laser excitation. To increase particle density, stress is applied to the crystal, which deforms the band structure and creates an effective trapping potential for the paraexcitons and two of the orthoexciton species. The trapped excitons decay by emitting light which is imaged on a spectrograph. Luminescence, therefore, is the principal method of detection. It contains information about the exciton energy spectrum, their spatial density distribution and, possibly, on whether an exciton condensate has formed.

**Model: Multispecies trapped boson gas** Our calculation of the thermodynamics of a  $K$ -component exciton system is based on the Hamiltonian typically used for a gas of weakly interacting structureless bosons. It is modified by introducing the sum over a species index  $i$ . In the grand canonical ensemble it reads:

$$\begin{aligned} \mathcal{H} = & \sum_{i=1}^K \int d^3\mathbf{r} \psi_i^\dagger(\mathbf{r}, t) \left( -\frac{\hbar^2 \nabla^2}{2M_i} + V_i(\mathbf{r}) - \mu_i \right) \psi_i(\mathbf{r}, t) \\ & + \frac{1}{2} \sum_{i,j=1}^K \int d^3\mathbf{r} h_{ij} \psi_i^\dagger(\mathbf{r}, t) \psi_j^\dagger(\mathbf{r}, t) \psi_j(\mathbf{r}, t) \psi_i(\mathbf{r}, t). \end{aligned} \quad (17)$$

Here,  $\psi_i(\mathbf{r}, t)$  is the bosonic field operator of exciton species  $i$ , with the respective trap potential  $V_i$  and the chemical potential  $\mu_i$ . We assume a contact potential for the exciton–exciton interaction, with the intra- and inter-species interaction strengths  $h_{ij} = 2\pi\hbar^2(M_i^{-1} + M_j^{-1})a_{ij}^s$  given by the respective s-wave scattering lengths  $a_{ij}^s$ .

The field operators  $\psi_i(\mathbf{r}, t)$  are decomposed using the Bogoliubov prescription  $\psi_i(\mathbf{r}, t) = \Phi_i(\mathbf{r}) + \tilde{\psi}_i(\mathbf{r}, t)$ , with the condensate wave functions  $\Phi_i(\mathbf{r}) = \langle \psi_i(\mathbf{r}, t) \rangle = \langle \psi_i(\mathbf{r}) \rangle$  and the operators of the noncondensed excitons  $\tilde{\psi}_i(\mathbf{r}, t)$ . Then the Heisenberg equations of motion  $i\hbar\partial_t\psi_i = [\psi_i, \mathcal{H}]$  give  $2K$  coupled equations (arguments dropped

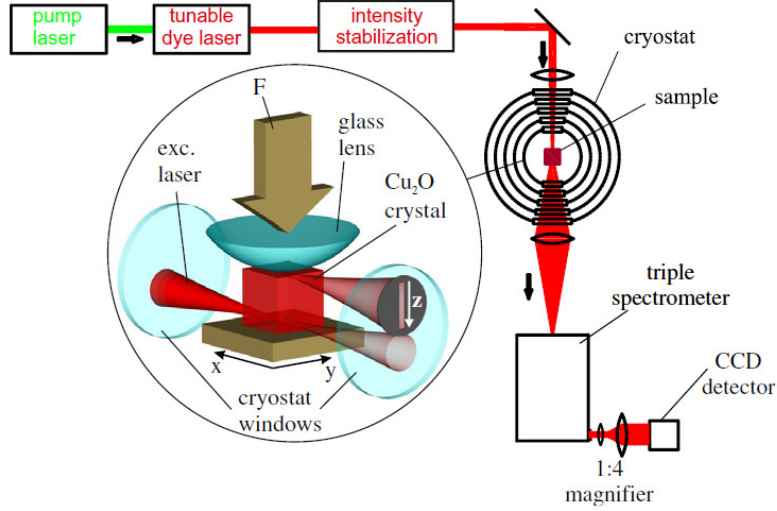


**Fig. 10:** Experimental setup. A small cuprous oxide crystal is cooled to ultralow temperatures in a cryostat. Along the  $z$ -axis, pressure is applied via a glass lens. Excitons are created by focusing a dye laser (propagating along the  $x$ -axis) close to the induced strain trap. The excitons diffuse towards the trap center, reaching thermal quasi-equilibrium. Their decay luminescence signal is monitored via a CCD-detector and spatially resolved along the  $y$ - and  $z$ -direction. Adapted from article VI.

for brevity), the so-called Gross-Pitaevskii equations for the condensates,

$$0 = \left( -\frac{\hbar^2 \nabla^2}{2M_i} + V_i - \mu_i + h_{ii}(n_{ii} + \tilde{n}_{ii}) + \sum_{j \neq i} h_{ij} n_{jj} \right) \Phi_i + h_{ii} \tilde{m}_{ii} \Phi_i^* + \sum_{j \neq i} h_{ij} (\tilde{n}_{ji} \Phi_j + \tilde{m}_{ji} \Phi_j^*), \quad (18)$$

and the equations of motion for the noncondensed excitons,

$$i\hbar \frac{\partial \tilde{\psi}_i}{\partial t} = \left( -\frac{\hbar^2 \nabla^2}{2M_i} + V_i - \mu_i + 2h_{ii} n_{ii} + \sum_{j \neq i} h_{ij} n_{jj} \right) \tilde{\psi}_i + h_{ii} m_{ii} \tilde{\psi}_i^\dagger + \sum_{j \neq i} h_{ij} (n_{ij} \tilde{\psi}_j + m_{ij} \tilde{\psi}_j^\dagger), \quad (19)$$

with the averages  $n_{ij} \equiv \Phi_j^* \Phi_i + \tilde{n}_{ij}$ ,  $m_{ij} \equiv \Phi_j \Phi_i + \tilde{m}_{ij}$ ,  $\tilde{n}_{ij} = \langle \tilde{\psi}_i^\dagger \tilde{\psi}_j \rangle$ , and  $\tilde{m}_{ij} = \langle \tilde{\psi}_i \tilde{\psi}_j \rangle$ . As a first approximation, we neglect the nondiagonal averages with  $j \neq i$  in Eqs. (18) and (19). Also, we suppose the extension of the potential trap to be large compared to the thermal de Broglie wavelength of the excitons. Then we can apply the local density approximation, i.e., we treat the exciton gas as locally homogeneous, setting  $\nabla^2 \rightarrow -|\mathbf{k}|^2$  with a wavevector  $\mathbf{k}$  in Eq. (19). For the same reason we neglect the kinetic energy term in (18). Then the spatial dependence enters our equations solely

through the external potentials  $V_i$ . With these simplifications, Eq. (19) is solved by a linear Bogoliubov transformation,

$$\tilde{\psi}_i = \sum_{\mathbf{k}} \left[ u_i(\mathbf{k}) b_i(\mathbf{k}) e^{-iE_i(\mathbf{k})t/\hbar} + v_i^*(\mathbf{k}) b_i^\dagger(\mathbf{k}) e^{iE_i(\mathbf{k})t/\hbar} \right], \quad (20)$$

with the creation and annihilation operators  $b_i^{(\dagger)}$  of new quasiparticles, so-called bogolons. The densities  $n_i^T \equiv \tilde{n}_{ii}$  of noncondensed excitons are given by

$$n_i^T(\mathbf{r}) = \int \frac{d^3\mathbf{k}}{8\pi^3} \left[ \frac{L_i(\mathbf{k}, \mathbf{r})}{E_i(\mathbf{k}, \mathbf{r})} \left( n_B(E_i(\mathbf{k}, \mathbf{r})) + \frac{1}{2} \right) - \frac{1}{2} \right] \Theta(E_i(\mathbf{k}, \mathbf{r})^2) \quad (21)$$

with  $n_B(E) = [\exp(E/k_B T) - 1]^{-1}$ . To guarantee gapless excitation spectra  $E_i$ , we apply the Popov approximation, neglecting the anomalous averages  $\tilde{m}_{ii}$  [44]. Then the bogolon dispersion reads

$$E_i(\mathbf{k}, \mathbf{r}) = \sqrt{L_i(\mathbf{k}, \mathbf{r})^2 - (h_{ii} n_i^c(\mathbf{r}))^2}, \quad (22)$$

$$L_i(\mathbf{k}, \mathbf{r}) = \frac{\hbar^2 k^2}{2M_i} + V_i(\mathbf{r}) - \mu_i + 2h_{ii} n_i(\mathbf{r}) + \sum_{j \neq i} h_{ij} n_j(\mathbf{r}), \quad (23)$$

with  $n_i^c \equiv |\Phi_i|^2$  and  $n_i \equiv n_{ii} = n_i^T + n_i^c$ . From the simplified Gross-Pitaevskii equation, the condensate densities follow as

$$n_i^c(\mathbf{r}) = \frac{1}{h_{ii}} \left( \mu_i - V_i(\mathbf{r}) - 2h_{ii} n_i^T(\mathbf{r}) - \sum_{j \neq i} h_{ij} n_j(\mathbf{r}) \right), \quad (24)$$

whenever this expression is nonnegative, while  $n_i^c(\mathbf{r}) = 0$  otherwise. Equations (21)-(24) have to be solved self-consistently.

**Luminescence spectrum** In the articles IV and V, we suppose that the luminescence intensity spectrum is determined by the excitonic spectral function according to the formula by Shi-Verechaka [44, 74]:

$$I_i(\mathbf{r}, \omega) \propto 2\pi |S_i(0)|^2 \delta(\hbar\omega' - \mu_i) n_i^c(\mathbf{r}) + \sum_{\mathbf{k} \neq 0} |S_i(\mathbf{k})|^2 n_B(\hbar\omega' - \mu_i) A_i(\mathbf{r}, \mathbf{k}, \hbar\omega' - \mu_i). \quad (25)$$

The first term in Eq. (25) contains the condensate peak, the second term accounts for the luminescence of non-condensed particles. The latter is given by the exciton spectral function, which follows from the Bogoliubov amplitudes  $u_i$  and  $v_i$  and the quasiparticle spectrum in (22):

$$A_i(\mathbf{r}, \mathbf{k}, \omega) = 2\pi\hbar \left[ u_i^2(\mathbf{k}, \mathbf{r}) \delta(\hbar\omega - E_i(\mathbf{k}, \mathbf{r})) - v_i^2(\mathbf{k}, \mathbf{r}) \delta(\hbar\omega + E_i(\mathbf{k}, \mathbf{r})) \right]. \quad (26)$$

In  $\text{Cu}_2\text{O}$ , orthoexciton decay takes place via phonon emission, so that  $\omega' = \omega - E_g/\hbar - \omega_{\text{phonon}}$  with  $E_g$  being the excitonic band gap. The paraexcitons decay directly, so we set  $\omega' = \omega - E_g/\hbar$  and  $S(\mathbf{k}) = S_0 \delta(\mathbf{k} - \mathbf{k}_0)$  with  $\mathbf{k}_0$  being the wavevector at the intersection of photon and exciton dispersions. Consequently, in our approximation, the paraexciton condensate with  $\mathbf{k} = 0$  does not contribute to the luminescence process.



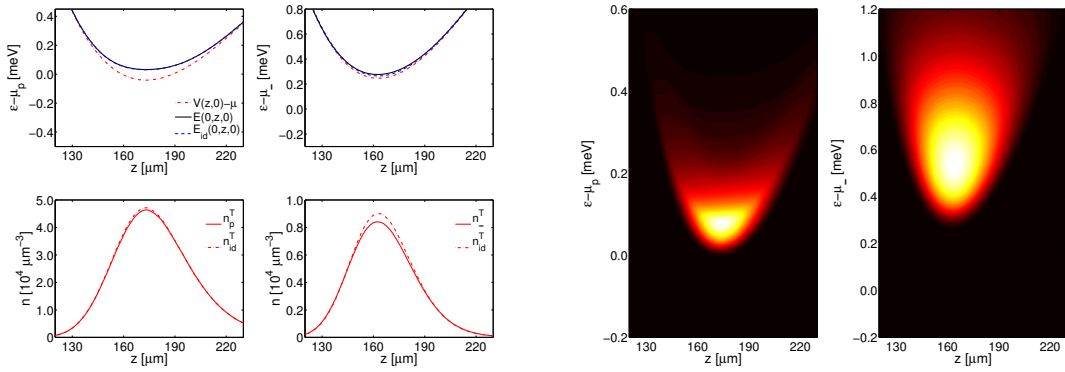


**Fig. 11:** Left side: Dispersions and density profiles in  $z$ -direction at  $(x, y) = (0, 0)$  for paraexcitons (left column) and orthoexcitons (right column) with  $T = 2.2\text{K}$ ,  $N_p = 5 \times 10^9$ , and  $N_- = N_+ = 5 \times 10^8$ . Right side: Corresponding luminescence spectra. Adapted from article IV.

**Results I: Multispecies luminescence** Figures 11-13 present our results for the equilibrium particle densities and emission spectra of trapped  $\text{Cu}_2\text{O}$  paraexcitons (labeled ‘ $p$ ’), and orthoexcitons (‘+’ and ‘-’). To account for the experimental situation, we convolute the emission spectrum in Eq. (25) with a slit function  $\exp[-(\omega/\Delta)^4]$ , with spectral resolution  $\Delta$ . Moreover, we consider the luminescence spectrum in  $z$ -direction, by integrating over the  $x$ - and  $y$ -directions. The respective (cylindrically symmetrical) trapping potentials  $V_i$  were fitted to experimental data. To illustrate our results, we assign each species one of two possible particle numbers,  $N_i = 5 \cdot 10^9$  and  $N_i = 5 \cdot 10^8$ , and vary the temperature around the respective single species critical values  $T_c^0 \approx 2\text{K}$  and  $T_c^0 \approx 1\text{K}$ . We note that the description of exciton-exciton interaction strengths is a long-standing problem. The values used here are deduced from the scattering lengths of the positronium problem given in Ref. [75]:  $h_{++} = h_{--} = 0.71 h_{pp}$ ,  $h_{p+} = h_{p-} = 0.33 h_{pp}$ , and  $h_{+-} = 1.77 h_{pp}$ , with  $h_{pp} = 7.5 \cdot 10^{-4} \mu\text{eV} \mu\text{m}^3$ .

In Fig.11 we set  $N_p = 5 \cdot 10^9$  and  $N_{\pm} = 5 \cdot 10^8$ , with  $T = 2.2 \text{ K}$  well above both of the single species critical temperatures. The interspecies interaction causes a noticeable shift of the orthoexciton population and a weak renormalization of the Bogoliubov dispersions  $E_i$ , which nevertheless roughly follow the external potentials. Since  $|\mathbf{k}_0| \approx 30 \mu\text{m}^{-1}$  is rather small, the zero-phonon emission spectrum of the paraexcitons resembles the minimal excitation energy  $E_p(\mathbf{k} = 0, z, \varrho = 0)$ , while for orthoexcitons, every  $\mathbf{k}$ -vector contributes and we find a broad energy distribution.

If we lower the temperature to  $T = 1.2 \text{ K}$ , the paraexcitons form a condensate. As can be seen in Fig.12, their dispersion is cut at the chemical potential, which exceeds the bare trapping potential. Now the luminescence spectrum shows a flat bottom and a weak secondary Bogolibov branch, both of which could act as experimental footprints of the otherwise undetectable paraexciton condensate. In contrast to the single species case, we find no orthoexciton condensate in the full calculation: The presence of multiple repulsive species lowers the critical temperature. Because of the different minimum positions of the para- and orthoexciton potentials, the thermal

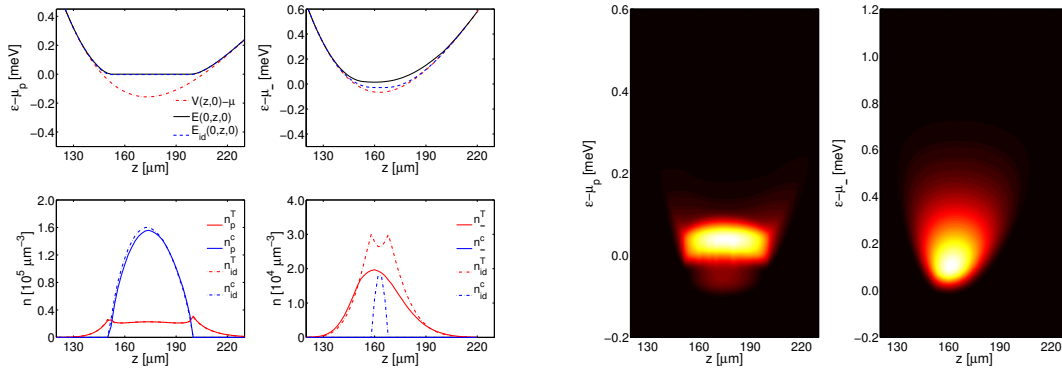


**Fig. 12:** Left side: Dispersions and density profiles in  $z$ -direction at  $(x, y) = (0, 0)$  for paraexcitons (left column) and orthoexcitons (right column) with  $T = 1.2\text{K}$ ,  $N_p = 5 \times 10^9$ , and  $N_- = N_+ = 5 \times 10^8$ . Right side: Corresponding luminescence spectra. Adapted from article IV.

orthoexciton cloud is pushed aside, which is reflected in their emission spectrum.

Next, we keep  $T = 1.2\text{K}$ , but exchange the particle numbers of para- and orthoexcitons. The results are shown in Fig.13. Both orthoexciton species condense and, due to their strong repulsion, separate into a ball-and-shell structure with finite overlap [37, 38]. With  $h_{+-}^2 > h_{++}h_{--}$ , our interaction parameters fulfill the condition for phase-separation of interacting trapped condensates [37, 39]. The combined orthoexciton emission spectrum shows no clear sign of this phase separation. However, the displacement of the noncondensed paraexciton cloud and the resulting distortion of the emission spectrum is strongest in the area of overlapping orthoexciton condensates. As we argued in article V, this W-shaped signature could provide an indirect footprint of a phase separation of orthoexciton condensates. If detected, it would suggest that  $h_{+-} > h_{++}$ .

If we lower the temperature to  $T = 0.8\text{K}$  (not shown) all the species condense. The ortho- and paraexciton condensates do not separate due to their weak interaction. The paraexciton spectrum develops a flat bottom and the aforementioned W-shaped distortion vanishes.

**Extended luminescence theory** The luminescence formula according to Shi [44] used in the articles IV and V takes into account “normal” processes that involve the annihilation of an exciton and subsequent creation of a photon. To be consistent with the Bogoliubov picture of condensed excitons, however, anomalous processes should also be included. The aim of article VII was to derive such an expression for the zero-phonon paraexciton decay luminescence.

As seen above, the Bogoliubov transformation converts the system of interacting excitons into a system of noninteracting bogolons with the operators  $b_{\mathbf{q}}^{(\dagger)}$  and the dispersion  $E_{\mathbf{q}}$ . Similarly, we write the photon field as a sum of oscillator modes with the operators  $a_{\mathbf{q}}^{(\dagger)}$  and the dispersion  $\omega_{\mathbf{q}} = qc_0/\sqrt{\epsilon_b}$ , where  $c_0$  is the vacuum velocity of light and  $\epsilon_b$  is the background dielectric constant. The interaction between

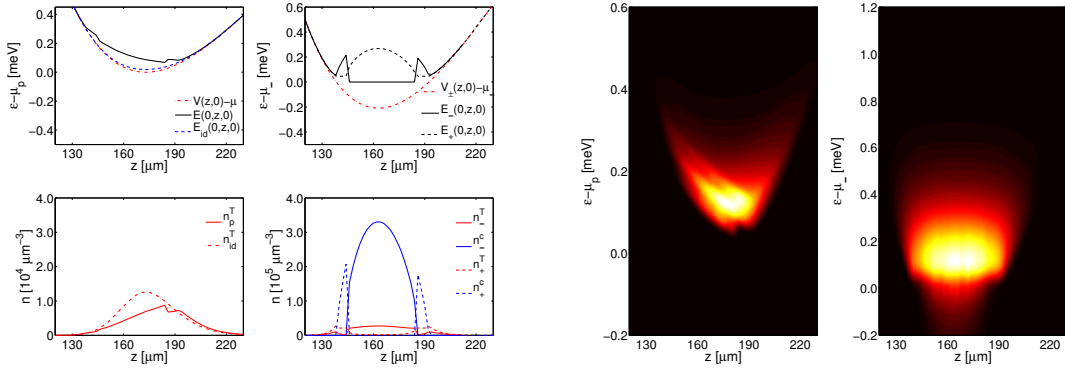


**Fig. 13:** Left side: Dispersions and density profiles in  $z$ -direction at  $(x, y) = (0, 0)$  for paraexcitons (left column) and orthoexcitons (right column) with  $T = 1.2\text{K}$ ,  $N_p = 5 \times 10^8$ , and  $N_- = N_+ = 5 \times 10^9$ . Right side: Corresponding luminescence spectra. Adapted from article IV.

bogolons and photons is given by the minimal coupling Hamiltonian [76],

$$\hat{H}_{xp} = -\frac{e}{m_0} \sum_j \hat{\mathbf{A}}(\mathbf{r}_j) \cdot \hat{\mathbf{p}}_j + \frac{e^2}{2m_0} \sum_j |\hat{\mathbf{A}}(\mathbf{r}_j)|^2, \quad (27)$$

with the mass  $m_0$ , the position  $\hat{\mathbf{r}}_j$ , and the momentum  $\hat{\mathbf{p}}_j$  of the  $j$ -th electron. We expand the position operator to lowest order in terms of the bogolon states  $|\Psi_{\mathbf{q}}^B\rangle$  and evaluate the Heisenberg equation of motion  $i\hbar\dot{\hat{\mathbf{p}}}_j = m_0[\hat{\mathbf{r}}_j, \hat{H}_x]$ . Writing the vector potential operator in terms of the photonic operators,  $\hat{\mathbf{A}}(\mathbf{r}) \propto \sum_{\mathbf{q}} (\hat{a}_{\mathbf{q}} + \hat{a}_{-\mathbf{q}}^\dagger)$ , the total Hamiltonian  $\hat{H} = \hat{H}_x + \hat{H}_p + \hat{H}_{xp}$  takes the form

$$\begin{aligned} \hat{H} = & \sum_{\mathbf{q}} E_{\mathbf{q}} \hat{b}_{\mathbf{q}}^\dagger \hat{b}_{\mathbf{q}} + \sum_{\mathbf{q}} \hbar\omega_{\mathbf{q}} \hat{a}_{\mathbf{q}}^\dagger \hat{a}_{\mathbf{q}} + i \sum_{\mathbf{q}} C_{\mathbf{q}} (\hat{a}_{\mathbf{q}} + \hat{a}_{-\mathbf{q}}^\dagger) (\hat{b}_{-\mathbf{q}} - \hat{b}_{\mathbf{q}}^\dagger) \\ & + \sum_{\mathbf{q}} D_{\mathbf{q}} (\hat{a}_{-\mathbf{q}} + \hat{a}_{\mathbf{q}}^\dagger) (\hat{a}_{\mathbf{q}} + \hat{a}_{-\mathbf{q}}^\dagger), \end{aligned} \quad (28)$$

with the coupling strength parameters  $D_{\mathbf{q}} = C_{\mathbf{q}}^2/E_{\mathbf{q}}$  and

$$C_{\mathbf{q}}^2 = \frac{\hbar^2 e^2}{4\varepsilon_0 \varepsilon_r m_0} \frac{f}{V} \frac{E_{\mathbf{q}}}{\hbar\omega_{\mathbf{q}}}, \quad f = \frac{2m_0 E_{\mathbf{q}}}{\hbar^2} |\langle \Psi_{\mathbf{q}}^B | \mathbf{e}_{\mathbf{q}\lambda} \cdot \sum_j \mathbf{r}_j | 0 \rangle|^2. \quad (29)$$

Here,  $f$  is the oscillator strength of paraexciton decay [77], which we do not derive microscopically, but replace with the experimentally obtained value. In the next step, we consider the (normal-ordered) field-field correlation function

$$g_{EE}^{(1)}(\mathbf{r}_1, t_1; \mathbf{r}_2, t_2) = \langle \hat{\mathbf{E}}^{(-)}(\mathbf{r}_2, t_2) \hat{\mathbf{E}}^{(+)}(\mathbf{r}_1, t_1) \rangle, \quad (30)$$

where  $\mathbf{E}^{(\pm)}$  are the field components of positive and negative frequencies [78]. The frequency-dependent intensity signal  $I(\mathbf{r}, \omega)$  follows from the Fourier transform of

this correlation function at  $\mathbf{r}_1 = \mathbf{r}_2 = \mathbf{r}$ , i.e.,

$$I(\mathbf{r}, \omega) \propto g_{EE}^{(1)}(\mathbf{r}, \mathbf{r}, \omega) = \frac{i\hbar^2}{2V\epsilon_0} \sum_{\mathbf{q}\mathbf{q}'} (1 + \cos \Theta) \sqrt{\omega_{\mathbf{q}}\omega_{\mathbf{q}'}} g_{aa}^{11<}(\mathbf{q}, \mathbf{q}', \omega) e^{i(\mathbf{q}-\mathbf{q}') \cdot \mathbf{r}}, \quad (31)$$

with  $\Theta = \angle(\mathbf{q}, \mathbf{q}')$ . In contrast to Eq. (25) the luminescence now depends on the photonic real-time correlation function

$$g_{aa}^{11<}(\mathbf{q}, \mathbf{q}', t_1, t_2) \equiv -i\hbar \langle \hat{a}_{\mathbf{q}'}^\dagger(t_2) \hat{a}_{\mathbf{q}}(t_1) \rangle. \quad (32)$$

To calculate  $g_{aa}^{11<}$ , a number of similar normal and anomalous real-time correlation functions of mixed photon and bogolon operators have to be evaluated (cf. Eq.(28) of article VII). To this end, we define corresponding Keldysh Green functions  $G_{XY}^{\alpha\beta}$  [46, 79] on the two-branch time contour. Based on the Heisenberg equations of motion of the operators  $\hat{a}_{\mathbf{q}}^{(\dagger)}$  and  $\hat{b}_{\mathbf{q}}^{(\dagger)}$  we arrive at a number of coupled selfconsistent Dyson equations on the contour, which can be analytically continued to the real time axis via the Langreth rules [80]. Assuming a steady-state, Fourier transformation results in a system of four coupled equations for  $g_{aa}^{11<}(\mathbf{q}, \mathbf{q}', \omega)$ ,  $g_{aa}^{21<}(\mathbf{q}, \mathbf{q}', \omega)$ , and the two respective retarded or advanced functions, a closed solution of which is still pending. The solution of the subsystem of retarded and advanced functions can be given straightforwardly,

$$g_{aa}^{11r/a}(\mathbf{q}, \mathbf{q}', \omega) = \frac{1}{\hbar} \delta(\mathbf{q} - \mathbf{q}') \times \frac{((\omega \pm i\epsilon) + \omega_{\mathbf{q}} + 2d_{\mathbf{q}})((\omega \pm i\epsilon)^2 - e_{\mathbf{q}}^2) + 2c_{\mathbf{q}}^2 e_{\mathbf{q}}}{((\omega \pm i\epsilon)^2 - \omega_{\mathbf{q}}^2 - 4d_{\mathbf{q}}\omega_{\mathbf{q}})((\omega \pm i\epsilon)^2 - e_{\mathbf{q}}^2) - 4c_{\mathbf{q}}^2 e_{\mathbf{q}}\omega_{\mathbf{q}}}. \quad (33)$$

with  $E_{\mathbf{q}} = \hbar e_{\mathbf{q}}$ ,  $C_{\mathbf{q}} = \hbar c_{\mathbf{q}}$ , and  $D_{\mathbf{q}} = \hbar d_{\mathbf{q}}$ . The poles of these functions give the excitation spectrum. We find four solutions  $(\omega \pm i\epsilon) = \pm \Omega_{\mathbf{q}}^{\pm}$ , with

$$\Omega_{\mathbf{q}}^{\pm 2} = \frac{1}{2}(e_{\mathbf{q}}^2 + \omega_{\mathbf{q}}^2 + 4d_{\mathbf{q}}\omega_{\mathbf{q}}) \pm \frac{1}{2}\sqrt{(e_{\mathbf{q}}^2 - \omega_{\mathbf{q}}^2 - 4d_{\mathbf{q}}\omega_{\mathbf{q}})^2 + 16c_{\mathbf{q}}^2 e_{\mathbf{q}}\omega_{\mathbf{q}}}. \quad (34)$$

This result is analogous to the Hopfield polariton spectrum [81] with its noncrossing upper and lower polariton branches. The energy  $E_{\mathbf{q}}$  is now the Bogoliubov dispersion of the interacting, condensed exciton system, so that the new quasiparticles will be called ‘‘bogolaritons’’ in the following. The corresponding photonic spectral function reads

$$A_{aa}(\mathbf{q}, \mathbf{q}', \omega) = 2\pi\delta(\mathbf{q} - \mathbf{q}') \left[ U_{\mathbf{q}}^{+2}\delta(\omega - \Omega_{\mathbf{q}}^+) + V_{\mathbf{q}}^{+2}\delta(\omega + \Omega_{\mathbf{q}}^+) + U_{\mathbf{q}}^{-2}\delta(\omega - \Omega_{\mathbf{q}}^-) + V_{\mathbf{q}}^{-2}\delta(\omega + \Omega_{\mathbf{q}}^-) \right]. \quad (35)$$

with the weights of the positive and negative upper and lower bogolariton branches given in Eqs. (38)-(41) of article VII. We note that, in contrast to the bogolon spectrum in Eq. (26), the bogolariton spectrum features four branches, even for  $n_c = 0$ . Only for  $C_{\mathbf{q}} = 0$ , the spectrum reverts to a single free photon branch.

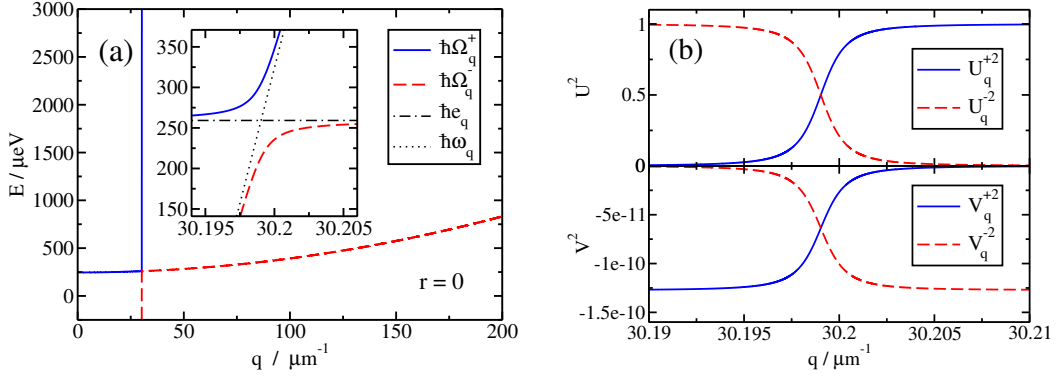


**Fig. 14:** Panel (a): Upper and lower bogolariton spectrum  $E = \hbar\Omega_{\mathbf{q}}^{\pm} - E_g - V_0 + \mu$  as a function of  $q$ , for  $r = 0$  and  $T = 2\text{K}$ . The inset magnifies the (avoided) crossing region of the free photon and bogolon dispersions. Panel (b): spectral weights of the upper and lower bogolariton spectrum, in dependence on  $q$ , for the same parameters. Adapted from article VII.

**Results II: Bogolariton spectrum** The numerical calculation of the paraexciton luminescence is carried out in two steps: First, we calculate self-consistently the paraexciton density distribution using a one-species version of Eqs. (21)-(24). For simplicity we consider a spherical harmonic trap  $V(r)$  fitted to the bottom of the experimentally observed trap potentials. The total exciton number is  $N = 10^{10}$ , which gives a critical temperature of  $T_c \approx 1.5\text{K}$ . Secondly, the resulting bogolon spectrum  $E_{\mathbf{q}}$  and the free photon dispersion  $\omega_{\mathbf{q}}$  are put into the bogolariton spectrum  $\Omega_{\mathbf{q}}^{\pm}$ . For the oscillator strength per unit cell we use the experimental values  $f = 4.7 \times 10^{-10}$  and  $V = (4.48\text{\AA})^3$ .

Figure 14(a) shows the resulting positive upper and lower branches of the bogolariton spectrum as a function of  $q$  at the trap center  $r = 0$ . The inset of Fig. 14(a) shows a zoom in on the crossing point of the uncoupled photon and bogolon dispersions. It illustrates how the upper and lower bogolariton branches avoid crossing, resulting in a gap with a width of  $2C_{\mathbf{q}} \approx 90\mu\text{eV}$ . Varying  $r$  shifts the energetic position of this gap according to  $E_{\mathbf{q}}(r)$ .

Figure 14(b) gives the  $q$ -dependence of the spectral weights  $U_{\mathbf{q}}^{\pm 2}$  and  $V_{\mathbf{q}}^{\pm 2}$  in the photonic spectral function. Far from the gap, the weights  $U_{\mathbf{q}}^{\pm 2}$  equal one or zero, representing the undisturbed photon states. Near the gap, they smoothly switch roles. In contrast to the weights  $v_{\mathbf{q}}$  of the bogolon mirror branch, the  $V_{\mathbf{q}}^{\pm}$  are finite even for  $n_c = 0$ . The weights of the mirror branches, however, are smaller by ten orders of magnitude, and they will be ignored in the following.

Combining our results for the dispersions and weights, Fig. 15 presents the photon spectral function  $A_{aa}(q, E)$  in the vicinity of the gap. The photon dispersion is considerably renormalized, with a hockey stick like structure at the gap. In contrast to the Shi-formula in Eq. (25), where the paraexciton luminescence was given by the single value  $q_0 = 30.2 \mu\text{m}^{-1}$  at the intersection bogolon and photon dispersions, the signal now depends on two critical wavenumbers  $q_0^{\pm}$ . For a given energy, we numerically determine the wavenumbers  $q_0^{\pm}$  so that  $E = \hbar\Omega_{\mathbf{q}}^{\pm}$ . As Fig. 15(b) shows,

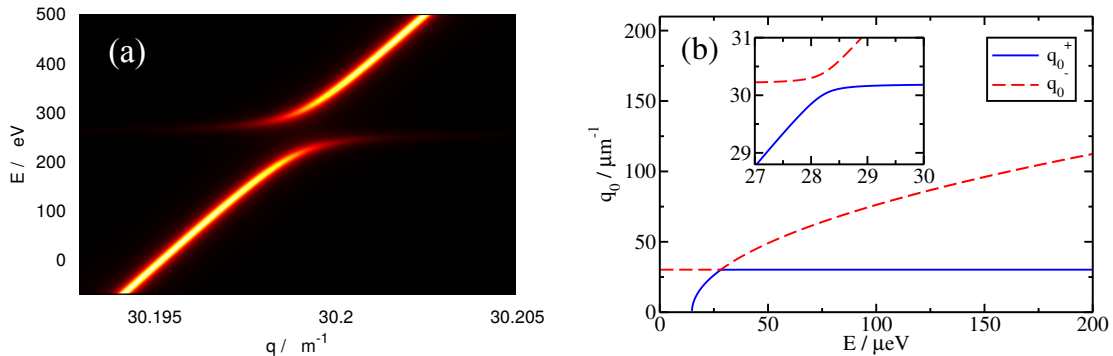


**Fig. 15:** Panel (a): Photonic spectral function as a function of  $q$  and  $E = \hbar\omega - E_g - V_0 + \mu$  in the avoided crossing region, for  $r = 0$  and  $T = 2\text{K}$ . Panel (b): Critical wavenumbers  $q_0^\pm$  as a function of  $E = \hbar\omega - E_g - V_0 + \mu$ , for  $r = 0$  and  $T = 2\text{K}$ . Adapted from article VII.

for energies  $E$  below the gap, the wavenumber  $q_0^+$  is undetermined and we find  $q_0^- \sim q_0$ . After  $E$  crosses the gap position, we find  $q_0^+ \sim q_0$ , while  $q_0^-$  grows due to the  $q^2$ -dependence of the bogolon dispersion. The smallest difference between  $q_0^+$  and  $q_0^-$  is found at the gap:  $q_0^- - q_0^+ = 0.38 \mu\text{m}^{-1}$ .

**Summary and outlook** We have presented a theoretical approach for the description of multi-component interacting excitonic gases in potential traps. Based on the grand canonical Hamiltonian of weakly interacting Bose gases in external potentials, we used the Bogoliubov prescription to derive self-consistent equations of motion for the condensed and noncondensed excitons. Applying the local density approximation and neglecting mixed-species averages, we arrived at Hartree-Fock-Bogoliubov equations for the densities of condensed and thermal excitons. The corresponding excitonic spectral functions yielded the systems luminescence signal via the formula by Shi and Verechaka [44].

Based on these equations, we have investigated numerically the interplay of three exciton species in  $\text{Cu}_2\text{O}$  and their influence on thermodynamical and spectral features for different combinations of temperature and particle numbers. Due to the mutual repulsion, the critical temperatures lower compared to the single species situation. In our local density approximation, the paraexciton condensate is invisible, due to wavevector conservation. However, signatures of a possible Bose-Einstein condensate might be found in the luminescence spectra of noncondensed particles: Our calculation predicts the formation of a flat bottom and weak second, bogolon mirror branch in the paraexciton spectrum. Moreover, since the para- and orthoexciton trap centers are not aligned, the paracondensate pushes the selfconsistent orthoexciton densities and spectra aside. In case of an orthoexciton condensate, the strong repulsion between orthoexciton species leads to a spatial separation of the respective condensates into a ball-and-shell structure. This is not obvious from the combined orthoexciton spectrum, but the para spectrum is distorted at the crossover region, providing an experimental footprint of this phase separation. If detected, the inter-

and intra-species interaction strengths of the ortho(+) and (−) species would satisfy the relation  $h_{+-} > h_{++}$ .

We extended our theory of the zero-phonon decay luminescence by using an interaction Hamiltonian that accounts for anomalous exciton-photon coupling terms. The resulting luminescence formula is dependent upon the interacting photonic Green functions, whose equations of motion were derived in a nonequilibrium Green function framework. We investigated the spectral features by means of the photonic spectral function. Near the former crossing point of free bogolon and photon dispersions, a hockey stick structure hints at the formation of polariton-like quasiparticles, which we call bogolaritons. The calculation predicts mirror branches even without the formation of a condensate, which, however, carry negligible spectral weight. In contrast to the Shi-formula, the luminescence signal will now be given by the spectral weight at two distinct wavevectors. The very next step of our calculations will be the solution of the equation of motion of the phononic correlation function.

In the future, the theory may be extended in several ways. Neglecting the Thomas–Fermi approximation, the full Gross–Pitaevskii equation for the condensate function in the external potential should be solved numerically. This would provide a better solution at the condensates boundaries. Moreover, the wavefunctions Fourier transform would include contributions with finite wavevectors, so that the paraexciton condensate may contribute to the luminescence.

The multi-component theory for the noncondensed particles could be improved by including the mixed-species averages. This would overcome the effective single-component picture with a pure mean-field coupling, but complicate the Bogoliubov transformation approach. Moreover, one could consider spectral broadening due to exciton-exciton interactions, i.e., go beyond the Hartree-Fock-Bogoliubov-Popov approximation by including higher order correlations on the level of the Beliaev approximation [82].

Our luminescence theory should be extended to orthoexciton decay, i.e., consider phonon assisted exciton-photon interaction within the self-consistent Green function calculation. Lastly, profound evidence for the creation of an exciton condensate would be the emission of coherent light. That is why the theoretical calculation of higher order correlation functions should be pursued.





## 2 Thesis Articles

### Author Contributions

#### Article I:

“Nonequilibrium transport through molecular junctions in the quantum regime,” T. Koch, J. Loos, A. Alvermann, and H. Fehske, *Phys. Rev. B* **84**, 125131 (2011)

All authors carved out the problem, outlined the calculation, and determined the scope of the article. J. Loos, A. Alvermann and T. Koch performed the analytical calculation. T. Koch performed the numerical calculation. The manuscript was written by J. Loos, A. Alvermann, and T. Koch and was edited by all authors.

#### Article II:

“Phonon-affected steady-state transport through molecular quantum dots,” T. Koch, H. Fehske, and J. Loos, *Phys. Scr.* **T151**, 014039 (2012)

All authors carved out the problem, outlined the calculation, and determined the scope of the article. J. Loos and T. Koch performed the analytical calculation. T. Koch performed the numerical calculation. The manuscript was written by J. Loos and T. Koch and was edited by all authors.

#### Article III:

“Thermoelectric effects in molecular quantum dots with contacts,” T. Koch, J. Loos, and H. Fehske, *Phys. Rev. B* **89**, 155133 (2014)

All authors carved out the problem, outlined the calculation, and determined the scope of the article. J. Loos and T. Koch performed the analytical calculation. T. Koch performed the numerical calculation. The manuscript was written by J. Loos and T. Koch and was edited by all authors.

#### Article IV:

“Interacting multicomponent exciton gases in a potential trap: Phase separation and Bose-Einstein condensation,” S. Sobkowiak, D. Semkat, H. Stolz, Th. Koch, and H. Fehske, *Phys. Rev. B* **82**, 064505 (2010)

All authors carved out the problem, outlined the calculation, and determined the scope of the article. S. Sobkowiak and D. Semkat performed the analytical calculations. S. Sobkowiak and Th. Koch performed the numerical calculations. S. Sobkowiak and Th. Koch wrote the manuscript which was edited by all authors.

**Article V:**

“Phase separation of multicomponent excitonic Bose-Einstein condensates,”  
S. Sobkowiak, D. Semkat, H. Stolz, Th. Koch, and H. Fehske, *Phys. Status Solidi C* **8**, 1178 (2011)

All authors carved out the problem, outlined the calculation, and determined the scope of the article. S. Sobkowiak and D. Semkat performed the analytical calculations. S. Sobkowiak and Th. Koch performed the numerical calculations. S. Sobkowiak wrote the manuscript which was edited by all authors.

**Article VI:**

“Condensation of excitons in Cu<sub>2</sub>O at ultracold temperatures: experiment and theory,” H. Stolz, R. Schwartz, F. Kieseling, S. Som, M. Kaupsch, S. Sobkowiak, D. Semkat, N. Naka, Th. Koch, and H. Fehske, *New J. Phys.* **14**, 105007 (2012)

All authors carved out the problem, outlined the calculations, and determined the scope of the article. H. Stolz, R. Schwartz, F. Kieseling, S. Som, M. Kaupsch, and N. Naka performed the experiments. H. Stolz, M. Kaupsch, S. Sobkowiak, D. Semkat, and Th. Koch performed the analytical calculations. H. Stolz, M. Kaupsch, and S. Sobkowiak performed the numerical calculations. H. Stolz, R. Schwartz, M. Kaupsch, S. Sobkowiak, and D. Semkat wrote the manuscript which was edited by all authors.

**Article VII:**

“Theory of zero-phonon decay luminescence of semiconductor excitons,”  
Th. Koch, D. Semkat, H. Stolz, and H. Fehske, *Fortschritte der Physik*, DOI: 10.1002/prop.201600068

All authors carved out the problem, outlined the calculation, and determined the scope of the article. Th. Koch and D. Semkat performed the analytical calculations. Th. Koch performed the numerical calculations. Th. Koch and D. Semkat wrote the manuscript which was edited by all authors.

Confirmed:

---

(Prof. Dr. Holger Fehske)

Greifswald, September 30, 2016

---

(Thomas Koch)

Greifswald, September 30, 2016

## Nonequilibrium transport through molecular junctions in the quantum regime

T. Koch,<sup>1</sup> J. Loos,<sup>2</sup> A. Alvermann,<sup>3</sup> and H. Fehske<sup>1</sup>

<sup>1</sup>*Institut für Physik, Ernst-Moritz-Arndt-Universität Greifswald, DE-17489 Greifswald, Germany*

<sup>2</sup>*Institute of Physics, Academy of Sciences of the Czech Republic, CZ-16200 Prague, Czech Republic*

<sup>3</sup>*Theory of Condensed Matter, Cavendish Laboratory, Cambridge CB3 0HE, United Kingdom*

(Received 3 May 2011; published 20 September 2011)

We consider a quantum dot, affected by a local vibrational mode and contacted to macroscopic leads, in the nonequilibrium steady-state regime. We apply a variational Lang-Firsov transformation and solve the equations of motion of the Green functions in the Kadanoff-Baym formalism up to a second order in the interaction coefficients. The variational determination of the transformation parameter through minimization of the thermodynamic potential allows us to calculate the electron/polaron spectral function and conductance for adiabatic to antiadiabatic phonon frequencies and weak to strong electron-phonon couplings. We investigate the qualitative impact of the quasiparticle renormalization on the inelastic electron tunneling spectroscopy signatures and discuss the possibility of a polaron induced negative differential conductance. In the high-voltage regime, we find that the polaron level follows the lead chemical potential to enhance resonant transport.

DOI: [10.1103/PhysRevB.84.125131](https://doi.org/10.1103/PhysRevB.84.125131)

PACS number(s): 72.10.-d, 71.38.-k, 73.21.La, 73.63.Kv

### I. INTRODUCTION

Recent advances in nanotechnology have made possible the creation of electronic devices with the active element being a single organic molecule. Such molecular junctions may be an alternative to semiconductor technology in the search for further miniaturization and novel transport properties. They can be described as quantum dots, i.e., as systems of finite size coupled to macroscopic leads acting as charge reservoirs. As with metallic or semiconducting junctions, energy level quantization determines transport. In addition, when being occupied by charge carriers, molecular quantum dots are susceptible to structural changes that may be induced by the interaction with optical phonons. As a consequence, vibrational signatures show up in the current-voltage characteristics. Moreover, they render inelastic tunneling spectroscopy (IETS), the primary experimental tool for the identification and characterization of molecular quantum dots.<sup>1,2</sup>

For a thorough understanding of the underlying transport mechanisms suitable theoretical models have to be studied. The simplest one is based on a modified Fano-Anderson model where the static impurity is replaced by a single site coupled to a local phonon mode. Then the current is given by the interacting dot spectral function and the voltage bias between the noninteracting macroscopic leads.<sup>3</sup> The transport properties of the system strongly depend on the relative time scales of the electronic and phononic subsystems.<sup>4</sup>

In the regime of fast electron motion and weak electron-phonon (EP) coupling, standard perturbation theory applies.<sup>5-7</sup> Here, IETS signatures result from the interference of (quasi)elastic and inelastic tunneling processes.<sup>8,9</sup> The calculated line shapes in the total current are found to be especially sensitive to changes in the dot-lead coupling parameter and the dot-level energy.<sup>10,11</sup> In general, both these quantities should be affected by conformational changes of the molecule. In the equilibrium situation, the question remains whether vibrational coupling leads to a broadening<sup>6</sup> or narrowing<sup>7</sup> of the linear conductance resonance as a function of the dot level.

On the other hand, in molecular quantum dots the vibrational frequency can be larger than the kinetic energy of

incident electrons. From the study of the Holstein molecular crystal model,<sup>12</sup> it is well known that in this regime, strong EP interaction may heavily reduce the “mobility” of the electrons through the formation of small polarons (electrons dressed by phonon clouds).<sup>13,14</sup> Consequently, for quantum dots, the formation of a local polaron is considered a possible mechanism for the observed nonlinear transport properties, such as hysteresis, negative differential conductance (NDC) and switching.<sup>15-18</sup> Approaches based on the application of a Lang-Firsov transformation<sup>19,20</sup> to the Hamiltonian suggest that the vibrational structure of the polaron state is revealed by distinct steps in the current-voltage signal.<sup>6,21,22</sup> Here, electron transport takes place via resonant tunneling through phonon sidebands.

In this paper, we investigate steady-state transport through molecular quantum dots for small-to-large dot-lead coupling and weak-to-strong EP interaction. Using the Meir-Wingreen current formula,<sup>3</sup> our main task is the determination of the interacting electronic spectral function of the quantum dot. As the background of our calculations we choose the formalism of Kadanoff-Baym,<sup>23</sup> which relies on the correspondence of the nonequilibrium Green functions of complex times to the real-time response functions. Starting from the Dyson equation, the general steady-state equations for the response functions will be deduced. The solution of the latter equations will lead to a nonequilibrium spectral function, which has a form analogous to the equilibrium one. The dot self-energy determining the spectral function will be calculated from the equations of motion of the Green functions up to a second order in the interaction coefficients.

Our approach is based on a variational Lang-Firsov transformation, which was developed for Holstein polarons at finite densities<sup>24</sup> and recently applied to the molecular quantum dot in equilibrium.<sup>25</sup> We extend these calculations to the nonequilibrium situation and to finite temperatures, whereby the dot self-energy will be calculated self-consistently to account for the density-dependent oscillator shift. The variational parameter of the Lang-Firsov transformation is determined numerically via the minimization of the thermodynamic

potential. In this way, we are able to interpolate between the self-consistent Born approximation (SCBA)<sup>11,26</sup> and the small-polaron approach<sup>22</sup> previously used in the weak and strong EP coupling limits. We note that already in the equilibrium case, our variational calculation introduces important corrections to the corresponding spectral functions that determine the conductance in the linear response theory. We reexamine the low-temperature equilibrium quantum dot system and analyze the occurrence of high-temperature phonon sidebands in the linear conductance.

In the nonequilibrium situation, we show the impact of the optimal polaron state on the IETS signatures mentioned above. For comparable electronic and phononic time scales, we study the crossover from coherent tunneling to sequential hopping via a transient polaron state, where the interplay of both resonant and off-resonant multiphonon processes leads to complicated electron tunneling spectra. Recently La Magna and Deretzis<sup>17</sup> applied a similar variational ansatz to an effective electron Hamiltonian and found polaron-formation-induced NDC. Considering the dependence of the current-voltage characteristics on the full spectral function, we critically discuss this effect.

The paper is organized as follows: Sec. II A introduces the model Hamiltonian and describes the variational Lang-Firsov transformation. In Secs. II B and II C, a formal steady-state solution to the equations of motion is presented. In Sec. II D, we derive an approximation to the polaronic self-energy that is self-consistent and depends on the variational parameter. The latter is determined from the numerical minimization of the thermodynamic potential that is deduced in Sec. II E. Section II F gives the relation between the electronic and polaronic spectral functions. In Sec. II G, the general current formula for arbitrary voltage is discussed and the special case of linear conductance is mentioned. Section III presents our numerical results and Sec. IV summarizes.

## II. THEORY

### A. General equations

Our considerations are based on the standard Hamiltonian of the single-site quantum dot model:

$$H = (\Delta - \mu)d^\dagger d - g\omega_0 d^\dagger d(b^\dagger + b) + \omega_0 b^\dagger b + \sum_{k,a} (\varepsilon_{ka} - \mu) c_{ka}^\dagger c_{ka} - \frac{1}{\sqrt{N}} \sum_{k,a} (t_{ka} d^\dagger c_{ka} + t_{ka}^* c_{ka}^\dagger d). \quad (1)$$

Here, the quantum dot is represented by the energy level  $\Delta$ , with the fermionic creation (destruction) operator  $d^\dagger$  ( $d$ ). The dot is coupled to a local phonon mode  $b^{(\dagger)}$  of energy  $\omega_0$ , with  $g$  being the dimensionless EP coupling strength. The  $\varepsilon_{ka}$  (for  $k = 1, \dots, N$ ) are the energies of noninteracting electrons in the left and right lead ( $a = L, R$ ) with the equilibrium chemical potential  $\mu$ . The corresponding operators  $c_{ka}^\dagger$  ( $c_{ka}$ ) create (annihilate) free fermions in the  $N$  lead states. The last term in Eq. (1) allows for dot-lead particle transfer.

We apply to the model (1) a variational Lang-Firsov transformation,<sup>17,19,25,27</sup> introducing two parameters  $\gamma$  and  $\bar{\gamma}$ :

$$\tilde{H} = S_2^\dagger(\bar{\gamma}) S_1^\dagger(\gamma) H S_1(\gamma) S_2(\bar{\gamma}), \quad (2)$$

$$S_1(\gamma) = \exp[\gamma g(b^\dagger - b)d^\dagger d], \quad (3)$$

$$S_2(\bar{\gamma}) = \exp[\bar{\gamma} g(b^\dagger - b)]. \quad (4)$$

$S_1(\gamma)$  describes the antiadiabatic limit where the phononic time scale is much faster than the electronic time scale and the deformation of the dot adjusts instantaneously to the presence of an electron. For  $\gamma = 1$ , it coincides with the shift transformation of the Lang-Firsov small polaron theory,<sup>19</sup> which eliminates the second term on the right-hand side of Eq. (1) and lowers the dot level by the polaron binding energy:

$$\varepsilon_p = g^2 \omega_0. \quad (5)$$

To account for the competition between polaron localization and charge transport, an incomplete Lang-Firsov transformation with  $\gamma \in [0, 1]$  is used where  $\gamma$  will be determined variationally. The second shift transformation  $S_2(\bar{\gamma})$  describes the regime of fast electron motion, where the quasistatic displacement of the equilibrium position of the oscillator affects transport. According to similar considerations in Ref. 27, the parameter  $\bar{\gamma}$  is fixed by the condition that the oscillator shift is stationary in the equilibrium and steady state. Then  $\bar{\gamma} = (1 - \gamma)n_d$ , with the dot occupation

$$n_d = \langle d^\dagger d \rangle, \quad (6)$$

where  $\langle \dots \rangle$  denotes the steady state mean value.

After the transformation, the Hamiltonian reads

$$\tilde{H} = \tilde{\eta} d^\dagger d - C_d(d^\dagger d - n_d) + \omega_0 b^\dagger b + \varepsilon_p(1 - \gamma)^2 n_d^2 + \sum_{k,a} \xi_{ka} c_{ka}^\dagger c_{ka} - \sum_{k,a} (C_{ka} d^\dagger c_{ka} + C_{ka}^\dagger c_{ka}^\dagger d), \quad (7)$$

with

$$\tilde{\eta} = \Delta - \mu - \varepsilon_p \gamma (2 - \gamma) - 2\varepsilon_p (1 - \gamma)^2 n_d, \quad (8)$$

$$\tilde{g} = \gamma g, \quad \xi_{ka} = \varepsilon_{ka} - \mu, \quad (9)$$

$$C_{ka} = \frac{t_{ka}}{\sqrt{N}} e^{-\tilde{g}(b^\dagger - b)}, \quad C_d = g\omega_0(1 - \gamma)(b^\dagger + b). \quad (10)$$

Here,  $\tilde{\eta}$  is the renormalized energy of the single dot level.  $C_{ka}$  and  $C_d$  are the renormalized interaction coefficients of the dot-lead transfer and the EP interaction, respectively. Note that now the operators  $d$  and  $b$  represent dressed electrons (in analogy to polarons) and the shifted local oscillator. The original electron and oscillator operators, now denoted by  $\tilde{d}$  and  $\tilde{b}$ , read

$$\tilde{d} = e^{\tilde{g}(b^\dagger - b)} d, \quad \tilde{b} = b + \tilde{g} d^\dagger d + (1 - \gamma) g n_d. \quad (11)$$

We describe the application of a potential difference between the leads by adding to Eq. (7) the interaction with the external fields  $\{U\}$  and define the voltage bias  $\Phi$  accordingly:

$$H_{\text{int}} = \sum_a U_a \sum_k c_{ka}^\dagger c_{ka}, \quad \text{with } U_a = -\delta\mu_a, \quad (12)$$

$$\Phi = (U_L - U_R)/e, \quad (13)$$

where  $e$  is the (negative) elementary charge. The response of the quantum dot is given by the polaronic nonequilibrium real-time Green functions:

$$g_{dd}(t_1, t_2; U) = -i \langle \mathcal{T} d_U(t_1) d_U^\dagger(t_2) \rangle, \quad (14)$$

$$g_{dd}^<(t_1, t_2; U) = i \langle d_U^\dagger(t_2) d_U(t_1) \rangle, \quad (15)$$

$$g_{dd}^>(t_1, t_2; U) = -i \langle d_U(t_1) d_U^\dagger(t_2) \rangle. \quad (16)$$

Remember that  $\langle \dots \rangle$  denotes the equilibrium average with respect to  $\tilde{H}$ , while the time dependence of the operators  $d^{(\dagger)}$  is now given by  $\tilde{H} + H_{\text{int}}$ . The time ordering operator in Eq. (14) is defined by

$$\mathcal{T} d_U(t_1) d_U^\dagger(t_2) = d_U(t_1) d_U^\dagger(t_2), \quad t_1 - t_2 > 0, \quad (17)$$

$$= -d_U^\dagger(t_2) d_U(t_1), \quad t_1 - t_2 < 0. \quad (18)$$

According to Kadanoff-Baym,<sup>23</sup> the real-time response functions (14)–(16) may be deduced using the equations of motion for the nonequilibrium Green functions of the complex time variables  $t = t_0 - i\tau$ ,  $\tau \in [0, \beta]$ , defined as

$$G_{dd}(t_1, t_2; U, t_0) = -\frac{i}{\langle S \rangle} \langle \mathcal{T}_\tau d(t_1) d^\dagger(t_2) S \rangle, \quad (19)$$

$$G_{dd}^<(t_1, t_2; U, t_0) = \frac{i}{\langle S \rangle} \langle \mathcal{T}_\tau d^\dagger(t_2) d(t_1) S \rangle, \quad (20)$$

$$G_{dd}^>(t_1, t_2; U, t_0) = -\frac{i}{\langle S \rangle} \langle \mathcal{T}_\tau d(t_1) d^\dagger(t_2) S \rangle, \quad (21)$$

where the order of  $t_1$  and  $t_2$  is fixed in  $G_{dd}^<$  and  $G_{dd}^>$ . The time dependence of all operators is determined by  $\tilde{H}$  and the external disturbance is explicit in the time-ordered exponential operator  $S$ :

$$S = \mathcal{T}_\tau \exp \left\{ -i \int_{t_0}^{t_0 - i\beta} dt H_{\text{int}}(t) \right\}. \quad (22)$$

In Eqs. (19)–(21) and (22), the operator  $\mathcal{T}_\tau$  orders times according to

$$\mathcal{T}_\tau d_U(t_1) d_U^\dagger(t_2) = d(t_1) d^\dagger(t_2), \quad i(t_1 - t_2) > 0, \quad (23)$$

$$= -d^\dagger(t_2) d(t_1), \quad i(t_1 - t_2) < 0. \quad (24)$$

In the following, the Green functions of “mixed” operators  $G_{cd}(k, a; t_1, t_2; U, t_0)$  and  $g_{cd}(k, a; t_1, t_2; U)$  will be used, which are defined similar to Eqs. (14)–(21). The functions  $g$  follow from the functions  $G$  through the limiting procedure  $t_0 \rightarrow -\infty$ .

### B. Equations of motion

We consider the polaronic dot Green function (19), where the index “ $dd$ ” will be omitted for the moment, and start from the Dyson equation in the matrix form:

$$[G^{(0)-1}(t_1, \bar{t}; U, t_0) - \Sigma(t_1, \bar{t}; U, t_0)] \bullet G(\bar{t}, t_2; U, t_0) = \delta(t_1 - t_2). \quad (25)$$

In Eq. (25), the matrix multiplication “ $\bullet$ ” is defined by  $\int_{t_0}^{t_0 - i\beta} d\bar{t} \dots$  and the  $\delta$  function of complex arguments is understood with respect to this integration. With the inverse

zeroth-order Green function

$$G^{(0)-1}(t_1, t_2) = \left( i \frac{\partial}{\partial t_1} - \tilde{\eta} \right) \delta(t_1 - t_2), \quad (26)$$

Eq. (25) gives for  $i(t_1 - t_0) < i(t_2 - t_0)$

$$\begin{aligned} & \left( i \frac{\partial}{\partial t_1} - \tilde{\eta} \right) G^<(t_1, t_2; U, t_0) \\ &= \int_{t_0}^{t_1} d\bar{t} \Sigma^>(t_1, \bar{t}; U, t_0) G^<(\bar{t}, t_2; U, t_0) \\ &+ \int_{t_1}^{t_2} d\bar{t} \Sigma^<(t_1, \bar{t}; U, t_0) G^<(\bar{t}, t_2; U, t_0) \\ &+ \int_{t_2}^{t_0 - i\beta} d\bar{t} \Sigma^<(t_1, \bar{t}; U, t_0) G^>(\bar{t}, t_2; U, t_0), \end{aligned} \quad (27)$$

where the self-energy functions  $\Sigma^{\lessgtr}$  are defined analogously to  $G^{\lessgtr}$ :

$$\Sigma^>(t_1, t_2; U, t_0) = \Sigma(t_1, t_2; U, t_0), \quad i(t_1 - t_2) > 0, \quad (28)$$

$$\Sigma^<(t_1, t_2; U, t_0) = \Sigma(t_1, t_2; U, t_0), \quad i(t_1 - t_2) < 0. \quad (29)$$

On the other hand, the matrix-transposed form of (25) yields

$$\begin{aligned} & \left( -i \frac{\partial}{\partial t_2} - \tilde{\eta} \right) G^<(t_1, t_2; U, t_0) \\ &= \int_{t_0}^{t_1} d\bar{t} G^>(t_1, \bar{t}; U, t_0) \Sigma^<(\bar{t}, t_2; U, t_0) \\ &+ \int_{t_1}^{t_2} d\bar{t} G^<(t_1, \bar{t}; U, t_0) \Sigma^<(\bar{t}, t_2; U, t_0) \\ &+ \int_{t_2}^{t_0 - i\beta} d\bar{t} G^<(t_1, \bar{t}; U, t_0) \Sigma^>(\bar{t}, t_2; U, t_0). \end{aligned} \quad (30)$$

Similarly to Eqs. (27) and (30), equations having  $G^>(t_1, t_2; U, t_0)$  on the left-hand side are obtained in the case  $i(t_1 - t_0) > i(t_2 - t_0)$ . After the limiting procedure  $t_0 \rightarrow -\infty$ , we arrive at the equations for the real-time response functions of the dot operators:

$$\begin{aligned} & \left( i \frac{\partial}{\partial t_1} - \tilde{\eta} \right) g^{\lessgtr}(t_1, t_2; U) \\ &= \int_{-\infty}^{t_1} d\bar{t} [\Sigma^>(t_1, \bar{t}; U) - \Sigma^<(t_1, \bar{t}; U)] g^{\lessgtr}(\bar{t}, t_2; U) \\ &- \int_{-\infty}^{t_2} d\bar{t} \Sigma^{\lessgtr}(t_1, \bar{t}; U) [g^>(\bar{t}, t_2; U) - g^<(\bar{t}, t_2; U)], \end{aligned} \quad (31)$$

$$\begin{aligned} & \left( -i \frac{\partial}{\partial t_2} - \tilde{\eta} \right) g^{\lessgtr}(t_1, t_2; U) \\ &= \int_{-\infty}^{t_1} d\bar{t} [g^>(t_1, \bar{t}; U) - g^<(t_1, \bar{t}; U)] \Sigma^{\lessgtr}(\bar{t}, t_2; U) \\ &- \int_{-\infty}^{t_2} d\bar{t} g^{\lessgtr}(t_1, \bar{t}; U) [\Sigma^>(\bar{t}, t_2; U) - \Sigma^<(\bar{t}, t_2; U)]. \end{aligned} \quad (32)$$

The latter equations are general; up to this point no special assumptions or approximations were made.

### C. Steady-state solution

Limiting ourselves to the steady-state regime, all functions of  $(t_1, t_2)$  will be supposed to depend only on  $t = t_1 - t_2$ . Then, after suitable change of the integration variables, the difference of the equations for  $g^<$  in Eqs. (31) and (32)

gives

$$\int_{-\infty}^{\infty} d\bar{t} [g^<(\bar{t}; U)\Sigma^>(t - \bar{t}; U) - g^>(\bar{t}; U)\Sigma^<(t - \bar{t}; U)] = 0, \quad (33)$$

while the differential equation for  $(g^> - g^<)$  following from Eq. (31) reads

$$\left(i \frac{\partial}{\partial t} - \tilde{\eta}\right)[g^>(t; U) - g^<(t; U)] = \int_0^{\infty} d\bar{t} [\Sigma^>(\bar{t}; U) - \Sigma^<(\bar{t}; U)][g^>(t - \bar{t}; U) - g^<(t - \bar{t}; U)] - \int_{-\infty}^0 d\bar{t} [\Sigma^>(t - \bar{t}; U) - \Sigma^<(t - \bar{t}; U)][g^>(\bar{t}; U) - g^<(\bar{t}; U)]. \quad (34)$$

Using the Fourier transformations of  $g^{\lessgtr}$  and  $\Sigma^{\lessgtr}$  with factors according to Kadanoff-Baym,<sup>23</sup> e.g.,

$$g^{\lessgtr}(\omega; U) = \mp i \int_{-\infty}^{\infty} dt g^{\lessgtr}(t; U) e^{i\omega t}, \quad (35)$$

$$g^{\lessgtr}(t; U) = \mp \int_{-\infty}^{\infty} \frac{d\omega}{2\pi i} g^{\lessgtr}(\omega; U) e^{-i\omega t}, \quad (36)$$

the following exact equations for the steady-state are obtained

$$g^<(\omega; U)\Sigma^>(\omega; U) - g^>(\omega; U)\Sigma^<(\omega; U) = 0, \quad (37)$$

$$\left[\omega - \tilde{\eta} - \mathcal{P} \int_{-\infty}^{\infty} \frac{d\omega'}{2\pi} \frac{\Sigma^>(\omega'; U) + \Sigma^<(\omega'; U)}{\omega - \omega'}\right][g^>(\omega; U) + g^<(\omega; U)] = [\Sigma^>(\omega; U) + \Sigma^<(\omega; U)] \mathcal{P} \int_{-\infty}^{\infty} \frac{d\omega'}{2\pi} \frac{g^>(\omega'; U) + g^<(\omega'; U)}{\omega - \omega'}. \quad (38)$$

If we define, in analogy to the equilibrium expressions,<sup>23</sup>

$$A(\omega; U) = g^>(\omega; U) + g^<(\omega; U), \quad (39)$$

$$g(z; U) = \int \frac{d\omega}{2\pi} \frac{A(\omega; U)}{z - \omega}, \quad (40)$$

$$\Gamma(\omega; U) = \Sigma^>(\omega; U) + \Sigma^<(\omega; U), \quad (41)$$

$$\Sigma(z; U) = \int \frac{d\omega}{2\pi} \frac{\Gamma(\omega; U)}{z - \omega}, \quad (42)$$

Eq. (38) takes the form

$$[\omega - \tilde{\eta} - \text{Re } \Sigma(\omega; U)]A(\omega; U) = \Gamma(\omega; U) \text{Re } g(\omega; U). \quad (43)$$

According to Eq. (39), we can write

$$g^<(\omega; U) = A(\omega; U)\bar{f}(\omega; U), \quad (44)$$

$$g^>(\omega; U) = A(\omega; U)[1 - \bar{f}(\omega; U)], \quad (45)$$

introducing the nonequilibrium distribution  $\bar{f}$ , which follows from the steady-state equation (37) and the definition (41) as

$$\bar{f}(\omega; U) = \frac{\Sigma^<(\omega; U)}{\Gamma(\omega; U)}. \quad (46)$$

Looking for a solution  $A(\omega; U)$  of Eq. (43), which would be equal to the equilibrium spectral function for  $\{U\} \rightarrow 0$ , we

assume (according to similar considerations in Ref. 23) that  $g(z; U)$  has the form

$$g(z; U) = \frac{1}{z - \tilde{\eta} - \Sigma(z; U)}. \quad (47)$$

Together with Eq. (40), Eq. (47) fulfils Eq. (43) identically, and the polaronic nonequilibrium spectral function becomes

$$A(\omega; U) = \frac{\Gamma(\omega; U)}{[\omega - \tilde{\eta} - \mathcal{P} \int \frac{d\omega'}{2\pi} \frac{\Gamma(\omega'; U)}{\omega - \omega'}]^2 + [\frac{\Gamma(\omega; U)}{2}]^2}. \quad (48)$$

### D. Self-energy

We determine the polaron self-energy  $\Sigma_{dd}$  from the equations of motion for the generalized Green functions of complex time, which were considered for the equilibrium case in Ref. 25. In particular, the coupled equations for  $G_{dd}$  and  $G_{cd}$  read

$$\begin{aligned} G_{dd}^{(0)-1}(t_1, \bar{t}) \bullet G_{dd}(\bar{t}, t_2; U, t_0) &= \delta(t_1 - t_2) \\ &+ \frac{i}{\langle S \rangle} \langle \mathcal{T}_{\tau} C_d(t_1) d(t_1) d^{\dagger}(t_2) S \rangle \\ &+ \sum_{k,a} \frac{i}{\langle S \rangle} \langle \mathcal{T}_{\tau} C_{ka}(t_1) c_{ka}(t_1) d^{\dagger}(t_2) S \rangle, \end{aligned} \quad (49)$$

$$\begin{aligned} G_{cc}^{(0)-1}(k, a; t_1, \bar{t}; U) \bullet G_{cd}(k, a; \bar{t}, t_2; U, t_0) \\ = \frac{i}{\langle S \rangle} \langle \mathcal{T}_{\tau} C_{ka}^{\dagger}(t_1) d(t_1) d^{\dagger}(t_2) S \rangle, \end{aligned} \quad (50)$$

where, in analogy to Eq. (26),

$$G_{cc}^{(0)-1}(k, a; t_1, t_2; U) = \left( i \frac{\partial}{\partial t_1} - \xi_{ka} - U_a \right) \delta(t_1 - t_2). \quad (51)$$

To deduce the functional differential equations for the self-energy  $\Sigma_{dd} = G_{dd}^{(0)-1} - G_{dd}^{-1}$ , in addition to the physical fields  $\{U\}$ , we introduce the fictitious fields  $\{V\}$  by adding to  $H_{\text{int}}$  (cf. Refs. 23, 25, and 28 )

$$\sum_{k,a} [V_{ka}(t)C_{ka}(t) + \bar{V}_{ka}(t)C_{ka}^\dagger(t)] + V_d(t)C_d(t). \quad (52)$$

In the same way as in Ref. 25, the averages on the right-hand side of Eqs. (49) and (50) are expressed by means of the functional derivatives of Green functions with respect to  $\{V\}$ . The resulting functional differential equation for  $\Sigma_{dd}$  is solved by iteration to the second order in the interaction coefficients defined in Eq. (10). The correlation functions of the interaction coefficients are evaluated supposing independent Einstein oscillators. Letting then  $\{V\} \rightarrow 0$ , the following self-consistent result is obtained

$$\Sigma_{dd}(t_1, t_2; U, t_0) = \Sigma_{dd}^{(1)}(t_1, t_2; U, t_0) + [g\omega_0(1 - \gamma)]^2 \times G_{dd}(t_1, t_2; U, t_0)F_3(t_1, t_2). \quad (53)$$

The result of the first iteration step,

$$\begin{aligned} \Sigma_{dd}^{(1)}(t_1, t_2; U, t_0) &= \sum_{k,a} |\langle C_{ka} \rangle|^2 G_{cc}^{(0)}(k, a; t_1, t_2; U) \\ &+ \sum_{k,a} |\langle C_{ka} \rangle|^2 G_{cc}^{(0)}(k, a; t_1, t_2; U) F_1(t_1, t_2), \end{aligned} \quad (54)$$

is independent of  $G_{dd}$ . The quasiequilibrium nonperturbed Green functions of the leads read

$$\begin{aligned} G_{cc}^{(0)<}(k, a; t_1, t_2; U) &= i e^{-i\xi_{ka}(t_1-t_2)} f(\xi_{ka} + U_a), \\ G_{cc}^{(0)>}(k, a; t_1, t_2; U) &= -i e^{-i\xi_{ka}(t_1-t_2)} [1 - f(\xi_{ka} + U_a)], \end{aligned} \quad (55)$$

with  $f(x) = (e^{\beta x} + 1)^{-1}$ . The functions  $F_1$  and  $F_3$  are given by  $F_1^<$  and  $F_3^<$  for  $i(t_1 - t_2) < 0$ , and by  $F_1^>$  and  $F_3^>$  for  $i(t_1 - t_2) > 0$ , respectively:

$$F_1^{\lessgtr}(t_1, t_2) = \exp\{\tilde{g}^2 [(n_B(\omega_0) + 1)e^{\mp i\omega_0(t_1-t_2)} + n_B(\omega_0)e^{\pm i\omega_0(t_1-t_2)}]\} - 1, \quad (56)$$

$$F_3^{\lessgtr}(t_1, t_2) = (n_B(\omega_0) + 1)e^{\mp i\omega_0(t_1-t_2)} + n_B(\omega_0)e^{\pm i\omega_0(t_1-t_2)}, \quad (57)$$

with  $n_B(x) = (e^{\beta x} - 1)^{-1}$ . In Eq. (53), we perform the limit  $t_0 \rightarrow -\infty$  and the continuation of the complex time variables to real times, while keeping the condition  $i(t_1 - t_2) < 0$  for  $\Sigma_{dd}^<$  and  $i(t_1 - t_2) > 0$  for  $\Sigma_{dd}^>$ . We arrive at

$$\begin{aligned} \Sigma_{dd}^{\lessgtr}(t_1, t_2; U) &= \Sigma_{dd}^{(1)\lessgtr}(t; U) + [(1 - \gamma)g\omega_0]^2 g_{dd}^{\lessgtr}(t_1, t_2; U) \\ &\times [(n_B(\omega_0) + 1)e^{\pm i\omega_0(t_1-t_2)} + n_B(\omega_0)e^{\mp i\omega_0(t_1-t_2)}], \end{aligned} \quad (58)$$

$$\begin{aligned} \Sigma_{dd}^{(1)\lessgtr}(t_1, t_2; U) &= \sum_{k,a} |\langle C_{ka} \rangle|^2 g_{cc}^{(0)\lessgtr}(k, a; t_1, t_2; U) \{I_0(\kappa) \\ &+ \sum_{s \geq 1} I_s(\kappa) 2 \sinh(s\theta) [(n_B(s\omega_0) + 1)e^{\pm is\omega_0(t_1-t_2)} \\ &+ n_B(s\omega_0)e^{\mp is\omega_0(t_1-t_2)}]\}, \end{aligned} \quad (59)$$

where

$$\theta = \frac{1}{2}\beta\omega_0, \quad \kappa = \frac{\tilde{g}^2}{\sinh\theta}, \quad (60)$$

$$I_s(\kappa) = \sum_{m=0}^{\infty} \frac{1}{m!(s+m)!} \left(\frac{\kappa}{2}\right)^{s+2m}, \quad (61)$$

and

$$g_{dd}^<(t_1, t_2; U) = - \int \frac{d\omega}{2\pi i} A(\omega; U) \bar{f}(\omega; U) e^{-i\omega(t_1-t_2)}, \quad (62)$$

$$g_{dd}^>(t_1, t_2; U) = \int \frac{d\omega}{2\pi i} A(\omega; U) [1 - \bar{f}(\omega; U)] e^{-i\omega(t_1-t_2)}. \quad (63)$$

Now we insert  $|\langle C_{ka} \rangle|^2 = (|t_{ka}|^2/N) \exp\{-\tilde{g}^2 \coth\theta\}$  in Eq. (59) and go from the  $k$  summation to the integration over the lead states with the help of the density of states of lead  $a$ :

$$\frac{1}{N} \sum_{k,a} |t_{ka}|^2 \dots \rightarrow \sum_a \int_{-\infty}^{\infty} d\omega |t_a(\omega)|^2 \varrho_a(\omega) \dots, \quad (64)$$

$$\varrho_a(\omega) = \frac{1}{N} \sum_k \delta(\omega - \varepsilon_{ka}). \quad (65)$$

We then Fourier transform Eq. (58) according to Eq. (35) and, after evaluating the resulting delta functions, obtain

$$\begin{aligned} \Sigma_{dd}^<(\omega; U) &= \Sigma_{dd}^{(1)<}(\omega; U) + [(1 - \gamma)g\omega_0]^2 [A(\omega - \omega_0; U) \\ &\times \bar{f}(\omega - \omega_0; U) n_B(\omega_0) + A(\omega + \omega_0; U) \\ &\times \bar{f}(\omega + \omega_0; U) (n_B(\omega_0) + 1)], \end{aligned} \quad (66)$$

$$\begin{aligned} \Sigma_{dd}^{(1)<}(\omega; U) &= e^{-\tilde{g}^2 \coth\theta} \sum_a \{I_0(\kappa) \Gamma_a^{(0)}(\omega + \mu) f(\omega + U_a) \\ &+ \sum_{s \geq 1} I_s(\kappa) 2 \sinh(s\theta) [n_B(\omega_0) \Gamma_a^{(0)}(\omega - s\omega_0 + \mu) \\ &\times f(\omega - s\omega_0 + U_a) + (n_B(\omega_0) + 1) \Gamma_a^{(0)}(\omega + s\omega_0 + \mu) \\ &\times f(\omega + s\omega_0 + U_a)]\}, \end{aligned} \quad (67)$$

$$\Gamma_a^{(0)}(\omega) = 2\pi |t_a(\omega)|^2 \varrho_a(\omega). \quad (68)$$

The function  $\Sigma_{dd}^<(\omega; U)$  can be understood as a generalized in-scattering function of polaron-like quasiparticles at the dot.<sup>29</sup> The second to fourth line in Eq. (67) accounts for multiple-phonon emission and, if  $T > 0$ , absorption processes. After some algebraic manipulations of the Bose- and Fermi-functions, the first-order self-energy (67) may be written in the

following form:

$$\Sigma_{dd}^{(1)<}(\omega; U) = \Gamma_L^{(1)}(\omega; U)f(\omega + U_L) + \Gamma_R^{(1)}(\omega; U)f(\omega + U_R), \quad (69)$$

$$\begin{aligned} \Gamma_a^{(1)}(\omega; U) = e^{-\tilde{\gamma}^2 \coth \theta} & \left( I_0(\kappa) \Gamma_a^{(0)}(\omega + \mu) + \sum_{s \geq 1} I_s(\kappa) 2 \sinh(s\theta) \{ \Gamma_a^{(0)}(\omega + \mu - s\omega_0) [n_B(s\omega_0) + 1 - f(\omega + U_a - s\omega_0)] \right. \\ & \left. + \Gamma_a^{(0)}(\omega + \mu + s\omega_0) [n_B(s\omega_0) + f(\omega + U_a + s\omega_0)] \right). \end{aligned} \quad (70)$$

Because  $\Sigma_{dd}^{>}(\omega; U)$  results from interchanging  $n_B \leftrightarrow (n_B + 1)$ ,  $f \leftrightarrow (1 - f)$  and  $\bar{f} \leftrightarrow (1 - \bar{f})$  in Eqs. (66)–(69), Eq. (41) gives

$$\begin{aligned} \Gamma(\omega; U) = \Gamma^{(1)}(\omega; U) + [(1 - \gamma)g\omega_0]^2 & \{ A(\omega - \omega_0; U) [n_B(\omega_0) + 1 - \bar{f}(\omega - \omega_0; U)] \\ & + A(\omega + \omega_0; U) [n_B(\omega_0) + \bar{f}(\omega + \omega_0; U)] \}, \end{aligned} \quad (71)$$

$$\Gamma^{(1)}(\omega; U) = \Gamma_L^{(1)}(\omega; U) + \Gamma_R^{(1)}(\omega; U). \quad (72)$$

From Eq. (71), the spectral function follows using Eq. (48). For any parameter  $\gamma < 1$ , the spectral function  $A$  and distribution  $\bar{f}$  have to be determined self-consistently. Furthermore, because the renormalized dot level defined in Eq. (8) depends on the dot occupation  $n_d$ , the latter has to fulfill the self-consistency condition

$$n_d = \int_{-\infty}^{\infty} \frac{d\omega}{2\pi} \bar{f}(\omega; U) A(\omega; U). \quad (73)$$

We note that for  $\gamma = 0$ , our results are equivalent to the SCBA.<sup>26</sup> For  $\gamma = 1$ , no self-consistency condition has to be fulfilled, as  $\Sigma_{dd} = \Sigma_{dd}^{(1)}$  and  $\tilde{\eta}$  is independent of  $n_d$ .

### E. Variational procedure

To determine the variational parameter  $\gamma$ , we minimize the thermodynamic potential  $\Omega$ , which is given by the partition function  $Q$  as

$$\Omega = -\frac{1}{\beta} \ln Q. \quad (74)$$

We assume the leads to be macroscopic objects, which are negligibly influenced by the states of the dot. Accordingly, the contributions of the leads to  $\Omega$  and to the mean energy  $\langle \tilde{H} \rangle$  give only additive constants. Since the electronic degrees of freedom of the dot are coupled to the oscillator ones by the second term on the right-hand side of Eq. (7), a decoupling approximation will be used to determine the electronic part of the thermodynamic potential.

As a consequence of the equation of motion, the following identity holds

$$\begin{aligned} \left( i \frac{\partial}{\partial t_1} - i \frac{\partial}{\partial t_2} \right) d^\dagger(t_2) d(t_1) \Big|_{t_2=t_1} \\ = \tilde{\eta} d^\dagger(t_1) d(t_1) - C_d d^\dagger(t_1) d(t_1) + H'(t_1). \end{aligned} \quad (75)$$

Here,  $H'$  represents the part of the Hamiltonian (7) that depends on the operators  $d^\dagger$  and  $d$ . As an approximation, we neglect the second term on the right-hand side of Eq. (75) and in  $H'$ . Taking the statistical averages on both sides of Eq. (75), remembering that

$$\langle d^\dagger(t_2) d(t_1) \rangle = -i g_{dd}^<(t_1, t_2; U) \quad (76)$$

and using Eq. (62),

$$\langle H' \rangle = \int \frac{d\omega}{2\pi} (2\omega - \tilde{\eta}) A(\omega; U) \bar{f}(\omega; U) \quad (77)$$

is obtained. To determine the corresponding electronic part of the thermodynamic potential,  $\Omega'$ , we consider the canonical ensemble given by the Hamiltonian  $H'_\lambda = H_0 + V_\lambda$ , where  $H_0 = \tilde{\eta} d^\dagger d$  and  $V_\lambda$  represents the interaction part of the Hamiltonian (7) with coefficients  $\lambda C_{ka}$  and  $\lambda C_d$ , for  $\lambda \in [0, 1]$ . Applying the result (77) gives

$$\langle V_\lambda \rangle_\lambda = 2 \int \frac{d\omega}{2\pi} (\omega - \tilde{\eta}) A_\lambda(\omega; U) \bar{f}(\omega; U). \quad (78)$$

Here,  $\langle \dots \rangle_\lambda$  denotes the dependence of the statistical average on  $\lambda$  and the indices  $\lambda$  on the right-hand side of Eq. (78) refer to the interaction coefficients in  $H'_\lambda$ . We use the well-known general relations<sup>23,30</sup> for the determination of  $\Omega'$ , namely,

$$\Omega' = \Omega'(\lambda = 1) = -\frac{1}{\beta} \ln Q(\lambda = 1), \quad (79)$$

$$\ln Q(\lambda = 1) = \ln Q(\lambda = 0) - \beta \int_0^1 d\lambda \frac{1}{\lambda} \langle V_\lambda \rangle_\lambda, \quad (80)$$

where

$$\ln Q(\lambda = 0) = \ln(1 + e^{-\tilde{\eta}\beta}). \quad (81)$$

To make the integration in Eq. (80) feasible, the general procedure leading to the thermodynamic potential outlined above will be carried out using the solution for the dot response in the first iteration step, described in the preceding section. In particular, the spectral function  $A_\lambda(\omega; U)$  is determined according to Eq. (48), using  $\Gamma_\lambda^{(1)}(\omega; U)$ , which is proportional to  $\lambda^2$ :  $\Gamma_\lambda^{(1)}(\omega; U) = \lambda^2 \Gamma^{(1)}(\omega; U)$ . Similarly,  $\bar{f}(\omega; U)$  is determined by Eq. (46) using  $\Sigma_{dd}^{(1)<}$  and  $\Gamma^{(1)}$  on the right-hand side. Note, however, that  $\tilde{\eta}$  will be determined from the electron density  $n_d$  corresponding to the complete self-energy  $\Sigma_{dd}^{\leq}(\omega; U)$ .

To complete the function  $\Omega$ , which is to be varied with respect to  $\gamma$ , we have to take into account the renormalization



of the oscillator energy given in the first line of Eq. (7). We finally obtain that

$$\begin{aligned} \Omega &= -\frac{1}{\beta} \ln(1 + e^{-\tilde{\eta}\beta}) + \varepsilon_p(1 - \gamma)^2 n_d^2 + \int_0^1 \frac{d\lambda}{\lambda} \int_{-\infty}^{+\infty} \frac{d\omega}{\pi} \\ &\quad \times \frac{(\omega - \tilde{\eta})\tilde{f}^{(1)}(\omega; U) \lambda^2 \Gamma^{(1)}(\omega; U)}{\left[\omega - \tilde{\eta} - \lambda^2 \mathcal{P} \int \frac{d\omega'}{2\pi} \frac{\Gamma^{(1)}(\omega'; U)}{\omega - \omega'}\right]^2 + \left[\lambda^2 \frac{\Gamma^{(1)}(\omega; U)}{2}\right]^2} \\ &= -\frac{1}{\beta} \ln(1 + e^{-\tilde{\eta}\beta}) + \varepsilon_p(1 - \gamma)^2 n_d^2 - \int \frac{d\omega}{\pi} \tilde{f}^{(1)}(\omega) \\ &\quad \times \left\{ \frac{\tilde{\eta} - \omega}{|\tilde{\eta} - \omega|} + \arctan \left[ \frac{\omega - \tilde{\eta} - \mathcal{P} \int \frac{d\omega'}{2\pi} \frac{\Gamma^{(1)}(\omega'; U)}{\omega - \omega'}}{\Gamma^{(1)}(\omega)/2} \right] \right\}. \end{aligned} \quad (82)$$

The parameter  $\gamma$  resulting from the variation of Eq. (82) is used to determine  $\Sigma_{dd}^{\lessgtr}(\omega; U)$  according to Eq. (66). The self-energy functions obtained in this way give the distribution function  $\tilde{f}(\omega; U)$  and the spectral function  $A(\omega; U)$  according to Eqs. (46) and (48), respectively.

#### F. Relation between electronic and polaronic functions

In the previous sections, the functions  $A(\omega; U)$  and  $g_{dd}^{\lessgtr}(\omega; U)$  in polaron representation were deduced. Because the current through the quantum dot will be given by the corresponding electronic functions  $\tilde{A}(\omega; U)$  and  $\tilde{g}_{dd}^{\lessgtr}(\omega; U)$ , we have to find a relation between these quantities. We start by decoupling the fermionic and bosonic degrees of freedom in the electronic dot Green function of complex times:

$$\begin{aligned} \tilde{G}_{dd}(t_1, t_2; U, t_0) &= -\frac{i}{\langle S \rangle} \langle \mathcal{T}_\tau \tilde{d}(t_1) \tilde{d}^\dagger(t_2) S \rangle \\ &\approx G_{dd}(t_1, t_2; U, t_0) \langle \mathcal{T}_\tau e^{\tilde{g}(b^\dagger - b)(t_1)} e^{-\tilde{g}(b^\dagger - b)(t_2)} \rangle. \end{aligned} \quad (83)$$

Assuming an independent Einstein oscillator, we find

$$\begin{aligned} \langle \mathcal{T}_\tau e^{\tilde{g}(b^\dagger - b)(t_1)} e^{-\tilde{g}(b^\dagger - b)(t_2)} \rangle &= e^{-\tilde{g}^2 \coth \theta} \left\{ I_0(\kappa) + \sum_{s \geq 1} I_s(\kappa) [e^{s\theta} e^{\pm i s \omega_0 (t_1 - t_2)} \right. \\ &\quad \left. + e^{-s\theta} e^{\mp i s \omega_0 (t_1 - t_2)}] \right\}, \end{aligned} \quad (84)$$

where the upper signs correspond to  $i(t_1 - t_2) > 0$  and the lower ones to  $i(t_1 - t_2) < 0$ . Going from the complex time variables to the real ones, the following relation between  $\tilde{g}_{dd}^{\lessgtr}(\omega; U)$  and  $g_{dd}^{\lessgtr}(\omega; U)$  is obtained

$$\begin{aligned} \tilde{g}_{dd}^{\lessgtr}(\omega; U) &= e^{-\tilde{g}^2 \coth \theta} \left\{ I_0(\kappa) g_{dd}^{\lessgtr}(\omega; U) \right. \\ &\quad \left. + \sum_{s \geq 1} I_s(\kappa) [e^{s\theta} g_{dd}^{\lessgtr}(\omega \pm s\omega_0; U) \right. \\ &\quad \left. + e^{-s\theta} g_{dd}^{\lessgtr}(\omega \mp s\omega_0; U)] \right\}. \end{aligned} \quad (85)$$

With the identities

$$e^{s\theta} = 2 \sinh(s\theta) [1 + n_B(s\omega_0)], \quad (86)$$

$$e^{-s\theta} = 2 \sinh(s\theta) n_B(s\omega_0), \quad (87)$$

the electronic function  $\tilde{g}_{dd}^{\lessgtr}(\omega; U)$  may be expanded as

$$\begin{aligned} \tilde{g}_{dd}^{\lessgtr}(\omega; U) &= e^{-\tilde{g}^2 \coth \theta} \left( I_0(\kappa) g_{dd}^{\lessgtr}(\omega; U) \right. \\ &\quad \left. + \sum_{s \geq 1} I_s(\kappa) 2 \sinh(s\theta) \{ [1 + n_B(s\omega_0)] g_{dd}^{\lessgtr}(\omega \pm s\omega_0; U) \right. \\ &\quad \left. + n_B(s\omega_0) g_{dd}^{\lessgtr}(\omega \mp s\omega_0; U) \} \right). \end{aligned} \quad (88)$$

Considering Eqs. (44) and (45), the electronic spectral function is obtained in terms of the polaronic one as

$$\begin{aligned} \tilde{A}(\omega; U) &= \tilde{g}_{dd}^{\lessgtr}(\omega; U) + \tilde{g}_{dd}^{\lessgtr}(\omega; U) \\ &= e^{-\tilde{g}^2 \coth \theta} \left( I_0(\kappa) A(\omega; U) + \sum_{s \geq 1} I_s(\kappa) 2 \sinh(s\theta) \right. \\ &\quad \left. \times \{ [n_B(s\omega_0) + \tilde{f}(\omega + s\omega_0; U)] A(\omega + s\omega_0; U) \right. \\ &\quad \left. + [n_B(s\omega_0) + 1 - \tilde{f}(\omega - s\omega_0; U)] A(\omega - s\omega_0; U) \} \right). \end{aligned} \quad (89)$$

#### G. Current

The operator of the electron current from lead  $a$  to the dot reads

$$\hat{J}_a = \frac{ie}{\sqrt{N}} \sum_k [t_{ka} \tilde{d}^\dagger c_{ka} - t_{ka}^* c_{ka}^\dagger \tilde{d}]. \quad (90)$$

To calculate the mean value  $J_a = \langle \hat{J}_a \rangle$ , the following connection of the expectation values to the real-time Green functions is used

$$\begin{aligned} i \langle \tilde{d}^\dagger c_{ka} \rangle &= \tilde{g}_{cd}^{\lessgtr}(k, a; t_1, t_1; U) \\ &= \int_{-\infty}^{\infty} \frac{d\omega}{2\pi} \tilde{g}_{cd}^{\lessgtr}(k, a; \omega; U), \end{aligned} \quad (91)$$

$$\begin{aligned} i \langle c_{ka}^\dagger \tilde{d} \rangle &= \tilde{g}_{dc}^{\lessgtr}(k, a; t_1, t_1; U) \\ &= - \int_{-\infty}^{\infty} \frac{d\omega}{2\pi} [\tilde{g}_{cd}^{\lessgtr}(k, a; \omega; U)]^*. \end{aligned} \quad (92)$$

We start from the nonequilibrium Green function of the complex time variables for the electron operators, namely,

$$\tilde{G}_{cd}(k, a; t_1, t_2; U, t_0) = -\frac{i}{\langle S \rangle} \langle \mathcal{T}_\tau c_{ka}(t_1) \tilde{d}^\dagger(t_2) S \rangle, \quad (93)$$

where  $S$  is given by Eq. (22). From the commutators with the Hamiltonian in the electron representation, the equation of motion is obtained

$$\begin{aligned} \left( i \frac{\partial}{\partial t_1} - \xi_{ka} - U_a \right) \tilde{G}_{cd}(k, a; t_1, t_2; U, t_0) \\ = -\frac{t_{ka}^*}{\sqrt{N}} \tilde{G}_{dd}(t_1, t_2; U, t_0). \end{aligned} \quad (94)$$

Equation (94) can be rewritten as

$$\begin{aligned} & \tilde{G}_{cd}(k, a; t_1, t_2; U, t_0) \\ & - \frac{t_{ka}^*}{\sqrt{N}} \int_{t_0}^{t_0 - i\beta} d\bar{t} G_{cc}^{(0)}(k, a; t_1, \bar{t}; U) \tilde{G}_{dd}(\bar{t}, t_2; U, t_0). \end{aligned} \quad (95)$$

Performing the limit  $t_0 \rightarrow -\infty$  while keeping  $i(t_1 - t_2) < 0$ , the following equation for the real-time response functions is obtained

$$\begin{aligned} & - \frac{\sqrt{N}}{t_{ka}^*} \tilde{g}_{cd}^<(k, a; t_1, t_2; U) \\ & = \int_{-\infty}^{t_1} d\bar{t} g_{cc}^{(0)>}(k, a; t_1, \bar{t}; U) \tilde{g}_{dd}^<(\bar{t}, t_2; U) \\ & + \int_{t_1}^{\infty} d\bar{t} g_{cc}^{(0)<}(k, a; t_1, \bar{t}; U) \tilde{g}_{dd}^<(\bar{t}, t_2; U) \\ & - \int_{t_2}^{\infty} d\bar{t} g_{cc}^{(0)<}(k, a; t_1, \bar{t}; U) \tilde{g}_{dd}^<(\bar{t}, t_2; U) \\ & - \int_{-\infty}^{t_2} d\bar{t} g_{cc}^{(0)<}(k, a; t_1, \bar{t}; U) \tilde{g}_{dd}^>(\bar{t}, t_2; U), \end{aligned} \quad (96)$$

where the quasiequilibrium functions of the noninteracting leads,  $g_{cc}^{(0)\lessgtr}$ , coincide with the expressions (55), with  $(t_1 - t_2)$  real. Based on Eq. (96), the formal manipulations presented in the Appendix, which are analogous to the considerations made in Ref. 3, finally lead to the following formula for the electron current from the lead  $a$  to the dot:

$$\begin{aligned} J_a & = \frac{e}{N} \sum_k |t_{ka}|^2 \int_{-\infty}^{\infty} d\omega \delta(\omega - \xi_{ka}) \\ & \times [f(\xi_{ka} + U_a) \tilde{A}(\omega; U) - \tilde{g}_{dd}^<(\omega; U)] \\ & = e \int_{-\infty}^{\infty} \frac{d\omega}{2\pi} \Gamma_a^{(0)}(\omega + \mu) \\ & \times [f(\omega + U_a) \tilde{A}(\omega; U) - \tilde{g}_{dd}^<(\omega; U)], \end{aligned} \quad (97)$$

where the electronic functions  $\tilde{g}_{dd}^<(\omega; U)$ ,  $\tilde{A}(\omega; U)$  are given by Eqs. (88) and (89), respectively. Since  $J_L = -J_R$  in steady state, the current formula acquires the well-known form<sup>3</sup>

$$\begin{aligned} J & = \frac{1}{2} (J_L - J_R) \\ & = \frac{e}{2} \int_{-\infty}^{\infty} \frac{d\omega}{2\pi} \Gamma^{(0)}(\omega + \mu) [f_L(\omega) - f_R(\omega)] \tilde{A}(\omega; U), \end{aligned} \quad (98)$$

with  $f_a(\omega) = f(\omega + U_a)$ . In Eq. (98), identical leads are assumed, so that  $\Gamma^{(0)}(\omega) \equiv \Gamma_L^{(0)}(\omega) = \Gamma_R^{(0)}(\omega)$ . As a check of our numerics, we find indeed that the condition  $J_L = -J_R$  holds, as expected for the SCBA. For vanishing voltage bias  $\Phi \rightarrow 0$ , we can express the current as  $J = -L\Phi$ , where the linear conductance

$$L = \lim_{\Phi \rightarrow 0} \{-J/\Phi\} \quad (99)$$

results from Eq. (98) as

$$\begin{aligned} L & = \frac{e^2}{2} \int_{-\infty}^{\infty} \frac{d\omega}{2\pi} \Gamma^{(0)}(\omega + \mu) [-f'(\omega)] \tilde{A}(\omega) \\ & = \frac{e^2}{2} \beta \int_{-\infty}^{\infty} \frac{d\omega}{2\pi} \Gamma^{(0)}(\omega + \mu) f(\omega) [1 - f(\omega)] \tilde{A}(\omega), \end{aligned} \quad (100)$$

and the electronic spectral function is now calculated in equilibrium.

### III. NUMERICAL RESULTS

As stated above, the spectral function, dot occupation, and  $\gamma$  have to be evaluated self-consistently. We do this in a two-step manner: (i) for fixed  $\gamma$  and a starting value  $n_d$  in Eq. (8) we calculate  $\Sigma_{dd}^{(1)}(\omega)$ ,  $\Gamma^{(1)}(\omega)$ . The corresponding  $A^{(1)}(\omega)$  and  $\tilde{f}^{(1)}(\omega)$  are inserted for  $A$  and  $\tilde{f}$  in the right-hand side of Eqs. (66) and (71). All functions are then iterated until convergence, which is signalled by

$$\max_{\omega} \{|A_{i+1}(\omega; U) - A_i(\omega; U)|\} < \delta, \quad (101)$$

with  $\delta$  being a predefined tolerance. In analogy to the occurrence of multiple stable solutions in the mean-field ansatz of Galperin *et al.*,<sup>15</sup> for strong EP coupling or high voltages, several roots of Eq. (73) may exist. We choose the root that minimizes the thermodynamic potential. (ii) We do this for all parameters  $\gamma$  to find the global minimum of  $\Omega[\gamma, n_d(\gamma)]$ . The corresponding parameter will be referred to as  $\gamma_{\min}$ .

In the following numerical calculations, we suppose identical leads and work in the wide-band limit, so that  $\Gamma^{(0)}(\omega) = \Gamma^{(0)}$  is energy independent.

The equilibrium state, as well as the transport properties of molecular junctions crucially depend on the time scales of the electronic and phononic subsystem. While the lifetime of an electron on the dot is given by the dot-lead coupling parameter,  $\tau_{el} \propto 1/\Gamma^{(0)}$ ,<sup>29</sup> the phononic time scale is given by the phonon energy  $\tau_{ph} \propto 1/\omega_0$ . The ratio  $\Gamma^{(0)}/\omega_0$  determines which subsystem is the faster one. Moreover, one should compare the polaron formation time  $\tau_{pol} \propto 1/\varepsilon_p$  to the electron lifetime. If the latter is long enough, i.e., if the ratio  $\varepsilon_p/\Gamma^{(0)}$  is large, a transient polaron can form at the dot. The parameter  $g^2$  will yield the mean number of phonons it contains.

#### A. Equilibrium situation, low temperature

We first consider the equilibrium low-temperature limit with  $\mu_L = \mu_R = \mu_{eq} = 0$  and  $T = 0.01$ . Before we study the physically more interesting regime of equal electronic and phononic time scales, we analyze the two limiting cases  $\Gamma^{(0)} \gg \omega_0$  and  $\Gamma^{(0)} \ll \omega_0$ . In the following,  $\omega_0 = 1$  fixes the energy unit.

##### 1. Limiting cases

In the adiabatic case  $\Gamma^{(0)} \gg \omega_0$ , the dot deformation adjusts quasistatically to the average electronic occupation. For small EP coupling, standard perturbation approaches are applicable and the expansion of the self-energy to second order leads to the Born-approximation (BA). On a higher level, the SCBA<sup>26</sup> provides a partial resummation of the perturbation series by replacing the zero-order Green function in the BA self-energy with the full Green function in a self-consistent way. As was mentioned above, our result (53) reduces to the SCBA for  $\gamma \rightarrow 0$ .

Figure 1(a) shows the electronic spectral function of the adiabatic quantum dot system with  $\Delta = 0$  and  $\varepsilon_p = 5$ . We

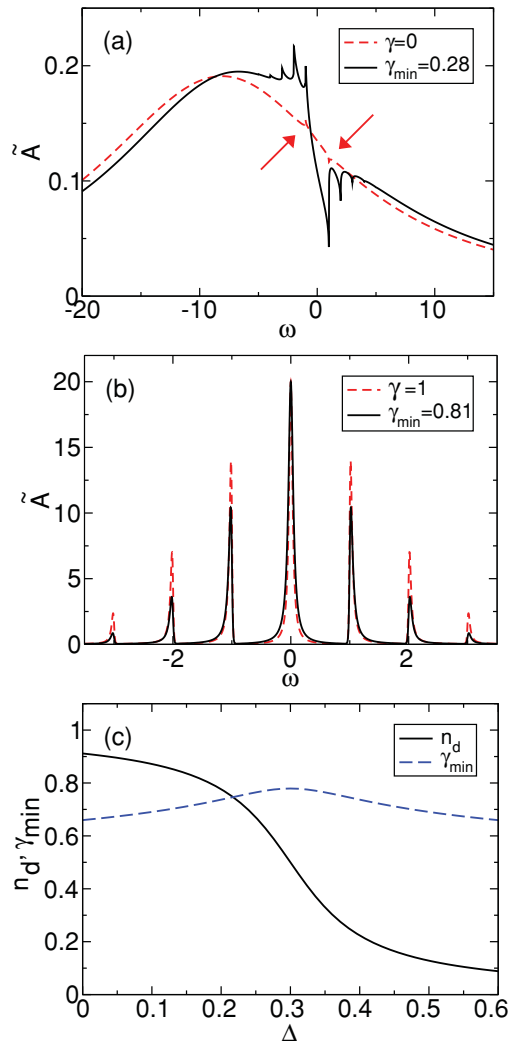


FIG. 1. (Color online) For model parameters  $T = 0.01$ ,  $\mu = 0$ , and  $\Phi = 0$ . (a) Electronic spectral functions for  $\Gamma^{(0)} = 10$ ,  $\varepsilon_p = 5$ , and  $\Delta = 0$  with  $\gamma = 0$  and  $\gamma_{\min} = 0.28$ , respectively. Arrows mark the phononic features for  $\gamma = 0$ . (b) Electronic spectral functions for  $\Gamma^{(0)} = 0.1$ ,  $\varepsilon_p = 1$ , and  $\Delta = 1$  with  $\gamma = 1$  and  $\gamma_{\min} = 0.81$ , respectively. (c) Dot occupation and variational parameter as functions of the bare dot level  $\Delta$  for  $\Gamma^{(0)} = 0.1$  and  $\varepsilon_p = 0.3$ .

compare the SCBA result ( $\gamma = 0$ ) to the result of the variational calculation, yielding  $\gamma_{\min} = 0.28$ . The SCBA spectrum consists of a single band, whose width is given by  $\Gamma^{(0)}$ . Due to the mean-field shift  $\propto n_d = 0.7$ , the renormalized dot level lies beneath the Fermi level of the leads (at  $\omega = 0$ ) and the dot acts as a tunneling well. Because of the short residence time of electrons, the effects of inelastic scattering at the dot are small. At  $\omega = -\omega_0$  ( $\omega = +\omega_0$ ), we find a small peak (dip) in  $\tilde{A}$  (see arrows) due to narrow logarithmic singularities in the denominator of Eq. (48).<sup>7</sup>

The variational calculation introduces several corrections to the spectrum. The finite  $\gamma_{\min}$  reduces the effective mean-field coupling, i.e., the last term in the polaron shift (8). Because it is not fully compensated by the  $n_d$ -independent contribution

to Eq. (8), the overall band shifts upward. In addition, situated at integer multiples of  $\omega_0$  from the lead chemical potential, several inelastic resonances form overlapping phononic sidebands. Because  $\tilde{A}(\omega = 0)$  is lowered, transport through the dot remains coherent, but with a slightly reduced tunneling amplitude.

In the strong coupling, antiadiabatic case  $\Gamma^{(0)} \ll \omega_0$ , the electron occupies the dot long enough to lose coherence and interact with the phonons. Several approaches<sup>20–22</sup> handle this regime by applying a complete Lang-Firsov transformation ( $\gamma = 1$ )<sup>19</sup> to the Hamiltonian, which gives the exact solution for the isolated molecule or when the finite occupation of the leads is neglected.<sup>31</sup> Consequently,  $\gamma_{\min}$  can be considered a measure of the small polaron character of the dot state.

Again we compare the corresponding limit  $\gamma = 1$  to the result of the variational calculation while setting  $\Delta = \varepsilon_p = 1$  [see Fig. 1(b)]. In the former case, the dot level is renormalized by the polaron binding energy and represented by the zero-phonon peak at  $\tilde{\Delta} = \Delta - \varepsilon_p = 0$ . In addition, we find pronounced peaks separated by  $\omega_0$ , signaling the emission of phonons by incident electrons and holes. The spectrum documents the formation of a long-living polaron state at the dot, with a mean number of phonons given by  $g^2 = 1$ .

For the same parameters, the variational calculation yields  $\gamma_{\min} = 0.81 < 1$  and we find a somewhat broader main peak and less spectral weight in the phonon sidebands ( $g^2 = 0.66$ ). Consequently, incoherent hopping transport through the dot takes place via an intermediate polaron state, whose spectral weight and lifetime are smaller than predicted by the complete ( $\gamma = 1$ ) Lang-Firsov calculation.

Figure 1(c) finally shows the dot occupation and variational parameter as functions of the dot level  $\Delta$  in the antiadiabatic case  $\Gamma^{(0)} = 0.1$ , but for small EP coupling  $\varepsilon_p = 0.3$ . In this regime, we find  $\gamma_{\min} \approx 0.7$ . This is in good quantitative agreement with the result of La Magna and Deretzis,<sup>17</sup> who applied a variational Lang-Firsov transformation to an effective electron model [cf. Fig. 2(b) in Ref. 17]. The above calculations show that, although the Lang-Firsov approach provides the correct physical mechanism, away from the very strong coupling limit, adiabatic corrections may not be neglected.

## 2. Intermediate dot-lead coupling regime

We now investigate the regime of comparable electronic and phononic time scales by setting  $\Gamma^{(0)} = 1$ . Figure 2 presents the results of the equilibrium calculation for zero to large EP coupling strengths. Shown here are, as functions of the bare dot level  $\Delta$ : the dot occupation  $n_d$  (a), the variational parameter  $\gamma_{\min}$  and the renormalized dot level  $\tilde{\eta}$  (b), and the linear conductance  $L$  (d). For fixed  $\varepsilon_p$  and  $\Delta$ , Fig. 2(c) gives the thermodynamic potential as a function of  $\gamma$  while Figs. 2(e) and 2(f) display the electronic spectral functions at  $\Delta = \varepsilon_p$ .

For  $\varepsilon_p = 0$ , the self-energy (53) is exact (black curves in Fig. 2) and the rigid dot acts as a tunneling barrier. As  $\Delta$  is lowered and the dot charges continuously, the linear conductance increases, reaching a maximum at  $\Delta = 0$ , where the dot level aligns with the lead chemical potentials and resonant tunneling is possible. The width of the conductance resonance is determined by the electron lifetime  $\Gamma^{(0)}$ .

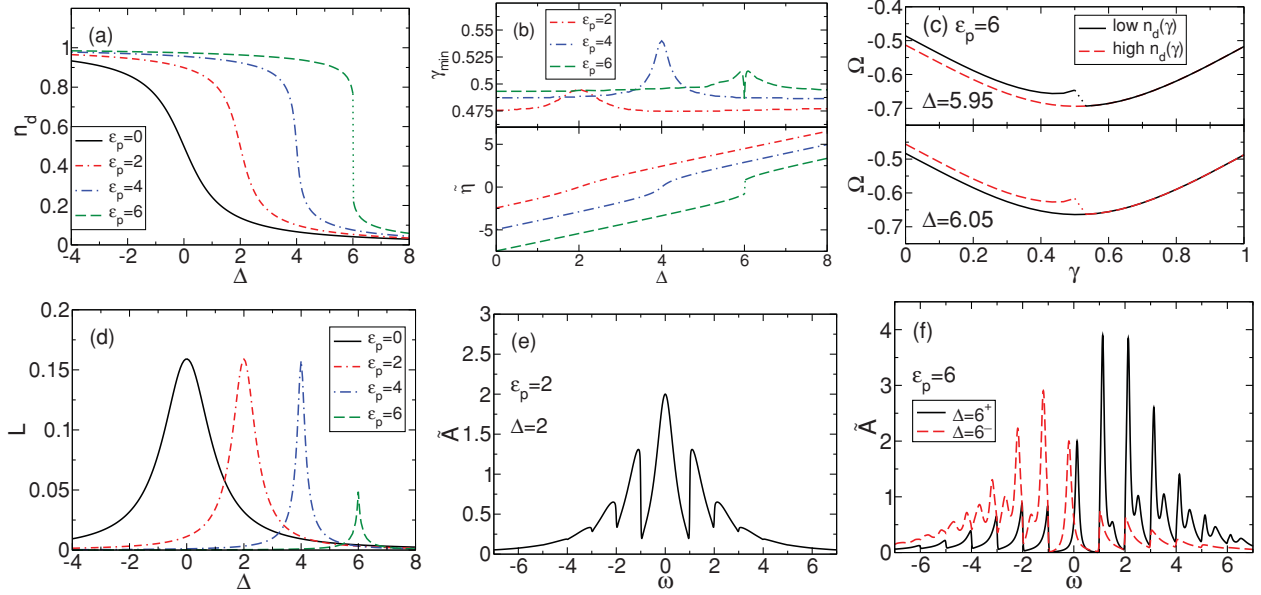


FIG. 2. (Color online) For model parameters  $\Gamma^{(0)} = 1$ ,  $T = 0.01$ ,  $\mu = 0$ , and  $\Phi = 0$ . (a) Dot occupation as a function of the bare dot level for several  $\varepsilon_p$ . (b) Variationally determined  $\gamma_{\min}$  and renormalized dot level as functions of the bare dot level  $\Delta$ . (c) Thermodynamic potential as a function of  $\gamma$  for  $\varepsilon_p = 6$  and  $\Delta$  in the vicinity of the discontinuous transition. Here, we consider the lower (black solid line) or upper (dashed red line) root of the self-consistency equation for  $n_d$ . (d) Linear conductance as a function of the bare dot level. (e) Electronic spectral function for  $\varepsilon_p = 2$  at resonance. (f) Electronic spectral functions for  $\varepsilon_p = 6$  and  $\Delta$  slightly above ( $\Delta = 6^+$ ) and below ( $\Delta = 6^-$ ) the discontinuous transition.

For finite  $\varepsilon_p$ , the variational parameter  $\gamma_{\min} \approx 0.5$  and grows only slightly at  $\Delta = \varepsilon_p$ . As expected, for equal electronic and phononic time scales we are far from the weak coupling ( $\gamma = 0$ ) and strong coupling ( $\gamma = 1$ ) limits. As a consequence of the EP coupling, the charging transition from  $n_d \approx 0$  to  $n_d \approx 1$  shifts to higher  $\Delta$  because of an overall lowering of the effective tunneling barrier. Due to the self-consistent mean-field coupling in Eq. (8), the transition becomes more rapid and even discontinuous for  $\varepsilon_p > 5$  (signalled by the dotted green lines). Here, the system switches between two stable solutions of Eq. (73) in analogy to the strong-coupling results of Refs. 15 and 17. Figure 2(c) shows the thermodynamic potential as a function of  $\gamma$  for  $\varepsilon_p = 6$  with  $\Delta$  slightly below and above resonance. For  $\gamma < 0.55$ , the effective mean-field coupling in Eq. (8) is so strong, that Eq. (73) has two roots. For  $\Delta < \varepsilon_p$ , the global minimum of the thermodynamic potential, situated at  $\gamma = 0.5$ , corresponds to high  $n_d$ . As  $\Delta$  crosses the resonance, the roots change roles and the relevant  $n_d$  jumps. An adiabatic phase transition from  $n_d = 0$  to  $n_d = 1$  was also found for a single electron at a vibrating quantum dot.<sup>14,32</sup> Rapid polaron formation and multistability are considered possible mechanisms for strongly nonlinear transport properties of molecular junctions such as NDC.<sup>15–17</sup>

From Fig. 2(a) we see that, in case of a continuous transition,  $n_d = 0.5$  whenever  $\Delta = \varepsilon_p$ . As can be easily checked from Eq. (8), at this point the renormalized dot level resonates with the lead chemical potentials, i.e.,  $\tilde{\eta} = 0$  irrespective of  $\gamma_{\min}$ . Figure 2(e) shows the corresponding electronic spectral function for moderate coupling  $\varepsilon_p = \Delta = 2$ . Few ( $\tilde{g}^2 = 0.5$ ) broad sidebands signal phonon emission by either

particles ( $\omega > 0$ ) or holes ( $\omega < 0$ ). The spectrum suggests that transmission remains coherent, but is governed by the slightly increased lifetime of the transient polaron state  $\propto 1/\tilde{\Gamma}^{(0)}$ , with  $\tilde{\Gamma}^{(0)} = 0.6$ . In case of a discontinuous charging, the dot level is shifted instantly across the resonance and there is no particle-hole symmetric situation, as is demonstrated by the spectral functions near the transition for  $\varepsilon_p = 6$  [see Fig. 2(f)]. Because  $\tilde{g}^2 = 1.5 > 1$ , spectral weight is shifted from the narrow main peak to multiphonon states, reducing the tunneling rate in the off-resonant situation considerably (Franck-Condon blockade).

The effects of the EP coupling on the linear response of the quantum dot can be seen in Fig. 2(d). Due to the rapid charging and the growing lifetime of the transient polaron, the symmetrical conductance resonance shifts and narrows. This result coincides with the findings of Entin-Wohlmann *et al.*<sup>7</sup> and contradicts the  $\varepsilon_p$ -dependent broadening shown in the work of Mitra *et al.*<sup>6</sup> Note that in case of a continuous transition, the maximum value of  $L$  is independent of the EP coupling strength because the dependence of  $L$  on  $\tilde{\Gamma}^{(0)}$  cancels in the low-temperature limit.<sup>7,33</sup> In the strong-coupling limit, the resonance is skipped and the linear-response signal lowers. In accordance with Refs. 7 and 6, we find no side peaks in the linear conductance at low temperatures. This is due to “floating” side bands<sup>6</sup> in the electronic spectral functions: for all  $\Delta$  the phonon signatures are offset by  $\omega_0$  below and above the lead Fermi level, as can be seen from Fig. 2(f). Consequently, they are not resolved in the low-temperature linear response. This fact is missed by single-particle approaches.<sup>21</sup>

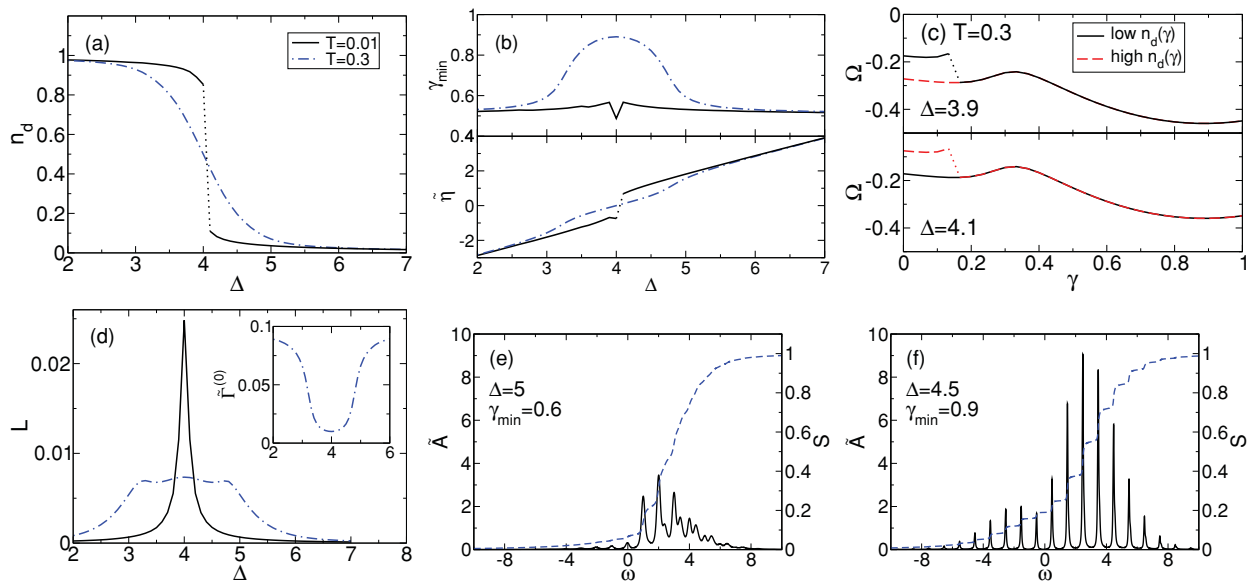


FIG. 3. (Color online) For model parameters  $\Gamma^{(0)} = 0.3$ ,  $\mu = 0$ ,  $\Phi = 0$ ,  $\varepsilon_p = 4$ , and several temperatures. (a) Dot occupation as a function of the bare dot level. (b) Variationally determined  $\gamma_{\min}$  and renormalized dot level as functions of the bare dot level. (c) Thermodynamic potential as a function of  $\gamma$  for  $T = 0.3$  and  $\Delta$  in the vicinity of the resonance. Here, we consider the lower (black solid line) or upper (dashed red line) root of the self-consistency equation for  $n_d$ . (d) Linear conductance as a function of the bare dot level. Inset: renormalized dot-lead coupling. (e) and (f) Electronic spectral function  $\tilde{A}$  and integrated spectral weight  $S$  for  $T = 0.3$  and  $\Delta = 5$  and  $\Delta = 4.5$ , respectively.

### B. Equilibrium, high temperature

In the following, we consider the effect of finite temperatures on the equilibrium properties of the quantum dot. We set  $\Gamma^{(0)} = 0.3$  and  $\varepsilon_p = 4$ , thereby entering the strong-coupling, nonadiabatic regime. Figure 3 shows the same quantities as Fig. 2, but compares the low-temperature result ( $T = 0.01$ , black curves) to our findings for  $T = 0.3$ , which, considering phonon energies in the order of 100 meV,<sup>2,34</sup> corresponds to room temperature.

Comparing the low-temperature result in Fig. 3(a) to the one for  $\varepsilon_p = 4$  in Fig. 2(a), we see that the reduction of the bare-electron tunneling rate increases the effective EP coupling strength in such a way that the charging transition becomes discontinuous. If we increase the temperature, the transition becomes continuous again. As Fig. 3(c) shows, for  $T = 0.3$  the optimal  $\gamma$  is situated in a region where only a single root of Eq. (73) exists [cf. Fig. 2(c)].

Moreover, at high temperatures the Fermi edges of the leads soften. Thermally excited lead electrons see a considerably reduced injection gap so that the charging transition becomes wide spread. We know from Sec. III A 1 that in the strong-coupling antiadiabatic regime at resonance, when phonon emission by electrons and holes is possible, the variational parameter  $\gamma_{\min}$  comes close to unity. At finite temperatures  $T \approx \omega_0$  absorption of free phonons by incident electrons opens additional inelastic transmission channels. Our ansatz accounts for this with  $\gamma_{\min}$  approaching one at  $\Delta \approx 4.5$  well above resonance. The polaron formation is signalled by two wiggles in the renormalized dot level. The impact on the linear conductance can be seen in Fig. 3(d): in

contrast to the low-temperature result, we now find three peaks in  $L$ .

Figures 3(e) and 3(f) compare the electronic spectral functions before and after the polaron formation. For  $\Delta = 5$  and  $\gamma_{\min} \approx 0.6$ , nearly all spectral weight lies in a few overlapping emission signals situated above the chemical potential. Because at  $T \approx \omega_0$  the floating condition mentioned in Sec. III A 2 is relaxed, we find a small phonon peak at the chemical potential. That is why the conductance resonance broadens with respect to the low-temperature result. For  $\Delta \rightarrow 4.5$ , the phonon peaks are shifted away from the chemical potential. As  $\gamma$  approaches one, the polaron lifetime  $\propto 1/\tilde{\Gamma}^{(0)}$  is increased by one order of magnitude [see inset Fig. 3(d)]. Consequently, the peaks in the spectral function narrow and spectral weight is transferred to higher-order phonon signals. The net linear response, being an average over transmission channels near the chemical potential, decreases and shapes the outer conductance peaks. At  $\Delta = \varepsilon_p = 4$  the narrow zero-phonon peak crosses the usual resonance. We note that the maximum value of  $L$  is smaller than in the low-temperature calculation.

### C. Nonequilibrium situation

The most important experimental technique for the characterization of molecular junctions is IETS. Experiments can be subdivided into nonresonant and resonant tunneling scenarios (RIETS). In the former, the energy of the molecular ion (i.e.,  $\tilde{\eta}$ ) lies far above the lead chemical potentials. Consequently, electron residence times are short and inelastic effects are small. In the latter, resonance is achieved via the application

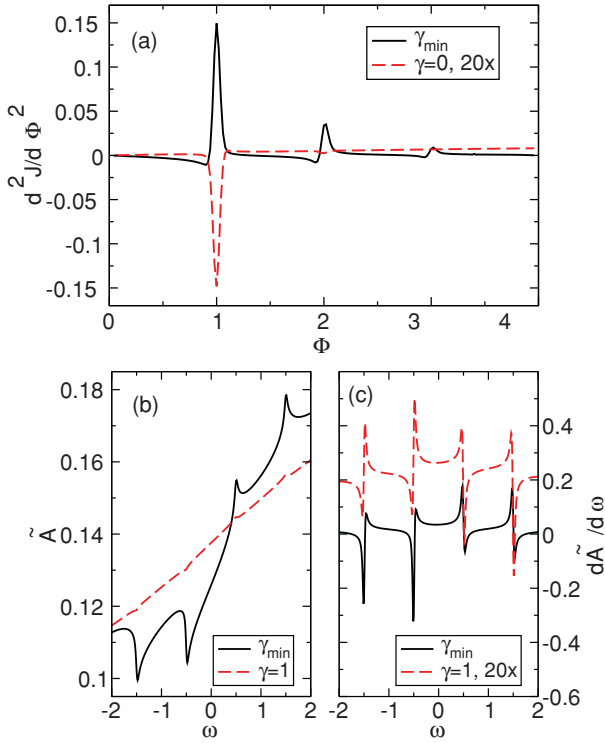


FIG. 4. (Color online) For model parameters  $T = 0.01$ ,  $\Gamma^{(0)} = 10$ ,  $\varepsilon_p = 2$ , and  $\Delta = 8$ . (a) Second derivative of the electron current as a function of the voltage bias for fixed  $\gamma = 0$  (scaled by a factor of 20) and variationally determined parameter  $\gamma_{\min}$ , respectively. (b) and (c) Electronic spectral functions and their first derivatives at  $\Phi = \omega_0$ , respectively.

of a gate voltage and strong EP interaction is expected. In both cases the current-voltage characteristics exhibit distinct features attributed to vibrational coupling at the junction. In analogy to the preceding sections, we will analyze the adiabatic and antiadiabatic limiting cases before considering equal phononic and electronic time scales.

### 1. Limiting cases

Figure 4(a) shows the second derivative of the total electron current as a function of the voltage in the nonresonant ( $\Delta = 8$ ) adiabatic regime ( $\Gamma^{(0)} = 10$ ) for intermediate EP coupling strength ( $\varepsilon_p = 2$ ). For fixed  $\gamma = 0$  we find a single dip at  $\Phi = \omega_0$ , where  $\tilde{\eta} = 6.8$ . Here, phonon-emission by incident electrons causes an additional inelastic tunneling current. Moreover, quasielastic processes involving the emission and subsequent absorption of a single phonon are no longer virtual, because the intermediate polaron state is only partially occupied. The tunneling current (98) is an integral over the energies of all incident and outgoing electrons and does not resolve the various tunneling processes. Therefore polaronic features are observed in the second derivative of  $J$ . As Persson showed,<sup>8</sup> the destructive interference of the elastic and quasielastic processes may overcompensate the positive inelastic contribution, leading to the dip in the IETS signal. In their SCBA analysis, Galperin *et al.*<sup>11</sup> demonstrated the strong

qualitative dependence of this signature on the dot level  $\Delta$  and the bare molecule-lead coupling  $\Gamma^{(0)}$ . Our ansatz allows for the polaronic renormalization of both these parameters; at  $\Phi = \omega_0$  the variational calculation gives an optimal  $\gamma_{\min} = 0.3$  and the effective dot level is further lowered ( $\tilde{\eta} = 6.4$  at  $\Phi = \omega_0$ ). As can be seen from the electronic spectral function in Fig. 4(b), the spectral weight of inelastic electron tunneling processes at  $\omega \geq \Phi/2 = 0.5$  grows at the cost of the elastic transmission at  $\omega = 0$ . As a consequence, the overall IETS signal now shows a pronounced peak at  $\Phi = \omega_0$  [note the scaling of the curves in Fig. 4(a)] and additional phonon features whenever the voltage crosses integer multiples of  $\omega_0$ . With the current being an integral over the quantum dot spectrum, the qualitative change in the one-phonon IETS signal can be traced back to the first derivative of  $\tilde{A}(\omega)$ ,<sup>10</sup> which can be seen in Fig. 4(c). When going from  $\gamma = 1$  to  $\gamma_{\min} = 0.3$ , the sum of the peak derivatives of  $\tilde{A}$  at  $\omega = \mu_{L,R} = \pm\Phi/2$  changes sign, showing that the inelastic tunneling current outweighs the destructive interference of the elastic channels.

Figures 5(a) and 5(b) present the total current and differential conductance as functions of the voltage in the resonant ( $\Delta = 2$ ) antiadiabatic regime ( $\Gamma^{(0)} = 0.1$ ) for intermediate EP coupling strength ( $\varepsilon_p = 2$ ). Because the voltage is raised symmetrically around the equilibrium chemical potential, the dot occupation as well as the renormalized dot level  $\tilde{\eta} = 0$  remain constant. Both the variational calculation and the  $\gamma = 1$  case exhibit steps in the total current and pronounced peaks in the differential conductance whenever the voltage equals multiple integers of  $2\omega_0$ . Here, resonant tunneling through phononic sidebands becomes possible. At  $\Phi \approx 12$ , the current saturates because now the so-called ‘‘Fermi window’’  $\omega \in [-\Phi/2, +\Phi/2]$  encompasses all phonon side bands [see Fig. 5(c)]. In the low-voltage region  $\Phi < 4$ , the optimal variational parameter differs considerably from one ( $\gamma_{\min} \approx 0.9$ ), thereby increasing the overall weight of the relevant few-phonon inelastic tunneling channels. As a consequence, the low-voltage current is larger than in the  $\gamma = 1$  case. Nevertheless, the growth of  $\gamma_{\min}$  along a current plateau dynamically shifts spectral weight from the corresponding resonant inelastic channel to higher lying bands outside the Fermi window. As can be seen from the inset of Fig. 5(b), the differential conductance is negative, which is in accordance with the polaron-induced NDC found by La Magna and Deretzis.<sup>17</sup> Only when an upward step (peak in  $d^2 J/d\Phi^2$ ) signals the opening of a nonresonant inelastic channel, the differential conductance becomes positive again.

### 2. Intermediate dot-lead coupling regime

We now turn to the regime of equal electronic and phononic time scales, setting  $\Gamma^{(0)} = 1$  and keeping  $T = 0.01$  and  $\varepsilon_p = 2$  fixed. First, we hold  $\Delta = 2$  at resonance, starting with  $\gamma_{\min} = 0.5$  and  $n_d = 0.5$  in equilibrium (cf. Fig. 2). Figure 6(a) presents the corresponding current-voltage characteristics. We compare the result of the variational calculation (black solid lines) to the case with fixed  $\gamma = 1$  (blue dashed lines) and to an effective electron model (red dash-dotted lines). The latter is obtained by setting  $g = 0$  in Eqs. (66) and (71) and inserting for  $\Gamma_a^{(0)}$  the renormalized dot-lead coupling  $\tilde{\Gamma}^{(0)}$  resulting from the variational calculation. It is comparable to earlier works

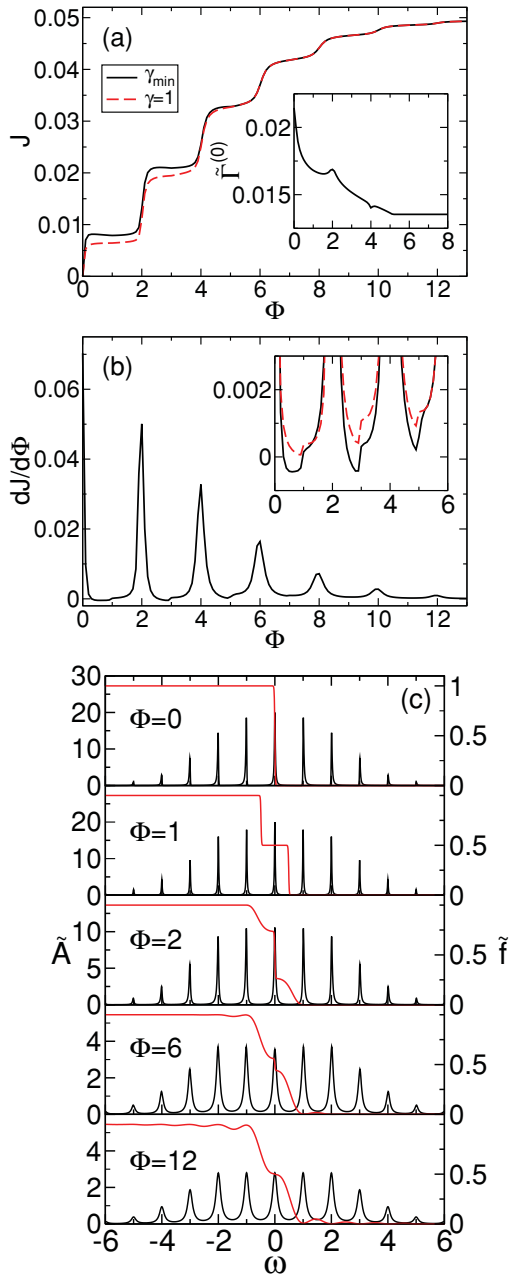


FIG. 5. (Color online) For model parameters  $T = 0.01$ ,  $\Gamma^{(0)} = 0.1$ ,  $\varepsilon_p = 2$ , and  $\Delta = 2$ . (a) Electron current as a function of the voltage bias, compared to the result with fixed  $\gamma = 1$ . Inset: renormalized dot-lead coupling. (b) Differential conductance as a function of the voltage bias. Inset: zoom on the low-voltage region. (c) Electronic spectral functions  $\tilde{A}$  and nonequilibrium electron distribution functions  $\tilde{f}$  for several voltages.

where the averaging over the phonon state leads to an effective electron Hamiltonian.<sup>17,35</sup>

With growing voltage, the variational parameter steadily increases and approaches one in the high-voltage limit  $\Phi > 6$ . The elastic transmission rate  $\tilde{\Gamma}^{(0)}$  shown in the inset of Fig. 6(a) decreases accordingly. It exhibits steps at integer multiples of

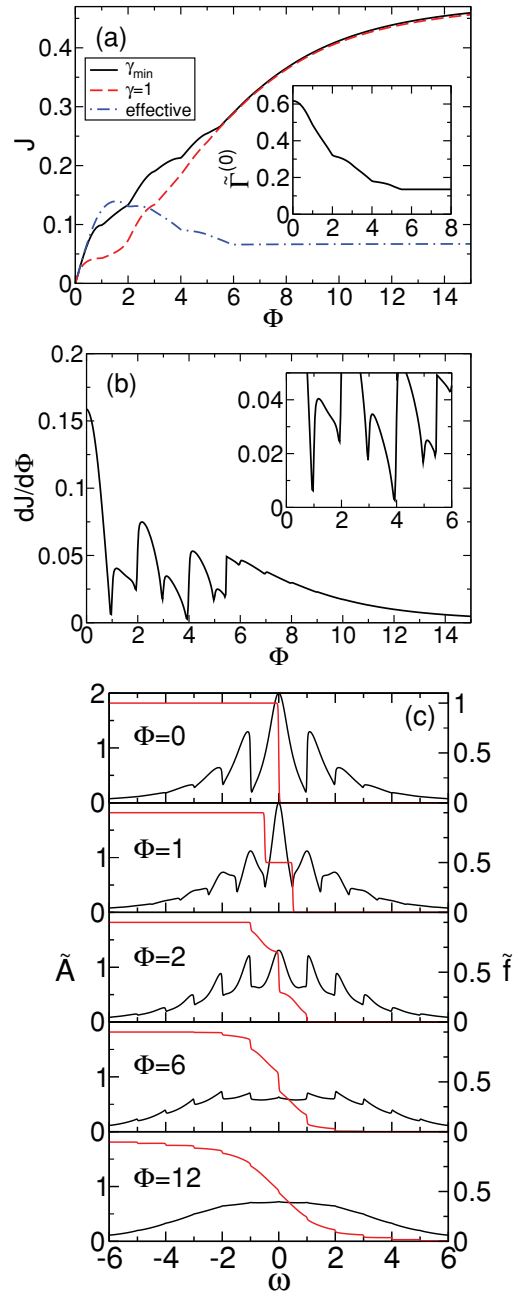


FIG. 6. (Color online)  $\Gamma^{(0)} = 1$ ,  $\Delta = 2$ , and  $\varepsilon_p = 2$ . (a) Electron current as a function of the voltage for the variational calculation ( $\gamma_{\min}$ ), compared to the result with fixed  $\gamma = 1$  as well as an effective electron model using renormalized parameters  $\tilde{\Gamma}^{(0)}$  and  $\tilde{\eta}$  determined by the variational calculation. (b) Differential conductance as a function of the voltage bias. Inset: zoom on the low-voltage region. (c) Electronic spectral functions  $\tilde{A}$  and nonequilibrium electron distribution functions  $\tilde{f}$  for several voltages.

$2\omega_0$ , suggesting that the polaron formation is especially rapid whenever a new resonant inelastic channel is accessible. The electronic spectral functions in Fig. 6(c) show that spectral weight is shifted from the zero-phonon peak to the overlapping phonon side bands.

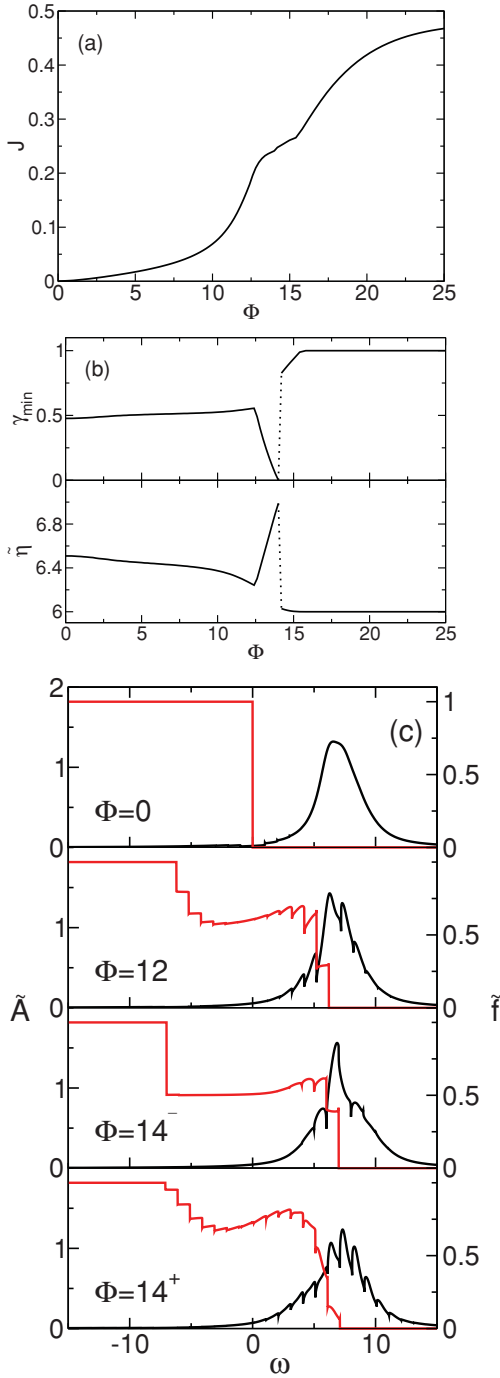


FIG. 7. (Color online)  $\Gamma^{(0)} = 1$ ,  $\Delta = 8$ , and  $\varepsilon_p = 2$ . (a) Electron current as a function of the voltage. (b) Variationally determined parameter  $\gamma_{\min}$  and renormalized dot-level as functions of the voltage. (c) Electronic spectral functions  $\tilde{A}$  and nonequilibrium electron distribution functions  $\tilde{f}$  for several voltages, e.g., slightly below ( $\Phi = 14^-$ ) and above ( $\Phi = 14^+$ ) the jump in  $\gamma_{\min}$ .

The current-voltage characteristics of the interacting results ( $\gamma_{\min}$  and  $\gamma = 1$ ) contain signatures of both limiting cases discussed in Sec. III C 1, as can be seen from the differential conductance in Fig. 6(b). As before, at voltages corresponding

to integer multiples of  $2\omega_0$ , steps in the current (peaks in the conductance) signal the onset of resonant inelastic tunneling. These steps are considerably broadened and overlap with the onset of nonresonant inelastic tunneling. As a consequence, the polaron-induced renormalization of the resonant channel is compensated and, in contrast to the low-voltage adiabatic regime,  $dJ/d\Phi$  remains strictly positive.

The effective electron model overestimates the current in the region  $\omega_0 < \Phi < 2\omega_0$ . Since the spectrum contains no phonon side bands, for  $\Phi > 2\omega_0$  the decrease of the elastic tunneling rate  $\propto \tilde{\Gamma}^{(0)}$  is not compensated by resonant or nonresonant inelastic transmission processes. Consequently, we find a considerably lower maximum current and, in accordance with the results of La Magna and Deretzis,<sup>17</sup> NDC in the intermediate-to-high-voltage region. We conclude that the polaron-induced renormalization of the dot-lead coupling is indeed a possible mechanism for NDC. Yet, the effective electron calculation misses the spectral features that are essential for electron transport at voltages exceeding  $\omega_0$ . The interplay of several inelastic transmission channels may heavily reduce or, for  $\Gamma^{(0)} \gtrsim \omega_0$ , even prevent the occurrence of NDC.

Another interesting consequence of the dynamic polaron formation can be observed in the high-voltage regime, where a crossover from nonresonant to resonant transport takes place. We keep the above system parameters, but start from the nonresonant equilibrium situation with  $\Delta = 8$ . The result is presented in Fig. 7. As the voltage is raised, the variational parameter as well as the effective dot level remain nearly constant and transport takes place via nonresonant inelastic tunneling. At  $\Phi = 12.4$ , the chemical potential of one lead resonates with  $\tilde{\eta} = 6.2$ , causing a broad step in the total current. When the voltage is raised further, the system maximizes its kinetic energy by decreasing the polaronic shift in such a way, that  $\tilde{\eta}$  stays locked to the lead chemical potential [see Fig. 7(b)]. As the spectral functions in Fig. 7(c) suggest, this happens at the cost of the inelastic transmission channels. As soon as  $\gamma_{\min} = 0$  and resonance of the zero-phonon level can no longer be maintained, the system reduces its potential energy by forming a transient polaron. Here,  $\gamma_{\min}$  jumps to one and the effective dot level is lowered by the full polaron binding energy  $\varepsilon_p$ . The spectral functions in the vicinity of this transition show that the spectral weight is redistributed to inelastic channels within the Fermi window. Consequently, the current shows no discontinuity or NDC at this point.

#### IV. SUMMARY

In this work, we investigate the steady-state transport through a vibrating molecular quantum dot. Within the Kadanoff-Baym formalism, the nonequilibrium dot self-energy is calculated to second order in the interaction coefficients. To describe the polaronic character of the quantum dot state, we apply a variational Lang-Firsov transformation and determine the degree of transformation self-consistently by minimizing the thermodynamic potential.

In this framework, we are able to study the molecular junction for all ratios of the dot-lead coupling to the energy of the local phonon mode, i.e., from the adiabatic to the antiadiabatic regime. Moreover, the EP interaction can be



varied from weak to strong coupling. Tuning the electronic dot level and the external voltage bias, we can finally consider resonant and off-resonant transport in the equilibrium and nonequilibrium situation.

In the adiabatic regime, we find important corrections to the result of the SCBA when the EP coupling grows: in the equilibrium off-resonant situation, the mean-field oscillator shift is reduced and spectral weight is transferred from elastic to inelastic channels. For finite voltages, we observe a pronounced peak in the electron tunneling signal, followed by several pronounced multiphonon features.

In the antiadiabatic regime, away from the very strong coupling limit, the weight of the transient polaron state is smaller than predicted by the complete Lang-Firsov transformation. Accordingly, the equilibrium linear conductance as well as the low-voltage resonant tunneling current increase, because few-phonon emission processes are amplified. As the voltage bias grows, the full Lang-Firsov polaron forms. Here, due to a dynamical renormalization of the dot-lead coupling, we find NDC along the resonant current plateaus.

Most notably, our variational approach also allows the investigation of the intermediate regime where the dot-lead coupling and the phonon energy are of the same order. For weak EP coupling, the linear conductance shows a single resonance peak as a function of the electronic dot level. When the coupling strength is increased, this peak narrows and shifts, signaling the crossover from coherent tunneling to sequential hopping via a long-living, transient polaron at the dot. For very strong coupling, the polaron formation takes place discontinuously, as the system switches between various metastable states. At finite temperatures, this transition becomes continuous again. At the same time, the equilibrium linear conductance signal broadens and shows distinct phonon side peaks. Thermally activated transport via phonon absorption induces polaron formation far from resonance. In the low-temperature nonequilibrium situation, the differential conductance remains positive for all voltages: the polaron-induced renormalization of the dot-lead coupling is compensated by the onset of off-resonant inelastic transport. In the off-resonant high-voltage regime, the polaron level follows the lead chemical potential to enhance resonant transport and maximize the kinetic energy.

Let us emphasize that we determine the current through the dot by means of an approximation to the electronic spectral function that contains inelastic features to all orders in the EP coupling. We compare our results to an effective electron model, which accounts for the electron-phonon interaction only via a renormalized dot-lead coupling parameter (e.g., in analogy to Ref. 17). For this model negative differential conductance is observed. This is because the effective electronic spectral function does not include inelastic features that affect transport for voltages exceeding the phonon frequency.

The present study may be extended in several directions: (i) description of hysteretic behavior in the strong-coupling, high-voltage regime, (ii) inclusion of the dynamics of the phonon subsystem by means of nonequilibrium phonon Green functions, and (iii) incorporation of Coulomb interaction at the dot to produce even stronger nonlinear effects through the

competition of a population-dependent repulsive dot potential with the polaronic level shift.

#### ACKNOWLEDGMENTS

This work was supported by Deutsche Forschungsgemeinschaft through SFB 652 B5. T.K. and H.F. acknowledge the hospitality at the Institute of Physics ASCR.

#### APPENDIX: DERIVATION OF THE CURRENT FORMULA

Deducing the current response in Sec. II G, the following real-time Green functions (defined according to Mahan<sup>31</sup>) are used

$$g^r(t_1, t_2) = \Theta(t_1 - t_2)g^>(t_1, t_2) + \Theta(t_2 - t_1)g^<(t_1, t_2), \quad (\text{A1})$$

$$g^{\bar{r}}(t_1, t_2) = \Theta(t_2 - t_1)g^>(t_1, t_2) + \Theta(t_1 - t_2)g^<(t_1, t_2), \quad (\text{A2})$$

where  $\Theta$  is the Heaviside function. The relations of  $g^r$  and  $g^{\bar{r}}$  to the retarded and advanced Green functions read

$$g^{\text{ret}} = g^r - g^< = g^> - g^{\bar{r}}, \quad (\text{A3})$$

$$g^{\text{adv}} = g^r - g^> = g^< - g^{\bar{r}}, \quad (\text{A4})$$

and Eq. (96) may be written as

$$\begin{aligned} & -\frac{\sqrt{N}}{t_{ka}^*} \tilde{g}_{cd}^<(k, a; t_1, t_2; U) \\ & = \int_{-\infty}^{\infty} d\bar{t}_1 g_{cc}^{(0)r}(k, a; t_1, \bar{t}_1; U) \tilde{g}_{dd}^<(\bar{t}_1, t_2; U) \\ & - \int_{-\infty}^{\infty} d\bar{t}_1 g_{cc}^{(0)<}(k, a; t_1, \bar{t}_1; U) \tilde{g}_{dd}^{\bar{r}}(\bar{t}_1, t_2; U). \end{aligned} \quad (\text{A5})$$

As far as the steady-state is concerned, all averages in the definitions of the Green functions above dependent only on the differences of time variables. Consequently, the integrals on the right-hand side of Eq. (A5) may be rewritten in the form of a convolution and the Fourier transformation of Eq. (A5) is

$$\begin{aligned} \tilde{g}_{cd}^<(k, a; \omega; U) & = -\frac{t_{ka}^*}{\sqrt{N}} \left[ g_{cc}^{(0)r}(k, a; \omega; U) \tilde{g}_{dd}^<(\omega; U) \right. \\ & \left. - g_{cc}^{(0)<}(k, a; \omega; U) \tilde{g}_{dd}^{\bar{r}}(\omega; U) \right]. \end{aligned} \quad (\text{A6})$$

Here, the Fourier transforms of the response functions are defined in the usual convention, i.e., without the factors  $\pm i$  introduced by Eqs. (35) and (36). In particular, the conventional Fourier transforms fulfill

$$[g^{\lessgtr}(\omega)]^* = -g^{\lessgtr}(\omega), \quad (\text{A7})$$

because the left-hand side of Eq. (35) is a real function. Taking into account the general property that  $[g^{\text{ret}}(\omega)]^* = g^{\text{adv}}(\omega)$ , the relations (A3), (A4) and (A7) give

$$[g^r(\omega)]^* = -g^{\bar{r}}(\omega). \quad (\text{A8})$$

With the help of Eqs. (A7) and (A8), the complex conjugate of  $\tilde{g}_{cd}^{\lessgtr}(k, a; \omega; U)$  in Eq. (92) is determined and the following formula for the current  $J_a$  results:

$$J_a = -\frac{e}{N} \sum_k |t_{ka}|^2 \int_{-\infty}^{\infty} \frac{d\omega}{2\pi} \{ [g_{cc}^{(0)r}(k, a; \omega; U) + g_{cc}^{(0)\bar{r}}(k, a; \omega; U)] \tilde{g}_{dd}^{\lessgtr}(\omega; U) - g_{cc}^{(0)<}(k, a; \omega; U) \times [\tilde{g}_{dd}^{\lessgtr}(\omega; U) + \tilde{g}_{dd}^{\lessgtr}(\omega; U)] \}. \quad (\text{A9})$$

Substituting the explicit forms of the free electron functions

$g_{cc}^{(0)\lessgtr}$  and using the relation  $g^r + g^{\bar{r}} = g^> + g^<$  following from Eqs. (A3) and (A4), we obtain

$$J_a = -\frac{e}{N} \sum_k |t_{ka}|^2 \int_{-\infty}^{\infty} \frac{d\omega}{2\pi} 2\pi \delta(\omega - \xi_{ka}) \{ -i \tilde{g}_{dd}^{\lessgtr}(\omega; U) + f(\xi_{ka} + U_a) i [\tilde{g}_{dd}^{\lessgtr}(\omega; U) - \tilde{g}_{dd}^{\lessgtr}(\omega; U)] \}. \quad (\text{A10})$$

Going back to the definitions of the Fourier transforms according to Eqs. (35) and (36), we arrive at Eq. (97) of Sec. II G.

- <sup>1</sup>K. W. Hipps and U. Mazur, *J. Phys. Chem.* **97**, 7803 (1993); M. A. Reed, C. Zhou, C. J. Muller, T. P. Burgin, and J. M. Tour, *Science* **278**, 252 (1997).
- <sup>2</sup>H. Park, J. Park, A. K. L. Lim, E. H. Anderson, A. P. Alivisatos, and P. L. McEuen, *Nature (London)* **407**, 57 (2000).
- <sup>3</sup>Y. Meir and N. S. Wingreen, *Phys. Rev. Lett.* **68**, 2512 (1992).
- <sup>4</sup>M. Galperin, M. A. Ratner, and A. Nitzan, *J. Phys. Condens. Matter* **19**, 103201 (2007).
- <sup>5</sup>C. Caroli, R. Combescot, D. Lederer, P. Nozieres, and D. Saint-James, *J. Phys. C* **5**, 21 (1971).
- <sup>6</sup>A. Mitra, I. Aleiner, and A. J. Millis, *Phys. Rev. B* **69**, 245302 (2004).
- <sup>7</sup>O. Entin-Wohlman, Y. Imry, and A. Aharony, *Phys. Rev. B* **80**, 035417 (2009).
- <sup>8</sup>B. N. J. Persson, *Physica Scripta* **38**, 282 (1988).
- <sup>9</sup>T. Mii, S. G. Tikhodeev, and H. Ueba, *Surface Science* **502**, 26 (2002).
- <sup>10</sup>T. Mii, S. G. Tikhodeev, and H. Ueba, *Phys. Rev. B* **68**, 205406 (2003).
- <sup>11</sup>M. Galperin, M. A. Ratner, and A. Nitzan, *J. Chem. Phys.* **121**, 11965 (2004).
- <sup>12</sup>T. Holstein, *Ann. Phys. (NY)* **8**, 325 (1959); **8**, 343 (1959).
- <sup>13</sup>G. Wellein and H. Fehske, *Phys. Rev. B* **56**, 4513 (1997); **58**, 6208 (1998); H. Fehske and S. A. Trugman, in *Polarons in Advanced Materials*, Springer Series in Material Sciences, Vol. 103, edited by A. S. Alexandrov (Canopus/Springer, Dordrecht, 2007), pp. 393–461.
- <sup>14</sup>H. Fehske, G. Wellein, J. Loos, and A. R. Bishop, *Phys. Rev. B* **77**, 085117 (2008).
- <sup>15</sup>M. Galperin, M. A. Ratner, and A. Nitzan, *Nano Lett.* **5**, 125 (2005).
- <sup>16</sup>S. Yeganeh, M. Galperin, and M. A. Ratner, *J. Am. Chem. Soc.* **129**, 13313 (2007); M. Galperin, A. Nitzan, and M. A. Ratner, *J. Phys. Condens. Matter* **20**, 374107 (2008).
- <sup>17</sup>A. La Magna and I. Deretzis, *Phys. Rev. Lett.* **99**, 136404 (2007).
- <sup>18</sup>A. S. Alexandrov and A. M. Bratkovsky, *Phys. Rev. B* **67**, 235312 (2003); A. M. Bratkovsky, in *Polarons in Advanced Materials*, Springer Series in Material Sciences, Vol. 103, edited by A. S. Alexandrov (Canopus/Springer, Dordrecht, 2007), p. 623; A. S. Alexandrov and A. M. Bratkovsky, *ibid.* **80**, 115321 (2009).
- <sup>19</sup>I. G. Lang and Y. A. Firsov, *Zh. Eksp. Teor. Fiz.* **43**, 1843 (1962).
- <sup>20</sup>N. S. Wingreen, K. W. Jacobsen, and J. W. Wilkins, *Phys. Rev. B* **40**, 11834 (1989).
- <sup>21</sup>U. Lundin and R. H. McKenzie, *Phys. Rev. B* **66**, 075303 (2002); J. X. Zhu and A. V. Balatsky, *ibid.* **67**, 165326 (2003).
- <sup>22</sup>M. Galperin, A. Nitzan, and M. A. Ratner, *Phys. Rev. B* **73**, 045314 (2006).
- <sup>23</sup>L. P. Kadanoff and G. Baym, *Quantum Statistical Mechanics* (Benjamin/Cummings, Reading, Massachusetts, 1962).
- <sup>24</sup>J. Loos, M. Hohenadler, and H. Fehske, *J. Phys. Condens. Matter* **18**, 2453 (2006); J. Loos, M. Hohenadler, A. Alvermann, and H. Fehske, *ibid.* **19**, 2362 (2007).
- <sup>25</sup>J. Loos, T. Koch, A. Alvermann, A. R. Bishop, and H. Fehske, *J. Phys. Condens. Matter* **21**, 395601 (2009); T. Koch, J. Loos, A. Alvermann, A. R. Bishop, and H. Fehske, *J. Phys. Conf. Ser.* **220**, 012014 (2010).
- <sup>26</sup>H. J. W. Haug and A. Jauho, *Quantum Kinetics in Transport and Optics of Semiconductors* (Springer, Berlin Heidelberg, 2008).
- <sup>27</sup>H. Fehske, D. Ihle, J. Loos, U. Trapper, and H. Büttner, *Z. Phys. B* **94**, 91 (1994).
- <sup>28</sup>J. Schnakenberg, *Z. Phys.* **190**, 209 (1966).
- <sup>29</sup>S. Datta, *Electronic Transport in Mesoscopic Systems* (Cambridge University Press, Cambridge, 1995).
- <sup>30</sup>A. L. Fetter and J. D. Walecka, *Quantum Theory of Many-Particle Systems* (McGraw-Hill, 1971).
- <sup>31</sup>G. D. Mahan, *Many-Particle Physics* (Kluwer Academic/Plenum, New York, 2000).
- <sup>32</sup>A. Alvermann and H. Fehske, *Phys. Rev. B* **77**, 045125 (2008).
- <sup>33</sup>J. Koch and F. von Oppen, *Phys. Rev. Lett.* **94**, 206804 (2005).
- <sup>34</sup>A. Bayman, P. K. Hansma, and W. C. Kaska, *Phys. Rev. B* **24**, 2449 (1981); R. Heid, L. Pintschovius, and J. M. Godard, *ibid.* **56**, 5925 (1997).
- <sup>35</sup>A. La Magna, I. Deretzis, and V. Privitera, *Eur. Phys. J. B* **70**, 311 (2009).

# Phonon-affected steady-state transport through molecular quantum dots

T Koch<sup>1</sup>, H Fehske<sup>1</sup> and J Loos<sup>2</sup>

<sup>1</sup> Institut für Physik, Ernst-Moritz-Arndt-Universität Greifswald, DE-17489 Greifswald, Germany

<sup>2</sup> Institute of Physics, Academy of Sciences of the Czech Republic, CZ-16200 Prague, Czech Republic

E-mail: [thomas.koch@physik.uni-greifswald.de](mailto:thomas.koch@physik.uni-greifswald.de)

Received 25 April 2012

Accepted for publication 27 June 2012

Published 30 November 2012

Online at [stacks.iop.org/PhysScr/T151/014039](http://stacks.iop.org/PhysScr/T151/014039)

## Abstract

We consider the transport through a vibrating molecular quantum dot contacted to macroscopic leads acting as charge reservoirs. In the equilibrium and nonequilibrium regimes, we study the formation of a polaron-like transient state at the quantum dot for all the ratios of the dot–lead coupling to the energy of the local phonon mode. We show that the polaronic renormalization of the dot–lead coupling is a possible mechanism for negative differential conductance. Moreover, the effective dot level follows one of the lead chemical potentials to enhance resonant transport, causing novel features in the inelastic tunneling signal. In the linear response regime, we investigate the impact of the electron–phonon interaction on the thermoelectrical properties of the quantum dot device.

PACS numbers: 72.10.–d, 71.38.–k, 73.21.La, 73.63.Kv

(Some figures may appear in color only in the online journal)

## 1. Introduction

Electronic devices featuring a single organic molecule as the active element, the so-called molecular junctions, are promising candidates in the search for further miniaturization and novel functionality. Such systems can be described as quantum dots: mesoscopic systems coupled to macroscopic charge and heat reservoirs.

Molecular junctions are susceptible to structural changes when being occupied by charge carriers. The local interaction with optical phonons becomes apparent as vibrational signatures in the current–voltage characteristics of the device [1–3], resulting from the interference of elastic and inelastic tunneling processes and the renormalization of the effective dot level energy [4–8]. When the vibrational energy and the electron–phonon (EP) interaction become sufficiently large, nonlinear phenomena emerge, such as hysteresis, switching and negative differential conductance (NDC). As is well known from the Holstein molecular crystal model [9, 10], strong EP interaction may heavily reduce the ‘mobility’ of electrons through the formation of small polarons [11–14]. Thus, the formation of a local polaron is considered a possible

mechanism for the observed nonlinear transport properties of molecular junctions [15].

Molecular junctions may also constitute efficient power generators or heat pumps. Their highly energy-dependent transmission together with the tunable level energy could be used to optimize the thermoelectrical figure of merit. In the weak dot–lead (DL) coupling limit, the theoretical efficiency approaches the Carnot value [16]. However, long electron residence times increase the effective EP coupling. Moreover, some level broadening is needed to ensure useable power output. That is why, for practical applications, the regime of comparable electronic and phononic time scales becomes interesting.

In this work, we calculate the steady-state charge and energy transport through the quantum dot for small-to-large DL coupling and weak-to-strong EP interaction. On the basis of a variational Lang–Firsov transformation [15, 17–21], we determine the nonequilibrium dot spectral function in the formalism of Kadanoff–Baym [22] and calculate the dot self-energy in a self-consistent way up to second order in the renormalized interaction coefficients. The variational parameter is determined numerically by minimizing the thermodynamic potential.

## 2. The model

We consider the standard Hamiltonian of the single-site quantum dot. It is based on a modified Fano–Anderson model with the static impurity being replaced by a single site coupled to a local phonon mode ( $\hbar = 1$ ):

$$H = (\Delta - \mu)d^\dagger d - g\omega_0 d^\dagger d(b^\dagger + b) + \omega_0 b^\dagger b + \sum_{k,a} (\varepsilon_{ka} - \mu) c_{ka}^\dagger c_{ka} - \frac{1}{\sqrt{N}} \sum_{k,a} \left( t_{ka} d^\dagger c_{ka} + t_{ka}^* c_{ka}^\dagger d \right). \quad (1)$$

The quantum dot is represented by the energy level  $\Delta$ , with the fermionic operators  $d^{(\dagger)}$ . It is coupled to a local phonon mode  $b^{(\dagger)}$  of energy  $\omega_0$ , with the dimensionless EP coupling strength  $g$ . The operators  $c_{ka}^{(\dagger)}$  (for  $k = 1, \dots, N$ ;  $a = \text{L,R}$ ) correspond to free electrons in the  $N$  states of the left and right the lead, with the energies  $\varepsilon_{ka}$  and the equilibrium chemical potential  $\mu$ . The last term in equation (1) allows for DL particle transfer.

To account for the competition between polaron localization and charge transport, we apply to model (1) an incomplete Lang–Firsov transformation [21], introducing the variational parameter  $\gamma \in [0, 1]$ . Then  $\tilde{H} = S_\gamma^\dagger H S_\gamma$ , with

$$S_\gamma = \exp\{g(b^\dagger - b)(\gamma d^\dagger d + (1 - \gamma)n_d)\}. \quad (2)$$

For  $\gamma = 1$ ,  $S_\gamma$  coincides with the shift-transformation of the Lang–Firsov small-polaron theory [17], which eliminates the EP coupling term in equation (1) and lowers the dot level by the polaron binding energy  $\varepsilon_p = g^2\omega_0$ . For  $\gamma < 1$ ,  $S_\gamma$  accounts for the quasi-static displacement of the equilibrium position of the oscillator, which is proportional to the dot mean occupation  $n_d = \langle d^\dagger d \rangle$ . After the transformation the Hamiltonian reads

$$\begin{aligned} \tilde{H} = & \tilde{\eta} d^\dagger d - g\omega_0(1 - \gamma)(b^\dagger + b)(d^\dagger d - n_d) \\ & + \omega_0 b^\dagger b + \varepsilon_p(1 - \gamma)^2 n_d + \sum_{k,a} (\varepsilon_{ka} - \mu) c_{ka}^\dagger c_{ka} \\ & - \frac{1}{\sqrt{N}} \sum_{k,a} \left( t_{ka} e^{-\gamma g(b^\dagger - b)} d^\dagger c_{ka} + t_{ka}^* e^{\gamma g(b^\dagger - b)} c_{ka}^\dagger d \right). \end{aligned} \quad (3)$$

In (3), the DL coupling is affected by the EP interaction. Furthermore, the bare dot level is renormalized:

$$\tilde{\eta} = \Delta - \mu - \varepsilon_p \gamma (2 - \gamma) - 2\varepsilon_p (1 - \gamma)^2 n_d. \quad (4)$$

Note that now  $d$  and  $b$  are the operators of dressed electrons (in analogy to polarons) and the shifted oscillator. The original electron and oscillator operators now read  $\tilde{d} = \exp\{\gamma g(b^\dagger - b)\} d$  and  $\tilde{b} = b + \gamma g d^\dagger d + (1 - \gamma) g n_d$ .

The application of a potential difference between the leads is described by adding to (3) the interaction with the external fields  $U_a = -\delta\mu_a$  and defining the voltage bias  $\Phi$ , with  $e$  being the negative elementary charge:

$$H_{\text{int}} = \sum_a U_a \sum_k c_{ka}^\dagger c_{ka}, \quad \Phi = (U_L - U_R)/e. \quad (5)$$

## 3. Theoretical approach

### 3.1. The polaronic spectral function in the Kadanoff–Baym formalism

For a finite voltage bias between the noninteracting macroscopic leads, the response of the quantum dot is given by the polaronic nonequilibrium real-time Green functions

$$g_{dd}^<(t_1, t_2; U) = i \langle d_U^\dagger(t_2) d_U(t_1) \rangle, \quad (6)$$

$$g_{dd}^>(t_1, t_2; U) = -i \langle d_U(t_1) d_U^\dagger(t_2) \rangle, \quad (7)$$

where the time dependence of  $d_U^{(\dagger)}$  is determined by  $\tilde{H} + H_{\text{int}}$ . According to Kadanoff–Baym [22], the real-time response functions may be deduced using the equations of motion for the nonequilibrium Green functions  $G_{dd}^{\gtrless}(t_1, t_2; U, t_0)$  of the complex time variables  $t = t_0 - i\tau$ ,  $\tau \in [0, \beta]$ . We base our calculations on the Dyson equation of the polaronic Green functions, which defines the polaronic self-energy  $\Sigma_{dd} = G_{dd}^{(0)-1} - G_{dd}^{-1}$ . For a given ordering of  $t_1, t_2$ , the equations of motion of the functions  $g_{dd}^{\gtrless}$  follow through the limiting procedure  $t_0 \rightarrow -\infty$ . Limiting ourselves to the steady-state regime, we suppose that all functions depend only on  $t = t_1 - t_2$ . After a Fourier transformation by the method used in [22], the following exact equations for the steady state are obtained [21]:

$$g_{dd}^<(\omega; U) \Sigma_{dd}^>(\omega; U) - g_{dd}^>(\omega; U) \Sigma_{dd}^<(\omega; U) = 0, \quad (8)$$

$$\begin{aligned} & [\omega - \tilde{\eta} - \text{Re} \Sigma_{dd}(\omega; U)] A(\omega; U) \\ & = \Gamma(\omega; U) \text{Re} g_{dd}(\omega; U). \end{aligned} \quad (9)$$

Here we defined, in analogy to the equilibrium case,

$$A(\omega; U) = g_{dd}^>(\omega; U) + g_{dd}^<(\omega; U), \quad (10)$$

$$g_{dd}(z; U) = \int \frac{d\omega}{2\pi} \frac{A(\omega; U)}{z - \omega}, \quad (11)$$

$$\Gamma(\omega; U) = \Sigma_{dd}^>(\omega; U) + \Sigma_{dd}^<(\omega; U), \quad (12)$$

$$\Sigma_{dd}(z; U) = \int \frac{d\omega}{2\pi} \frac{\Gamma(\omega; U)}{z - \omega}, \quad (13)$$

where  $A(\omega; U)$  is the polaronic nonequilibrium spectral function. According to equation (10), we can write

$$g_{dd}^<(\omega; U) = A(\omega; U) \bar{f}(\omega; U), \quad (14)$$

$$g_{dd}^>(\omega; U) = A(\omega; U) (1 - \bar{f}(\omega; U)), \quad (15)$$

introducing the nonequilibrium distribution  $\bar{f}$ , which follows from equations (8) and (12) as

$$\bar{f}(\omega; U) = \frac{\Sigma_{dd}^<(\omega; U)}{\Gamma(\omega; U)}. \quad (16)$$

For the Green function  $g_{dd}$  in equation (11) we use the ansatz  $g_{dd}(z; U) = 1/(z - \tilde{\eta} - \Sigma_{dd}(z; U))$  and find the following formal solution to equation (9):

$$A(\omega; U) = \frac{\Gamma(\omega; U)}{\left(\omega - \tilde{\eta} - \mathcal{P} \int \frac{d\omega'}{2\pi} \frac{\Gamma(\omega'; U)}{\omega - \omega'}\right)^2 + \left(\frac{\Gamma(\omega; U)}{2}\right)^2}. \quad (17)$$

To deduce a functional differential equation for the self-energy  $\Sigma_{dd}$ , we add to  $H_{\text{int}}$  in equation (5) the interaction with fictitious external fields  $\{V\}$  (cf [19–23]). The equations of motion of the polaronic Green functions are then expressed by means of the functional derivatives of  $\Sigma_{dd}$  with respect to  $\{V\}$ . The resulting equations for  $\Sigma_{dd}^{\lessgtr}$  are solved iteratively to second order in the renormalized EP and DL interaction coefficients in (3), while the correlation functions of the interaction coefficients are evaluated supposing independent Einstein oscillators. We then let  $\{V\} \rightarrow 0$  and perform the limit  $t_0 \rightarrow -\infty$ . A subsequent Fourier transformation yields

$$\begin{aligned} \Sigma_{dd}^{\lessgtr}(\omega; U) &= \Sigma_{dd}^{(1)\lessgtr}(\omega; U) + [(1 - \gamma)g\omega_0]^2 \\ &\times \left[ A(\omega - \omega_0; U) \bar{f}(\omega - \omega_0; U) n_B(\omega_0) \right. \\ &\left. + A(\omega + \omega_0; U) \bar{f}(\omega + \omega_0; U) (n_B(\omega_0) + 1) \right], \end{aligned} \quad (18)$$

$$\begin{aligned} \Sigma_{dd}^{(1)\lessgtr}(\omega; U) &= \sum_a \left\{ I_0(\kappa) \tilde{\Gamma}_a^{(0)}(\omega + \mu) n_F(\omega + U_a) \right. \\ &+ \sum_{s \geq 1} I_s(\kappa) 2 \sinh(s\theta) \left[ \tilde{\Gamma}_a^{(0)}(\omega - s\omega_0 + \mu) \right. \\ &\times n_B(s\omega_0) n_F(\omega - s\omega_0 + U_a) + \tilde{\Gamma}_a^{(0)}(\omega + s\omega_0 + \mu) \\ &\left. \left. \times (n_B(s\omega_0) + 1) n_F(\omega + s\omega_0 + U_a) \right] \right\}, \end{aligned} \quad (19)$$

with  $n_F(\omega) = (e^{\beta\omega} + 1)^{-1}$ ,  $n_B(\omega) = (e^{\beta\omega} - 1)^{-1}$  and

$$\tilde{\Gamma}_a^{(0)}(\omega) = e^{-\gamma^2 g^2 \coth \theta} \Gamma_a^{(0)}(\omega), \quad (20)$$

$$\Gamma_a^{(0)}(\omega) = 2\pi |t_a(\omega)|^2 \varrho_a(\omega), \quad (21)$$

$$\varrho_a(\omega) = \frac{1}{N} \sum_k \delta(\omega - \varepsilon_{ka}), \quad (22)$$

$$\theta = \frac{1}{2} \beta \omega_0, \quad \kappa = \frac{\gamma^2 g^2}{\sinh \theta} \quad (23)$$

$$I_s(\kappa) = \sum_{m=0}^{\infty} \frac{1}{m!(s+m)!} \left(\frac{\kappa}{2}\right)^{s+2m}. \quad (24)$$

The function  $\Sigma_{dd}^{\lessgtr}(\omega; U)$  describes the in-scattering of polaron-like quasiparticles at the dot [24]. It accounts for multiple phonon emission/absorption processes at finite temperature and with finite particle densities.  $\Sigma_{dd}^{\lessgtr}(\omega; U)$  results from interchanging  $n_B \leftrightarrow (n_B + 1)$ ,  $n_F \leftrightarrow (1 - n_F)$  and  $\bar{f} \leftrightarrow (1 - \bar{f})$  in equation (18). Then the spectral function follows using equations (12) and (17). As we see from equation (18), for any  $\gamma < 1$  the functions  $A$  and  $\bar{f}$  have to be determined self-consistently. Moreover, the renormalized

dot level (4) depends on the dot occupation  $n_d$ , which also has to fulfill a self-consistency condition:

$$n_d = \int_{-\infty}^{\infty} \frac{d\omega}{2\pi} \bar{f}(\omega; U) A(\omega; U). \quad (25)$$

To determine the variational parameter  $\gamma$ , we minimize the thermodynamic potential  $\Omega$ . We use a decoupling approximation between the electron and oscillator degrees of freedom and neglect the influence of the dot states on the leads. We consider an ensemble given by (3), but with the EP and DL interaction coefficients being multiplied by  $\lambda \in [0, 1]$ . Then the thermodynamic potential follows from the well-known general relations in [22, 25]:

$$\begin{aligned} \Omega &= -\frac{1}{\beta} \ln(1 + e^{-\beta\tilde{\eta}}) + \varepsilon_p (1 - \gamma)^2 n_d^2 \\ &+ 2 \int_0^1 d\lambda \frac{1}{\lambda} \int \frac{d\omega}{2\pi} (\omega - \tilde{\eta}) A_\lambda(\omega; U) \bar{f}_\lambda(\omega; U). \end{aligned} \quad (26)$$

To make the integration in equation (26) feasible, we determine  $A_\lambda$  from equation (17) with the self-energy in the first iteration step, i.e.  $\Gamma_\lambda^{(1)} = \lambda^2 (\Sigma_{dd}^{(1)\lessgtr} + \Sigma_{dd}^{(1)\lessgtr})$ . Correspondingly,  $\bar{f}_\lambda^{(1)}$  follows from equation (16) using  $\Sigma_{dd}^{(1)\lessgtr}$  and  $\Gamma^{(1)}$ . However,  $\tilde{\eta}$  will be determined from the dot occupation  $n_d$  resulting from the complete self-energy. The parameter  $\gamma$  that minimizes the thermodynamic potential determines  $\Sigma_{dd}^{\lessgtr}(\omega; U)$  and, consequently, the complete functions  $\bar{f}(\omega; U)$  and  $A(\omega; U)$ .

### 3.2. Electron current and linear response thermopower

The operator of the electron current from lead  $a$  to the dot reads

$$\hat{J}_a = \frac{ie}{\sqrt{N}} \sum_k \left[ t_{ka} \tilde{d}^\dagger c_{ka} - t_{ka}^* c_{ka}^\dagger \tilde{d} \right], \quad (27)$$

with the negative elementary charge  $e$ . We determine the mean value  $J_a = \langle \hat{J}_a \rangle$  using the connection of the required expectation values to the real-time ‘mixed’ Green functions  $g_{cd}(k, a; t_1, t_2; U)$ , which are defined similar to equations (6) and (7) [21]. In the following, we assume identical leads and work in the wide-band approximation, i.e. we set  $\Gamma_a^{(0)}(\omega) = \Gamma_0 = \text{const}$ . Then the steady-state charge current through the dot,  $J = (J_L - J_R)/2$ , reads as

$$J = \frac{e\Gamma_0}{2} \int_{-\infty}^{\infty} \frac{d\omega}{2\pi} \tilde{A}(\omega; U) [n_F(\omega + U_L) - n_F(\omega + U_R)], \quad (28)$$

with the electronic spectral function  $\tilde{A}(\omega; U)$ . The latter is obtained in terms of the polaronic spectral function as follows [21]:

$$\begin{aligned} \tilde{A}(\omega; U) &= e^{-\gamma^2 g^2 \coth \theta} \left\{ I_0(\kappa) A(\omega; U) + \sum_{s \geq 1} I_s(\kappa) 2 \sinh(s\theta) \right. \\ &\times \left( [n_B(s\omega_0) + \bar{f}(\omega + s\omega_0; U)] A(\omega + s\omega_0; U) \right. \\ &\left. \left. + [n_B(s\omega_0) + 1 - \bar{f}(\omega - s\omega_0; U)] A(\omega - s\omega_0; U) \right) \right\}. \end{aligned} \quad (29)$$

Moreover, we define the differential conductance  $G$  of the quantum dot system as

$$G = \frac{dJ}{d\Phi}. \quad (30)$$

In the linear response regime, we suppose the application of an infinitesimal voltage bias  $\Phi = \delta\mu/e$  and temperature difference  $\delta T$  between the leads. Then we can expand the current to first order in  $\delta\mu$  and  $\delta T$  as [26]

$$J = L \frac{\delta\mu}{e} + X \frac{\delta T}{T}, \quad (31)$$

where  $L$  is the linear response conductance and  $X$  is the thermoelectric coefficient. Both quantities follow from the linearization of the Fermi functions in equation (28) around the equilibrium chemical potential  $\mu$  and the equilibrium temperature  $T$ :

$$\begin{aligned} L &= \lim_{\delta\mu \rightarrow 0} \left\{ eJ/\delta\mu \right\} \Big|_{\delta T=0} \\ &= \frac{e^2\Gamma_0}{2} \beta \int_{-\infty}^{\infty} \frac{d\omega}{2\pi} \tilde{A}(\omega) n_F(\omega) (1 - n_F(\omega)), \end{aligned} \quad (32)$$

$$\begin{aligned} X &= \lim_{\delta T \rightarrow 0} \left\{ TJ/\delta T \right\} \Big|_{\delta\mu=0} \\ &= \frac{e\Gamma_0}{2} \beta \int_{-\infty}^{\infty} \frac{d\omega}{2\pi} \omega \tilde{A}(\omega) n_F(\omega) (1 - n_F(\omega)). \end{aligned} \quad (33)$$

In (32) and (33), the electronic spectral function is calculated in equilibrium. With the help of these transport coefficients we define the linear response thermopower

$$S = \frac{eX}{TL}, \quad (34)$$

which is a measure of the thermoelectric efficiency of the quantum dot system.

### 3.3. The weak electron–phonon coupling limit

The current formula (28) and the expressions for the linear response coefficients in equations (32) and (33) have a simple structure, because all the effects of the EP interaction are contained in the electronic spectral function  $\tilde{A}$ . However, our approximation to the spectral function includes terms of arbitrarily high order in the EP coupling strength  $g$ : for  $\gamma > 0$ , this can be seen explicitly in the summations over  $s$  in equations (19) and (29), which describe inelastic (quasielastic) processes involving the emission and absorption of an unequal (equal) number of phonons. As long as  $\gamma < 1$ , high order terms will also result from the iterative calculation of the self-consistent equation (18). Via the denominator of the polaronic spectral function in equation (17), the transport channels will be affected by a voltage-dependent renormalization of the effective dot level and the real part of the self-energy. Lastly, all these contributions are functions of the optimal parameter  $\gamma_{\min}$ , which itself will be voltage dependent. This will lead to complicated current–voltage characteristics in the numerical evaluation of equation (28), which are presented in the next section.

For a better understanding of the numerical results, we want to gain more insight into the different EP coupling effects and their dependence on the parameter  $\gamma$ . To this end, we consider the limit of small EP coupling strengths  $g$  and low voltages  $\Phi < 2\omega_0$ . Then we can expand the self-energy and the spectral function to second order in  $g$  around the noninteracting (i.e. zeroth-order) results. In doing so, we work in the wide-band approximation  $\Gamma_a^{(0)}(\omega) = \Gamma_0 = \text{const}$  and consider low temperatures  $T \ll \omega_0$ , so that  $n_B(\omega_0) \approx 0$ . First, we set  $g = 0$  in equations (18) and (19) and obtain the zeroth-order functions

$$\Gamma^{(0)}(\omega) = 2\Gamma_0, \quad (35)$$

$$A^{(0)}(\omega) = \frac{2\Gamma_0}{(\omega - \Delta + \mu)^2 + \Gamma_0^2}, \quad (36)$$

$$\tilde{f}^{(0)}(\omega; U) = \frac{1}{2} \left( n_F(\omega + U_L) + n_F(\omega + U_R) \right), \quad (37)$$

$$n_d^{(0)} = \int_{-\infty}^{\infty} \frac{d\omega}{2\pi} \tilde{f}^{(0)}(\omega; U) A^{(0)}(\omega). \quad (38)$$

Equations (35)–(38) are the exact solution for  $g = 0$  and describe a rigid quantum dot acting as a tunneling barrier between the leads. Next, we substitute  $A^{(0)}$  and  $\tilde{f}^{(0)}$  for  $A$  and  $\tilde{f}$  in equation (18), which corresponds to the first step in the self-consistent calculation. Moreover, for  $T \ll \omega_0$ , we expand the rhs of equation (19) to second order in  $g$ , whereby only the terms with  $s = 0, 1$  contribute. The resulting approximation of the function  $\Gamma$  can be written as

$$\Gamma(\omega; U) \approx \Gamma^{(0)}(\omega) + \Gamma^{(2)}(\omega; U), \quad (39)$$

with the second-order correction

$$\begin{aligned} \Gamma^{(2)}(\omega; U) &= -2\gamma^2 g^2 \Gamma_0 + 2\gamma^2 g^2 \Gamma_0 \\ &\quad \times \left( \tilde{f}^{(0)}(\omega + \omega_0; U) + 1 - \tilde{f}^{(0)}(\omega - \omega_0; U) \right) \\ &\quad + [(1 - \gamma)g\omega_0]^2 \left[ A^{(0)}(\omega + \omega_0) \tilde{f}^{(0)}(\omega + \omega_0; U) \right. \\ &\quad \left. + A^{(0)}(\omega - \omega_0) (1 - \tilde{f}^{(0)}(\omega - \omega_0; U)) \right]. \end{aligned} \quad (40)$$

The second-order renormalization of the dot level results from substituting  $n_d^{(0)}$  for  $n_d$  in equation (25). Then  $\tilde{\eta}$  is approximated as  $\tilde{\eta} \approx \Delta - \mu + \tilde{\eta}^{(2)}$ , with

$$\tilde{\eta}^{(2)} = -\varepsilon_p \gamma (2 - \gamma) - 2\varepsilon_p (1 - \gamma)^2 n_d^{(0)}. \quad (41)$$

Consequently, we expand the polaronic spectral function in equation (17) with respect to the second-order corrections  $\Gamma^{(2)}$  and  $\tilde{\eta}^{(2)}$  and obtain

$$A(\omega) \approx A^{(0)}(\omega) + A^{(2)}(\omega; U), \quad (42)$$

with

$$\begin{aligned} A^{(2)}(\omega; U) &= \left( \frac{A^{(0)}(\omega)}{2\Gamma_0} \right)^2 \\ &\quad \times \left\{ 4\Gamma_0(\omega - \Delta + \mu) \left( \tilde{\eta}^{(2)} + \text{Re}\Sigma_{dd}^{(2)}(\omega; U) \right) \right. \\ &\quad \left. + \left( (\omega - \Delta + \mu)^2 - \Gamma_0^2 \right) \Gamma^{(2)}(\omega; U) \right\} \end{aligned} \quad (43)$$

and

$$\text{Re}\Sigma_{dd}^{(2)}(\omega; U) = \mathcal{P} \int \frac{d\omega'}{2\pi} \frac{\Gamma^{(2)}(\omega'; U)}{\omega - \omega'}. \quad (44)$$

Now we replace the polaronic spectral functions on the rhs of equation (29) with the approximation in equation (42), and keep only terms up to second order in  $g$ . Then the small coupling approximation to the electronic spectral function follows as

$$\begin{aligned} \tilde{A}(\omega; U) &\approx A^{(0)}(\omega) - \gamma^2 g^2 A^{(0)}(\omega) + A^{(2)}(\omega; U) \\ &+ \gamma^2 g^2 \left[ A^{(0)}(\omega + \omega_0) \tilde{f}^{(0)}(\omega + \omega_0; U) \right. \\ &\left. + A^{(0)}(\omega - \omega_0) (1 - \tilde{f}^{(0)}(\omega - \omega_0; U)) \right]. \quad (45) \end{aligned}$$

If we insert  $\Gamma^{(2)}$  from equation (40) into equation (43) and substitute the resulting expression for  $A^{(2)}$  in equation (45), the electronic spectral function can be written as the sum of five terms,

$$\begin{aligned} \tilde{A}(\omega; U) &\approx A^{(0)}(\omega) + \tilde{A}_{\text{DL}}^{(2)}(\omega) + \tilde{A}_{\Sigma}^{(2)}(\omega; U) \\ &+ \tilde{A}_{\eta}^{(2)}(\omega; U) + \tilde{A}_{\text{inel}}^{(2)}(\omega; U), \quad (46) \end{aligned}$$

whereby  $A^{(0)}$  is given in equation (36) and we have defined

$$\tilde{A}_{\text{DL}}^{(2)}(\omega) = -\frac{\gamma^2 g^2}{\Gamma_0} \left( A^{(0)}(\omega) \right)^2 (\omega - \Delta + \mu)^2, \quad (47)$$

$$\tilde{A}_{\eta}^{(2)}(\omega; U) = \frac{1}{\Gamma_0} \left( A^{(0)}(\omega) \right)^2 (\omega - \Delta + \mu) \tilde{\eta}^{(2)}, \quad (48)$$

$$\begin{aligned} \tilde{A}_{\Sigma}^{(2)}(\omega; U) &= \frac{1}{\Gamma_0} \left( A^{(0)}(\omega) \right)^2 (\omega - \Delta + \mu) \text{Re}\Sigma_{dd}^{(2)}(\omega; U), \\ &\quad (49) \end{aligned}$$

$$\begin{aligned} \tilde{A}_{\text{inel}}^{(2)}(\omega; U) &= \gamma^2 g^2 \left[ A^{(0)}(\omega + \omega_0) \tilde{f}^{(0)}(\omega + \omega_0; U) \right. \\ &+ A^{(0)}(\omega - \omega_0) (1 - \tilde{f}^{(0)}(\omega - \omega_0; U)) \left. \right] \\ &+ \left( \frac{A^{(0)}(\omega)}{2\Gamma_0} \right)^2 \left( (\omega - \Delta + \mu)^2 - \Gamma_0^2 \right) \\ &\times \left\{ 2\gamma^2 g^2 \Gamma_0 \left( \tilde{f}^{(0)}(\omega + \omega_0; U) + 1 - \tilde{f}^{(0)}(\omega - \omega_0; U) \right) \right. \\ &+ [(1 - \gamma)g\omega_0]^2 \left[ A^{(0)}(\omega + \omega_0) \tilde{f}^{(0)}(\omega + \omega_0; U) \right. \\ &\left. \left. + A^{(0)}(\omega - \omega_0) (1 - \tilde{f}^{(0)}(\omega - \omega_0; U)) \right] \right\}. \quad (50) \end{aligned}$$

The function  $\tilde{A}_{\text{DL}}^{(2)}(\omega)$  results from the second term on the rhs of equation (45) and the first term in equation (40). It accounts (to second order) for the polaronic renormalization of the DL coupling, which gives an overall reduction of the electronic density of states, apart from the resonance at  $\omega = \Delta - \mu$ . The terms  $\tilde{A}_{\eta}^{(2)}(\omega; U)$  and  $\tilde{A}_{\Sigma}^{(2)}(\omega; U)$  represent the voltage-dependent renormalization of the energy levels and contain  $\gamma$  implicitly. Finally,  $\tilde{A}_{\text{inel}}^{(2)}(\omega; U)$  denotes the inelastic contribution to the spectral function, which results from tunneling processes that involve the emission of a single phonon at the quantum dot. It includes all the terms in the electronic spectral function (45) that contain the functions  $\tilde{f}^{(0)}(\omega + \omega_0; U)$  and  $1 - \tilde{f}^{(0)}(\omega - \omega_0; U)$  explicitly.

As a consequence, it is finite only for  $|\omega| > \omega_0$  and produces phononic sidebands in the dot spectrum. However, via  $\text{Re}\Sigma_{dd}^{(2)}$  the inelastic channels also contribute to the renormalization of the spectrum at  $|\omega| < \omega_0$ . Most notably, for  $\omega \rightarrow \pm\omega_0 + U_a$ ,  $\text{Re}\Sigma_{dd}^{(2)}$  causes logarithmic divergences in the spectral function. If we evaluate the function  $\tilde{f}^{(0)}$  for  $T \rightarrow 0$  in equation (40), then  $\text{Re}\Sigma_{dd}^{(2)}$  follows from equation (44) and contains the logarithmic divergent term

$$(1 - \gamma)^2 \frac{g^2 \omega_0^2 \Gamma_0}{4\pi} \left\{ \sum_a \frac{\ln((\omega - \omega_0 + U_a)^2)}{(\omega - \omega_0 - \Delta + \mu)^2 + \Gamma_0^2} - \sum_a \frac{\ln((\omega + \omega_0 + U_a)^2)}{(\omega + \omega_0 - \Delta + \mu)^2 + \Gamma_0^2} \right\}. \quad (51)$$

This term corresponds to the result of Entin-Wohlman *et al* [27], but is modified by the prefactor  $(1 - \gamma)^2$ . Moreover, there is a new contribution to  $\text{Re}\Sigma_{dd}^{(2)}$ , namely the term

$$\gamma^2 \frac{g^2 \Gamma_0}{4\pi} \sum_a \ln \left( \frac{(\omega - \omega_0 + U_a)^2}{(\omega + \omega_0 + U_a)^2} \right). \quad (52)$$

For  $\Phi = 0$  the logarithmic divergence appearing in  $\text{Re}\Sigma_{dd}^{(2)}(\omega; U)$  for  $\omega \rightarrow \omega_0$  has the overall prefactor

$$\frac{g^2 \Gamma_0}{4\pi} \left( \gamma^2 + \frac{(1 - \gamma)^2 \omega_0^2}{(\Delta - \mu)^2 + \Gamma_0^2} \right), \quad (53)$$

so that in the adiabatic (antiadiabatic) limit  $\omega_0 \ll \Gamma_0$  ( $\omega_0 \gg \Gamma_0$ ), an increase in  $\gamma$  raises (lowers) the overall weight of the divergences in the spectral function.

If we insert equations (47)–(50) into the current formula (28), we obtain the respective second-order corrections to the noninteracting current  $J^{(0)}$  and the differential conductance, i.e.

$$J \approx J^{(0)} + J_{\text{DL}}^{(2)} + J_{\eta}^{(2)} + J_{\Sigma}^{(2)} + J_{\text{inel}}^{(2)}, \quad (54)$$

$$G \approx G^{(0)} + G_{\text{DL}}^{(2)} + G_{\eta}^{(2)} + G_{\Sigma}^{(2)} + G_{\text{inel}}^{(2)}. \quad (55)$$

For example, for  $T \rightarrow 0$  the second-order inelastic tunneling current reads

$$\begin{aligned} J_{\text{inel}}^{(2)} &= \frac{e^2 \Gamma_0^2 g^2}{4\pi} \Theta(\Phi - \omega_0) \\ &\times \left( \int_{-U_{\text{R}}}^{-U_{\text{L}} - \omega_0} d\omega \left\{ \gamma^2 \frac{(\omega - \Delta + \mu)^2 - \Gamma_0^2}{[(\omega - \Delta + \mu)^2 + \Gamma_0^2]^2} \right. \right. \\ &+ \gamma^2 \frac{1}{(\omega + \omega_0 - \Delta + \mu)^2 + \Gamma_0^2} + (1 - \gamma)^2 \omega_0^2 \\ &\times \frac{(\omega - \Delta + \mu)^2 - \Gamma_0^2}{[(\omega + \omega_0 - \Delta + \mu)^2 + \Gamma_0^2] [(\omega - \Delta + \mu)^2 + \Gamma_0^2]^2} \left. \right\} \\ &+ \int_{-U_{\text{R}} + \omega_0}^{-U_{\text{L}}} d\omega \left\{ \gamma^2 \frac{(\omega - \Delta + \mu)^2 - \Gamma_0^2}{[(\omega - \Delta + \mu)^2 + \Gamma_0^2]^2} \right. \\ &+ \gamma^2 \frac{1}{(\omega - \omega_0 - \Delta + \mu)^2 + \Gamma_0^2} + (1 - \gamma)^2 \omega_0^2 \\ &\times \frac{(\omega - \Delta + \mu)^2 - \Gamma_0^2}{[(\omega - \omega_0 - \Delta + \mu)^2 + \Gamma_0^2] [(\omega - \Delta + \mu)^2 + \Gamma_0^2]^2} \left. \right\} \right). \quad (56) \end{aligned}$$

It is finite only for  $\Phi \geq \omega_0$ , so that the onset of the inelastic tunneling processes will cause a jump in the differential conductance. In general, explicit analytical expressions for the second-order contributions to the differential conductance cannot be derived, since the optimal parameter  $\gamma_{\min}$  is an unknown function of the voltage. However, if we suppose that the derivative of  $\gamma_{\min}(\Phi)$  is continuous, then for a symmetrical voltage drop  $U_R = -U_L = e\Phi/2$ , the jump in the differential conductance follows from equation (56) as

$$G_{\text{inel}}^{(2)} \Big|_{\Phi=\omega_0} = \frac{e^2 \Gamma_0^2 g^2}{2\pi} \left( \gamma^2 \frac{(\frac{\omega_0}{2} - \Delta + \mu)^2}{[(\frac{\omega_0}{2} - \Delta + \mu)^2 + \Gamma_0^2]^2} + \gamma^2 \frac{(-\frac{\omega_0}{2} - \Delta + \mu)^2}{[(\frac{\omega_0}{2} - \Delta + \mu)^2 + \Gamma_0^2]^2} + (1 - \gamma)^2 \omega_0^2 \right) \times \frac{(\frac{\omega_0}{2} - \Delta + \mu)^2 (-\frac{\omega_0}{2} - \Delta + \mu)^2 - \Gamma_0^4}{[(\frac{\omega_0}{2} - \Delta + \mu)^2 + \Gamma_0^2]^2 [(-\frac{\omega_0}{2} - \Delta + \mu)^2 + \Gamma_0^2]^2}. \quad (57)$$

Again, for  $\gamma \rightarrow 0$  only the last term on the rhs of equation (57) remains and coincides with the result of Entin-Wohlman *et al* [27]. As has been discussed in [27], this term is negative if the following condition is fulfilled:

$$\Gamma_0^2 > \left| \frac{\omega_0^2}{4} - (\Delta - \mu)^2 \right|. \quad (58)$$

Then, at  $\Phi = \omega_0$ , it may cause a downward step in the differential conductance. However, the new terms  $\propto \gamma^2$  in equation (57) are always positive. For large enough  $\gamma$ , they outweigh the negative contribution to (57), so that the overall conductance jumps upwards even if the condition in equation (58) is fulfilled.

## 4. Results and discussion

In the following numerical calculations,  $\omega_0 = 1$  is fixed as the unit of energy and we set  $\mu = 0$  and  $T = 0.01$ . We work in the wide-band approximation, with the large bandwidth of the leads  $W = 60$  and  $\Gamma_a^{(0)}(\omega) = \Gamma_0 \Theta(\omega^2 - (W/2)^2)$ . The phononic time scale is fixed by  $1/\omega_0$ , while the electronic time scale is given by  $1/\Gamma_0$  and is used to determine which subsystem is the faster one. We will analyze the adiabatic and antiadiabatic limiting cases before considering comparable phononic and electronic time scales. In doing so, we use the ratio  $\varepsilon_p/\Gamma_0$  as a measure of the EP interaction strength.

For small to large DL coupling, we calculate the polaronic spectral function  $A$  and the dot occupation  $n_d$  self-consistently and determine the variational parameter  $\gamma_{\min}$  by numerically minimizing the thermodynamical potential  $\Omega$  as a function of  $\gamma$ . From  $A$ , the electronic spectral function  $\tilde{A}$  as well as the linear response coefficients  $L$ ,  $X$  and the particle current  $J$  follow. For finite voltages, the differential conductance  $G$  is calculated numerically.

Depending on the bare dot level  $\Delta$ , we distinguish between the off-resonant ( $\Delta \neq \varepsilon_p$ ) and the resonant ( $\Delta = \varepsilon_p$ ) configuration. In the latter case we find that  $n_d = 0.5$  is a root of (25) and we see from equation (4) that the renormalized dot level resonates with the equilibrium chemical potential, i.e.  $\tilde{\eta} = 0$ , for all  $\gamma_{\min}$ .

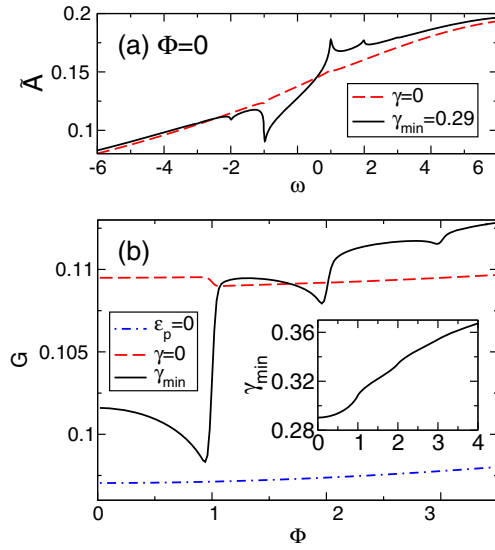


**Figure 1.** For model parameters  $T = 0.01$ ,  $\Gamma_0 = 10$ ,  $\varepsilon_p = 2$  and  $\Delta = 8$ . (a) Electronic spectral functions at  $\Phi = 0$  for fixed  $\gamma = 0$  and variationally determined parameter  $\gamma_{\min} = 0.29$ . (b) Differential conductance as a function of the voltage bias for  $\gamma = 0$  and  $\gamma_{\min}$  in comparison with the noninteracting case  $\varepsilon_p = 0$ . Inset:  $\gamma_{\min}$  as a function of the voltage bias.

### 4.1. Polaron-induced negative differential conductance

In their work, La Magna and Deretzis [15] suggested that the variationally determined renormalization of the DL coupling is a possible mechanism for the observed nonlinear behavior of the differential conductance. We investigate whether this remains true within our approximation, which, in contrast to the effective electron model in [15], accounts for vibrational features in the electronic spectral function to all orders in the EP coupling.

First we consider the adiabatic regime for weak EP coupling by setting  $\Gamma_0 = 10$  and  $\varepsilon_p = 2$ . We vary the voltage bias  $0 < \Phi < 4$  and determine the differential conductance  $G$ . In doing so, we choose an off-resonant configuration with  $\Delta = 8$  fixed, so that the dot occupation is small and remains nearly constant during our calculations:  $n_d \approx 0.3$ .

As a starting point, figure 1(a) displays the electronic spectral function at  $\Phi = 0$  for the variationally determined parameter  $\gamma_{\min}$  (black line) and compares it to the result of a calculation where we kept  $\gamma = 0$  fixed instead of determining  $\gamma_{\min}$  variationally. In general, due to the large DL coupling parameter  $\Gamma_0$ , the electronic spectral function consists of a single wide band. For finite EP coupling, vibrational features arise at  $\omega = \pm\omega_0$ . These features can be attributed to logarithmic divergences in  $\text{Re}\Sigma_{dd}$ , as the second-order approximation in equation (51) suggests. While they are hardly noticeable for  $\gamma = 0$ , the weight of the logarithmic divergences increases strongly in the variational calculation, which yields the optimal parameter  $\gamma_{\min} = 0.29$ . This observation agrees with our discussion in the previous section: for the parameters used, equation (53) predicts an increase in the weight of the logarithmic contributions by a factor of about 15 with respect to the  $\gamma = 0$  case. Note, however, that any divergences in the spectrum will be smeared



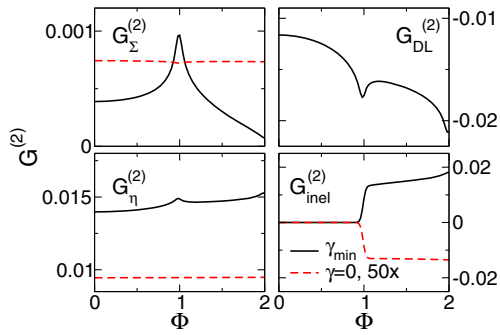


**Figure 2.** For the same parameters as in figure 1. The various second-order contributions to the total differential conductance.

out in our results due to the low but finite temperature and a numerical constraint: we evaluate the self-energy slightly above the real  $\omega$ -axis to prevent the unphysical loss of spectral weight.

In figure 1(b), the black line presents our result for the total differential conductance  $G$  as a function of the voltage, with the inset showing the optimal parameter  $\gamma_{\min}$ . We compare the variational calculation to the cases  $\gamma = 0$  and  $\varepsilon_p = 0$ . For a better understanding of the results of figure 1(b), the four panels in figure 2 show the various second-order contributions to the total differential conductance. From figure 1(b), it follows that for finite EP coupling the overall conductance grows with respect to the noninteracting case. Since we are considering the off-resonant regime, this can be attributed mainly to the lowering of the effective dot level. Accordingly, for  $\gamma = 0$ , we see in figure 2 that the function  $G_{\eta}^{(2)}$  accounts for almost all the increase in the conductance. For finite  $\gamma_{\min}$  the effective dot level is lowered even further, but the positive contribution  $G_{\eta}^{(2)}$  is nearly compensated for by the polaronic renormalization of the DL coupling, which is shown in the upper right panel of figure 2. With growing voltage, the optimal parameter  $\gamma_{\min}$  increases. As the renormalization of the DL coupling grows stronger, a pronounced dip forms in the differential conductance. This mechanism is crucial for the interpretation of our calculations, as we will see below.

At  $\Phi = 1$ , phonon emission by incident electrons becomes possible and opens up an inelastic tunneling channel. In the case of  $\gamma = 0$ , we find a small downward step in the conductance signal, since with  $\Gamma_0 = 10$  and  $\Delta = 8$ , the condition in equation (58) is fulfilled. As we discussed in the previous section, for finite  $\gamma_{\min}$  the first two terms on the rhs of equation (57) can outweigh the third, negative term. Accordingly, our numerics show a relatively large upward step in the differential conductance (note the different scaling factors in the lower right panel of figure 2).

Next we investigate the polaronic renormalization in the antiadiabatic limit ( $\Gamma_0 = 0.1$ ) with strong EP coupling ( $\varepsilon_p = 2$ ). We choose the resonant configuration  $\Delta = \varepsilon_p$ . For these parameters, we expect the formation of a polaron-like transient state at the quantum dot. This is confirmed by the electronic spectral function in figure 3(a), which features several narrow phononic bands. In the low-voltage region we find that  $\gamma_{\min} \approx 0.9$ , i.e. the weight of the variational polaron

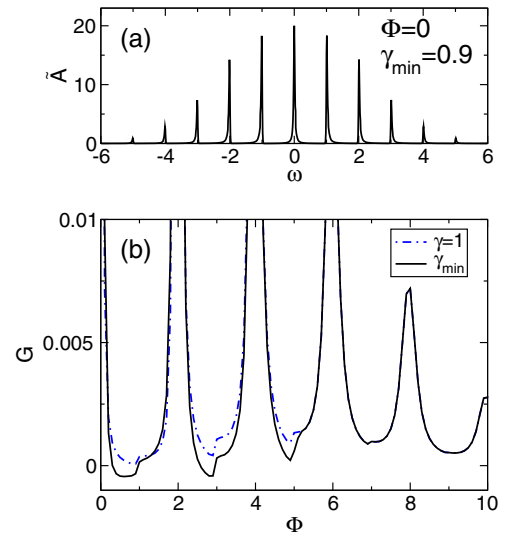


**Figure 3.** For model parameters  $T = 0.01$ ,  $\Gamma_0 = 0.1$ ,  $\varepsilon_p = 2$  and  $\Delta = 2$ . (a) Electronic spectral function of the variational calculation for  $\Phi = 0$  and  $\gamma_{\min} = 0.9$ . (b) Differential conductance as a function of the voltage bias, compared to the result with fixed  $\gamma = 1$ .

state is smaller than predicted by the complete Lang–Firsov transformation.

Figure 3(b) compares the differential conductance as a function of the voltage bias for fixed  $\gamma = 1$  and the optimal  $\gamma_{\min}$ . Just as in the adiabatic regime considered above, we note small steps in the conductance at  $\Phi = 1, 3$  and  $5$  that signal the onset of inelastic transport. In addition, a second kind of vibrational feature can be found: pronounced conductance peaks arise whenever the voltage equals multiple integers of  $2\omega_0$ . Here, resonant transport takes place through the polaronic side bands in  $\tilde{A}$ . For  $\gamma = 1$  the differential conductance stays strictly positive, but approaches zero between these well-separated peaks. As seen for the adiabatic case, in the full calculation the polaronic renormalization grows stronger with increasing voltage bias. As a consequence, in the low-voltage region the differential conductance becomes negative between the resonance peaks. Note, however, that at  $\Phi = 1$  and  $\Phi = 3$  the positive nonresonant conductance steps, although carrying little weight, render the differential conductance positive again.

Thanks to our variational approach, we are able to investigate the interesting regime of comparable electronic and phononic energies. To this end, we set  $\Gamma_0 = 1$  and consider intermediate EP coupling  $\varepsilon_p = 2$ . As before, we examine the resonant, electron–hole-symmetric situation with  $\Delta = 2$ . Figure 4(a) shows the electronic spectral function at zero voltage, where the variational calculation yields  $\gamma_{\min} \approx 0.5$ . Due to comparable electronic and phononic time scales, the width of the few phononic side bands is of the order of their spacing.

In figure 4(b), we compare the conductance signal of the variational calculation to both, the  $\gamma = 0$  and  $\gamma = 1$  cases. In the low-voltage regime, we have  $\gamma_{\min} \gtrsim 0.5$  and the DL coupling is moderately renormalized. As the voltage grows, the variational parameter steadily increases and, as

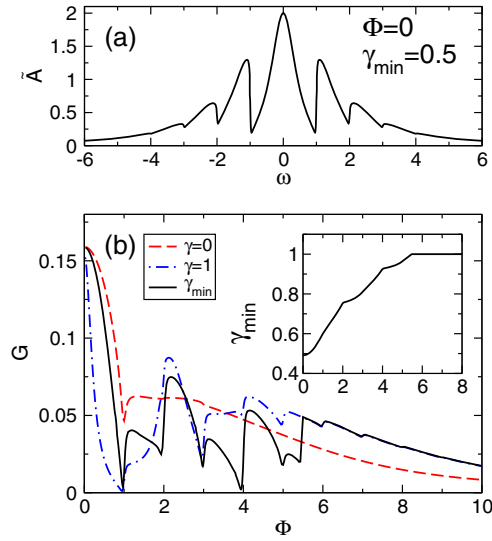


**Figure 4.** For model parameters  $T = 0.01$ ,  $\Gamma_0 = 1$ ,  $\Delta = 2$  and  $\varepsilon_p = 2$ . (a) Electronic spectral function in the variational calculation for  $\Phi = 0$  and  $\gamma_{\min} = 0.5$ . (b) Differential conductance as a function of voltage for the variational calculation ( $\gamma_{\min}$ ), compared to the results with fixed  $\gamma = 0$  and  $\gamma = 1$ . Inset: optimized variational parameter as a function of the voltage.

can be seen in the inset of figure 4(b), the polaron effect strengthens whenever a new resonant inelastic channel is accessible. The vibrational features in the conductance signal are heavily modulated by the voltage-dependent polaronic renormalization: in contrast to the cases with fixed  $\gamma$ , there is no clear distinction between resonant peaks at  $\Phi = 2, 4$  and off-resonant steps at  $\Phi = 1, 3$  and  $5$ , since the latter become peaks, too. Due to the comparable phononic and electronic time scales, both kinds of vibrational features have nearly the same spectral weight. Moreover, the differential conductance approaches zero between the broad conductance peaks, but no NDC is observed.

To sum up, the polaron formation involves the redistribution of spectral weight in the local density of states and, most importantly, the renormalization of the effective DL coupling. For strong EP interaction, it is indeed a possible mechanism for NDC. However, for small to intermediate coupling, the NDC is suppressed when multi-phonon transport processes are taken into account.

#### 4.2. Effective dot level

In the following, we present another interesting consequence of the variational polaronic renormalization, which concerns the effective dot level.

We choose a slightly off-resonant configuration with  $\Delta = 0$  and  $\varepsilon_p > 0$ , so that in contrast to the above calculations, the effective dot level is not pinned to the equilibrium chemical potential. We decrease the bare DL coupling slightly ( $\Gamma_0 = 0.33$ ) and consider weak to intermediate EP coupling strengths. Figure 5(a) compares the differential conductance for  $\gamma = 0$  to the variational calculation. For weak EP coupling, figure 5(b) shows the second-order approximations  $G_{\Sigma}^{(2)}$  and

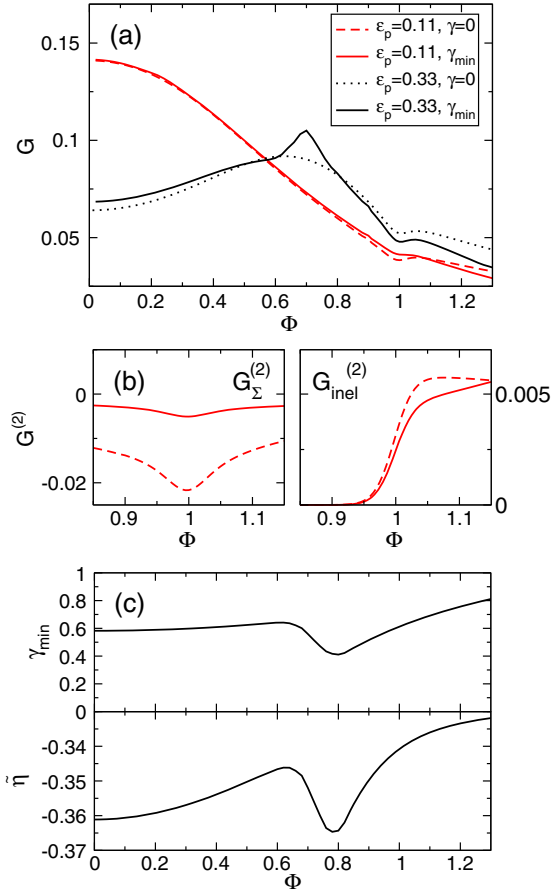


**Figure 5.** For  $T = 0.01$ ,  $\Gamma_0 = 0.33$  and  $\Delta = 0$ . (a) Differential conductance as a function of voltage for the variational calculation ( $\gamma_{\min}$ ), compared to the results with fixed  $\gamma = 0$ . (b) Second-order contributions to the differential conductance for  $\varepsilon_p = 0.11$ . (c) Variationally determined parameter  $\gamma_{\min}$  and renormalized dot level  $\tilde{\eta}$  as functions of the voltage for  $\varepsilon_p = 0.33$ .

$G_{\text{inel}}^{(2)}$ . Figure 5(c) finally presents the optimal parameter  $\gamma_{\min}$  and the effective dot level  $\tilde{\eta}$  as functions of the voltage.

With  $\varepsilon_p = 0.11$ , the system parameters correspond to the case of high zeroth-order transmission presented in figure 5(a) in the work of Entin-Wohlman *et al* [27]. Our result for  $\gamma = 0$  is in good agreement with [27]. The conductance maximum lies near  $\Phi = 0$  and we find a small conductance dip at  $\Phi = 1$ , which is caused by the logarithmic divergence in  $\text{Re}\Sigma_{dd}$ . In the full calculation for  $\varepsilon_p = 0.11$ , we find that  $\gamma_{\min} = 0.75$  at  $\Phi = 1$ . Here the dip in the total conductance vanishes. The second-order approximation in the left panel of figure 5(b) suggests that this is mainly due to a reduction of the weight of the logarithmic divergence in  $\text{Re}\Sigma_{dd}$ . From figure 5(b) we can also see that the jump in  $G_{\text{inel}}^{(2)}$  is positive for both  $\gamma = 0$  and  $\gamma_{\min}$ , since condition (58) is not fulfilled for the given parameters. Moreover, in the variational calculation the height of the conductance jump is reduced with respect to the  $\gamma = 0$  result, which can be confirmed using equation (57).

If we increase the EP coupling to  $\varepsilon_p = 0.33$ , the dip in the total conductance reappears. But most importantly, instead of a broad conductance resonance, we find a peak-like feature

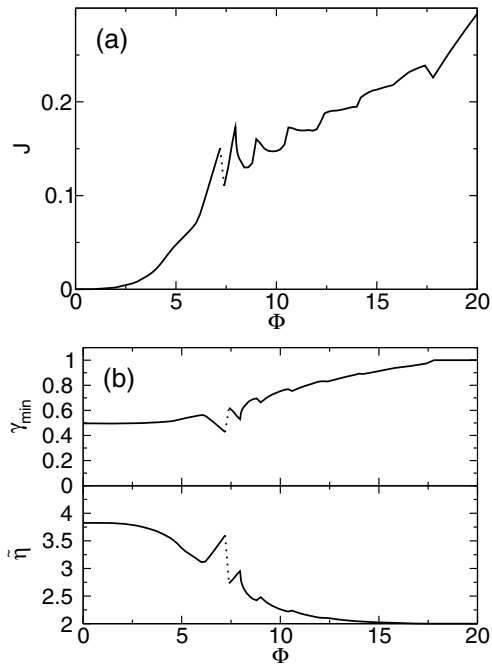


**Figure 6.** For model parameters  $T = 0.01$ ,  $\Gamma_0 = 1$ ,  $\Delta = 10$  and  $\varepsilon_p = 8$ . (a) Electron current as a function of the voltage. (b) Variationally determined parameter  $\gamma_{\min}$  and renormalized dot level  $\tilde{\eta}$  as functions of the voltage.

at  $\Phi = 0.7$ . As we see from figure 5(c), with increasing voltage  $\tilde{\eta}$  shifts upwards until at  $\Phi = 0.62$  it approaches the chemical potential of a lead. For  $0.65 < \Phi < 0.8$ , the variational parameter decreases in such a way that  $\tilde{\eta}$  stays in resonance with the lead chemical potential. The decrease in  $\gamma_{\min}$  reduces the renormalization of the DL coupling. Thereby, the system maximizes the resonant tunneling current with respect to the  $\gamma = 0$  case and a new peak-like conductance feature is observed in figure 5(a). This ‘sticking’ of the effective dot level to the lead chemical potentials is the second main result of our variational calculations.

Now we consider the off-resonant scenario  $\Delta = 10$  for strong EP coupling  $\varepsilon_p = 8$ . The results are presented in figure 6 (note that figure 6(a) shows the total current). As expected, the effective dot level  $\tilde{\eta}$  sinks notably with growing voltage, until at  $\Phi = 6.2$  it begins to grow linearly, following the upper lead chemical potential. Again, the differential conductance grows considerably. In contrast to the intermediate EP coupling case,  $\gamma_{\min}$  jumps from 0.4 to 0.6 when the system switches between two local minima in the thermodynamic potential. The resulting discontinuities in  $\tilde{\eta}$  and  $\tilde{\Gamma}_0$  cause a noticeable drop in the total current. As the voltage grows further,  $\gamma_{\min}$  decreases again. Now the first phonon side band at  $\tilde{\eta} + \omega_0$  sticks to the lead chemical potential and the conductance grows once more. A similar behavior, involving the second and third side bands, is found at  $\Phi \approx 9$  and  $\Phi \approx 10.5$ , respectively, until  $\gamma_{\min} = 1$  in the high-voltage limit. Moreover, due to the strong EP coupling, the upward steps in the current are followed by regions with NDC.

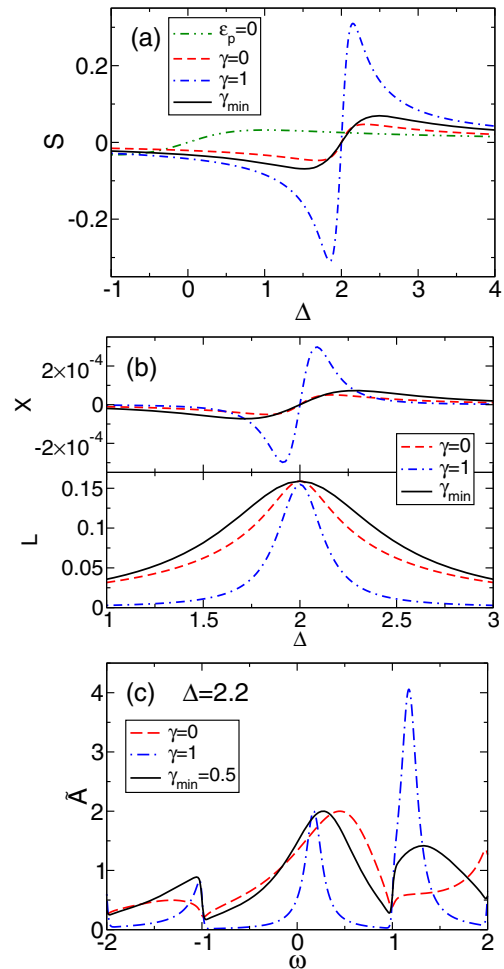


**Figure 7.** For model parameters  $T = 0.01$ ,  $\Gamma_0 = 1$ ,  $\varepsilon_p = 2$  and  $\Phi = 0$ . (a) Thermopower as a function of the bare dot level in the noninteracting ( $\varepsilon_p = 0$ ) and the interacting system. (b) Thermoelectric response  $X$  and linear conductance  $L$  as functions of the bare dot level. (c) Electronic spectral functions at  $\Delta = 2.2$  for  $\gamma = 0, 1$  and  $\gamma_{\min} = 0.5$ .

#### 4.3. Thermopower

Finally, we investigate the thermoelectric response of the molecular junction in the physically most interesting regime of intermediate DL coupling. Setting  $\Gamma_0 = 1$ , we consider the equilibrium situation  $\Phi = 0$ . For  $\varepsilon_p = 2$ , we compare the variational calculation to the cases with fixed  $\gamma = 0, 1$  and to the noninteracting system  $\varepsilon_p = 0$ . Figure 7(a) shows the linear response thermopower  $S$  as a function of the bare dot level, while figure 7(b) presents the thermoelectric coefficient and the linear response conductance.

In general,  $S$  features two resonances of opposite sign. For  $\varepsilon_p = 2$  they are located at  $\Delta \approx \varepsilon_p \pm 0.2$ . In the small polaron limit  $\gamma = 1$ , our calculation predicts a substantial increase in the maximum thermopower with respect to all the other cases. This can be explained with the help of the respective electronic spectral functions plotted in figure 7(c) for  $\Delta = 2.2$ . In the case of  $\gamma = 0$ , the spectral function features a broad band around the Fermi edge at  $\omega = 0$ . The states with high energies  $\omega > 0$  have only slightly more

spectral weight than the states with low energies  $\omega < 0$ . Because the integrand on the rhs of equation (33) is weighted by  $\omega$ , the resulting thermoelectric response coefficient  $X$  is small. Physically, this means that a small temperature difference between the leads induces the flow of high-energy particles through the quantum dot, which, in principle, can result in a voltage drop across the junction. In the case of  $\gamma = 0$  however, the current is compensated for by a nearly equal counterflow of low-energy carriers, so that the overall thermoelectric effect is small. If  $\Delta$  is lowered to 1.8, the low-energy states have the larger spectral weight and the thermoelectric response coefficient changes sign. For  $\Delta = \varepsilon_p = 2$ , the spectral function is symmetric around  $\omega = 0$  so that the net charge current induced by the temperature difference vanishes and we have  $X = 0$ .

For  $\gamma = 1$ , the strong renormalization of the DL coupling reduces the width of the bands in the spectral function in figure 7(c). As a result, near the Fermi edge the relative weight of the high-energy states increases, so that the dot acts as a more effective energy filter. The unfavorable counterflow of low-energy charge carriers is suppressed and the thermoelectric response  $X$  grows considerably (see figure 7(b)). As can also be seen in figure 7(b), the linear response conductance  $L$  in equation (32) decreases when  $\gamma$  is set from zero to one, since it depends only on the (shrinking) spectral weight around the Fermi edge. This, too, boosts the thermopower  $S$ .

At  $\Delta = 2.2$  the variational calculation yields  $\gamma_{\min} = 0.5$ , so that the width of the zero-phonon band lies between the other results. Consequently, this is also true for the maximum value of  $X$ . Note, however, that our variational calculation maximizes the linear response conductance  $L$  with respect to both limiting cases, so that the maximum thermopower is only slightly larger than for  $\gamma = 0$ . We conclude that the local EP interaction can, in principle, enhance the maximum thermopower of the quantum dot device. However, for intermediate DL coupling strengths the small polaron picture with  $\gamma = 1$  greatly overestimates the effect.

## 5. Concluding remarks

To summarize, adopting a generalized variational Lang–Firsov transformation, we calculate the interacting spectral function of a molecular quantum dot for small-to-large DL coupling and weak-to-strong EP interaction. We investigate the impact of the formation of a polaronic dot state on the steady-state current–voltage characteristics, as well as on the linear response thermopower of the system.

In the case of strong EP interaction, the voltage-dependent polaronic renormalization of the DL coupling causes NDC. For comparable electronic and phononic time scales, this effect is diminished by transport through overlapping phonon side bands.

We find that in the off-resonant or ungated configuration, the renormalized dot level follows the lead chemical potentials. This process generates new peaks in the differential conductance signal.

In the equilibrium situation, the EP coupling enhances the thermopower of the quantum dot device, albeit by a smaller factor than predicted in the small polaron limit.

This work may be extended in several directions. Most notably, in the nonequilibrium regime, one should investigate

the impact of the observed NDC on the thermoelectric properties of the molecular junction. The dynamics and heating of the vibrational subsystem could be included by means of nonequilibrium phonon Green functions [28]. Moreover, in the light of recent advances in nanotechnology and experimental studies, new geometries have come into focus, such as multi-terminal junctions or a molecule placed on an Aharonov–Bohm ring [29].

## Acknowledgments

This work was supported by Deutsche Forschungsgemeinschaft through SFB 652 B5. TK and HF acknowledge the hospitality at the Institute of Physics ASCR.

## References

- [1] Higgs K W and Mazur U 1993 *J. Phys. Chem.* **97** 7803
- [2] Reed M A, Zhou C, Muller C J, Burgin T P and Tour J M 1997 *Science* **278** 252
- [3] Park H, Park J, Lim A K L, Anderson E H, Alivisatos A P and McEuen P L 2000 *Nature* **407** 57
- [4] Persson B N J 1988 *Phys. Scr.* **38** 282
- [5] Mii T, Tikhodeev S G and Ueba H 2002 *Surf. Sci.* **502** 26
- [6] Mii T, Tikhodeev S G and Ueba H 2003 *Phys. Rev. B* **68** 205406
- [7] Galperin M, Ratner M A and Nitzan A 2004 *J. Chem. Phys.* **121** 11965
- [8] Galperin M, Ratner M A and Nitzan A 2007 *J. Phys.: Condens. Matter* **19** 103201
- [9] Holstein T 1959 *Ann. Phys., NY* **8** 325
- [10] Holstein T 1959 *Ann. Phys., NY* **8** 343
- [11] Wellein G and Fehske H 1997 *Phys. Rev. B* **56** 4513
- [12] Wellein G and Fehske H 1998 *Phys. Rev. B* **58** 6208
- [13] Fehske H and Trugman S A 2007 *Polarons in Advanced Materials (Springer Series in Material Sciences vol 103)* ed A S Alexandrov (Dordrecht: Canopus/Springer) pp 393–461
- [14] Fehske H, Wellein G, Loos J and Bishop A R 2008 *Phys. Rev. B* **77** 085117
- [15] La Magna A and Deretzis I 2007 *Phys. Rev. Lett.* **99** 136404
- [16] Humphrey T E, Newbury R, Taylor R P and Linke H 2002 *Phys. Rev. Lett.* **89** 116801
- [17] Lang I G and Firsov Y A 1962 *Zh. Eksp. Teor. Fiz.* **43** 1843  
Lang I G and Firsov Y A 1963 *Sov. Phys. JETP* **16** 1301 (Engl. transl.)
- [18] Fehske H, Ihle D, Loos J, Trapper U and Büttner H 1994 *Z. Phys. B* **94** 91
- [19] Loos J, Koch T, Alvermann A, Bishop A R and Fehske H 2009 *J. Phys.: Condens. Matter* **21** 395601
- [20] Koch T, Loos J, Alvermann A, Bishop A R and Fehske H 2010 *J. Phys. Conf. Ser.* **220** 012014
- [21] Koch T, Loos J, Alvermann A and Fehske H 2011 *Phys. Rev. B* **84** 125131
- [22] Kadanoff L P and Baym G 1962 *Quantum Statistical Mechanics* (Reading, MA: Benjamin-Cummings)
- [23] Schnakenberg J 1966 *Z. Phys.* **190** 209
- [24] Datta S 1995 *Electronic Transport in Mesoscopic Systems* (Cambridge: Cambridge University Press)
- [25] Fetter A L and Walecka J D 1971 *Quantum Theory of Many-Particle Systems* (New York: McGraw-Hill)
- [26] Entin-Wohlman O, Imry Y and Aharony A 2010 *Phys. Rev. B* **82** 115314
- [27] Entin-Wohlman O, Imry Y and Aharony A 2009 *Phys. Rev. B* **80** 035417
- [28] Galperin M, Nitzan A and Ratner M A 2007 *Phys. Rev. B* **75** 155312
- [29] Entin-Wohlman O and Aharony A 2012 *Phys. Rev. B* **85** 085401

**Thermoelectric effects in molecular quantum dots with contacts**T. Koch,<sup>1</sup> J. Loos,<sup>2</sup> and H. Fehske<sup>1</sup><sup>1</sup>*Institut für Physik, Ernst-Moritz-Arndt-Universität Greifswald, DE-17489 Greifswald, Germany*<sup>2</sup>*Institute of Physics, Academy of Sciences of the Czech Republic, CZ-16200 Prague, Czech Republic*

(Received 25 November 2013; revised manuscript received 8 April 2014; published 24 April 2014)

We consider the steady-state thermoelectric transport through a vibrating molecular quantum dot that is contacted to macroscopic leads. For moderate electron-phonon interaction strength and comparable electronic and phononic timescales, we investigate the impact of the formation of a local polaron on the thermoelectric properties of the junction. We apply a variational Lang-Firsov transformation and solve the equations of motion in the Kadanoff-Baym formalism up to second order in the dot-lead coupling parameter. We calculate the thermoelectric current and voltage for finite temperature differences in the resonant and inelastic tunneling regimes. For a near resonant dot level, the formation of a local polaron can boost the thermoelectric effect because of the Franck-Condon blockade. The line shape of the thermoelectric voltage signal becomes asymmetrical due to the varying polaronic character of the dot state and in the nonlinear transport regime, vibrational signatures arise.

DOI: [10.1103/PhysRevB.89.155133](https://doi.org/10.1103/PhysRevB.89.155133)

PACS number(s): 72.10.-d, 71.38.-k, 73.21.La, 73.63.Kv

**I. INTRODUCTION**

Molecular junctions are electronic devices that consist of an organic quantum dot that is contacted by two macroscopic leads. Modern nanotechnology allows for the reliable fabrication of systems where the dots are single aromatic rings, molecular wires [1], C<sub>60</sub> fullerenes [2,3], or carbon nanotubes [4]. They are a promising candidates in the search for further miniaturization of electronic and thermoelectric devices [5].

Transport through such systems is determined by the discrete levels of the dot, whose position relative to the Fermi energy can be tuned, e.g., with the help of a third (gate) electrode [6]. The level broadening depends on the dot-lead coupling strength, which can be manipulated via the lead distance or through the choice of different metal-molecule anchoring groups [7]. In addition to these two external parameters, electron-phonon (EP) interaction influences transport through molecular junctions: when it is occupied by charge carriers, the molecule may undergo structural changes or vibrations that correspond to the excitation of local optical phonons of considerable energy. They show up as vibrational signatures in the current-voltage characteristics of the device [2,8].

A temperature difference between the leads induces a current of charge carriers across the junction. This thermoelectric effect is measured by recording, for constant temperature difference, the voltage bias necessary to cancel this current [9]. The quotient of the temperature difference and the thermovoltage, the so-called thermopower, can be used to probe the systems Fermi energy [10] and the vibronic structure of the molecule's state [11,12]. Most of the experimental findings are well understood within a linear response formulation of the thermopower [13]. However, the applied temperature differences can be tens of degrees Kelvin, i.e., larger than the dot-lead coupling energy. Some features of the measured voltage histograms, such as side peaks and temperature dependent widths [9], are not accounted for in the linear theory. That is why, recently, the discussion of the thermopower has been extended to the nonlinear regime [14,15]. Then the question arises, how the thermoelectric coefficients can be generalized. Our approach in the present work is motivated by the experimental situation; for a given temperature bias, we

determine the thermovoltage numerically by minimizing the thermally induced charge current.

We base our calculations on the Anderson-Holstein model. Here, the organic molecule is represented by a single energy level and a local optical mode, which is linearly coupled to the electron on this level. The quantum dot is connected to two macroscopic leads, while the local mode is coupled to a phonon bath. The current between the leads is given by the interacting dot density of states [16]. Based on such models, different methods have been applied, such as the numerical [17,18] and functional renormalization group [19], rate equations [11,20], master equations [12,14,21], and nonequilibrium Keldysh Green functions [22] to describe transport through the dot for small-to-large dot-lead coupling and weak-to-strong EP interaction.

In the antiadiabatic, strong EP coupling regime, typically, a Lang-Firsov transformation [23] is applied, based on the exact solution of the isolated dot. It predicts the formation of a local polaron, which reduces the effective dot-lead coupling exponentially. This could be beneficial for the thermoelectric response of the system [14,24]. For practical applications, however, a moderate level broadening is needed to ensure usable power output. Moreover, long electron residence times and strong EP interaction may lead to the accumulation of energy at the dot and, consequently, to its degradation [25]. Because of this, the regime of comparable electronic and phononic time scales and intermediate EP interaction becomes interesting.

To account for the polaronic character of the dot-state away from the strong EP coupling, antiadiabatic limit, we use an approach that is based on a variational form of the Lang-Firsov transformation [26]. For the polaron problem, the variational Lang-Firsov approach has been proven to give reliable results in the whole electron-phonon coupling and phonon frequency regime, even in the most physically difficult polaron crossover region [27]. Here, the polaron variational parameter is determined by minimizing the relevant thermodynamical potential.

In previous work [28], we considered the steady-state current response of the quantum dot to a finite voltage difference between the leads. In doing so, we assumed that the

temperatures of the leads and of the phonon bath are all equal. The calculations in these papers were based on the Kadanoff-Baym formalism [29], which relies on the relation between the real-time response functions and the nonequilibrium Green functions of the complex time variables.

The present work will focus on the thermoelectric effects induced by a finite temperature difference between the leads. Section II A introduces the model and the variational ansatz we employ to describe a vibrating quantum dot that is coupled to a phonon heat bath and two macroscopic leads at different temperatures. Because for such a setup, the temperature is not constant throughout the system, the reasonings of our earlier approach [28] have to be modified. That is why in Sec. II B we generalize the Kadanoff-Baym method such that the steady-state equation of the response functions, as well as their formal solution deduced in Ref. [28], are applicable to the present case. In Sec. II C, we then derive an approximation for the polaronic self-energy, and Sec. II D provides the relation between the polaronic and electronic spectral functions, the latter of which enters the current formula. In Sec. II E, we derive the thermodynamic potential which will be used to determine the variational parameter numerically. Section III presents our numerical results. The main conclusions and future prospects can be found in Sec. IV.

## II. THEORY

### A. Model and variational ansatz

We consider a molecular quantum dot in the three-terminal configuration depicted in Fig. 1, which will be modelled by the following Hamiltonian:

$$H = (\Delta - \mu)d^\dagger d - g\omega_0 d^\dagger d(b^\dagger + b) + \omega_0 b^\dagger b + \sum_{k,a} (\varepsilon_{ka} - \mu)c_{ka}^\dagger c_{ka} - \frac{1}{\sqrt{N}} \sum_{k,a} (t_{ka} d^\dagger c_{ka} + t_{ka}^* c_{ka}^\dagger d). \quad (1)$$

Here, the quantum dot is represented by a single energy level  $\Delta$  with the fermionic operators  $d^{(\dagger)}$ . It interacts with a local optical phonon mode  $b^{(\dagger)}$  of energy  $\omega_0$ , where the EP coupling strength is given by the so-called polaron binding energy,

$$\varepsilon_p = g^2 \omega_0. \quad (2)$$

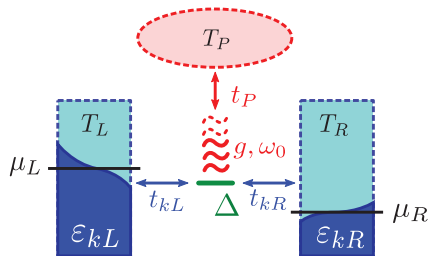


FIG. 1. (Color online) Sketch of the quantum dot model. The electronic level  $\Delta$  is coupled to two macroscopic leads, each in its own thermal equilibrium with different temperatures  $T_{L,R}$  and chemical potentials  $\mu_{L,R}$ . The dot electrons interact with an optical phonon mode of energy  $\omega_0$  that is coupled to a phonon bath at temperature  $T_P$ .

By the last term in Eq. (1), the dot is coupled to left ( $a = L$ ) and right ( $a = R$ ) leads, each of which contains  $N$  free electrons with the energies  $\varepsilon_{ka}$  and the corresponding fermionic operators  $c_{ka}^{(\dagger)}$ , respectively. In equilibrium, the dot-lead system is characterized by a common chemical potential  $\mu$  and a global temperature  $T$ .

In the nonequilibrium situation, a voltage difference between the leads is described by adding to (7) the term

$$H_{\text{int}} = \sum_a U_a \sum_k c_{ka}^\dagger c_{ka} \quad (3)$$

with the voltage bias

$$\Phi = (U_L - U_R)/e, \quad (4)$$

where  $e < 0$  is the electron charge. In addition, we consider a temperature difference between the macroscopic leads, whereby each lead is supposed to stay in its own thermal equilibrium with the temperatures  $T_L$  and  $T_R$ , respectively. We also suppose that the local oscillator is coupled to its own heat bath, which has the temperature  $T_P$ . In accordance with Entin-Wohlman [30], we assume that the coupling to this heat bath (indicated as  $t_P$  in Fig. 1) far exceeds the EP-coupling strength, so that the phonon population at the dot is given by the Bose-Einstein distribution:

$$n_B(\omega) = (e^{\beta_P \omega} - 1)^{-1} \quad \text{with} \quad \beta_P = (k_B T_P)^{-1}. \quad (5)$$

In the following calculations, we suppose that  $T_P = T_R = T$  and  $T_L \neq T$  in general. Moreover, all energies will be taken with respect to the equilibrium chemical potential, i.e.,  $\mu = 0$ . We raise the voltage bias symmetrically around  $\mu$ , i.e.,  $\mu_L = -e\Phi/2$  and  $\mu_R = e\Phi/2$ .

To account for the polaron localization at the dot, we apply to the Hamiltonian (1) an incomplete Lang-Firsov transformation  $S_\gamma$  [26,28], introducing the variational parameter  $\gamma \in [0, 1]$ :

$$\tilde{H} = S_\gamma^\dagger H S_\gamma, \quad S_\gamma = \exp[\gamma g(b^\dagger - b)d^\dagger d]. \quad (6)$$

The transformed Hamiltonian then reads

$$\tilde{H} = \tilde{\Delta} d^\dagger d - C_d d^\dagger d + \omega_0 b^\dagger b + \sum_{k,a} \varepsilon_{ka} c_{ka}^\dagger c_{ka} - \sum_{k,a} (C_{ka} d^\dagger c_{ka} + C_{ka}^\dagger c_{ka}^\dagger d), \quad (7)$$

where the renormalization of the dot level and the interaction coefficients depends on the parameter  $\gamma$ :

$$\tilde{\Delta} = \Delta - \varepsilon_p \gamma (2 - \gamma), \quad \tilde{g} = \gamma g, \quad (8)$$

$$C_{ka} = \frac{t_{ka}}{\sqrt{N}} e^{-\tilde{g}(b^\dagger - b)}, \quad C_d = g\omega_0(1 - \gamma)(b^\dagger + b). \quad (9)$$

Now  $d$  and  $b$  are the operators of dressed electrons (in analogy to polarons) and the shifted local oscillator. The original electron and oscillator operators read  $\tilde{d} = \exp[\gamma g(b^\dagger - b)]d$  and  $\tilde{b} = b + \gamma g d^\dagger d$ , respectively.

### B. Response functions and steady-state equations

In our previous works [28], we considered the electron current response of a molecular quantum dot that was initially in equilibrium with the leads as well as with the phononic bath at a common, fixed temperature. Our calculations were based on the Kadanoff-Baym theory [29]. At first, we summarize

the aspects of this nonequilibrium response theory that are essential for the present setting.

The relevant response functions are represented by the real-time Green functions of the dot-operators  $d^{(\dagger)}$  and the lead operators  $c_{ka}^{(\dagger)}$ , e.g.,

$$g_{dd}(t_1, t_2; U) = -i \langle \mathcal{T} d_U(t_1) d_U^\dagger(t_2) \rangle, \quad (10)$$

$$g_{dd}^<(t_1, t_2; U) = i \langle d_U^\dagger(t_2) d_U(t_1) \rangle, \quad (11)$$

$$g_{dd}^>(t_1, t_2; U) = -i \langle d_U(t_1) d_U^\dagger(t_2) \rangle. \quad (12)$$

The functions  $g_{cd}$  of the ‘‘mixed’’ operators  $c_{ka}^{(\dagger)}$  and  $d^{(\dagger)}$  are defined in an analogous way. In Eqs. (10)–(12), the time dependence of  $d_U^{(\dagger)}$  is determined by  $\tilde{H} + H_{\text{int}}$ . The symbol  $\mathcal{T}$  means the standard time-ordering operator so that the function  $g_{dd}$  is equal to the functions  $g_{dd}^<(t_1, t_2; U)$  and  $g_{dd}^>(t_1, t_2; U)$  for  $t_1 < t_2$  and  $t_1 > t_2$ , respectively. The statistical average  $\langle \dots \rangle$  corresponds to the equilibrium state at the temperature  $T$  before the disturbance was turned on. Going to the interaction representation, the Heisenberg operators  $d_U$  are expressed as

$$d_U(t) = V^{-1}(t) d(t) V(t), \quad (13)$$

$$V(t) = \mathcal{T}_\tau \exp \left[ -i \int_{-\infty}^t dt' H_{\text{int}}(t') \right]. \quad (14)$$

The real-time response functions may be deduced using the equations of motion for the nonequilibrium Green functions of the complex time variables  $t = t_0 - i\tau$ ,  $\tau \in [0, \beta]$ , defined as

$$G_{dd}(t_1, t_2; U, t_0) = -\frac{i}{\langle S \rangle} \langle \mathcal{T}_\tau d(t_1) d^\dagger(t_2) S \rangle, \quad (15)$$

$$S = \mathcal{T}_\tau \exp \left[ -i \int_{t_0}^{t_0 - i\beta} dt H_{\text{int}}(t) \right]. \quad (16)$$

The time dependence of the operators in Eq. (15) is determined by  $\tilde{H}$  only, while the external disturbance is explicit in the time-ordered exponential operator  $S$ . The operation  $\mathcal{T}_\tau$  orders the operators by the imaginary parts of the times  $t_1$  and  $t_2$ , so that  $G_{dd}(t_1, t_2; U, t_0) = G_{dd}^>(t_1, t_2; U, t_0)$  for  $i(t_1 - t_2) > 0$  and  $G_{dd}(t_1, t_2; U, t_0) = G_{dd}^<(t_1, t_2; U, t_0)$  for  $i(t_1 - t_2) < 0$ . To find the relation between the functions  $G_{dd}^{\lessgtr}$  and  $g_{dd}^{\lessgtr}$ , the function  $G_{dd}$  is considered for  $i(t_1 - t_2) < 0$ :

$$G_{dd}^<(t_1, t_2; U, t_0) = \frac{i}{\langle U(t_0, t_0 - i\beta) \rangle} \times \langle U(t_0, t_0 - i\beta) U^{-1}(t_0, t_2) d^\dagger(t_2) U(t_0, t_2) \times U^{-1}(t_0, t_1) d(t_1) U(t_0, t_1) \rangle, \quad (17)$$

where

$$U(t_0, t) = \mathcal{T}_\tau \exp \left[ -i \int_{t_0}^t dt' H_{\text{int}}(t') \right]. \quad (18)$$

The continuation of  $U(t_0, t)$  and  $V(t)$  to analytic functions of the time variables leads to the identification of  $U(t_0, t)$  with  $V(t)$  in the limit  $t_0 \rightarrow -\infty$ . Consequently, the connection of the analytic functions  $G_{dd}^{\lessgtr}$  and  $g_{dd}^{\lessgtr}$  is given by

$$\lim_{t_0 \rightarrow -\infty} G_{dd}^{\lessgtr}(t_1, t_2; U, t_0) = g_{dd}^{\lessgtr}(t_1, t_2; U), \quad (19)$$

with similar relations for the functions  $G_{cd}^{\lessgtr}$  and  $g_{cd}^{\lessgtr}$ .

It is evident that the derivation of Eq. (19) outlined above does not refer to some special properties of the statistical ensemble, nor to the physical meaning of  $\beta$ . In this way, it is possible to generalize the definition (15) for  $G_{dd}$  assuming the mean value  $\langle \dots \rangle$  to be unspecified and the complex-time variable to be defined in the interval  $t \in [t_0, t_0 - i\sigma]$ , where the time-ordering parameter  $\sigma$  has no specific physical meaning. We assume that before the disturbance (3) was turned on, the system was in a steady state with the temperatures  $T_L$ ,  $T_R$  of the left and right leads, and  $T_P$  of the phonon bath. The function  $G_{dd}$  defined in this way does not have the properties of the temperature ( $\beta$ ) dependent Green function in Eq. (15), it rather represents a functional of the ordered operators which we use to determine the real-time response functions  $g_{dd}$ .

To do this, we define, in analogy to the self-energy, the function  $\Sigma_{dd}(t_1, t_2; U, t_0)$  by the equation

$$[G_{dd}^{(0)-1}(t_1, \bar{t}) - \Sigma_{dd}(t_1, \bar{t}; U, t_0)] \bullet G_{dd}(\bar{t}, t_2; U, t_0) = \delta(t_1 - t_2), \quad (20)$$

with the inverse zeroth-order function

$$G_{dd}^{(0)-1}(t_1, t_2) = \left( i \frac{\partial}{\partial t_1} - \tilde{\Delta} \right) \delta(t_1 - t_2). \quad (21)$$

In Eq. (20), the matrix multiplication ‘‘ $\bullet$ ’’ is defined by the integration  $\int_{t_0}^{t_0 - i\sigma} d\bar{t} \dots$  containing the time-ordering parameter  $\sigma$ . The  $\delta$  function of complex arguments is understood with respect to this integration. The inverse function to  $G_{dd}$  is given as  $G_{dd}^{-1}(t_1, t_2; U, t_0) = G_{dd}^{(0)-1}(t_1, t_2) - \Sigma_{dd}(t_1, t_2; U, t_0)$ . The deduction of the steady-state equations for the real-time functions  $g^<(t_1, t_2; U)$  and  $g^>(t_1, t_2; U)$  by the limiting procedure  $t_0 \rightarrow -\infty$  is analogous to that given in Ref. [28]. Defining the Fourier transformations according to Kadanoff-Baym [29],

$$g_{dd}^{\lessgtr}(\omega; U) = \mp i \int_{-\infty}^{\infty} dt g_{dd}^{\lessgtr}(t; U) e^{i\omega t}, \quad (22)$$

and, similarly for  $\Sigma^{\lessgtr}(\omega; U)$ , the solution of the steady-state equations may be written as follows:

$$A(\omega; U) = g_{dd}^>(\omega; U) + g_{dd}^<(\omega; U), \quad (23)$$

$$g_{dd}^<(\omega; U) = A(\omega; U) \bar{f}(\omega; U), \quad (24)$$

$$\bar{f}(\omega; U) = \frac{\Sigma_{dd}^<(\omega; U)}{\Gamma(\omega; U)}, \quad (25)$$

$$\Gamma(\omega; U) = \Sigma_{dd}^>(\omega; U) + \Sigma_{dd}^<(\omega; U), \quad (26)$$

with the nonequilibrium polaronic spectral function

$$A(\omega; U) = \frac{\Gamma(\omega; U)}{[\omega - \tilde{\Delta} - \mathcal{P} \int \frac{d\omega'}{2\pi} \frac{\Gamma(\omega'; U)}{\omega - \omega'}]^2 + [\frac{\Gamma(\omega; U)}{2}]^2}. \quad (27)$$

### C. Self-energy

According to the preceding section, the concrete form of the steady-state solution for the special choice of interactions is determined by the functions  $\Sigma_{dd}^{\lessgtr}$ . To find an explicit expression for  $\Sigma_{dd}^{\lessgtr}$ , we start with the equations of motion for  $G_{dd}$  and  $G_{cd}$ , which are given by the commutators of the operators  $d^{(\dagger)}$  and

$c_{ka}^{(\dagger)}$  with  $\tilde{H}$ . As a purely formal device, we add to  $H_{\text{int}}$  in Eq. (3) the interaction with fictitious external fields  $\{V\}$ . The equations of motion of  $G_{dd}$  and  $G_{cd}$  are then expressed by means of the functional derivatives of  $\Sigma_{dd}$  with respect to these fields. The resulting equations for  $\Sigma_{dd}^{\leq}$  are solved iteratively. We then let  $\{V\} \rightarrow 0$  and perform the limit  $t_0 \rightarrow -\infty$ . In the following calculations, we will use the self-energy function after the first iteration step [28]:

$$\begin{aligned} \Sigma_{dd}^{(1)\leq}(t_1, t_2; U) &= \sum_{k,a} |C_{ka}|^2 g_{cc}^{(0)\leq}(k, a; t_1, t_2; U) \\ &\times \left( I_0(\kappa) + \sum_{s \geq 1} I_s(\kappa) 2 \sinh(s\theta) \right. \\ &\times \{ [n_B(s\omega_0) + 1] e^{\pm i s \omega_0 (t_1 - t_2)} \\ &\left. + n_B(s\omega_0) e^{\mp i s \omega_0 (t_1 - t_2)} \right), \end{aligned} \quad (28)$$

where we have defined

$$\theta = \frac{1}{2} \omega_0 \beta_P, \quad \kappa = \frac{\tilde{g}^2}{\sinh \theta}, \quad (29)$$

$$I_s(\kappa) = \sum_{m=0}^{\infty} \frac{1}{m!(s+m)!} \left( \frac{\kappa}{2} \right)^{s+2m}. \quad (30)$$

The Bose function  $n_B$  in (28) contains the phonon-bath temperature  $T_P$  according to Eq. (5), while the zeroth-order functions of the leads depend on the different temperatures  $T_R$  and  $T_L$ :

$$g_{cc}^{(0)<}(k, a; t_1, t_2; U) = i e^{-i \varepsilon_{ka} t} f_a(\varepsilon_{ka} + U_a), \quad (31)$$

$$g_{cc}^{(0)>}(k, a; t_1, t_2; U) = -i e^{-i \varepsilon_{ka} t} [1 - f_a(\varepsilon_{ka} + U_a)], \quad (32)$$

with the lead Fermi-functions

$$f_a(\omega) = (e^{\beta_a \omega} + 1)^{-1}, \quad \beta_a = (k_B T_a)^{-1}. \quad (33)$$

The Fourier transformation of Eq. (28) leads to

$$\begin{aligned} \Sigma_{dd}^{(1)<}(\omega; U) &= \sum_a \left( I_0(\kappa) \tilde{\Gamma}_a^{(0)}(\omega) f_a(\omega + U_a) + \sum_{s \geq 1} I_s(\kappa) 2 \sinh(s\theta) \right. \\ &\times \left. \{ \tilde{\Gamma}_a^{(0)}(\omega - s\omega_0) n_B(s\omega_0) f_a(\omega - s\omega_0 + U_a) + \tilde{\Gamma}_a^{(0)}(\omega + s\omega_0) [n_B(s\omega_0) + 1] f_a(\omega + s\omega_0 + U_a) \} \right), \end{aligned} \quad (34)$$

with the renormalized dot-lead coupling function

$$\tilde{\Gamma}_a^{(0)}(\omega) = e^{-\tilde{g}^2 \coth \theta} \Gamma_a^{(0)}(\omega), \quad (35)$$

which depends on the lead density of states:

$$\Gamma_a^{(0)}(\omega) = 2\pi |t_a(\omega)|^2 \frac{1}{N} \sum_k \delta(\omega - \varepsilon_{ka}). \quad (36)$$

From Eq. (34),  $\Sigma_{dd}^{(1)>}(\omega; U)$  results by interchanging  $n_B \leftrightarrow (n_B + 1)$  and  $f_a \leftrightarrow (1 - f_a)$ . Note that Eq. (34) is similar to our result for the self-energy in Ref. [28], but now  $f$  is replaced by the individual lead Fermi-functions  $f_a$  that were defined in (33). If we insert the approximation (34) into Eq. (26), we find

$$\Gamma^{(1)}(\omega; U) = \Gamma_L^{(1)}(\omega; U) + \Gamma_R^{(1)}(\omega; U), \quad (37)$$

$$\begin{aligned} \Gamma_a^{(1)}(\omega; U) &= I_0(\kappa) \tilde{\Gamma}_a^{(0)}(\omega) + \sum_{s \geq 1} I_s(\kappa) 2 \sinh(s\theta) \{ \tilde{\Gamma}_a^{(0)}(\omega - s\omega_0) [n_B(s\omega_0) + 1 - f_a(\omega + U_a - s\omega_0)] \\ &+ \tilde{\Gamma}_a^{(0)}(\omega + s\omega_0) [n_B(s\omega_0) + f_a(\omega + U_a + s\omega_0)] \}. \end{aligned} \quad (38)$$

From the functions  $\Gamma^{(1)}(\omega; U)$  and  $\Sigma_{dd}^{(1)<}(\omega; U)$ , the first-order spectral function  $A^{(1)}(\omega; U)$ , the distribution function  $\tilde{f}^{(1)}(\omega; U)$  and the response functions  $g_{dd}^{(1)\gtrless}(\omega; U)$  follow according to Eqs. (27), (25), and (24), respectively.

#### D. Electron current

The operator of the particle current from lead  $a$  to the dot reads

$$\hat{J}_a = \frac{i}{\sqrt{N}} \sum_k (t_{ka} \tilde{d}^\dagger c_{ka} - t_{ka}^* c_{ka}^\dagger \tilde{d}). \quad (39)$$

Its mean value  $J_a = \langle \hat{J}_a \rangle$  is given by the real-time response functions  $\tilde{g}_{cd}$  of the electron operators, which are defined in analogy to Eqs. (11) and (12), e.g.,

$$i \langle \tilde{d}^\dagger c_{ka} \rangle = \tilde{g}_{cd}^<(k, a; t_1, t_1; U). \quad (40)$$

We determine  $\tilde{g}_{cd}$  based on the equation of motion of the corresponding function  $\tilde{G}_{cd}(k, a; t_1, t_2; U, t_0)$  of complex-time variables:

$$\begin{aligned} \tilde{G}_{cd}(k, a; t_1, t_2; U, t_0) &= -\frac{t_{ka}^*}{\sqrt{N}} G_{cc}^{(0)}(k, a; t_1, \bar{t}; U) \\ &\bullet \tilde{G}_{dd}(\bar{t}, t_2; U, t_0). \end{aligned} \quad (41)$$



The current  $J_a$  results as

$$J_a = \int_{-\infty}^{\infty} \frac{d\omega}{2\pi} \Gamma_a^{(0)}(\omega) [f_a(\omega + U_a) \tilde{A}^{(1)}(\omega; U) - \tilde{g}_{dd}^{(1)<}(\omega; U)], \quad (42)$$

where  $\tilde{A}^{(1)}$  and  $\tilde{g}_{dd}^{(1)<}$  are the electronic dot spectral function and response function. In the steady-state regime, our approximation conserves the particle current:  $J_L + J_R = 0$ . In the following, identical leads are assumed and we work in the wide-band limit where  $\Gamma_L^{(0)}(\omega) = \Gamma_R^{(0)}(\omega) \equiv \Gamma_0$ . Then the total particle current through the dot,  $J = (J_L - J_R)/2$ , is given by

$$J = \frac{\Gamma_0}{2} \int_{-\infty}^{\infty} \frac{d\omega}{2\pi} \tilde{A}^{(1)}(\omega; U) [f_L(\omega + U_L) - f_R(\omega + U_R)]. \quad (43)$$

Based on Eq. (43), we determine the electron current through the quantum dot numerically. We note that in the present work we are only interested in the current response to finite voltage biases and temperature differences between the leads. The generation of an electronic response merely by the interaction with a hot phonon bath would require different, energy-dependent densities of states in the leads, as was shown in Ref. [30]. In our calculations however, we consider identical

lead densities of states. That is why  $J = 0$  for all  $T_p$ , as long as  $T_L = T_R$  and  $\Phi = 0$ .

To find a relation between the polaronic and electronic functions, we decouple the fermionic and bosonic degrees of freedom in the electronic response function as is customary [31,32],

$$\tilde{g}_{dd}^{<}(t_1, t_2; U) \approx g_{dd}^{<}(t_1, t_2; U) \langle e^{-\tilde{g}(b^\dagger - b)t_2} e^{\tilde{g}(b^\dagger - b)t_1} \rangle, \quad (44)$$

As stated in Sec. II A, the local oscillator is supposed to be strongly coupled to the heat bath. Accordingly, we neglect the influence of the EP interaction on the dynamics of the phonon subsystem and evaluate the bosonic correlation function in (44) using Eq. (5). The first-order electronic response functions then read

$$\begin{aligned} \tilde{g}_{dd}^{(1)\leq}(\omega; U) &= e^{-\tilde{g}^2 \coth \theta} \left( I_0(\kappa) g_{dd}^{(1)\leq}(\omega; U) + \sum_{s \geq 1} I_s(\kappa) 2 \sinh(s\theta) \right. \\ &\quad \times \{ [1 + n_B(s\omega_0)] g_{dd}^{(1)\leq}(\omega \pm s\omega_0; U) \\ &\quad \left. + n_B(s\omega_0) g_{dd}^{(1)\geq}(\omega \mp s\omega_0; U) \} \right). \end{aligned} \quad (45)$$

The corresponding electronic spectral function  $\tilde{A}^{(1)}(\omega; U)$  follows according to the steady-state equation (23) as

$$\begin{aligned} \tilde{A}^{(1)}(\omega; U) &= \tilde{g}_{dd}^{(1)<}(\omega; U) + \tilde{g}_{dd}^{(1)>}(\omega; U) = e^{-\tilde{g}^2 \coth \theta} \left( I_0(\kappa) A^{(1)}(\omega; U) + \sum_{s \geq 1} I_s(\kappa) 2 \sinh(s\theta) \right. \\ &\quad \times \{ [n_B(s\omega_0) + \tilde{f}^{(1)}(\omega + s\omega_0; U)] A^{(1)}(\omega + s\omega_0; U) + [n_B(s\omega_0) + 1 - \tilde{f}^{(1)}(\omega - s\omega_0; U)] \\ &\quad \left. \times A^{(1)}(\omega - s\omega_0; U) \} \right). \end{aligned} \quad (46)$$

### E. Variational procedure

To determine the optimal variational parameter  $\gamma_{\min}$ , we have to minimize the relevant thermodynamic potential. This poses a problem, since for finite  $\Delta T$ , the effective temperature determining the statistics of the dot electron is not known. It will be given by the constitution of the steady state due to the coupling of the dot with the surroundings. In the present paper, we suppose  $\gamma$  to be mainly determined by the EP interaction terms contained in Eq. (1), since the variational parameter was introduced to characterize the polaronlike quasilocalization of the dot electron. Therefore we assume the equilibrium thermodynamic potential of the system, before the temperature and voltage differences were turned on, to be a reasonable first approximation for the variational function. The use of the well-known “ $\lambda$  trick” to take the interaction terms from  $\tilde{H}$  into account results in [29]:

$$\begin{aligned} \Omega &= -\frac{1}{\beta} \ln(1 + e^{-\tilde{\Delta}\beta}) \\ &\quad + 2 \int_0^1 \frac{1}{\lambda} \int \frac{d\omega}{2\pi} (\omega - \tilde{\Delta}) A_\lambda^{(1)}(\omega) f(\omega). \end{aligned} \quad (47)$$

The function  $A_\lambda^{(1)}$  represents the first-order equilibrium spectral function if the interaction coefficients in Eq. (7) are multiplied by the factor  $\lambda$ . If we write  $A_\lambda^{(1)}$  in terms of  $\Gamma_\lambda^{(1)} = \lambda^2 \Gamma^{(1)}$ , we can carry out the  $\lambda$  integration and find

$$\begin{aligned} \Omega &= - \int_{-\infty}^{\infty} \frac{d\omega}{\pi} f(\omega) \left\{ \frac{\pi}{2} \right. \\ &\quad \left. + \arctan \left[ \frac{\omega - \tilde{\Delta} - \mathcal{P} \int \frac{d\omega'}{2\pi} \frac{\Gamma^{(1)}(\omega')}{\omega - \omega'}}{\Gamma^{(1)}(\omega)/2} \right] \right\}. \end{aligned} \quad (48)$$

Via  $\tilde{\Delta}$  and  $\Gamma^{(1)}$ , the thermodynamic potential  $\Omega$  is a function of  $\gamma$ . For given parameters  $\varepsilon_p$ ,  $\Gamma_0$ ,  $\omega_0$ ,  $\Delta$ , and  $T$ , the optimal variational parameter  $\gamma_{\min}$  will be determined in equilibrium, i.e., for  $\Delta T = 0$  and  $\Phi = 0$ , by minimizing  $\Omega$ . We then keep  $\gamma_{\min}$  fixed and calculate the self-energy, the spectral function and the resulting particle current for finite voltages or temperature differences between the leads.

### III. NUMERICAL RESULTS

Depending on the type of molecular junction, the energies of the characteristic vibrational modes range from the order

of 10 meV in small molecules [33] to several 100 meV in  $C_{60}$  molecules [2]. In the following calculations, the corresponding model parameter  $\omega_0$  will be used as the unit of energy, i.e., we keep  $\omega_0 = 1$  fixed and set  $\hbar = 1$ ,  $|e| = 1$ , and  $k_B = 1$ . We assume identical leads and work in the wide band approximation, so that the dot-lead coupling is determined by a single parameter:  $\Gamma_L^{(0)}(\omega) = \Gamma_R^{(0)}(\omega) \equiv \Gamma_0$ . Furthermore, we consider low equilibrium temperatures,  $T/\omega_0 \ll 1$ . Then, according to Eq. (35), the renormalized dot-lead coupling parameter is approximately given as

$$\tilde{\Gamma}_0 \approx \Gamma_0 e^{-\gamma^2 \varepsilon_p / \omega_0}. \quad (49)$$

Usually, the ratio of the bare dot-lead coupling parameter  $\Gamma_0$  to the phonon energy  $\omega_0$  is used to determine whether the system is in the adiabatic ( $\Gamma_0 \gg \omega_0$ ) or anitadiabatic ( $\Gamma_0 \ll \omega_0$ ) regime. Recently, Eidelstein *et al.* [18] argued that for strong EP interaction, i.e.,  $\varepsilon_p/\omega_0 > 1$ , the antiadiabatic regime can be extended to  $\Gamma_0 \lesssim \omega_0$  as long as the exponential renormalization of the dot-lead coupling parameter in (49) is so strong that  $\tilde{\Gamma}_0 \ll \omega_0$ . In this case, the ‘‘mobility’’ of passing charge carriers is reduced, so far, that the local oscillator is still fast enough to adjust to them individually. Because then the physics is essentially those of the antiadiabatic regime, it can be called the ‘‘extended antiadiabatic regime’’ [18]. Only when  $\tilde{\Gamma}_0$  approaches  $\omega_0$  the system crosses over to the adiabatic regime.

To investigate the latter situation, in the present work, we consider comparable electronic and phononic timescales  $\Gamma_0 \lesssim \omega_0$  and moderate EP coupling  $\varepsilon_p \gtrsim \omega_0$ . Since in our approach, the polaronic renormalization in Eq. (49) also depends on the value of the variational parameter  $\gamma \in [0, 1]$ , we can interpolate between the extended adiabatic regime and the aforementioned crossover regime.

### A. Dot state in the crossover regime

To understand the thermoelectric response of the dot, we first investigate the dots electronic spectral function in equilibrium. Thereby we keep the parameters  $\omega_0 = 1$ ,  $T = 0.01$ ,  $\Phi = 0$ ,  $\Delta T = 0$ , and  $\varepsilon_p = 2$  fixed and consider two parameter sets for  $\Gamma_0$  and  $\Delta$ .

The first set is  $\Gamma_0 = 1$  and  $\Delta = 2$ , which means that the electronic and phononic subsystems react on a similar timescale and the dot level acts as a tunneling barrier between the leads. For these parameters, our variational calculation yields an optimal  $\gamma_{\min} = 0.59$ . As a consequence, the effective dot level given in Eq. (8) is lowered to near resonance,  $\tilde{\Delta} = 0.33$ . Moreover, the effective dot-lead coupling is reduced by about half,  $\tilde{\Gamma}_0 \approx 0.5$ , and we are in the aforementioned crossover regime [18].

For the second parameter set, we reduced the dot-lead coupling to  $\Gamma_0 = 0.5$  (meaning the phononic subsystem is the faster one) and raised the bare dot level to  $\Delta = 2.5$ . This results in  $\gamma_{\min} = 0.54$ ,  $\tilde{\Gamma}_0 = 0.28$ , and  $\tilde{\Delta} = 0.91$ , so that the renormalized dot level is still far from resonance.

The electronic spectral functions for the first and second parameter set are presented as the black curves in Figs. 2(a) and 2(b), respectively. We compare them to two limiting cases: the red dashed curves represent the small polaron limit, where we set  $\gamma = 1$  instead of the optimal  $\gamma_{\min}$ . Then  $S_\gamma$  in Eq. (6)

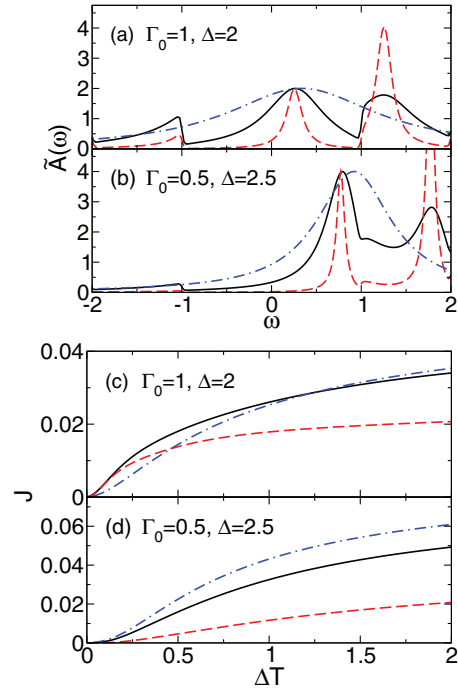


FIG. 2. (Color online) For  $\omega_0 = 1$ ,  $T = 0.01$ , and  $\varepsilon_p = 2$ . (a) Electronic equilibrium spectral function for  $\Gamma_0 = 1$ ,  $\Delta = 2$ ,  $\gamma_{\min} = 0.59$ ,  $\tilde{\Delta} = 0.33$ , and  $\tilde{\Gamma}_0 = 0.5$ . The variational calculation (black lines) is compared to the small polaron limit  $\gamma = 1$  (red dashed lines) and to the result for  $\varepsilon_p = 0$  (blue dot-dashed lines). In the latter two cases, we set  $\Delta$  in such a way that  $\tilde{\Delta}$  is the same as in the variational calculation. (b) Same as (a), but for  $\Gamma_0 = 0.5$ ,  $\Delta = 2.5$ ,  $\gamma_{\min} = 0.54$ ,  $\tilde{\Delta} = 0.91$ , and  $\tilde{\Gamma}_0 = 0.28$ . (c) and (d) For the same parameters as in (a) and (b), thermally induced current  $J$  as a function of the temperature difference  $\Delta T$  between the leads.

corresponds to the complete Lang-Firsov transformation. In this case, we have  $\tilde{\Gamma}_0 = 0.14$  and  $0.07$ , respectively, and the system is described as being in the extended antiadiabatic regime. The blue dot-dashed curves follow from setting  $\varepsilon_p = 0$ , which represents a rigid quantum dot without EP interaction. In both limiting cases, we set  $\Delta$  in such a way, that  $\tilde{\Delta}$  is the same as in the respective variational calculation.

In general, for  $\varepsilon_p = 0$ , the electronic spectral function features a single broad band centered at  $\omega = \Delta$ . From setting  $g = 0$  in Eqs. (37) and (27), we see that it has a Lorentzian shape and its width is given by the bare dot-lead coupling parameter  $\Gamma_0$ . For finite EP interaction and  $\gamma = 1$ , the polaronic character of the dot state is signalled by the appearance of several narrow side bands, which are given by the terms with  $s \geq 1$  in Eq. (46). These side bands represent the emission and absorption of optical phonons by the incident electrons. Their width is determined mainly by the small parameter  $\tilde{\Gamma}_0$  and their maxima are located multiple integers of  $\omega_0$  away from the central (zero-phonon) peak.

Note, however, that the phonon peak corresponding to  $\omega = \tilde{\Delta} - \omega_0$  is suppressed in Figs. 2(a) and 2(b), and only a small shoulder at  $\omega = -\omega_0$  remains. This is a consequence of Pauli blocking and can be understood from Eqs. (34) and (38);

for small  $\Delta T$ , we have  $n_B(s\omega_0) \approx 0$  and the Fermi functions of both leads are nearly steplike. Then, on the right hand sides of Eqs. (34) and (38), only the terms proportional to  $I_0(\kappa)$  contribute in the region  $\omega \in [-\omega_0 + |\Phi|/2, +\omega_0 - |\Phi|/2]$ . From Eq. (25), we see that  $\tilde{f} = (f_L + f_R)/2$  in this region and, consequently, only the term proportional to  $I_0(\kappa)$  on the right hand side of Eq. (46) contributes to the spectral function. This “floating” of the phonon bands has been discussed for linear electric transport through molecular quantum dots [34]. As we will see, it is also the reason why the low-temperature thermoelectric response is determined by the shape and position of the zero-phonon peak alone.

The variational dot state, due to the moderate renormalization, features broad, overlapping side bands. Still, we find a considerable shift of spectral weight to higher energies and a suppression of the zero-phonon peak. The resulting reduction of the low-energy tunneling rate is a main consequence of the polaron formation and is known as the Franck-Condon blockade [17].

### B. Thermally-induced current

In the following, we calculate the particle current through the junction that results from a finite temperature difference  $\Delta T$  between the leads. Let us again consider the two sets of parameters used in Sec. III A. Keeping the respective variational parameters  $\gamma_{\min}$  fixed, we increase the temperature difference  $\Delta T$ , whereby  $T_L = T + \Delta T$  and  $T_P = T_R = T$ . This induces a net particle current through the junction, which is depicted as a function of  $\Delta T$  in Figs. 2(c) and 2(d). For the first parameter set, we find that the EP interaction enhances the thermally induced current for small temperature differences. However, it reduces the current throughout the temperature range for the second parameter set.

This can be understood from Eq. (43): the net current through the dot depends on the electronic nonequilibrium spectral function and the difference of the Fermi distribution functions of the left and right lead. For zero voltage bias and small temperature differences, the term  $f_L(\omega) - f_R(\omega)$  in Eq. (43) differs from zero only in the narrow region  $\omega \in [-\Delta T, +\Delta T]$  and changes sign at  $\omega = 0$ . Physically, this means that the temperature difference between the leads induces a flow of hot charge carriers from the left to the right lead, since  $f_L(\omega) - f_R(\omega)$  is positive for  $\omega > 0$ . This current, however, is compensated by a counterflow of cold carriers at  $\omega < 0$ , where  $f_L(\omega) - f_R(\omega)$  is negative. Since  $\tilde{\Delta} > 0$  in our calculations, dot states above the Fermi energy have more spectral weight than the states below the Fermi energy. The net particle current is positive, i.e., it goes from the left to the right lead. The magnitude of the current is determined by the relative weight of the two flows, i.e., by the slope of the dot spectral function around the Fermi energy.

That is why the effect of the polaron formation on the thermally induced current crucially depends on the specific values of  $\tilde{\Delta}$  and  $\tilde{\Gamma}_0$ . For the first parameter set, the dot level  $\tilde{\Delta} = 0.33$  lies near the Fermi surface. In this situation, the polaronic renormalization of the effective dot-lead coupling increases the slope of  $\tilde{A}(\omega)$  at  $\omega = 0$ , as can be seen in Fig. 2(a). Consequently, in Fig. 2(c) the low-temperature thermoelectric current grows with respect to the noninteracting case. For

the second parameter set (corresponding to the nonresonant situation), the effect is reversed: the slope of  $\tilde{A}(\omega)$  decreases and the thermoelectric response of the vibrating molecule is smaller than that of the rigid quantum dot.

For both parameter sets, we find that, as  $\Delta T \rightarrow \infty$ , the maximum thermo-current is largest in the case of zero EP interaction. This can also be understood from Eq. (43). For large  $\Delta T$ , the region  $\omega \in [-\Delta T, +\Delta T]$  grows and  $f_L(\omega) - f_R(\omega)$  is finite far from the Fermi surface. Now the thermoelectric current is given not by the slope of  $\tilde{A}(\omega)$  at  $\omega = 0$  but by the ratio of the integrated spectral weight below and above the Fermi surface. Because  $T_P$  is low, the phonon bands in  $\tilde{A}$  are weighted according to a Poisson distribution with the parameter  $\tilde{g}^2 = \gamma^2 \varepsilon_p / \omega_0$ . As  $\gamma$  grows, a considerable portion of the total spectral weight is shifted to the phonon bands at  $\omega > 1$ . Even for large temperature differences, their contribution to the thermocurrent will be exponentially small, and the maximum current decreases with respect to the rigid quantum dot.

### C. Thermovoltage

We have seen how, in general, a temperature difference  $\Delta T$  between the leads will induce a particle current through the dot. In a typical experiment, this thermoelectric effect is measured by applying a voltage difference  $\Phi$  in such a way that the thermally induced current is compensated:  $J(\Delta T, \Phi) = 0$  for finite  $\Delta T$  and  $\Phi$ . The determination of the so-called thermovoltage,  $\Phi_0$ , and its dependence on the EP coupling will be the subject of the following numerical calculations. Thereby, we use the second parameter set from Sec. III A, i.e.,  $\omega_0 = 1$ ,  $T = 0.01$ ,  $\varepsilon_p = 2$ ,  $\Delta = 2.5$ , and  $\Gamma_0 = 0.5$ , resulting in  $\gamma_{\min} = 0.54$ ,  $\tilde{\Gamma}_0 = 0.28$ , and  $\tilde{\Delta} = 0.91$ .

To understand the mechanism, we first consider a finite but fixed temperature difference  $\Delta T = 0.25$ . For  $\Phi = 0$ , the corresponding electronic spectral function is shown as the black curve in Fig. 3(a), where it is again compared to the noninteracting case and the small polaron limit. We calculate the total current  $J$  as a function of the voltage bias  $\Phi$ , whereby  $\mu_L = \Phi/2$  and  $\mu_R = -\Phi/2$ . The results are depicted in Fig. 3(b).

For negative voltages, the current signal is in qualitative agreement with the results of previous works [28]. In a nutshell, the formation of a polaronlike state at the dot reduces the zero-bias conductance due to the Franck-Condon blockade, but for growing voltage, we find steps in the current signal whenever  $\Phi/2 = -\tilde{\Delta} - n\omega_0$ , with  $n \in [0, 1, 2, \dots]$ . Here, the chemical potential of the right lead crosses the phonon side bands in  $\tilde{A}$  and resonant transport of electrons takes place via the emission and subsequent absorption of an equal number of phonons. The right lead is the cold one and has a steplike Fermi function. Because of this, the width of the current steps is mainly determined by the width of the phonon bands in the spectral function, i.e., by  $\tilde{\Gamma}_0$ . In the variational calculation, the bands overlap considerably [see Fig. 3(a)] and the resonant steps in the current-voltage signal are smeared out.

For positive voltage bias, we find no current steps even in the small polaron limit. Now it is the chemical potential of the hot left lead that crosses the renormalized dot level and the phonon bands. The width of the resonant tunneling steps in  $J(\Phi)$  does not depend on  $\tilde{\Gamma}_0$  alone but also on the width of the soft

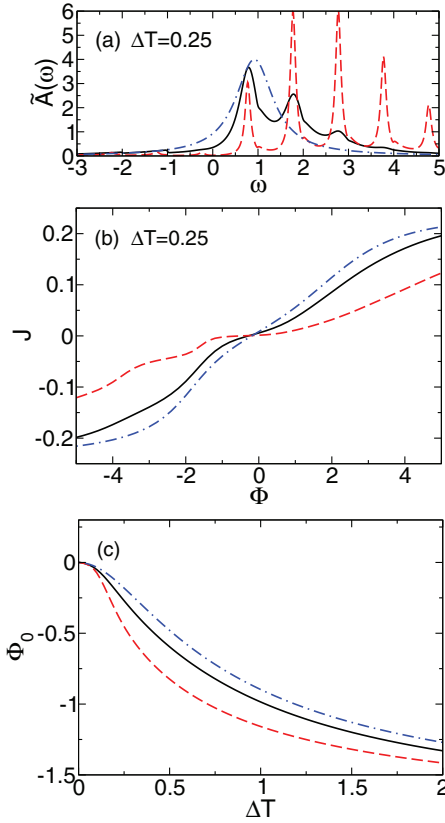


FIG. 3. (Color online) For the same parameters as in Figs. 2(b) and 2(d), i.e.,  $\omega_0 = 1$ ,  $T = 0.01$ ,  $\varepsilon_p = 2$ ,  $\Gamma_0 = 0.5$ ,  $\Delta = 2.5$ ,  $\gamma_{\min} = 0.54$ ,  $\tilde{\Delta} = 0.91$ , and  $\tilde{\Gamma}_0 = 0.28$ . (a) Electronic spectral functions for fixed  $\Delta T = 0.25$  and  $\Phi = 0$ . We compare the variational calculation (black line) to the small polaron limit  $\gamma = 1$  (red dashed line) and to the result for  $\varepsilon_p = 0$  (blue dot-dashed line). (b) Current  $J$  as a function of the voltage difference  $\Phi$  between the leads for fixed  $\Delta T = 0.25$ . (c) Thermovoltage  $\Phi_0$  as a function of  $\Delta T$ .

Fermi-surface. Since  $\Delta T = 0.25$  is of the order of  $\omega_0$ , the current steps are smeared out and therefore no longer discernible.

Based on the current-voltage signal we now determine the thermovoltage  $\Phi_0$  as a function of  $\Delta T$  numerically and show the result in Fig. 3(c). We find that for small temperature differences, the absolute value of  $\Phi_0$  grows strongest for  $\gamma = 1$ . This is a consequence of the reduced electrical conductance of the quantum dot in the small polaron picture; for a given  $\Delta T$ , relatively large voltages are necessary to compensate the corresponding thermocurrent. For large temperature differences, we find a maximum value  $\Phi_0 = -1.5$  for all three data sets given in Fig. 3(c). This voltage corresponds to the position of the zero-phonon step in  $J(\Phi)$  in Fig. 3(b). Here, the systems conductance grows considerably and any thermally induced current can easily be compensated by a slight growth in  $\Phi$ .

#### D. Varying the dot level

In the previous sections, we chose the bare dot level  $\Delta$  in such a way, that the renormalized level  $\tilde{\Delta}$  was equal in

the scenarios with and without EP interaction. In this way, we concentrated on the influence of the renormalized dot-lead coupling on the thermovoltage. However, in an experimental situation, the dot level may be manipulated, e.g., by applying a gate voltage through a third electrode, in order to optimize the thermoelectric effect. To investigate this situation, we now consider  $\Delta$  as our free parameter. For each  $\Delta$ , we temporarily set  $\Phi = 0$  and  $\Delta T = 0$  to determine the optimal parameter  $\gamma_{\min}$ . We then keep  $\gamma_{\min}$  fixed, set  $\Delta T$  to a finite value and calculate the thermovoltage  $\Phi_0$ . The remaining parameters are the same as in Sec. III C, i.e.,  $\omega_0 = 1$ ,  $T = 0.01$ ,  $\varepsilon_p = 2$ , and  $\Gamma_0 = 0.5$ .

First, we consider a small temperature difference  $\Delta T = 0.1$ . Our result for the thermovoltage as a function of the bare dot level is presented in Fig. 4(a). In general,  $\Phi_0(\Delta)$  features two resonances of opposite sign and goes to zero when the renormalized dot level crosses the Fermi surface, i.e., when  $\tilde{\Delta} = \Delta - \varepsilon_p \gamma (2 - \gamma) = 0$ . At this point, the spectral function is symmetrical around  $\omega = 0$ , and the thermoelectric flow and counterflow between the leads cancel exactly. As  $|\tilde{\Delta}|$  grows, the net thermocurrent and, consequently, the thermovoltage increases. In accordance with our results in Sec. III C, the maximum thermovoltage is largest in the small polaron picture due to the strong renormalization of the dot-lead coupling. When  $|\tilde{\Delta}|$  grows further and the zero phonon peak shifts away from the Fermi surface, the dot density of states near  $\omega = 0$  decreases, and the thermoelectric effect vanishes again.

In Fig. 4(a), the small polaron result is shifted from the  $\varepsilon_p = 0$  curve by the value of the polaron binding energy  $\varepsilon_p$ , which can be understood from setting  $\gamma = 1$  in Eq. (8). In both cases, the thermovoltage signal runs linearly through zero. We note that for growing  $T$  (not shown here) its slope reduces, while the position of the positive (negative) resonance shifts to lower (higher)  $\Delta$ . In this regard, our result resembles the sawtoothlike thermopower signal that was predicted in Ref. [20] and experimentally measured in Ref. [6]. There, the periodicity of the thermopower oscillations was determined by the difference in the ground-state energies for different numbers of electrons on the dot. In our model however, we only account for a single dot electron. That is why we only observe a single ‘‘tooth,’’ i.e., only two thermovoltage resonances in Fig. 4(a).

Moreover, we find no side peaks in the thermoelectric signal that could be attributed to the phonon side bands in  $\tilde{A}$ . This is a consequence of the floating effect discussed in Sec. III A; since the thermovoltages in Fig. 4(a) are small, the expression  $f_L(\omega + U_L) - f_R(\omega + U_R)$  in Eq. (43) differs from zero only within the region  $\omega \in [-\omega_0 + |\Phi_0|/2, +\omega_0 - |\Phi_0|/2]$ . In this region, the phonon side bands in  $\tilde{A}(\omega)$  are suppressed and do not contribute to the thermoelectric transport. That is why the resonance signal in Fig. 4(a) is given by the varying position of the zero-phonon peak only.

Consequently, in Fig. 4(a) the variational calculation with its moderate renormalization of the dot-lead coupling predicts a weaker resonance signal than the small polaron picture, which is also shifted from the result for the rigid dot by less than  $\varepsilon_p$ . We find that in contrast to the two limiting cases, the strength of the resonance now depends on the sign of  $\Phi_0$ . This can be understood from Fig. 4(b), where we show the optimal variational parameter as a function of the dot level.

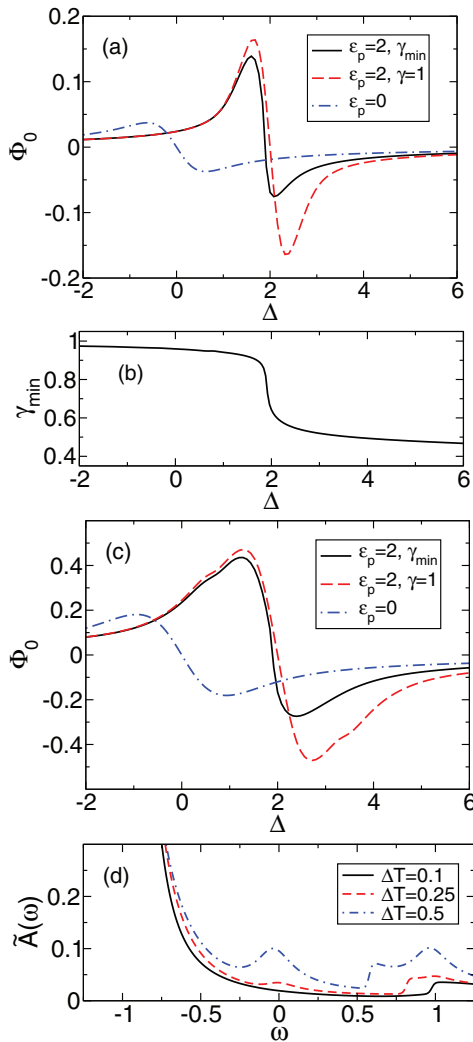


FIG. 4. (Color online) For  $\omega_0 = 1$ ,  $T = 0.01$ ,  $\varepsilon_p = 2$ ,  $\Gamma_0 = 0.5$ , as in Fig. 3. (a) Thermovoltage  $\Phi_0$  as a function of the bare dot level  $\Delta$  for  $\Delta T = 0.1$ . We compare the variational calculation (black line) to the small polaron limit  $\gamma = 1$  (red dashed line) and the case with zero EP coupling (blue dash-dot line). (b) Optimal variational parameter  $\gamma_{\min}$  as a function of the bare dot level. (c) Same as (a) but with  $\Delta T = 0.25$ . (d) Electronic spectral functions for  $\Delta = 0.8$ ,  $\gamma_{\min} = 0.95$  and several temperature differences.

For  $\tilde{\Delta} > 0$ , we have  $\gamma_{\min} \approx 0.5$  like in the previous sections. When the renormalized dot level crosses the Fermi surface,  $\gamma_{\min}$  approaches 1 and a small transient polaron forms at the dot. Then the thermoelectric effect increases.

Figure 4(c) shows the thermovoltage signals after having raised the temperature difference to  $\Delta T = 0.25$ . As expected, for all three cases, the heights and widths of the resonances grow with respect to Fig. 4(a). More importantly, for finite EP coupling, the curves now feature side bands at a distance of  $\omega_0$  from their maximum resonances. This becomes possible because for large temperature differences the floating condition for the phonon bands is relaxed; since  $\Delta T \lesssim \omega_0$ , the Fermi surface of the hot left lead softens considerably. Now, the

terms with  $s \geq 1$  on the right hand side of Eq. (46) contribute to the spectral function even for  $\omega \in [-\omega_0 + |\Phi_0|/2, +\omega_0 - |\Phi_0|/2]$ . For example, Fig. 4(d) shows the electronic spectral function in the variational calculation for  $\Delta = 0.8$  and several temperature differences. Since  $\gamma_{\min} \approx 1$ , we have  $\tilde{\Delta} \approx -1.1$ . For growing  $\Delta T$ , a small peak appears near the Fermi-surface that is related to the polaronic state with one phonon at  $\omega = \tilde{\Delta} + \omega_0 \approx 0$ . When, for varying  $\Delta$ , this peak crosses the Fermi surface, the side peak in the thermovoltage signal in Fig. 4(c) appears. Note, however, that the floating condition still holds for the cold right lead, as can be seen from the shoulder appearing near  $\omega = 1$  in Fig. 4(d). As the thermovoltage grows, the window  $\omega \in [-\omega_0 + |\Phi_0|/2, +\omega_0 - |\Phi_0|/2]$  closes and the shoulder shifts towards  $\omega = 0$ .

#### IV. SUMMARY AND OUTLOOK

In this work, we investigated the steady-state thermoelectric transport through a vibrating molecular quantum dot in the crossover regime far from the antiadiabatic limit. Within a Kadanoff-Baym formalism that is generalized to account for different lead temperatures, the nonequilibrium dot self-energy was calculated to second order in the dot-lead interaction coefficient. In order to account for the polaronic character of the dot state, we applied a variational small-polaron transformation and determined the degree of transformation by minimizing the relevant thermodynamic potential.

In essence, we calculated the current induced by a finite temperature difference between the leads. For small temperature differences, the influence of the electron-phonon (EP) interaction strongly depends on the specific system parameters; for a near-resonant dot level, the interacting quantum dot acts as a more efficient energy filter and the thermo-current increases. In the tunneling regime, however, we found a reduction of the thermo-current due to the decreasing density of states near the Fermi surface.

In order to relate our results to experiment, we determined the thermovoltage required to compensate the thermally induced particle current at a given temperature difference. We found that in principle the Franck-Condon blockade boosts the thermovoltage through the reduction of the systems electrical conductance. For intermediate EP coupling, the small polaron picture overestimates this effect.

Finally, we determined the thermovoltage as a function of the dots energy level. Because of Pauli blocking, we found no phonon features in the low-temperature thermoelectric signal. However, our variational calculation predicts an asymmetrical line shape due to the formation of a small polaron as the dot level drops beneath the equilibrium Fermi energy. For large temperature differences of the order of the phonon energy, Pauli blocking is relaxed and the thermovoltage signal features multiple resonances that can be attributed to resonant transport through vibrational dot states.

The present study should be considered a first step in applying our variational ansatz to the thermoelectric transport through molecular junctions. Although it captures the essential physics, it must be extended in several directions. Most importantly, we have yet to consider energy transport through the junction. The efficiency of energy deposition by the excitation of local phonons will strongly depend on the

effective EP interaction, i.e., on the polaronic character of the dot state. To investigate the subsequent heating or cooling of the molecule, the effective temperature of the dot electrons has to be determined numerically, for which several methods have been proposed [22]. This should have some influence on the variational parameter  $\gamma$  as well. In our previous works, a voltage-dependent variational parameter was responsible for the junctions negative differential conductance. Therefore it would be highly desirable to carry this nonlinear behavior over to the discussion of thermoelectric transport.

Another worthwhile extension of our work concerns Coulomb interaction effects. Recently, Andergassen *et al.* [35] argued for the negative- $U$  Anderson model (which neglects the coupling to the phonon degrees of freedom however) that the resulting charge Kondo effect leads to a large enhancement of the linear response thermopower due to the highly asymmetric dot spectral function. This effect was shown to be tunable applying a gate voltage. It would be interesting to reexamine

this problem for a model with additional EP interaction, using our variational scheme, since—as we have demonstrated in Sec. III D—the effective EP interaction (described by the variational parameter) is strongly influenced by the gate voltage. In this connection, we like to stress that for a combined Holstein-Hubbard quantum dot model it has been shown that strong EP coupling may result in a net attractive Coulomb interaction [36]. Then, depending on the energy of the dot level, a variational ansatz might be able to interpolate between the positive- $U$  Holstein-Hubbard dot model and the effective anisotropic Kondo model regime investigated in Ref. [35].

#### ACKNOWLEDGMENTS

This work was supported by Deutsche Forschungsgemeinschaft through SFB 652 B5. T.K. and H.F. acknowledge the hospitality at the Institute of Physics ASCR.

- 
- [1] J. A. Malen, P. Doak, K. Baheti, T. D. Tilley, R. A. Segalman, and A. Majumdar, *Nano Lett.* **9**, 1164 (2009).
- [2] K. J. Franke and J. I. Pascual, *J. Phys. Condens. Matter* **24**, 394002 (2012).
- [3] C. Evangelii, K. Gillemot, E. Leary, M. T. González, G. Rubio-Bollinger, C. J. Lambert, and N. Agrait, *Nano Lett.* **13**, 2141 (2013).
- [4] E. Pop, D. Mann, J. Cao, Q. Wang, K. Goodson, and H. Dai, *Phys. Rev. Lett.* **95**, 155505 (2005); R. Leturcq, C. Stampfer, K. Inderbitzin, L. Durrer, C. Hierold, E. Mariani, M. G. Schultz, F. von Oppen, and K. Ensslin, *Nat. Phys.* **5**, 327 (2009).
- [5] M. Galperin, M. A. Ratner, and A. Nitzan, *J. Phys. Condens. Matter* **19**, 103201 (2007); Y. Dubi and M. Di Ventra, *Rev. Mod. Phys.* **83**, 131 (2011).
- [6] R. Scheibner, M. König, D. Reuter, A. D. Wieck, C. Gould, H. Buhmann, and L. W. Molenkamp, *New J. Phys.* **10**, 083016 (2008); H. Song, Y. Kim, Y. H. Jang, H. Jeong, M. A. Reed, and T. Lee, *Nature (London)* **462**, 1039 (2009).
- [7] Z.-L. Cheng, R. Skouta, H. Vazquez, J. R. Widawsky, S. Schneebeli, W. Chen, M. S. Hybertsen, R. Breslow, and L. Venkataraman, *Nat. Nanotechnol.* **6**, 353 (2011).
- [8] M. A. Reed, C. Zhou, C. J. Muller, T. P. Burgin, and J. M. Tour, *Science* **278**, 252 (1997); H. Park, J. Park, A. K. L. Lim, E. H. Anderson, A. P. Alivisatos, and P. L. McEuen, *Nature (London)* **407**, 57 (2000).
- [9] P. Reddy, S.-Y. Jang, R. A. Segalman, and A. Majumdar, *Science* **315**, 1568 (2007).
- [10] K. Baheti, J. A. Malen, P. Doak, P. Reddy, S.-Y. Jang, T. D. Tilley, A. Majumdar, and R. A. Segalman, *Nano Lett.* **8**, 715 (2008).
- [11] J. Koch, F. von Oppen, Y. Oreg, and E. Sela, *Phys. Rev. B* **70**, 195107 (2004).
- [12] G. Schaller, T. Krause, T. Brandes, and M. Esposito, *New J. Phys.* **15**, 033032 (2013).
- [13] S.-H. Ke, W. Yang, S. Curtarolo, and H. U. Baranger, *Nano Lett.* **9**, 1011 (2009).
- [14] M. Leijnse, M. R. Wegewijs, and K. Flensberg, *Phys. Rev. B* **82**, 045412 (2010).
- [15] J. P. Bergfield, M. A. Solis, and C. A. Stafford, *ACS Nano* **4**, 5314 (2010); B. C. Hsu, C.-W. Chiang, and Y.-C. Chen, *Nanotechnology* **23**, 275401 (2012).
- [16] Y. Meir and N. S. Wingreen, *Phys. Rev. Lett.* **68**, 2512 (1992).
- [17] A. Jovchev and F. B. Anders, *Phys. Rev. B* **87**, 195112 (2013).
- [18] E. Eidelstein, D. Goberman, and A. Schiller, *Phys. Rev. B* **87**, 075319 (2013).
- [19] M. A. Laasko, D. M. Kennes, S. G. Jakobs, and V. Meden, [arXiv:1309.6118v1](https://arxiv.org/abs/1309.6118v1).
- [20] C. W. J. Beenakker and A. A. M. Staring, *Phys. Rev. B* **46**, 9667 (1992).
- [21] R. Sánchez and M. Büttiker, *Phys. Rev. B* **83**, 085428 (2011); S. Juergens, F. Haupt, M. Moskalets, and J. Splettstoesser, *ibid.* **87**, 245423 (2013).
- [22] M. Galperin, A. Nitzan, and M. A. Ratner, *Phys. Rev. B* **75**, 155312 (2007).
- [23] I. G. Lang and Y. A. Firsov, *Zh. Eksp. Teor. Fiz.* **43**, 1843 (1962) [*Sov. Phys. JETP* **16**, 1301 (1963)].
- [24] T. E. Humphrey, R. Newbury, R. P. Taylor, and H. Linke, *Phys. Rev. Lett.* **89**, 116801 (2002).
- [25] G. Schulze, K. J. Franke, A. Gagliardi, G. Romano, C. S. Lin, A. L. Rosa, T. A. Niehaus, T. Frauenheim, A. Di Carlo, A. Pecchia, and J. I. Pascual, *Phys. Rev. Lett.* **100**, 136801 (2008).
- [26] A. La Magna and I. Deretzis, *Phys. Rev. Lett.* **99**, 136404 (2007); A. La Magna, I. Deretzis, and V. Privitera, *Eur. Phys. J. B* **70**, 311 (2009).
- [27] H. Fehske, D. Ihle, J. Loos, U. Trapper, and H. Büttner, *Z. Phys. B* **94**, 91 (1994); H. Fehske, J. Loos, and G. Wellein, *ibid.* **104**, 619 (1997).
- [28] T. Koch, J. Loos, A. Alvermann, and H. Fehske, *Phys. Rev. B* **84**, 125131 (2011); T. Koch, H. Fehske, and J. Loos, *Physica Scripta* **2012**, 014039 (2012).
- [29] L. P. Kadanoff and G. Baym, *Quantum Statistical Mechanics* (Benjamin/Cummings Publishing Company, Reading, Massachusetts, 1962).
- [30] O. Entin-Wohlman, Y. Imry, and A. Aharony, *Phys. Rev. B* **82**, 115314 (2010).

- [31] U. Lundin and R. H. McKenzie, *Phys. Rev. B* **66**, 075303 (2002); J.-X. Zhu and A. V. Balatsky, *ibid.* **67**, 165326 (2003).
- [32] M. Galperin, A. Nitzan, and M. A. Ratner, *Phys. Rev. B* **73**, 045314 (2006).
- [33] N. B. Zhitenev, H. Meng, and Z. Bao, *Phys. Rev. Lett.* **88**, 226801 (2002).
- [34] A. Mitra, I. Aleiner, and A. J. Millis, *Phys. Rev. B* **69**, 245302 (2004).
- [35] S. Andergassen, T. A. Costi, and V. Zlatić, *Phys. Rev. B* **84**, 241107 (2011).
- [36] P. S. Cornaglia, H. Ness, and D. R. Grempel, *Phys. Rev. Lett.* **93**, 147201 (2004).





## Interacting multicomponent exciton gases in a potential trap: Phase separation and Bose-Einstein condensation

S. Sobkowiak, D. Semkat, and H. Stolz  
*Institut für Physik, Universität Rostock, 18051 Rostock, Germany*

Th. Koch and H. Fehske  
*Institut für Physik, Ernst-Moritz-Armdt-Universität Greifswald, 17489 Greifswald, Germany*  
(Received 3 May 2010; published 5 August 2010)

The system under consideration is a multicomponent gas of interacting paraexcitons and orthoexcitons confined in a three-dimensional potential trap. We calculate the spatially resolved optical emission spectrum due to interband transitions involving weak direct and phonon-mediated exciton-photon interactions. For each component, the occurrence of a Bose-Einstein condensate changes the spectrum in a characteristic way so that it directly reflects the constant chemical potential of the excitons and the renormalization of the quasiparticle excitation spectrum. Moreover, the interaction between the components leads, in dependence on temperature and particle number, to modifications of the spectra indicating phase separation of the subsystems. Typical examples of density profiles and luminescence spectra of ground-state paraexcitons and orthoexcitons in  $\text{Cu}_2\text{O}$  are given.

DOI: 10.1103/PhysRevB.82.064505

PACS number(s): 78.20.-e, 78.30.-j, 71.35.Lk

### I. INTRODUCTION

Excitons in semiconductors have been promising candidates for the observation of Bose-Einstein condensation for several decades. At present, cuprous oxide ( $\text{Cu}_2\text{O}$ ) is in the focus of experimental efforts due to the large binding energy and long lifetime of the exciton states. In order to obtain sufficiently high densities, entrapment by an external potential is an approved method.

The theoretical description of excitons in potential traps has been carried out so far mostly in the frame of a model of ideal bosons. Concepts for the inclusion of the interaction are well known from the theory of atomic condensates<sup>1-4</sup> and first applications to excitons exist, too.<sup>5</sup> Recent investigations in the framework of a mean-field formalism in local-density approximation (LDA) have shown distinct signatures of a condensate in the decay luminescence spectrum of the non-condensed excitons.<sup>6</sup> It is the aim of the present paper to introduce a generalization of this theory to a multicomponent gas of interacting paraexcitons and orthoexcitons, where the consequences of the interaction on the condensation process are of particular interest. We show results for the densities of the individual components and their spatially resolved luminescence spectra for several parameter regimes and highlight experimentally relevant cases.

### II. THERMODYNAMICS OF EXCITONS IN A POTENTIAL TRAP

The thermodynamics of a one-component Bose gas has been investigated in detail, see, e.g., Refs. 1-4. First applications of these concepts to excitons have been presented in Ref. 5 and, looking at spectral signatures of a condensate, in Ref. 6. In analogy to generalizations for multicomponent atomic gases, e.g., Refs. 7-12 and spinor polaritons, e.g., Refs. 13 and 14, in the following, we generalize this approach to the case of multiple species of excitons, i.e.,

paraexcitons and orthoexcitons, adopting a mean-field coupling scheme between the components.<sup>15</sup>

The multicomponent exciton gas is considered in second quantization. We start from the Hamiltonian for a  $K$ -component system in the grand-canonical ensemble,

$$\mathcal{H} = \sum_{i=1}^K \int d\mathbf{r} \psi_i^\dagger(\mathbf{r}, t) \left[ -\frac{\hbar^2 \nabla^2}{2M_i} + V_i(\mathbf{r}) - \mu_i \right] \psi_i(\mathbf{r}, t) + \frac{1}{2} \sum_{i,j=1}^K \int d\mathbf{r} h_{ij} \psi_i^\dagger(\mathbf{r}, t) \psi_j^\dagger(\mathbf{r}, t) \psi_j(\mathbf{r}, t) \psi_i(\mathbf{r}, t) \quad (1)$$

with respective external potentials  $V_i$  and chemical potentials  $\mu_i$  for each species. We assume a contact potential for the exciton-exciton interaction with the matrix  $h_{ij}$  containing the intraspecies and interspecies interaction strengths. Its components are given by the  $s$ -wave scattering lengths  $a_{ij}^s$ ,

$$h_{ij} = 2\pi\hbar^2 \left( \frac{1}{M_i} + \frac{1}{M_j} \right) a_{ij}^s. \quad (2)$$

The Bose field operator  $\psi_i$  obeys the Heisenberg equation of motion

$$i\hbar \frac{\partial \psi_i(\mathbf{r}, t)}{\partial t} = \left[ -\frac{\hbar^2 \nabla^2}{2M_i} + V_i(\mathbf{r}) - \mu_i \right] \psi_i(\mathbf{r}, t) + \sum_{j=1}^K h_{ij} \psi_j^\dagger(\mathbf{r}, t) \psi_j(\mathbf{r}, t) \psi_i(\mathbf{r}, t). \quad (3)$$

We decompose the field operators  $\psi_i$  in the usual fashion,

$$\psi_i(\mathbf{r}, t) = \Phi_i(\mathbf{r}) + \tilde{\psi}_i(\mathbf{r}, t), \quad (4)$$

where  $\Phi_i$  is the (scalar) condensate wave function with  $\Phi_i(\mathbf{r}) = \langle \psi_i(\mathbf{r}, t) \rangle = \langle \psi_i(\mathbf{r}) \rangle$  and  $\tilde{\psi}_i$  is the operator of the thermal excitons. Inserting the decomposition Eq. (4) into Eq. (3) and

following the steps of Ref. 1, we obtain (arguments dropped for the sake of brevity)

$$0 = \left[ -\frac{\hbar^2 \nabla^2}{2M_i} + V_i - \mu_i + h_{ii}(n_{ii} + \tilde{n}_{ii}) + \sum_{j \neq i} h_{ij} n_{jj} \right] \Phi_i + h_{ii} \tilde{m}_{ii} \Phi_i^* + \sum_{j \neq i} h_{ij} (\tilde{n}_{ji} \Phi_j + \tilde{m}_{ji} \Phi_j^*) \quad (5)$$

and

$$i\hbar \frac{\partial \tilde{\psi}_i}{\partial t} = \left( -\frac{\hbar^2 \nabla^2}{2M_i} + V_i - \mu_i + 2h_{ii} n_{ii} + \sum_{j \neq i} h_{ij} n_{jj} \right) \tilde{\psi}_i + h_{ii} m_{ii} \tilde{\psi}_i^\dagger + \sum_{j \neq i} h_{ij} (n_{ij} \tilde{\psi}_j + m_{ij} \tilde{\psi}_j^\dagger) \quad (6)$$

with  $n_{ij} \equiv \Phi_j^* \Phi_i + \tilde{n}_{ij}$ ,  $m_{ij} \equiv \Phi_j \Phi_i + \tilde{m}_{ij}$ , and the normal and anomalous averages  $\tilde{n}_{ij} = \langle \tilde{\psi}_i^\dagger \tilde{\psi}_j \rangle$  and  $\tilde{m}_{ij} = \langle \tilde{\psi}_i \tilde{\psi}_j^\dagger \rangle$ , respectively. Equation (5) generalizes the familiar Gross-Pitaevskii equation by including (i) the coupling to the thermal excitons and (ii) the coupling of multiple components.

In a first approximation, we neglect all nondiagonal averages, i.e.,  $\tilde{m}_{ij} = \tilde{n}_{ij} = m_{ij} = n_{ij} = 0 \quad \forall i \neq j$ , reducing Eqs. (5) and (6) to effective one-species equations with an additional mean-field contribution from the other species,

$$0 = \left[ -\frac{\hbar^2 \nabla^2}{2M_i} + V_i - \mu_i + h_{ii}(n_{ii} + \tilde{n}_{ii}) + \sum_{j \neq i} h_{ij} n_{jj} \right] \Phi_i + h_{ii} \tilde{m}_{ii} \Phi_i^*, \quad (7)$$

$$i\hbar \frac{\partial \tilde{\psi}_i}{\partial t} = \left( -\frac{\hbar^2 \nabla^2}{2M_i} + V_i - \mu_i + 2h_{ii} n_{ii} + \sum_{j \neq i} h_{ij} n_{jj} \right) \tilde{\psi}_i + h_{ii} m_{ii} \tilde{\psi}_i^\dagger. \quad (8)$$

Thanks to this simplification, Eq. (8) can be formally solved by a Bogoliubov transformation,

$$\tilde{\psi}_i = \sum_{\sigma} [u_i(\sigma) a_i(\sigma) e^{-iE_i(\sigma)t/\hbar} + v_i^*(\sigma) a_i^\dagger(\sigma) e^{iE_i(\sigma)t/\hbar}], \quad (9)$$

where  $\sigma$  enumerates the quasiparticle states. Thereby the Bogoliubov amplitudes  $u_i$  and  $v_i$  satisfy the relation  $\sum_{\sigma} [u_i(\sigma)^2 - v_i(\sigma)^2] = 1$ . The excitation spectrum  $E_i(\sigma)$  is given by the solution of the eigenvalue problem,

$$\begin{pmatrix} \mathcal{L}_i & h_{ii} m_{ii} \\ -h_{ii} m_{ii}^* & -\mathcal{L}_i \end{pmatrix} \begin{pmatrix} u_i(\sigma) \\ v_i(\sigma) \end{pmatrix} = E_i(\sigma) \begin{pmatrix} u_i(\sigma) \\ v_i(\sigma) \end{pmatrix} \quad (10)$$

with

$$\mathcal{L}_i = -\frac{\hbar^2 \nabla^2}{2M_i} + V_i - \mu_i + 2h_{ii} n_{ii} + \sum_{j \neq i} h_{ij} n_{jj}. \quad (11)$$

Equations (7) and (10) are the multicomponent generalizations of the Hartree-Fock-Bogoliubov equations. They represent a system of  $3K$  equations which are coupled via the interaction matrix elements  $h_{ij}$ .

To guarantee gapless spectra, we next apply the Popov approximation, i.e., we neglect the anomalous averages  $\tilde{m}_{ii}$  in Eqs. (7) and (10) and find

$$0 = \left[ -\frac{\hbar^2 \nabla^2}{2M_i} + V_i - \mu_i + h_{ii}(n_{ii} + \tilde{n}_{ii}) + \sum_{j \neq i} h_{ij} n_{jj} \right] \Phi_i \quad (12)$$

and

$$\begin{pmatrix} \mathcal{L}_i & h_{ii} \Phi_i^2 \\ -h_{ii} \Phi_i^{*2} & -\mathcal{L}_i \end{pmatrix} \begin{pmatrix} u_i(\sigma) \\ v_i(\sigma) \end{pmatrix} = E_i(\sigma) \begin{pmatrix} u_i(\sigma) \\ v_i(\sigma) \end{pmatrix}. \quad (13)$$

Since the extension of the potential trap is large compared to the typical length scale of the system (e.g., the thermal de Broglie wavelength of the excitons), we can use the LDA. Then the excitons are treated as a locally homogeneous system and the spatial dependence enters only via the trap potential. In that case, the Bogoliubov equations are readily solved, yielding the density  $n_i^T \equiv \tilde{n}_{ii}$  of thermally excited excitons as

$$n_i^T(\mathbf{r}) = \int \frac{d^3 \mathbf{k}}{8\pi^3} \left[ \frac{L_i(\mathbf{k}, \mathbf{r})}{E_i(\mathbf{k}, \mathbf{r})} \left\{ n_B[E_i(\mathbf{k}, \mathbf{r})] + \frac{1}{2} \right\} - \frac{1}{2} \right] \times \Theta[E_i(\mathbf{k}, \mathbf{r})^2] \quad (14)$$

with  $n_B(E) = [\exp(E/k_B T) - 1]^{-1}$  being the usual Bose function. The excitation spectrum  $E_i$  is explicitly given by

$$E_i(\mathbf{k}, \mathbf{r}) = \sqrt{L_i(\mathbf{k}, \mathbf{r})^2 - [h_{ii} n_i^c(\mathbf{r})]^2}, \quad (15)$$

$$L_i(\mathbf{k}, \mathbf{r}) = \frac{\hbar^2 k^2}{2M_i} + V_i(\mathbf{r}) - \mu_i + 2h_{ii} n_i(\mathbf{r}) + \sum_{j \neq i} h_{ij} n_j(\mathbf{r}) \quad (16)$$

with  $n_i^c \equiv |\Phi_i|^2$  and  $n_i \equiv n_{ii} = n_i^T + n_i^c$ . In consistence with the LDA, we apply the Thomas-Fermi approximation to the Gross-Pitaevskii equation, neglecting the kinetic-energy term in Eq. (12). Then we obtain finally for the densities of the condensates

$$n_i^c(\mathbf{r}) = \frac{1}{h_{ii}} \left[ \mu_i - V_i(\mathbf{r}) - 2h_{ii} n_i^T(\mathbf{r}) - \sum_{j \neq i} h_{ij} n_j(\mathbf{r}) \right] \times \Theta \left[ \mu_i - V_i(\mathbf{r}) - 2h_{ii} n_i^T(\mathbf{r}) - \sum_{j \neq i} h_{ij} n_j(\mathbf{r}) \right]. \quad (17)$$

Expressions (14)–(17) have to be solved self-consistently. Although they look very similar to the one-component case, a coupling between the components appears via  $L_i$  and  $n_i^c$ .

In what follows we calculate the densities of excitons in  $\text{Cu}_2\text{O}$  in a strain induced potential trap.<sup>16</sup> In addition to the paraexcitons (labeled “p”), two spin projections of orthoexcitons are captured by the trap, denoted by “+” and “−,” while the zero component is expelled and plays no role. Thus, the number of components  $K=3$ . In addition to the usual symmetry of the interaction matrix,  $h_{ij} = h_{ji}$  with  $i, j = p, +, -$ , in our case it holds that  $h_{++} = h_{--}$  and  $h_{p+} = h_{p-}$ , leaving four independent parameters  $h_{pp}$ ,  $h_{++}$ ,  $h_{p+}$ , and  $h_{+-}$ . As extensive works on two-component systems<sup>7-9,12</sup> have shown, one of the most interesting aspects of multicomponent systems—the occurrence of phase separation—is closely tied to the proportions of interspecies and intraspecies interaction strengths.

According to Eq. (2), the interaction strengths are given by the  $s$ -wave scattering lengths of the corresponding channels, which can be obtained by the solution of the four-particle scattering problem. The case of positronium-positronium scattering some time ago received much attention<sup>17–19</sup> and quite reliable values of the scattering length for both the singlet and the triplet channel have been obtained. In contrast, the description of exciton-exciton interaction is a long-standing problem and so far no satisfying solution for the general case has been obtained. Especially for  $\text{Cu}_2\text{O}$ , we expect a strong effect of the nonparabolicity of the valence band<sup>20</sup> and of the rather large electron-hole exchange interaction<sup>21</sup> on the scattering lengths. Therefore, the values we deduced from the scattering lengths of the positronium problem given in Ref. 17 ( $h_{++}=0.71 h_{pp}$ ,  $h_{p+}=0.33 h_{pp}$ , and  $h_{+-}=1.77 h_{pp}$  with  $h_{pp}=7.5 \times 10^{-4} \mu\text{eV} \mu\text{m}^3$ ), should be considered as representative, only. Nevertheless, they allow to show the general behavior of the multicomponent exciton system. In the calculation we also neglect the difference in the paraexciton and orthoexciton mass due to the  $k$ -dependent exchange interaction.<sup>22</sup>

### III. LUMINESCENCE SPECTRUM

Excitons decay by emitting photons. This takes place either directly, whereby momentum conservation requires that only excitons with the same momentum as the emitted photons are involved, or with assistance of momentum supplying phonons such that all exciton states can participate in the optical emission. Because the optical wavelength of the emission is much smaller than the trapped exciton cloud, we apply a local approximation to the emission spectrum, which, for the homogeneous case, is determined by the excitonic spectral function  $A(\mathbf{k}, \omega)$ ,<sup>23,24</sup>

$$I_i(\mathbf{r}, \omega) \propto 2\pi |S_i(\mathbf{k}=0)|^2 \delta(\hbar\omega' - \mu_i) n_i^c(\mathbf{r}) + \sum_{\mathbf{k} \neq 0} |S_i(\mathbf{k})|^2 n_B(\hbar\omega' - \mu_i) A_i(\mathbf{r}, \mathbf{k}, \hbar\omega' - \mu_i) \quad (18)$$

with  $S_i(\mathbf{k})$  representing the exciton-photon coupling. The spectral function is given by the Bogoliubov amplitudes  $u_i$  and  $v_i$  and the quasiparticle spectrum in Eq. (15),

$$A_i(\mathbf{r}, \mathbf{k}, \omega) = 2\pi \hbar \{ u_i^2(\mathbf{k}, \mathbf{r}) \delta[\hbar\omega - E_i(\mathbf{k}, \mathbf{r})] - v_i^2(\mathbf{k}, \mathbf{r}) \delta[\hbar\omega + E_i(\mathbf{k}, \mathbf{r})] \}. \quad (19)$$

In order to account for a finite spectral resolution being important for comparison with measured spectra, we convolute the spectral intensity, Eq. (18), with a slit function of the shape  $\exp[-(\omega/\Delta)^4]$ . Here,  $\Delta$  is a measure for the spectral resolution. Furthermore, in a typical experimental situation, one images a small stripe of width  $2\Delta x$  elongated along the  $z$  direction onto the entrance slit of a spectrograph. Integrating over the  $y$  direction perpendicular to  $z$  we obtain the spatially resolved spectrum of the thermal excitons (in the following, the direct condensate contribution is not considered),

$$I_i(\omega, z) \propto \int_{-\Delta x}^{\Delta x} dx \int_{-\infty}^{\infty} dy \int d\mathbf{k} |S_i(\mathbf{k})|^2 u_i^2(\mathbf{k}, \mathbf{r}) \times n_B[E_i(\mathbf{k}, \mathbf{r})] \exp[-\varepsilon_-^4(\omega', \mathbf{k}, \mathbf{r})] - \int_{-\Delta x}^{\Delta x} dx \int_{-\infty}^{\infty} dy \int d\mathbf{k} |S_i(\mathbf{k})|^2 v_i^2(\mathbf{k}, \mathbf{r}) \times n_B[-E_i(\mathbf{k}, \mathbf{r})] \exp[-\varepsilon_+^4(\omega', \mathbf{k}, \mathbf{r})] \quad (20)$$

with  $\varepsilon_{\pm}(\omega', \mathbf{k}, \mathbf{r}) \equiv [\hbar\omega' - \mu \pm E(\mathbf{k}, \mathbf{r})]/\Delta$ .

In the case of phonon-assisted transitions (being relevant for the orthoexcitons), we have  $\omega' = \omega - E_{gX}/\hbar - \omega_{\text{phonon}}$  with  $E_{gX}$  being the excitonic band gap of the semiconductor. We assume  $S(\mathbf{k})$  to be a constant. Then the first term in Eq. (18) gives rise to a  $\delta$ -shaped luminescence line at the position of the chemical potential with a strength determined by the condensate density.

For trapped paraexcitons, the zero-phonon decay is relevant and can be treated by setting  $\omega' = \omega - E_{gX}/\hbar$  and  $S(\mathbf{k}) = S_0 \delta(\mathbf{k} - \mathbf{k}_0)$ . Here  $\mathbf{k}_0$  is the wave vector of the intersection of photon and exciton dispersion. Its modulus is given by  $k_0 = E_{gX} n / \hbar c$ , where  $n$  is the refraction index and  $c$  is the vacuum velocity of light. Due to the form of  $S(\mathbf{k})$ , the condensate itself does not contribute to the direct luminescence process.

However, as discussed for the one-component exciton gas in Ref. 6, in case of a potential trap there will be indirect signatures of the condensate in the spatially resolved luminescence spectrum. The spectral line shape follows the density distribution in the trap, which in turn is bordered by the minimal excitation energy  $E(\mathbf{k}=0, \mathbf{r})$ . For a noncondensed gas the latter quantity is roughly parabolic due to the trapping potential while it is zero in the presence of a condensate. Thus with increasing particle number (or decreasing temperature) the flat bottom of the spectrum of thermal excitons may be a footprint of Bose-Einstein condensation.

### IV. RESULTS

We evaluate the density distributions of the trapped excitons in an iterative way. In each step, we keep the distributions of two of the components fixed. Under the constraint of fixed particle number, we iterate the subset of Eqs. (14)–(17) belonging to the third component to self-consistency. We cycle through the components until self-consistency of the whole system, Eqs. (14)–(17), is achieved.

Depending on the temperature and particle numbers in the trap, there may occur six distinct situations, featuring a condensate of (i) none of the species, (ii) only the paraexcitons, (iii) only one species of orthoexcitons, (iv) both species of orthoexcitons, (v) paraexcitons and one species of orthoexcitons, and (vi) all species. To analyze these cases, we set the particle numbers of each component to one of two values:  $N_i = 5 \times 10^9$  or  $N_i = 5 \times 10^8$  for  $i = p, +, -$ , respectively. We get a rough estimate of the corresponding critical temperatures by applying a harmonic approximation to the Hertzian potentials. Then, a simple Thomas-Fermi calculation for the single-component case<sup>25</sup> yields  $T_c^0 \approx 2$  K for  $N = 5 \times 10^9$  and  $T_c^0 \approx 1$  K for  $N = 5 \times 10^8$ .

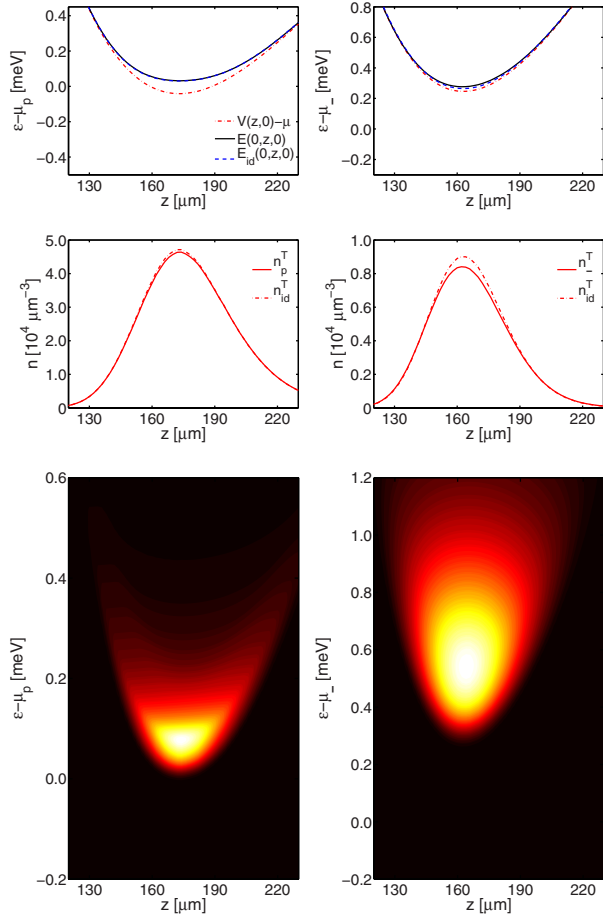


FIG. 1. (Color online) Potentials and density profiles in  $z$  direction at  $(x, y) = (0, 0)$ , and luminescence spectra for paraexcitons (left column) and ortho(-)excitons (right column) for a temperature of  $T = 2.2$  K and particle numbers of  $N_p = 5 \times 10^9$  and  $N_- = N_+ = 5 \times 10^8$  in the trap. The corresponding chemical potentials are  $\mu_p = -2260$   $\mu\text{eV}$  and  $\mu_- = \mu_+ = -5920$   $\mu\text{eV}$ . Upper row: external trap potential  $V_i$ , quasiparticle energy at  $\mathbf{k} = 0$  shifted by  $\mu$  (i.e., renormalized potential)  $E(0, z, 0)$ , and the same quantity without interspecies interaction  $E_{id}(0, z, 0)$ . Middle row: densities of thermal excitons with ( $n^T$ ) and without interspecies interaction ( $n_{id}^T$ ). Lower row: luminescence spectra.

For our calculations, we use values of  $\Delta = 41$   $\mu\text{eV}$  for the spectral resolution and  $\Delta x = 25$   $\mu\text{m}$  for the entrance slit of the spectrograph being typical for a triple high-resolution spectrograph used in the current experiments which are underway.<sup>26</sup> In the following figures we show the respective trap potentials  $V_i$ , minimal excitation energies  $E_i(\mathbf{k} = 0, z, \varrho = 0)$ , and density distributions of paraexcitons and orthoexcitons versus the  $z$  coordinate. We compare the results to the case without intercomponent interaction (labeled “id”).

We first investigate case (i) by setting  $N_p = 5 \times 10^9$ ,  $N_{\pm} = 5 \times 10^8$ , and a temperature  $T = 2.2$  K well above both of the estimated critical values. As Fig. 1 shows, in the absence of any condensate, the line shapes  $E_i(\mathbf{k} = 0, z, \varrho = 0)$  roughly follow the external potentials and the presence of multiple

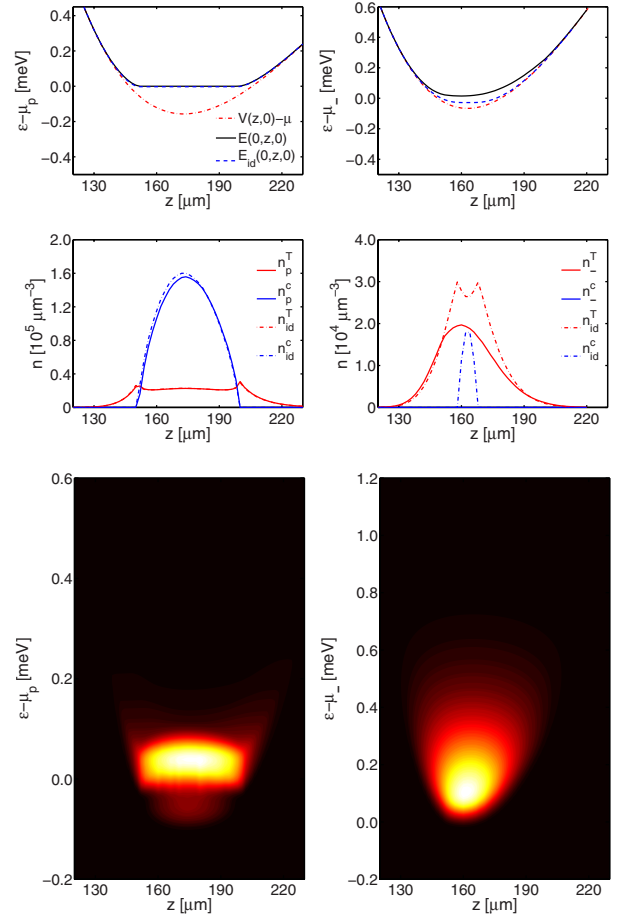


FIG. 2. (Color online) Same presentation as in Fig. 1 but for a temperature of  $T = 1.2$  K and particle numbers of  $N_p = 5 \times 10^9$  and  $N_- = N_+ = 5 \times 10^8$  in the trap. The chemical potentials are  $\mu_p = -2140$   $\mu\text{eV}$  and  $\mu_- = \mu_+ = -5610$   $\mu\text{eV}$ . In the middle row, additionally the densities of condensed excitons with ( $n^c$ ) and without interspecies interaction ( $n_{id}^c$ ) appear.

components causes only a weak additional renormalization. Both paraexciton and orthoexciton densities—the latter being equal for + and - species—concentrate in the centers of their traps. A noticeable redistribution of the orthoexcitons with respect to the one-component case results from the large number of paraexcitons as well as from the ortho-ortho interaction. The corresponding luminescence spectra of thermal excitons are shown in Fig. 1, lower row. Because the modulus of the photon vector  $|\mathbf{k}_0| \approx 30$   $\mu\text{m}^{-1}$  is rather small, the integrated zero-phonon spectrum of the paraexcitons almost directly resembles the minimal excitation energy  $E_p(\mathbf{k} = 0, z, \varrho = 0)$ . In the case of orthoexcitons, every  $\mathbf{k}$  vector contributes and we find a broad energy distribution above  $E_{\pm}(\mathbf{k} = 0, z, \varrho = 0)$ .

Keeping the particle numbers constant, we lower the temperature to  $T = 1.2$  K and show case (ii) in Fig. 2. Now the renormalized potential of the paraexcitons (Fig. 2, upper left panel) is cut at the chemical potential causing an almost flat bottom of the luminescence spectrum (Fig. 2, lower left panel). Again the densities of thermal and condensed paraexc-

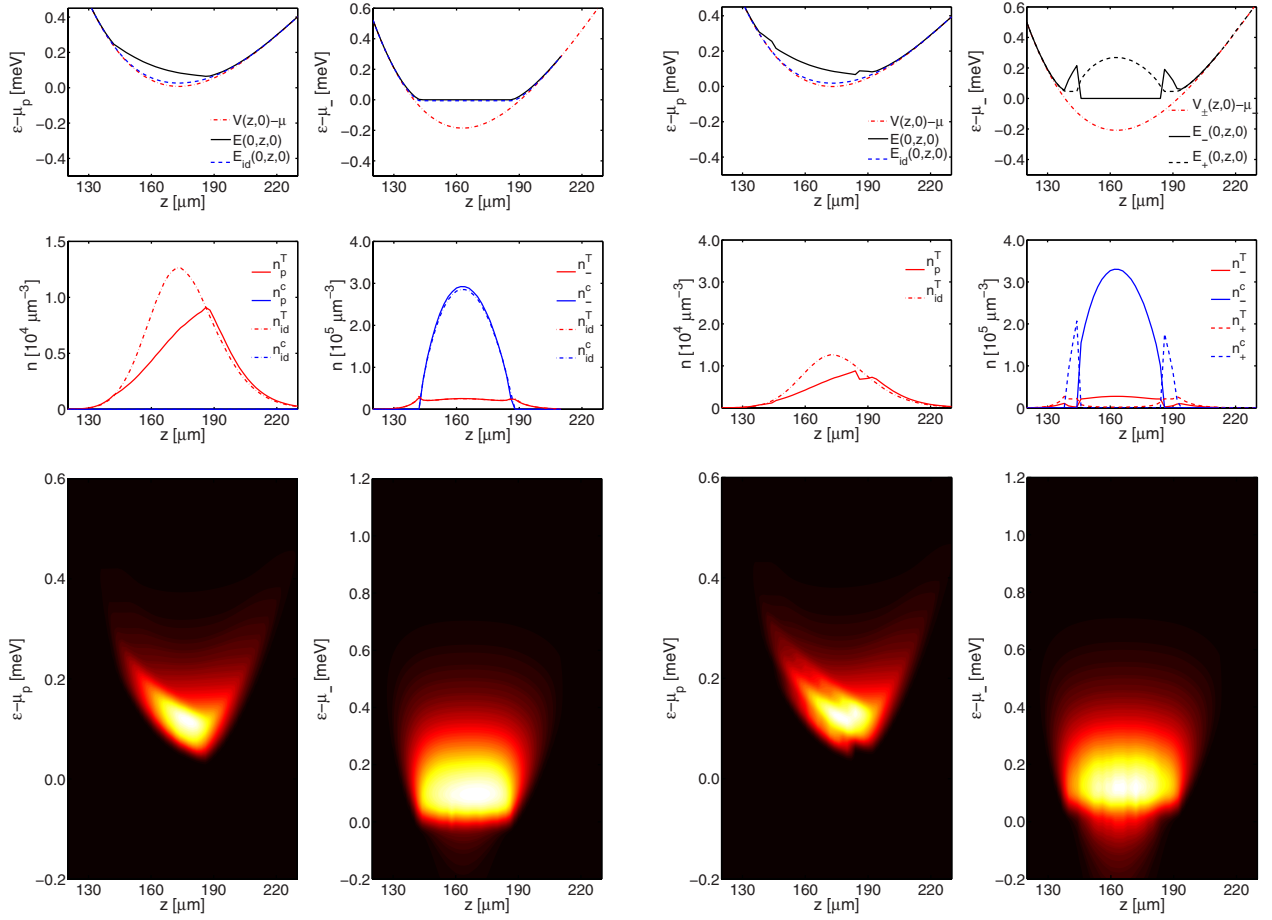


FIG. 3. (Color online) Same presentation as in Fig. 1 but for a temperature of  $T=1.2$  K and particle numbers of  $N_p=N_+=5 \times 10^8$  and  $N_-=5 \times 10^9$  in the trap. The chemical potentials are  $\mu_p=-2310 \mu\text{eV}$ ,  $\mu_+=-5550 \mu\text{eV}$ , and  $\mu_-=-5490 \mu\text{eV}$ .

citons show no significant deviation from the single component case (Fig. 2, middle left panel). In contrast, while isolated orthoexcitons would have been condensed, there is no orthocondensate in the fully interacting case, which shows that the presence of multiple repulsive components lowers the critical temperature. Due to the even higher concentration of paraexcitons and the different minimum positions of the external potentials ( $z_p=174 \mu\text{m}$  and  $z_{\pm}=164 \mu\text{m}$ ), the thermal orthoexcitons are slightly pushed aside (Fig. 2, middle right panel). Their spectrum (Fig. 2, lower right panel) is qualitatively nearly unchanged with respect to case (i). However, due to the lower temperature, the spectrum is less widespread. Furthermore, the chemical potential nearly touches the renormalized potential causing already a smoother curvature of the spectral shape.

If we exchange the particle numbers of paraexcitons and one species of orthoexcitons, i.e.,  $N_+=5 \times 10^9$ ,  $N_p=N_-=5 \times 10^8$ , we realize case (iii), which is presented in Fig. 3. While in this case the density distributions of thermal and condensed ortho(+)excitons deviate only weakly from the one-component case, the displacement of the thermal

FIG. 4. (Color online) Same presentation as in Fig. 1 but for a temperature of  $T=1.2$  K and particle numbers of  $N_p=5 \times 10^8$  and  $N_-=N_+=5 \times 10^9$  in the trap. The chemical potentials are  $\mu_p=-2300 \mu\text{eV}$ ,  $\mu_-=-5420 \mu\text{eV}$ , and  $\mu_+=-5470 \mu\text{eV}$ .

paraexcitons is expressed in a heavily distorted zero-phonon spectrum.

Increasing also the particle number of the remaining orthospecies by an order of magnitude, we generate case (iv), depicted in Fig. 4. As Shi *et al.*<sup>9</sup> showed, even for finite temperature the condition for phase separation of mutually interacting trapped condensates coincides with the  $T=0$  result of Ho and Shenoy:<sup>7</sup>  $h_{+-}^2 > h_{++}h_{--}$ . Due to their strong repulsion, the two orthocondensates fulfill this condition and separate into a ball-and-shell structure with finite overlap, as seen in Refs. 7 and 8. Yet, as found in Ref. 12, at  $T>0$  no pure + or - phases exist and the respective thermal particles are not entirely expelled. References 8 and 27 pointed out that in general the component with the weaker self-interaction forms the outer shell. In the case of orthoexcitons, this criterion does not apply and the labels + and - can be interchanged in all the results presented here. In principle, there should exist an unstable solution with equal distributions of the orthocondensates. The breaking of this symmetry is a consequence of our iterative numerical method. Because of the symmetry of the interaction, the paraexcitons react to the combined density of the orthoexciton species. That is

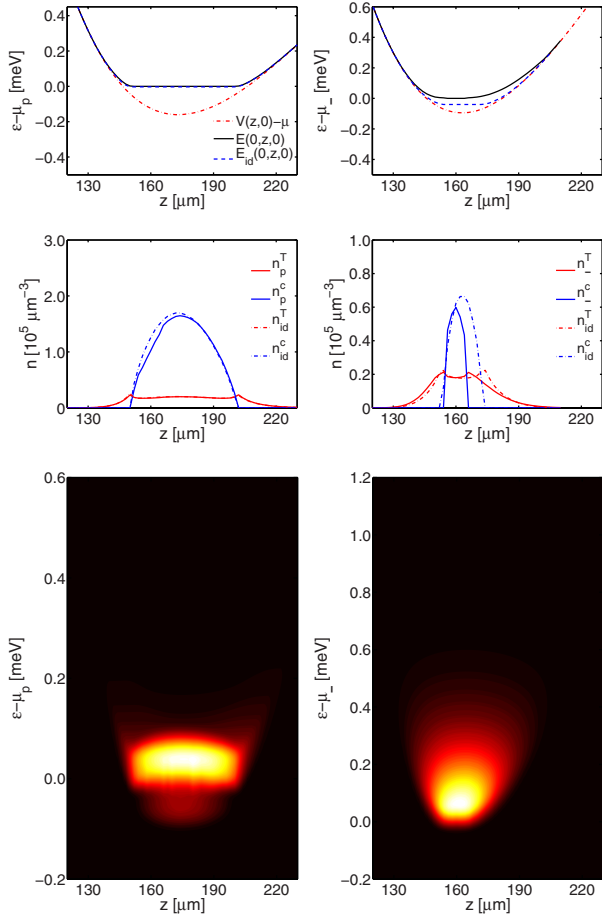


FIG. 5. (Color online) Same presentation as in Fig. 1 but for a temperature of  $T=1.05$  K and particle numbers of  $N_p=5 \times 10^9$  and  $N_-=N_+=5 \times 10^8$  in the trap. The chemical potentials are  $\mu_p=-2140 \mu\text{eV}$ ,  $\mu_-=-5585 \mu\text{eV}$ , and  $\mu_+=-5580 \mu\text{eV}$ .

why the distortion of the paraspectrum is strongest in the area of overlapping orthocondensates.

Let us switch back to the parameters of case (ii), i.e.,  $N_p=5 \times 10^9$  and  $N_+=N_-=5 \times 10^8$ , and lower the temperature to  $T=1.05$  K. As Fig. 5 shows, besides condensed paraexcitons we now find a small condensate of only one species of orthoexcitons [case (v)]. While in the single-component case, for  $N_+=N_-$ , both orthospecies have the same critical temperature, now the mutual repulsion prevents the simultaneous condensation of the second species. We have to lower the temperature to  $T=0.8$  K, to get condensates of all the components [case (vi), Fig. 6]. While the orthospecies again form a ball-and-shell structure, orthocondensate and paracondensate do not separate because of their weak interaction ( $h_{p+}^2 < h_{pp}h_{++}$ ).

## V. CONCLUSION AND OUTLOOK

We have presented a theoretical approach for the description of multicomponent interacting excitonic gases in potential traps. The resulting system of equations has been subject

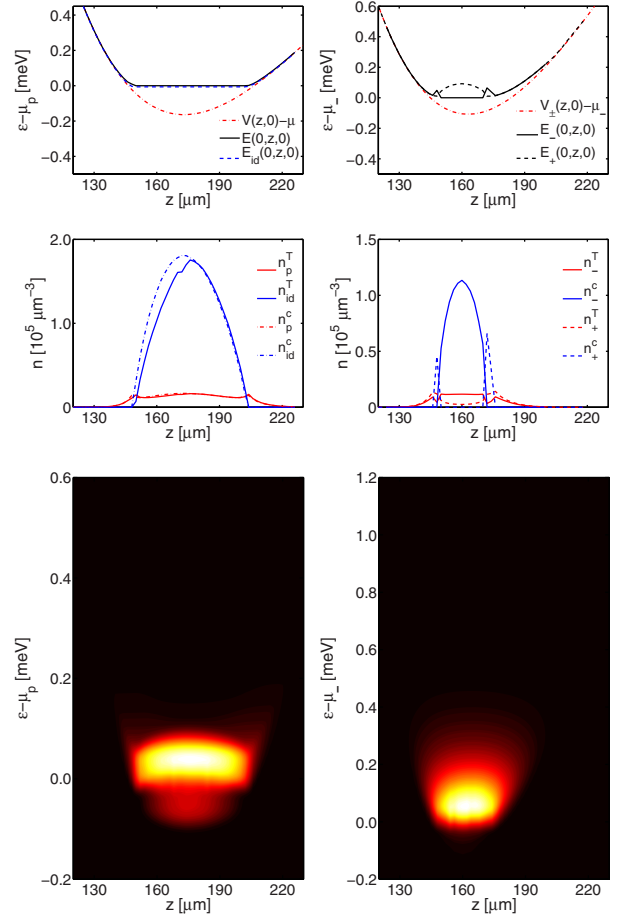


FIG. 6. (Color online) Upper and lower row: same presentation as in Fig. 1, middle row: density profiles and potentials for paraexcitons (left column) and both orthospecies (right column) for a temperature of  $T=0.8$  K and particle numbers of  $N_p=5 \times 10^9$  and  $N_-=N_+=5 \times 10^8$  in the trap. The chemical potentials are  $\mu_p=-2140 \mu\text{eV}$ ,  $\mu_-=-5560 \mu\text{eV}$ , and  $\mu_+=-5570 \mu\text{eV}$ .

to a number of approximations to make it numerically feasible. Finally, coupled multicomponent equations for the densities of thermal excitons in Hartree-Fock-Bogoliubov-Popov approximation and the condensate densities following from the Gross-Pitaevskii equation in Thomas-Fermi approximation have been obtained and numerically solved. Compared to previous calculations,<sup>6</sup> an experimentally realistic, anharmonic trap potential has been used. Six “typical” (but not necessarily experimentally realizable) situations leading to Bose-Einstein condensate in one or more of the species have been compared. The spatially resolved decay luminescence spectra of thermal paraexcitons and orthoexcitons exhibit clear signatures of a condensate. On the one hand, there is a flat bottom at the chemical potential known from the single-component case.<sup>6</sup> On the other hand, the interspecies interaction causes additional modifications of the spectra: if there is a condensate in one of the species, the spectrum of the respective other component is clearly distorted.

TABLE I. Summary of cases (i)–(vi): occurrence of a condensate in one or more species, of spatial separation between ortho(+) ( $o_+$ ) and ortho(–) ( $o_-$ ) excitons and of a deformation of the thermal paraexciton spectrum in dependence on temperature and particle numbers.

Case No.	Temperature (K)	$N_p/5 \times 10^9$	$N_+/5 \times 10^9$	$N_-/5 \times 10^9$	Condensate?	Orthoexciton separation?	Paraspectrum deformation?
(i)	2.2	1	0.1	0.1			
(ii)	1.2	1	0.1	0.1	$p$		
(iii)	1.2	0.1	0.1	1	$o_-$		√
(iv)	1.2	0.1	1	1	$o_+, o_-$	√	√
(v)	1.05	1	0.1	0.1	$p, o_-$		
(vi)	0.8	1	0.1	0.1	$p, o_+, o_-$	√	

In a typical experiment in the bulk or involving rather shallow potential traps, orthoexcitons are produced by laser excitation, but are converted fast into paraexcitons at a rate of  $0.3 \text{ ns}^{-1}$ .<sup>28,29</sup> Therefore, under quasiequilibrium conditions, the particle number ratio orthoexciton/paraexciton is small which corresponds to the cases (i), (ii), (v), and (vi). By increasing the stress, however, the conversion rate decreases by more than an order of magnitude.<sup>29</sup> By continuous excitation of orthoexcitons, therefore, it should be possible to obtain higher orthoexciton/paraexciton ratios like in cases (iii) and (iv). For an exciton number of  $5 \times 10^9$ , the density in the center of the trap is about  $10^{17} \text{ cm}^{-3}$  which is experimentally achievable. The same holds for the considered temperatures of  $T=0.8 \dots 2.2 \text{ K}$ .<sup>26</sup>

Table I summarizes the essential information obtained from the cases (i)–(vi) discussed above. Obviously, three conclusions can be drawn: first, if the temperature is low enough (below the respective critical temperature), every species can form a condensate. Its primary signature is a flat bottom of the respective spectrum. Second, a spatial separation occurs only between the condensates of the two orthospecies, because of their strong repulsion. It shows up only in the densities, not in the combined spectrum. There-

fore, it is important for future experiments to measure also the spectrally integrated density profile. Third, at occurrence of any orthocondensate but no paracondensate, the paraspectrum is distorted in a characteristic way indicating a condensate in at least one of the *other* species.

The presented theory is obviously only a first step toward a deeper understanding of the physics of trapped excitons. To go beyond that includes the solution of the Gross-Pitaevskii equation (without the Thomas-Fermi approximation) and the inclusion of anomalous densities already on the single-component level. Moreover, a general multicomponent theory requires the consideration of mixed averages which overcomes the effective single-component picture but complicates the Bogoliubov transformation remarkably.

#### ACKNOWLEDGMENTS

We would like to thank G. Manzke and F. Richter (Rostock), and A. Alvermann (Greifswald) for many fruitful discussions. This work was supported by the Deutsche Forschungsgemeinschaft via Collaborative Research Center SFB 652, projects B1 and B5.

<sup>1</sup>A. Griffin, *Phys. Rev. B* **53**, 9341 (1996).

<sup>2</sup>F. Dalfovo, S. Giorgini, L. P. Pitaevskii, and S. Stringari, *Rev. Mod. Phys.* **71**, 463 (1999).

<sup>3</sup>T. Bergeman, D. L. Feder, N. L. Balazs, and B. I. Schneider, *Phys. Rev. A* **61**, 063605 (2000).

<sup>4</sup>N. P. Proukakis and B. Jackson, *J. Phys. B* **41**, 203002 (2008).

<sup>5</sup>L. A. Bányai, A. M. Bundaru, and H. Haug, *Phys. Rev. B* **70**, 045201 (2004).

<sup>6</sup>H. Stolz and D. Semkat, *Phys. Rev. B* **81** 081302(R) (2010).

<sup>7</sup>T. L. Ho and V. B. Shenoy, *Phys. Rev. Lett.* **77**, 3276 (1996).

<sup>8</sup>E. P. Bashkin and A. V. Vagov, *Phys. Rev. B* **56**, 6207 (1997).

<sup>9</sup>H. Shi, W. M. Zheng, and S. T. Chui, *Phys. Rev. A* **61**, 063613 (2000).

<sup>10</sup>W. Zhang, S. Yi, and L. You, *Phys. Rev. A* **70**, 043611 (2004).

<sup>11</sup>M.-S. Chang, Q. Qin, W. Zhang, L. You, and M. S. Chapman, *Nat. Phys.* **1**, 111 (2005).

<sup>12</sup>B. Van Schaeybroeck, [arXiv:0901.3048](https://arxiv.org/abs/0901.3048) (unpublished).

<sup>13</sup>I. A. Shelykh, G. Malpuech, and A. V. Kavokin, *Phys. Status*

*Solidi A* **202**, 2614 (2005).

<sup>14</sup>J. Kasprzak, R. André, L. S. Dang, I. A. Shelykh, A. V. Kavokin, Yu. G. Rubo, K. V. Kavokin, and G. Malpuech, *Phys. Rev. B* **75**, 045326 (2007).

<sup>15</sup>S. Sobkowiak, Diploma thesis, Universität Rostock, 2010.

<sup>16</sup>D. W. Snoke and V. Negoita, *Phys. Rev. B* **61**, 2904 (2000).

<sup>17</sup>J. Shumway and D. M. Ceperley, *Phys. Rev. B* **63**, 165209 (2001).

<sup>18</sup>K. Oda, T. Miyakawa, H. Yabu, and T. Suzuki, *J. Phys. Soc. Jpn.* **70**, 1549 (2001).

<sup>19</sup>I. A. Ivanov, J. Mitroy, and K. Varga, *Phys. Rev. A* **65**, 022704 (2002).

<sup>20</sup>M. French, R. Schwartz, H. Stolz, and R. Redmer, *J. Phys.: Condens. Matter* **21**, 015502 (2009).

<sup>21</sup>G. Kuwabara, M. Tanaka, and H. Fukutani, *Solid State Commun.* **21**, 599 (1977).

<sup>22</sup>G. Dasbach, D. Fröhlich, R. Klieber, D. Suter, M. Bayer, and H. Stolz, *Phys. Rev. B* **70**, 045206 (2004).

SOBKOWIAK *et al.*

PHYSICAL REVIEW B **82**, 064505 (2010)

<sup>23</sup>H. Shi, G. Verechaka, and A. Griffin, *Phys. Rev. B* **50**, 1119 (1994).

<sup>24</sup>H. Haug and H. Kranz, *Z. Phys. B: Condens. Matter* **53**, 151 (1983).

<sup>25</sup>L. Pitaevskii and S. Stringari, *Bose-Einstein Condensation* (Ox-

ford University Press, New York, 2003).

<sup>26</sup>R. Schwartz, N. Naka, and H. Stolz (unpublished).

<sup>27</sup>P. Öhberg and S. Stenholm, *Phys. Rev. A* **57**, 1272 (1998).

<sup>28</sup>S. Denev and D. W. Snoke, *Phys. Rev. B* **65**, 085211 (2002).

<sup>29</sup>J. P. Wolfe and J. I. Jang, *Solid State Commun.* **134**, 143 (2005).



# Phase separation of multicomponent excitonic Bose-Einstein condensates

S. Sobkowiak<sup>\*1</sup>, D. Semkat<sup>1</sup>, H. Stolz<sup>1</sup>, Th. Koch<sup>2</sup>, and H. Fehske<sup>2</sup>

<sup>1</sup> Institut für Physik, Universität Rostock, 18051 Rostock, Germany

<sup>2</sup> Institut für Physik, Ernst-Moritz-Arndt-Universität Greifswald, 17489 Greifswald, Germany

Received 13 August 2010, accepted 30 September 2010

Published online 1 February 2011

**Keywords** excitons, Bose-Einstein condensation, cuprous oxide

\* Corresponding author: e-mail siegfried.sobkowiak@uni-rostock.de, Phone: +49-381-4986927, Fax: +49-381-4986922

For the observation of Bose-Einstein condensation, excitons in cuprous oxide are regarded as promising candidates due to their large binding energy and long lifetime. High particle densities may be achieved by entrapment in a stress induced potential. We consider a multicomponent gas of interacting para- and orthoexcitons in

cuprous oxide confined in a three-dimensional potential trap. Based on the Hartree-Fock-Bogoliubov theory, we calculate density profiles as well as decay luminescence spectra which exhibit signatures of the separation of the Bose-condensed phases.

© 2011 WILEY-VCH Verlag GmbH & Co. KGaA, Weinheim

**1 Introduction** The theoretical framework for trapped dilute interacting bosonic gases is well known from the theory of atomic condensates [1–4]. First applications to excitonic systems exist, as well [5]. Recent investigations in the framework of a mean-field formalism in local density approximation suggest distinct signatures of a condensate in the decay luminescence spectrum of the thermal excitons [6–8]. Works on two-component systems [9–12] have shown that the occurrence of phase separation is closely tied to the proportions of inter- and intra-species interaction strengths. Yet, the description of exciton-exciton interaction is a long-standing problem. Experimental results and theoretical predictions for the interaction strengths vary within an order of magnitude [13,5,14]. As an example, we present numerical results for the densities and the spatially resolved luminescence spectra of the three component system of excitons in cuprous oxide (Cu<sub>2</sub>O), i.e., para-, ortho(+)-, and ortho(–)excitons, trapped in a strain induced potential [15]. We show how spectral features may reveal phase separation, thereby yielding a minimum estimate of the relative strength of the mutual interactions.

## 2 Multicomponent exciton systems

**2.1 Thermodynamics** We consider a  $K$ -component exciton gas in second quantization, starting from the

Hamiltonian in the grand canonical ensemble:

$$\mathcal{H} = \sum_{i=1}^K \int d^3\mathbf{r} \psi_i^\dagger(\mathbf{r}, t) \left( -\frac{\hbar^2 \nabla^2}{2M_i} + V_i(\mathbf{r}) - \mu_i \right) \psi_i(\mathbf{r}, t) + \frac{1}{2} \sum_{i,j=1}^K \int d^3\mathbf{r} h_{ij} \psi_i^\dagger(\mathbf{r}, t) \psi_j^\dagger(\mathbf{r}, t) \psi_j(\mathbf{r}, t) \psi_i(\mathbf{r}, t), \quad (1)$$

where  $V_i$  represents the external (trap) potentials and  $\mu_i$  the chemical potentials. We assume a contact potential for the exciton-exciton interaction, with the intra- and inter-species interaction strengths  $h_{ij} = 2\pi\hbar^2 (M_i^{-1} + M_j^{-1}) a_{ij}^s$  given by the respective  $s$ -wave scattering lengths  $a_{ij}^s$ .

The Bose field operators  $\psi_i(\mathbf{r}, t)$  are decomposed in the usual fashion,  $\psi_i(\mathbf{r}, t) = \Phi_i(\mathbf{r}) + \tilde{\psi}_i(\mathbf{r}, t)$ , with the condensate wave functions  $\Phi_i(\mathbf{r}) = \langle \psi_i(\mathbf{r}, t) \rangle = \langle \psi_i(\mathbf{r}) \rangle$  and the operators of the thermal excitons  $\tilde{\psi}_i(\mathbf{r}, t)$ . The Heisenberg equations of motion  $i\hbar\partial_t \psi_i = [\psi_i, \mathcal{H}]$  result in  $2K$  coupled equations (arguments dropped for brevity): the Gross-Pitaevskii equations (GPE) for the condensates,

$$0 = \left( -\frac{\hbar^2 \nabla^2}{2M_i} + V_i - \mu_i + h_{ii}(n_{ii} + \tilde{n}_{ii}) + \sum_{j \neq i} h_{ij} n_{jj} \right) \Phi_i + h_{ii} \tilde{m}_{ii} \Phi_i^* + \sum_{j \neq i} h_{ij} \left( \tilde{n}_{ji} \Phi_j + \tilde{m}_{ji} \Phi_j^* \right), \quad (2)$$

© 2011 WILEY-VCH Verlag GmbH & Co. KGaA, Weinheim

and the equations of motion for the thermal excitons,

$$i\hbar \frac{\partial \tilde{\psi}_i}{\partial t} = \left( -\frac{\hbar^2 \nabla^2}{2M_i} + V_i - \mu_i + 2h_{ii}n_{ii} + \sum_{j \neq i} h_{ij}n_{jj} \right) \tilde{\psi}_i + h_{ii}m_{ii}\tilde{\psi}_i^\dagger + \sum_{j \neq i} h_{ij} \left( n_{ij}\tilde{\psi}_j + m_{ij}\tilde{\psi}_j^\dagger \right). \quad (3)$$

Here  $n_{ij} \equiv \Phi_j^* \Phi_i + \tilde{n}_{ij}$ ,  $m_{ij} \equiv \Phi_j \Phi_i + \tilde{m}_{ij}$ , with the averages  $\tilde{n}_{ij} = \langle \tilde{\psi}_i^\dagger \tilde{\psi}_j \rangle$  and  $\tilde{m}_{ij} = \langle \tilde{\psi}_i \tilde{\psi}_j \rangle$ . For simplicity, we neglect all non-diagonal averages, i.e., the last terms on the r.h.s of (2) and (3) and subsequently obtain effective one-component equations with mean field contributions from the respective other components. Because the extension of the potential trap is large compared to the thermal de-Broglie wavelength of the excitons, we apply a local density approximation to (3), setting  $\nabla^2 \rightarrow -|\mathbf{k}|^2$  with a wave vector  $\mathbf{k}$ . For the same reason, we apply the Thomas-Fermi approximation to the GPE, thus neglecting the kinetic energy term in (2). With the above simplifications, Eq. (3) is solved by a Bogoliubov transformation

$$\tilde{\psi}_i = \sum_{\mathbf{k}} \left[ u_i(\mathbf{k}) a_i(\mathbf{k}) e^{-iE_i(\mathbf{k})t/\hbar} + v_i^*(\mathbf{k}) a_i^\dagger(\mathbf{k}) e^{iE_i(\mathbf{k})t/\hbar} \right]. \quad (4)$$

The densities  $n_i^T \equiv \tilde{n}_{ii}$  of thermally excited excitons are given by

$$n_i^T(\mathbf{r}) = \int \frac{d^3\mathbf{k}}{8\pi^3} \left[ \frac{L_i(\mathbf{k}, \mathbf{r})}{E_i(\mathbf{k}, \mathbf{r})} \left( n_B(E_i(\mathbf{k}, \mathbf{r})) + \frac{1}{2} \right) - \frac{1}{2} \right] \times \Theta(E_i(\mathbf{k}, \mathbf{r})^2) \quad (5)$$

with  $n_B(E) = [\exp(E/k_B T) - 1]^{-1}$ . To guarantee gapless excitation spectra  $E_i$ , we neglect all anomalous averages  $\tilde{m}_{ii}$  (Popov approximation) and obtain

$$E_i(\mathbf{k}, \mathbf{r}) = \sqrt{L_i(\mathbf{k}, \mathbf{r})^2 - (h_{ii}n_i^c(\mathbf{r}))^2}, \quad (6)$$

$$L_i(\mathbf{k}, \mathbf{r}) = \frac{\hbar^2 k^2}{2M_i} + V_i(\mathbf{r}) - \mu_i + 2h_{ii}n_i(\mathbf{r}) + \sum_{j \neq i} h_{ij}n_j(\mathbf{r}), \quad (7)$$

with  $n_i^c \equiv |\Phi_i|^2$  and  $n_i \equiv n_{ii} = n_i^T + n_i^c$ .

From the simplified GPEs, the condensate densities follow as

$$n_i^c(\mathbf{r}) = \frac{1}{h_{ii}} \left( \mu_i - V_i(\mathbf{r}) - 2h_{ii}n_i^T(\mathbf{r}) - \sum_{j \neq i} h_{ij}n_j(\mathbf{r}) \right), \quad (8)$$

if this expression is non-negative, and  $n_i^c(\mathbf{r}) = 0$  otherwise. Equations (5) to (8) have to be solved self-consistently. Although they look similar to the one-component case, the coupling between the components appears in  $L_i$  and  $n_i^c$ .

**2.2 Luminescence spectrum** Excitons decay by emitting photons. We apply a local approximation to the

emission spectrum, which is determined by the excitonic spectral function  $A(\mathbf{k}, \omega)$  [16, 17]:

$$I_i(\mathbf{r}, \omega) \propto 2\pi |S_i(\mathbf{k} = 0)|^2 \delta(\hbar\omega' - \mu_i) n_i^c(\mathbf{r}) + \sum_{\mathbf{k} \neq 0} |S_i(\mathbf{k})|^2 n_B(\hbar\omega' - \mu_i) A_i(\mathbf{r}, \mathbf{k}, \hbar\omega' - \mu_i), \quad (9)$$

with the exciton-photon coupling  $S_i(\mathbf{k})$ . The spectral function is given by the Bogoliubov amplitudes  $u_i$  and  $v_i$ , and by the quasiparticle spectrum in (6):

$$A_i(\mathbf{r}, \mathbf{k}, \omega) = 2\pi\hbar \left[ u_i^2(\mathbf{k}, \mathbf{r}) \delta(\hbar\omega - E_i(\mathbf{k}, \mathbf{r})) - v_i^2(\mathbf{k}, \mathbf{r}) \delta(\hbar\omega + E_i(\mathbf{k}, \mathbf{r})) \right]. \quad (10)$$

In  $\text{Cu}_2\text{O}$ , the decay of orthoexcitons takes place via momentum supplying phonons, such that all exciton states  $\mathbf{k}$  participate and  $\omega' = \omega - E_{gX}/\hbar - \omega_{\text{phonon}}$ , with  $E_{gX}$  being the excitonic band gap. The paraexcitons decay without phonons, i.e.,  $\omega' = \omega - E_{gX}/\hbar$ . Here, energy and momentum conservation only allow for processes, where the wave vectors of excitons and photons are equal, so that  $S(\mathbf{k}) = S_0 \delta(\mathbf{k} - \mathbf{k}_0)$ , with  $|\mathbf{k}_0| = E_{gX} n / \hbar c$ . Therefore, the condensate does not contribute to the zero-phonon process. Despite this, there are indirect signatures of the condensate in the spatially resolved luminescence spectrum of the non-condensed excitons [6].

In a typical experiment, one images a small stripe of width  $2\Delta x$  elongated along the  $z$ -direction onto the entrance slit of a spectrograph. Thus, by integrating (9) over the  $x$ - and  $y$ -directions perpendicular to  $z$ , we obtain the spatially resolved spectrum. Moreover, we account for the finite spectral resolution  $\Delta$  by convoluting the spectral intensity with a slit function of the shape  $\exp\{-(\omega/\Delta)^2\}$ . For our calculations, we use values of  $\Delta = 25 \mu\text{eV}$  for the spectral resolution and  $\Delta x = 25 \mu\text{m}$  for the entrance slit of the spectrograph being typical for a triple high-resolution spectrograph used in the current experiments which are underway [18].

**3 Results** We calculated the density distributions and the luminescence spectra of the trapped excitons for three different choices of the interaction strength between ortho(+)- and ortho(-)excitons ( $h_{+-}$ ). The interaction strengths are calculated from the scattering lengths given in [13] ( $h_{++} = h_{--} = 0.71h_{pp}$ ,  $h_{p+} = h_{p-} = 0.33h_{pp}$ , and  $h_{+-} = 1.77h_{pp}$  with  $h_{pp} = 5.4 \times 10^{-4} \mu\text{eV}\mu\text{m}^3$ ). Taking the value for  $h_{+-}$  given by Shumway and Ceperley [13] as  $h_{SC}$  we chose: (i)  $h_{+-} = h_{SC}/5$ ; (ii)  $h_{+-} = h_{SC}/3$ ; and (iii)  $h_{+-} = h_{SC}$  while keeping the others fixed. The used trap potentials  $V_i$  are fitted to experimental data taken from [18]. The minimum of the paraexciton trap is  $-1981 \mu\text{eV}$  and the minimum of the orthoexciton trap is  $-8158 \mu\text{eV}$ . Note that we neglect the difference in paraexciton and orthoexciton mass due to the  $\mathbf{k}$ -dependent exchange interaction [19].

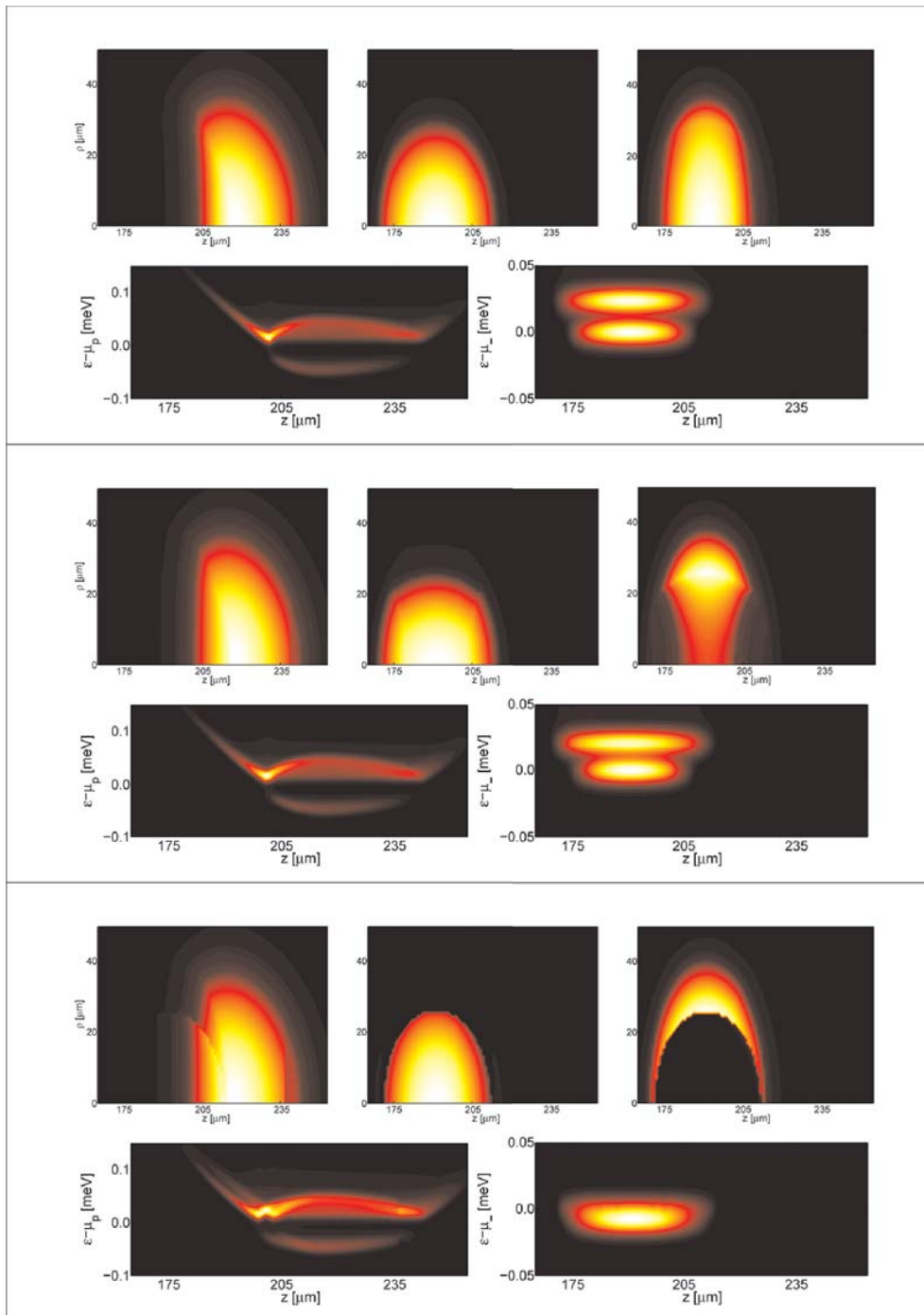


**Figure 1** Three different subsets of exciton densities and luminescence spectra for para-, ortho(+)- and ortho(-)excitons for  $T = 0.7$  K and a total particle number of  $N_p = 10^{10}$  paraexcitons and  $N_- = N_+ = 10^{10}$  orthoexcitons in the trap. Each subset contains 5 images with the exciton densities in the first row (from left to right para-, ortho(+)- and ortho(-)excitons) and the spectra for the para- (left) and orthoexcitons (right) in the second row. Taking  $h_{+-}$  given by Shumway and Ceperley [13] as  $h_{SC}$  the subsets represent from top to bottom: (i)  $h_{+-} = h_{SC}/5$ ; (ii)  $h_{+-} = h_{SC}/3$ ; and (iii)  $h_{+-} = h_{SC}$  while taking all other interaction strengths as given in [13].

The results of the numerical calculations are shown in Fig. 1. The densities are visualized as contour plots including thermal and condensed excitons using cylindrical coordinates  $(\rho, z)$ . The densities are independent of  $\varphi$  due to the trap geometry. The thermal excitons form the darker rim of the bright condensate spots. The second rows show the luminescence spectrum of the paraexcitons and the combined spectrum of the orthoexcitons. The latter contains the condensate signals, i.e., the first term on the r.h.s of (9), assuming  $S(\mathbf{k})$  is a  $\mathbf{k}$ -independent constant.

At a temperature of  $T = 0.7$  K, all three exciton species show Bose–Einstein condensation. The condition for phase separation of the orthoexcitons is approximately  $h_{+-}^2 > h_{++}h_{--}$  [9] and becomes in the considered system  $h_{+-} > h_{++}$  since  $h_{+-} = h_{--}$ . In case (i) where  $h_{+-}$  is considerably smaller than  $h_{++}$  the ortho-condensates are nearly completely mixed. Due to the different minimum positions of the respective external potentials, the thermal paraexcitons are pushed aside by the combined orthoexciton densities. The spectrum of the orthoexcitons is dominated by two condensate peaks at the chemical potentials  $\mu_- = -8013$   $\mu\text{eV}$  and  $\mu_+ = -7990$   $\mu\text{eV}$ . In case of the paraexcitons, only the zero-phonon spectral line contributes. It reveals the existence of a condensate via the flat bottom at  $\varepsilon - \mu_p = 0$  [6–8].

Increasing  $h_{+-}$  to  $h_{SC}/3$  yields the results shown in case (ii). Here  $h_{+-}$  is slightly smaller than  $h_{++}$  and the condensates are still mixed in a wide area. However, a starting of the separation can be observed. Nevertheless, the spectra for the para- and orthoexcitons as well as the paraexciton density are not changed qualitatively with respect to case (i).

In case (iii) the condition for phase separation,  $h_{+-} > h_{++}$ , is fulfilled and the ortho-condensates form a ball-and-shell structure with finite overlap. Incidentally, the difference in their chemical potentials is smaller than the spectral resolution so that the combined ortho-spectrum gives no evidence of the phase separation. However, in the region of overlapping ortho-condensates we find a noticeable depletion of paraexcitons, which results in a W-shaped distortion of the para-spectrum when compared to case (i) or (ii).

When the interaction strength  $h_{+-}$  is further increased, no qualitative changes with respect to case (iii) are found. For  $T > 0$  there are no pure (+) or (–) phases [12] and the spectral features described in case (iii) remain.

**4 Conclusion and outlook** Our simulations for the experimentally relevant example cuprous oxide have shown that at finite temperatures a possible phase separation of excitonic condensates may not be reflected in their combined luminescence spectrum. However, in the case of cuprous oxide, the single spectral line of the direct paraexciton decay may constitute a rather sensitive probe for the spatial structure of the orthoexciton density distribution. Specific distortions in the paraexciton spec-

trum would provide an experimental footprint of a phase separation of orthoexciton condensates. If detected, the interaction strength of the (+) and (–) species would satisfy the relation  $h_{+-} > h_{++}$ .

Omitting the Thomas–Fermi approximation or one of the other approximations used, might lead to results that quantitatively differ from the ones presented here. However, the above conclusions are mainly based on the existence of a finite overlap of separated condensates and should remain valid even if the spectra and densities are calculated beyond the used approximations. Also the calculations for the luminescence spectrum could be enhanced using more advanced approaches [20]. Further research is required to address these issues.

**Acknowledgements** We would like to thank G. Manzke and W.-D. Kraeft (Rostock), and A. Alvermann (Cambridge) for many fruitful discussions. This work was supported by the Deutsche Forschungsgemeinschaft via Collaborative Research Center SFB 652, projects B1 and B5.

## References

- [1] A. Griffin, Phys. Rev. B **53**, 9341 (1996).
- [2] F. Dalfovo, S. Giorgini, L. P. Pitaevskii, and S. Stringari, Rev. Mod. Phys. **71**, 463 (1999).
- [3] T. Bergeman, D. L. Feder, N. L. Balazs, and B. I. Schneider, Phys. Rev. A **61**, 063605 (2000).
- [4] N. P. Proukakis and B. Jackson, J. Phys. B **41**, 203002 (2008).
- [5] L. A. Bányai, A. M. Bundaru, and H. Haug, Phys. Rev. B **70**, 045201 (2004).
- [6] H. Stolz and D. Semkat, Phys. Rev. B **81** 081302(R) (2010).
- [7] S. Sobkowiak, D. Semkat, H. Stolz, Th. Koch, and H. Fehske, Phys. Rev. B **82**, 064505 (2010).
- [8] S. Sobkowiak, Diploma thesis, Universität Rostock, 2010 (unpublished).
- [9] T. Ho and V. B. Shenoy, Phys. Rev. Lett. **77**, 3276 (1996).
- [10] E. P. Bashkin and A. V. Vagov, Phys. Rev. B **56**, 6207 (1997).
- [11] H. Shi, W. Zheng and S. Chui, Phys. Rev. A **61**, 063613 (2000).
- [12] B. Van Schaeybroeck, arXiv:0901.3048v1.
- [13] J. Shumway and D. M. Ceperley, Phys. Rev. B **63**, 165209 (2001).
- [14] J. Brandt, D. Fröhlich, Ch. Sandfort, M. Bayer, H. Stolz, and N. Naka, Phys. Rev. Lett. **99**, 217403 (2007).
- [15] D. W. Snoke and V. Negoita, Phys. Rev. B **61**, 2904 (2000).
- [16] H. Shi, G. Verechaka, and A. Griffin, Phys. Rev. B **50**, 1119 (1994).
- [17] H. Haug and H. Kranz, Z. Phys. B **53**, 151 (1983).
- [18] R. Schwartz, N. Naka, and H. Stolz, submitted to NJP.
- [19] G. Dasbach, D. Fröhlich, R. Klieber, D. Suter, M. Bayer, and H. Stolz, Phys. Rev. B **70**, 045206 (2004).
- [20] F. Richter, M. Florian, and K. Henneberger, Phys. Rev. B **78**, 205114 (2008).

## Condensation of excitons in $\text{Cu}_2\text{O}$ at ultracold temperatures: experiment and theory

Heinrich Stolz<sup>1,5</sup>, Rico Schwartz<sup>1</sup>, Frank Kieseling<sup>1</sup>,  
Sunipa Som<sup>1</sup>, Maria Kaupsch<sup>1</sup>, Siegfried Sobkowiak<sup>1</sup>,  
Dirk Semkat<sup>1</sup>, Nobuko Naka<sup>2,3</sup>, Thomas Koch<sup>4</sup>  
and Holger Fehske<sup>4</sup>

<sup>1</sup> Institut für Physik, Universität Rostock, D-18051 Rostock, Germany

<sup>2</sup> Department of Physics, Kyoto University, Kyoto 606-8502, Japan

<sup>3</sup> PRESTO, JST, 4-1-8 Honcho Kawaguchi, Saitama 332-0012, Japan

<sup>4</sup> Institut für Physik, Ernst-Moritz-Arndt-Universität Greifswald,  
D-17487 Greifswald, Germany

E-mail: [heinrich.stolz@uni-rostock.de](mailto:heinrich.stolz@uni-rostock.de)

*New Journal of Physics* **14** (2012) 105007 (37pp)

Received 18 May 2012

Published 10 October 2012

Online at <http://www.njp.org/>

doi:10.1088/1367-2630/14/10/105007

**Abstract.** We present experiments on the luminescence of excitons confined in a potential trap at milli-Kelvin bath temperatures under continuous-wave (cw) excitation. They reveal several distinct features like a kink in the dependence of the total integrated luminescence intensity on excitation laser power and a bimodal distribution of the spatially resolved luminescence. Furthermore, we discuss the present state of the theoretical description of Bose–Einstein condensation of excitons with respect to signatures of a condensate in the luminescence. The comparison of the experimental data with theoretical results with respect to the spatially resolved as well as the integrated luminescence intensity shows the necessity of taking into account a Bose–Einstein condensed excitonic phase in order to understand the behaviour of the trapped excitons.

<sup>5</sup> Author to whom any correspondence should be addressed.



Content from this work may be used under the terms of the [Creative Commons Attribution-NonCommercial-ShareAlike 3.0 licence](https://creativecommons.org/licenses/by-nc-sa/3.0/). Any further distribution of this work must maintain attribution to the author(s) and the title of the work, journal citation and DOI.

**Contents**

<b>1. Introduction</b>	<b>2</b>
<b>2. Experiment</b>	<b>4</b>
2.1. Experimental setup . . . . .	4
2.2. Application of the rate model to cw-excitation . . . . .	6
2.3. Experimental results . . . . .	8
<b>3. Theory</b>	<b>20</b>
3.1. Thermodynamics of trapped excitons . . . . .	20
3.2. Theory of decay luminescence . . . . .	21
3.3. Results . . . . .	22
3.4. Discussion . . . . .	25
3.5. Excitons in local equilibrium . . . . .	27
<b>4. Conclusions and outlook</b>	<b>29</b>
<b>Acknowledgments</b>	<b>31</b>
<b>Appendix A. Strain Hamiltonian for electron–hole states</b>	<b>31</b>
<b>Appendix B. Exciton relaxation</b>	<b>32</b>
<b>Appendix C. Thermal behaviour of the dilution refrigerator and the sample</b>	<b>32</b>
<b>References</b>	<b>36</b>

**1. Introduction**

Almost 50 years ago, excitons [1, 2] were identified as particularly interesting candidates for Bose–Einstein condensation (BEC), as they consist of an electron and a hole in a semiconductor, both fermions bound to form a bosonic excitation and thus resembling most closely neutral atoms of usual matter. Due to their rather small mass comparable to the free electron mass, it was speculated that for exciton densities of the order of  $10^{18} \text{ cm}^{-3}$ —easily achievable by absorption of photons—critical temperatures of some 10 K may be reached.

Due to their unique properties, the excitons of the so-called yellow series in the semiconductor cuprous oxide ( $\text{Cu}_2\text{O}$ ) are still considered the most promising candidates for excitonic BEC [3–5]. This is related to the large binding energy of 150 meV, which shifts the Mott density to  $3 \times 10^{18} \text{ cm}^{-3}$  at cryogenic temperatures [6, 7]. Made up from doubly degenerate valence and conduction bands, the ground state of this series splits into the triply degenerate orthoexciton and the non-degenerate paraexciton, which is the energetically lowest exciton state, lying  $\Delta = 12.1 \text{ meV}$  below the orthoexciton states. Due to the positive parity of the bands, the orthoexciton is only weakly optically allowed (quadrupole transition with oscillator strength  $3 \times 10^{-9}$  [8]), while the paraexciton as a pure triplet state with respect to the electron and hole spins [9] is optically forbidden in all orders. Its decay is only possible via an odd parity optical phonon resulting in a long lifetime in the microsecond range during which thermodynamic quasi-equilibrium may be reached.

As in all physical systems for which BEC has been demonstrated up to now, excitons should be confined in a potential trap. This has the advantage that (i) the diffusion process, which reduces the exciton density, is suppressed and (ii) the critical number of particles required

for the phase transition decreases much faster with temperature than in free space. The critical particle number is given by

$$N_{\text{crit}} = \zeta(3) \left( \frac{k_{\text{B}}T}{\hbar\Omega_0} \right)^3, \quad (1)$$

where  $\Omega_0$  is the average oscillator frequency of the trapping potential and  $\zeta$  denotes the Riemann Zeta function [10].

Despite the promising properties mentioned above, all previous studies to create a dense gas of excitons in  $\text{Cu}_2\text{O}$  either in a bulk crystal or in a potential trap did not demonstrate conclusively excitonic BEC [4, 11–15]. The main reason for this failure turned out to be the existence of a very efficient exciton–exciton annihilation process that sets in at high exciton densities and whose rate scales with the square of the exciton density  $n$

$$\frac{dn}{dt} = -an^2. \quad (2)$$

Due to the rather large value of  $a$  of the order of  $10^{-16} \text{ cm}^3 \text{ ns}^{-1}$ , this process was believed to prevent the formation of a BEC of paraexcitons.

However, in recent experiments using pulsed excitation, we have found in agreement with earlier studies [16] that this process can be damped in shallow potential traps by almost two orders of magnitude [17]. While this allowed the accumulation of large exciton numbers, the temperatures in these experiments were still too high to undercut the critical temperature for BEC, which was predicted to require a bath temperature as low as 100 mK at experimental conditions. Furthermore, the high pulse energies needed to create sufficient exciton numbers resulted in a substantial heating of the exciton gas during the laser pulse. Our strategy to overcome these problems was twofold: firstly, we reduced the temperature of the He bath as much as possible by preventing thermal radiation from the surroundings to reach the sample. In this way we reached a minimum temperature of 35 mK for zero incident laser power, which increases at laser powers of about 1 mW to 250 mK within 1 h. Secondly, we switched over to cw-excitation, for which the possibility of creating large paraexciton numbers has been demonstrated recently [18]. By reducing the thermal load, we were able to get to effective exciton temperatures as low as 200 mK at low excitation power. The main advantage of cw-excitation, however, is the possibility of achieving a quasi-equilibrium situation in which the decay rate of excitons is cancelled by the formation and relaxation rate of the species in the trap. This allows us to drive the system through the various possibly existing phases by simply changing the excitation power of the driving laser, as was exemplified by the condensation experiments of exciton polaritons in semiconductor microcavities (for a review, see [19]). In contrast to polariton systems, the lifetime broadening for paraexcitons is extremely small due to their long lifetime of the order of  $\mu\text{s}$ . Therefore, we can neglect any damping effects due to the excitonic decay in the spectra [20, 21].

The paper is organized as follows. In section 2, we briefly sketch the experimental setup and present a typical set of experimental results which reflect a variety of experimental conditions obtained by changing the bath temperature and the excitation conditions. We concentrate in particular on the spatial profiles of the luminescence intensity and on the totally integrated intensity dependent on the excitation power. These results are analysed theoretically in section 3 by calculating the excitonic luminescence of an interacting Bose gas on a mean field level. Thereby, we start with the usual assumption of global equilibrium and then extend the theory to the case of excitons in local thermodynamic equilibrium. Finally, we compare the theoretical

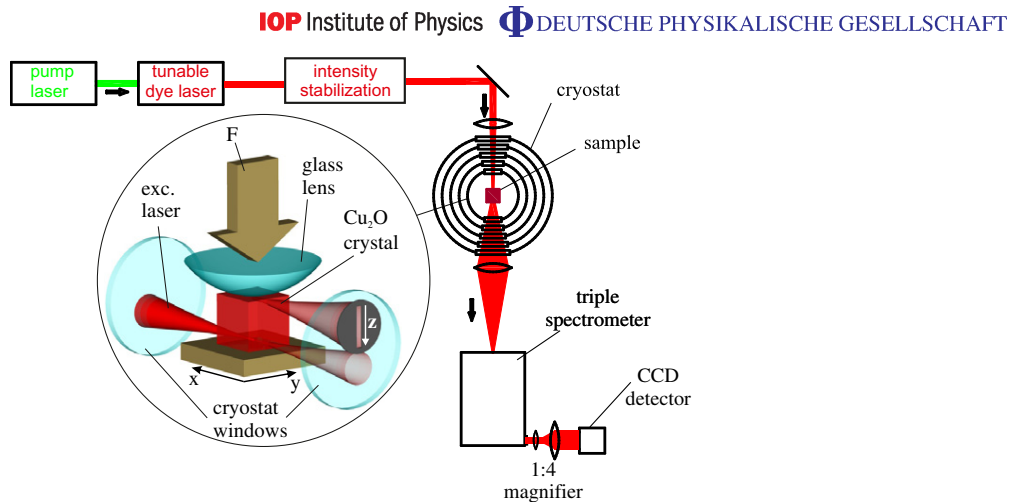


**Figure 1.** Main features of the experimental setup. Excitons are created by a dye laser propagating along the  $x$ -direction normal to the strain axis ( $z$ -direction). The laser was focused either directly into the trap or onto a spot close to the trap. In the latter case the excitons diffuse towards the trap due to the gradient force initiated by the potential trap. The emission out of the trap is monitored by spatially resolving along the  $y$ - and  $z$ -directions, while integrating along the  $x$ -direction.

results with the measurements and show that there is excellent qualitative agreement if we take into account the occurrence of a Bose–Einstein condensate of excitons. Section 4 gives our conclusions and an outlook to further experiments.

## 2. Experiment

### 2.1. Experimental setup

For the studies at subkelvin temperatures, we used the same experimental setup as reported previously [17], but implemented a narrow-band tunable dye laser (Coherent CR599, laser dye Rhodamin 6G) pumped by a 5 W green solid state laser (Verdi 5), see figure 1. The laser power was stabilized by a closed feedback loop to within 1%, the laser frequency and line width ( $<0.5$  GHz) were measured with a wavemeter (High Finesse WS7, resolution 60 MHz). In order to enhance both the spectral and spatial resolutions, we employed a fourfold magnification optical imaging system between the spectrometer exit slit and the detector.

For the experiments we used natural cuprous oxide crystals originally found in Namibia in the form of millimetre sized cubic specimens with well defined facets (see [18] for details). The quality of these samples was checked according to a low defect density, leading to long paraexciton lifetimes up to  $1 \mu\text{s}$ . For such samples, previous high resolution absorption measurements in a magnetic field revealed a paraexciton line width as narrow as 80 neV, demonstrating their extreme high quality [22].

The potential trap for the confinement of the exciton gas was made by the well-known Hertzian stress technique [11, 14, 23, 24], where a spherical stressor made of glass (radius 7.75 mm) is pressed with a force  $F$  against a flat surface of the crystal along a direction which we denote as the  $z$ -direction (figure 1). As a result, a confining potential is generated in



**Table 1.** Parameters for the trapping potential and rate model.

Parameter	Value
Potential curvature $\alpha_{\parallel}$	$0.1334 \mu\text{eV } \mu\text{m}^{-2}$
Potential curvature $\alpha_{\perp}$	$0.0733 \mu\text{eV } \mu\text{m}^{-2}$
Lifetime of paraexcitons	650 ns
Ortho–para conversion rate	$0.2 \text{ ns}^{-1\text{a}}$
Two-body decay rate $A_{\text{PP}}$	$2 \times 10^{-18} \text{ cm}^3 \text{ ns}^{-1\text{b}}$
Two-body decay rate $A_{\text{OO}}$	$4.9 \times 10^{-17} \text{ cm}^3 \text{ ns}^{-1}$
Relaxation rate $\Gamma_{\text{rel}}$	$6 \times 10^7 \text{ s}^{-1}$
Potential trap minimum $V_0$	1.35 meV

<sup>a</sup> Taken from [16].

<sup>b</sup> Due to the lower strain, the two-body decay rate  $A_{\text{PP}}$  is reduced by a factor of two compared to [17].

which the energies of ortho- and paraexcitons are lowered compared to the bulk. This potential  $V_{\text{ext}}(x, y, z)$  can be calculated from the known strain parameters of the yellow exciton states (for a recent calculation with refined parameters see [18]). To achieve agreement between the calculated potential profiles and the experimentally measured low energy border lines of the spatio-spectral images, we had to use a stressor radius 50% larger than the nominal one [17]. For a simple description, we decompose the potential trap and give in table 1 the parameters of the harmonic oscillator potential along  $z$ ,  $V(z) = \alpha_{\parallel}(z - z_0)^2 - V_0$ , and of the two-dimensional harmonic oscillator normal to  $z$  in the  $xy$  plane,  $V(x, y) = \alpha_{\perp}(x^2 + y^2)$ .

As the resonant creation process of the excitons we used the indirect absorption process involving an odd parity optical  $\Gamma_3^-$ -phonon into the orthoexcitons in the trap (see inset in figure 2). These orthoexcitons quickly transformed into paraexcitons. The laser beam was positioned about  $100 \mu\text{m}$  away from the trap centre in the positive  $z$ -direction, i.e. away from the stressor lens. In order to confine the primarily created orthoexcitons in the trap and to avoid any excitation outside the trap, which may lead to losses of the excitons, we tuned the energy of the laser photons to slightly ( $\approx 0.5 \text{ meV}$ ) below the onset of the phonon sideband in the bulk (at  $2048.56 \text{ meV}$ ). Through this process, about half of the incoming photons are transformed into excitons.

To detect the primarily excited orthoexcitons for the calibration of the number of excited excitons, we have chosen the  $\mathbf{k}$ -vector of the excitation beam along the direction of observation.

In the experimental setup (figure 1), the emitted light was imaged onto the entrance slit of a high resolution triple spectrograph (T64000, Jobin Yvon) usable either in subtractive or additive mode with a diffraction-limited spatial resolution of the order of  $10 \mu\text{m}$ . The astigmatism of the spectrograph was corrected by a cylindrical lens (focal length  $F = -1000 \text{ mm}/F = 1000 \text{ mm}$  for subtractive and additive dispersions, respectively) in front of the entrance slit [18]. To obtain a  $z$ -resolved spectrum  $I(z, \omega)$ , along the direction of the applied strain, the luminescence from a small strip of width  $2\Delta y$  centred in the trap was integrated along the  $x$ -direction perpendicular to  $z$  (see figure 1). Detection was done either by an intensified charge-coupled device (CCD) camera (Andor iStar) which could be gated with a minimum temporal resolution of 5 ns or with a nitrogen cooled CCD camera with high quantum efficiency (Andor Newton), which allowed long integration times.

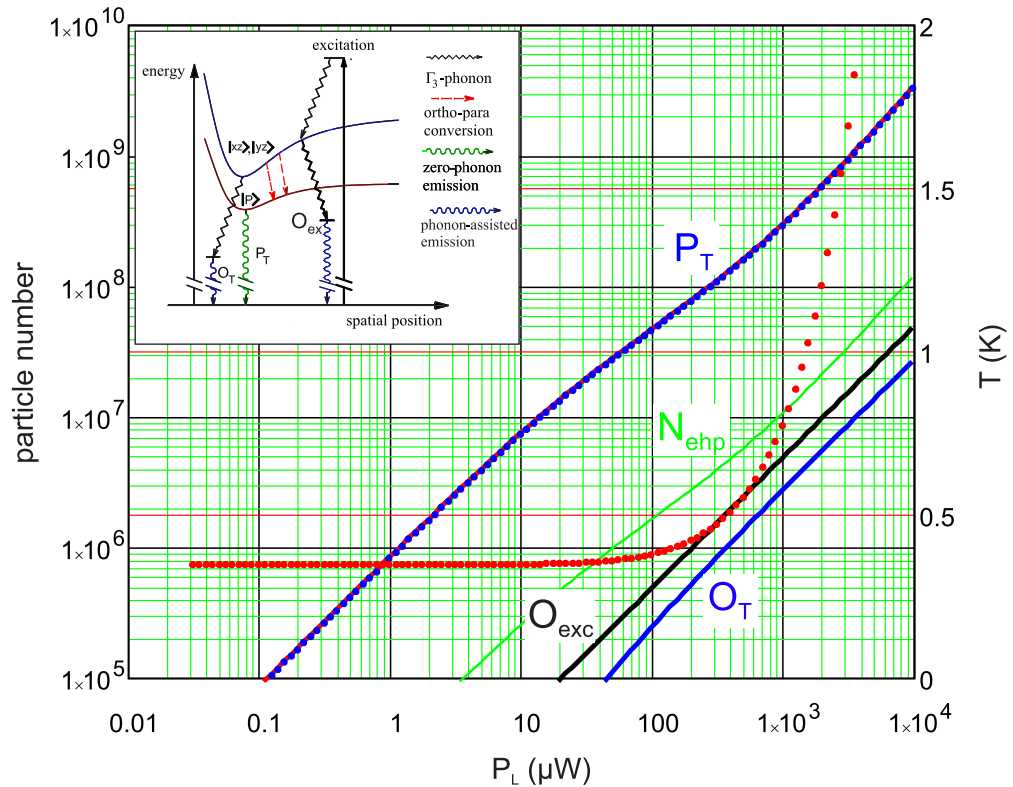


**Figure 2.** Numbers of para- and orthoexcitons and unbound electron–hole pairs and effective exciton temperature (dotted red line) as a function of excitation laser power as expected from the rate model. The inset schematically shows the laser excitation process to create the orthoexcitons, their conversion into paraexcitons and the luminescence processes to detect the excitons.

## 2.2. Application of the rate model to cw-excitation

With some adaptations, the rate model developed in [17] can also be applied to describe the cw experiments. These concern the following:

- Even under resonant excitation of excitons, a considerable density of unbound electron–hole pairs is generated [25]. This implies that the formation of an exciton from the hot electron–hole pair generated in the two-body decay (Auger-like process) takes a finite time comparable with other exciton relaxation times, e.g. the ones related to phonon scattering. In a fast initial relaxation stage with a duration of several picoseconds [26], the carriers thermalize by longitudinal optical (LO) and longitudinal acoustic (LA) phonon scattering. For a strained crystal with an exciton potential trap, these electron–hole pairs will then undergo different relaxation scenarios depending on whether the strain also causes a trapping potential for the unbound electron–hole pairs or not. In the latter case, the electrons and holes will diffuse from the place of generation (the potential trap) into the whole crystal and form excitons which themselves will drift again into the trap. In the former case, the electron–hole pairs will stay inside their trap and form a stable electron–hole plasma cloud with a density which is three orders of magnitude smaller than

the exciton concentration according to the results in [25]. As derived in appendix A, strain leads to a trapping potential for unbound electron–hole pairs which is similar to that for the paraexcitons. To take this effect into account, we included in the rate model the unbound electron–hole pairs with a total number of  $N_{\text{ehp}}$ . They are generated via the two-body decay of the ortho- and paraexcitons and recombine with a rate  $\Gamma_{\text{rc}}N_{\text{ehp}}^2$ . The recombination rate should depend on temperature in the same way as the two-body decay of the excitons ( $\propto T^{-3/2}$ ).

Due to heating and incomplete relaxation, the excitons may not cool down to bath temperature. We can describe this effect by assuming an effective exciton temperature  $T_{\text{eff}}$ , a cooling time of 200 ns [17] and heating processes due to the energy release by ortho–para conversion  $C_{\text{O}} = 10$  meV per exciton, Auger-like two-body decay with  $C_{\text{XX}} = 2$  eV per exciton pair, and a non-radiative decay of paraexcitons (guessed release  $C_{\text{P}} = 0.25$  eV per exciton). The temperature rise due to this heating is characterized by a constant  $C_{\text{heat}}$  which was adjusted to  $C_{\text{heat}} = 7 \times 10^9$  KJ $^{-1}$ .

We thus obtain the following set of rate equations for the numbers of primarily excited orthoexcitons ( $O_{\text{exc}}$ ), trapped ortho- and paraexcitons ( $O_{\text{T}}$  and  $P_{\text{T}}$ , respectively), and unbound electron–hole pairs  $N_{\text{ehp}}$ , and the effective exciton temperature  $T_{\text{eff}}$ :

$$\frac{dO_{\text{exc}}}{dt} = N_0 G(t) - \Gamma_{\text{rel}} O_{\text{exc}} - \Gamma_{\text{OP}} O_{\text{exc}} - \Gamma_{\text{O}} O_{\text{exc}}, \quad (3)$$

$$\frac{dO_{\text{T}}}{dt} = \Gamma_{\text{rel}} O_{\text{exc}} - \Gamma_{\text{OP}} O_{\text{T}} - 2A_{\text{OO}} O_{\text{T}}^2 - A_{\text{OP}} O_{\text{T}} P_{\text{T}} - \Gamma_{\text{O}} O_{\text{T}} + \frac{1}{2} \Gamma_{\text{rc}} N_{\text{ehp}}^2, \quad (4)$$

$$\frac{dP_{\text{T}}}{dt} = \Gamma_{\text{OP}} O_{\text{T}} + \Gamma_{\text{OP}} O_{\text{exc}} - 2A_{\text{PP}} P_{\text{T}}^2 - \Gamma_{\text{P}} P_{\text{T}} - A_{\text{OP}} O_{\text{T}} P_{\text{T}} + \frac{1}{4} \Gamma_{\text{rc}} N_{\text{ehp}}^2, \quad (5)$$

$$\frac{dN_{\text{ehp}}}{dt} = A_{\text{PP}} P_{\text{T}}^2 + A_{\text{OO}} O_{\text{T}}^2 + A_{\text{OP}} O_{\text{T}} P_{\text{T}} - \Gamma_{\text{rc}} N_{\text{ehp}}^2 - \Gamma_{\text{ehp}} N_{\text{ehp}}, \quad (6)$$

$$\begin{aligned} \frac{dT_{\text{eff}}}{dt} = & C_{\text{heat}} [C_{\text{XX}} (A_{\text{PP}} P_{\text{T}}^2 + A_{\text{OO}} O_{\text{T}}^2 + A_{\text{OP}} O_{\text{T}} P_{\text{T}}) \\ & + C_{\text{O}} \Gamma_{\text{OP}} (O_{\text{T}} + O_{\text{exc}}) + C_{\text{P}} \Gamma_{\text{P}} P_{\text{T}}] - \Gamma_{\text{cool}} (T_{\text{eff}} - T_{\text{fin}}). \end{aligned} \quad (7)$$

Here,  $T_{\text{fin}}$  denotes the final temperature to which the exciton gas would relax without additional heating. In an equilibrium situation, this would correspond to the bath temperature.

To simulate the cw-excitation, we solved the system of rate equations by assuming for  $G(t)$  a rectangular shaped excitation pulse of width  $\Delta T_{\text{L}} = 25 \mu\text{s}$  and a unit pulse area. The number of initially excited excitons  $N_0$  is given by

$$N_0 = \frac{A P_{\text{L}}}{\hbar \omega_{\text{L}}} \Delta T_{\text{L}}, \quad (8)$$

with the conversion factor from incident laser photons into primarily excited excitons  $A = 0.45$ . All other parameters are taken from [17]. Since we used the same sample under similar conditions, the calculation allows us to obtain the number of para- and orthoexcitons in the trap dependent on laser power, whereby we approximate the accuracy to  $\pm 50\%$ . In figure 2 we

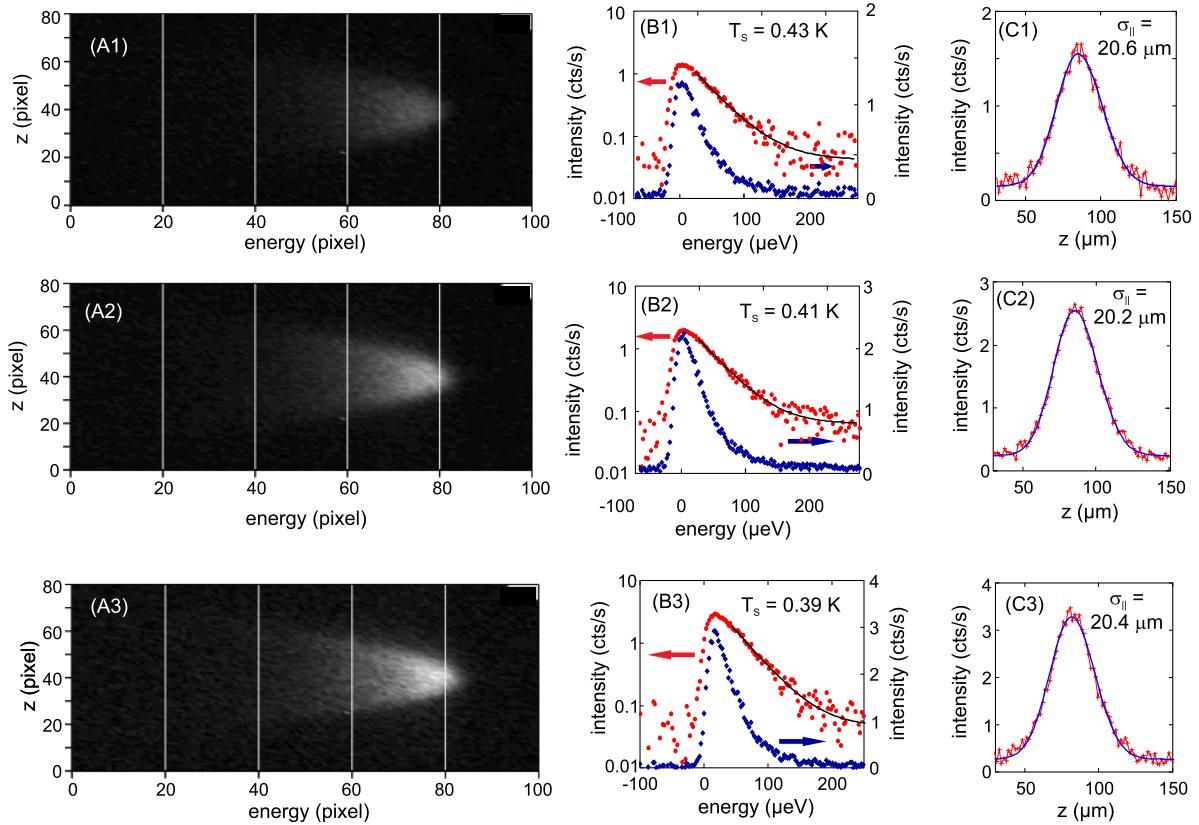


**Figure 3.** Spectra and spatial luminescence profiles at low excitation power  $P_L$  with  $P_L = 1.5 \mu\text{W}$  (upper row),  $P_L = 3 \mu\text{W}$  (middle row) and  $P_L = 5 \mu\text{W}$  (lower row).  $T_s$  denotes the temperature extracted from the high-energy tail of the spectra.

show a set of typical results. The final temperature  $T_{\text{fin}} = 0.35 \text{ K}$  was chosen to reproduce the experimentally observed temperature dependence in figure 5B. The results at high power levels do change somewhat due to the temperature dependence of the Auger process, but not by more than 20% by varying  $T_{\text{fin}}$  from 0.2 to 0.5 K.

The number of paraexcitons in the trap at low laser powers turns out to be determined by two parameters, the paraexciton lifetime  $1/\Gamma_P$  and the fraction of absorbed photons  $A$ . From figure 2 one can estimate the number of paraexcitons in the trap to be about  $8 \times 10^6$  for a laser power of  $10 \mu\text{W}$ . The number of unbound electron–hole pairs would be around  $3 \times 10^5$ . At power levels of 1 mW, which was the maximum laser power used in the mK experiments, paraexciton numbers of  $2 \times 10^8$  can be realized and the number of electron–hole pairs increases to  $10^7$ . Assuming thermal equilibrium, this would correspond to densities of about  $n_P = 2 \times 10^{16} \text{ cm}^{-3}$  and  $n_{\text{chp}} = 10^{14} \text{ cm}^{-3}$ .

### 2.3. Experimental results

**2.3.1. Low excitation power.** The first experimental results we want to show were obtained at rather low laser excitation powers between 1 and  $5 \mu\text{W}$  with high spectral resolution (figure 3).

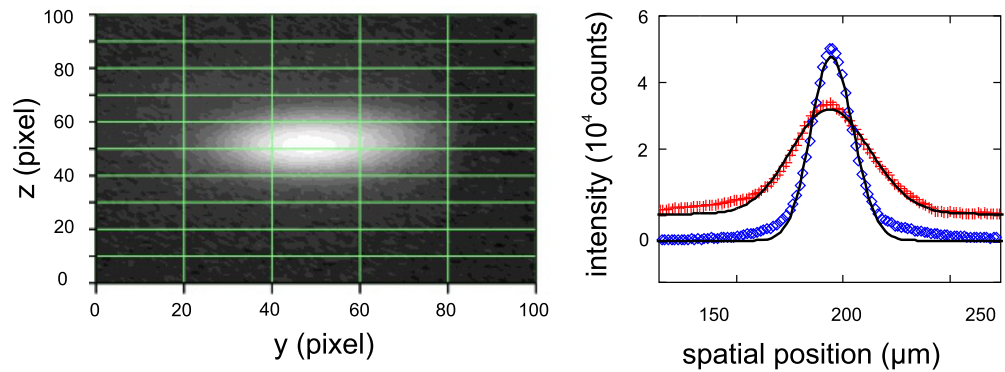


**Figure 4.** Left panel: spatial image of the exciton cloud at a low excitation power of  $P_L = 30 \mu\text{W}$ . Right panel: marginal intensity distributions along  $z$  (blue circles) and  $y$  (red circles) with fits to Gaussians according to equation (9).

Excitation was performed via the phonon-assisted absorption of the orthoexcitons with an energy slightly below the bulk exciton gap as described in section 2.1. Orthoexcitons were converted rapidly into paraexcitons and relaxed down to the bottom of the trap.

From the  $z$ -resolved spectra (A panels) we obtained the  $z$ -integrated spectra (B panels) and the  $z$ -profiles (C panels). As already can be seen in the  $z$ -resolved spectra, there is no change in both the spectral and spatial distributions, only an increase in the overall intensity which is almost proportional to the laser power. This demonstrates that we are in the linear excitation regime and that bimolecular decay processes are not important. The high-energy tail of the spectra can be fitted quite well by a Boltzmann distribution with an effective exciton temperature of about 0.4 K. A two-dimensional spatial image of the exciton cloud was obtained by using the spectrometer in the subtractive mode, the output stage at zero wavelength and by setting the intermediate slit of the subtractive stage to just let past the emission from the paraexcitons in the trap. A typical example is shown in figure 4. The spatial profiles are described by simple Gaussian distributions

$$I(y, z) = n_0 \exp(-y^2/\sigma_{\perp}^2) \exp(-z^2/\sigma_{\parallel}^2) \quad (9)$$

with width parameters  $\sigma_{\perp}$  and  $\sigma_{\parallel}$  of about  $20 \mu\text{m}$ .

According to the theoretical predictions in thermal equilibrium (see section 3), the width parameters are related to the curvature of the trap  $\alpha$  and temperature  $T$  by

$$\sigma_{\perp, \parallel} = \sqrt{\frac{k_B T}{\alpha_{\perp, \parallel}}}. \quad (10)$$

However, the ratio of the resulting width parameters does not fit the ratio of the potential curvatures as obtained from the strain calculation. It comes out about 30% larger. As the origin of this broadening we identified a small vibrational motion of the sample in the  $y$ -direction of the order of  $10 \mu\text{m}$  which could be directly observed by imaging a submicron sized needle. For a quantitative theoretical model of the light emission of the excitons, this effect has to be taken into account.

Using the curvature parallel to the  $z$ -direction from table 1, and subtracting the spatial blurring due to the diffraction of our optical imaging setup ( $7 \mu\text{m}$ ), we obtain from the spatial

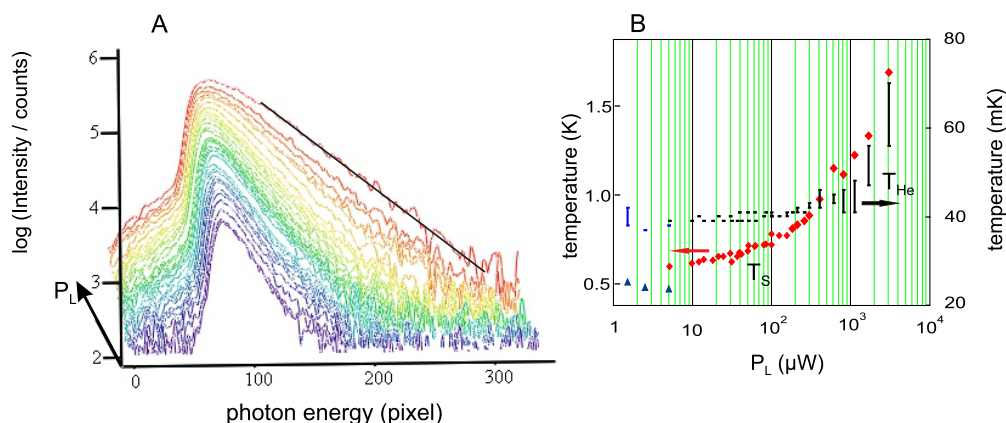


**Figure 5.** Panel A: series of spectra taken at increasing laser powers  $P_L$  from  $5 \mu\text{W}$  to  $3 \text{mW}$  in a logarithmic intensity scale. The spectral position is given in CCD-pixels, 1 pixel corresponds to  $2.5 \mu\text{eV}$ . Panel B: spectral temperature  $T_s$  as obtained from a Boltzmann fit of the high-energy tail of the spectra shown in panel A (left ordinate) and the temperature of the mixing chamber  $T_{\text{He}}$  (right ordinate).

profiles temperatures of about  $0.45 \text{K}$ , in good agreement with those from the spectra. At first sight, we would conclude that the excitons are in a state of quasi-thermal equilibrium, albeit with a temperature which is more than an order of magnitude larger than the bath temperature, which in these experiments was around  $38 \text{mK}$ . There are two possible explanations for this difference:

- (i) The heating of the exciton cloud due to the excess kinetic energy of about  $8 \text{meV}$  in the ortho–para conversion process or due to the exciton–exciton annihilation process. The excess electronic energy is in both cases converted into phonons and finally increases the temperature of the lattice which, however, is unknown in the present experiment. This heat has to be transferred into the surrounding He bath, where it would lead to an increase in the temperature of the mixing chamber, which could be measured during the experiment.

Indeed we observe this heating effect at higher laser powers. As shown in figure 5, the effective exciton temperature and the temperature of the mixing chamber rise from their initial values very steeply to above  $P_L = 1000 \mu\text{W}$ . Presuming a well-defined relation between the lattice temperature of the crystal and that of the mixing chamber, we have to conclude from these data that, at low laser powers, the heating effect is not present and the lattice temperature should be close to that of the He bath at very low laser powers. This conclusion is also in agreement with the results of the rate model presented in the foregoing section. There the heating of the exciton cloud starts at laser powers well above  $100 \mu\text{W}$  and is not present at low powers.

- (ii) The discrepancy of the lattice temperature  $T_{\text{latt}}$  and that of the exciton cloud may result because the excitons do not reach global thermodynamic equilibrium during their finite lifetime. This standard point of view means that, due to elastic exciton–exciton scattering, a quasi-thermal equilibrium state is established very fast with a temperature above that of the lattice. Hereafter, the exciton gas cools down to the lattice temperature by the emission of acoustic phonons. The time-scale of this process increases with decreasing lattice

temperature. In an external potential provided by the trap, the excitons are additionally driven by force and drift terms into the potential minimum, as described by the Boltzmann equation [27]. The detailed balance of these processes is determined by the interplay between the various exciton relaxation mechanisms.

In a recent paper, we published a detailed numerical simulation by solving the Boltzmann transport equation for excitons in a potential trap under pulsed optical excitation considering phonon relaxation and exciton–exciton annihilation [28]. The simulation indeed showed a strong non-equilibrium situation. While the local exciton energy distribution was reached within the exciton lifetime of several 100 ns and with an equilibrium with the lattice down to temperatures above 300 mK, the spatial distribution, which is governed by the force and drift terms, remained much broader than when in thermal equilibrium. For the case of still lower lattice temperatures, which was not considered in [28], we obtain local thermodynamic quasi-equilibrium also at temperatures down to 50 mK by including elastic exciton–exciton scattering as is shown in detail in appendix B. Albeit in this range the exciton temperature does not come down to the lattice temperature within the exciton lifetime, it is much lower than the observed values of  $T_s$ . According to these results, in our experiments we should expect a non-equilibrium situation in which the excitons are in a local quasi-thermal equilibrium with a temperature  $T_X$ , which we assume to be the same at all points in the trap. Globally, the exciton distribution will be quite different, but still can be described approximately by a Gaussian dependence on position.

Considering the effect of such a situation on the experimentally measured luminescence spectra, we recall that only excitons near  $k_0$  participate in light emission, where  $\mathbf{k}_0$  is the wave vector of the intersection of the photon and exciton dispersions. Its modulus is given by  $k_0 = E_{gX}n/\hbar c$ , with  $E_{gX}$  being the excitonic band gap,  $n$  the refraction index and  $c$  the vacuum velocity of light. This means, we observe the exciton distribution function  $f_{\text{eq}}(\mathbf{k}, \mathbf{r})$  only at one point in local  $k$ -space. Furthermore, due to energy conservation, at a certain spectral position  $\hbar\omega$  we only observe those excitons which are at that spatial position in the trap where the trap potential  $V_{\text{ext}}(\mathbf{r}) = \hbar\omega - E_0 - \varepsilon_0$ . Here,  $E_0$  is the energy of the trap bottom and  $\varepsilon_0$  is the kinetic energy of the excitons at  $k_0$ . If we have a spatial distribution

$$n(r) \propto \exp(-r^2/\sigma^2), \quad (11)$$

this yields a spectral distribution of the form

$$I(\hbar\omega) \propto \exp(-(\hbar\omega - E_0 - \varepsilon_0)/(\alpha\sigma^2)), \quad (12)$$

which suggests a Boltzmann distribution with an effective temperature  $T_s = \alpha\sigma^2/k_B$ . Then the spectral distribution of luminescence intensity in reality describes the spatial distribution and vice versa. Therefore, it has to result in the same effective exciton temperature, which is also a consistency check for the trap potential. Consequently, we will designate this temperature as the *spatial temperature*  $T_s$  of the exciton cloud. Obviously,  $T_s$  corresponds to  $T_{\text{eff}}$  of the rate model, cf equation (7). On the other hand, it is not possible to extract the local effective exciton temperature  $T_X$  from the intensity of the zero-phonon transition. This would require a spectroscopic technique which is sensitive to the local exciton distribution like the transitions between 1S and 2P exciton states (see [29, 30]). Hence, at the present stage of measurements, all we can state is that  $T_X$  may differ considerably from both the lattice temperature, which will set a minimum value, and the spatial temperature, which will set a maximum value, as in the latter case we would have global equilibrium.

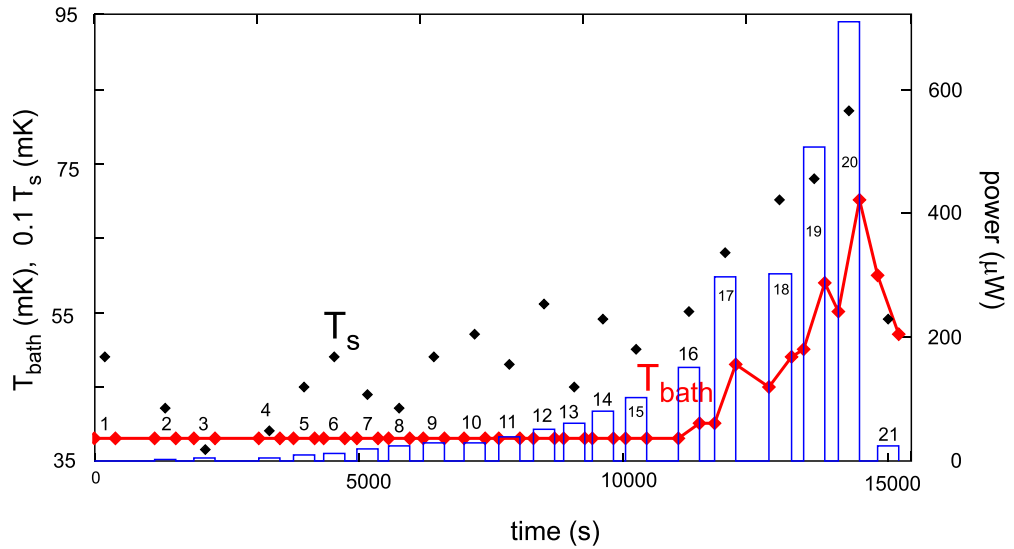


**Figure 6.** Time profiles of laser power (blue bars), the temperature of the mixing chamber (red diamonds) and the spatial temperature (black diamonds) for the measurements shown in figure 7. The red line is a guide for the eye.

**2.3.2. Power-dependent experiments.** In the following section we will present a series of measurements under controlled conditions of excitation and cooling times such that we are able to influence the thermodynamic state of the system in order to optimize any possible phase transition. The laser power ranged from below  $1 \mu\text{W}$  to about  $700 \mu\text{W}$ . For each measurement we noted the temperature of the mixing chamber (He bath temperature  $T_{\text{bath}}$ ) at the beginning and at the end. Between the measurements, the laser beam was blocked, so that the crystal could cool down (see figure 6).

In order to obtain the best signal-to-noise ratio, the ICCD camera was operated in the photon counting mode. Here, the CCD-chip is read out after a short exposure time ( $T_1$ ) and the positions of the single photon peaks are determined and stored. A single photon is identified if the signal falls between a lower and an upper discriminator level (which was adjusted so that only single photon signals fall in this range). For a number  $N_{\text{acc}}$  of accumulations, the data are summed in the memory. Advantages of this method are that signals due to cosmic rays are easily detected and eliminated and that one can estimate the error of the intensity signal due to the Poissonian statistics as the square root of the number of photons collected at each pixel. Due to the Poissonian statistics, the probability of detecting  $n$  photons is given by

$$P_n = \frac{\lambda^n}{n!} \exp(-\lambda), \quad (13)$$

where  $\lambda$  is the average photon number for each exposure. As we detect only single photons and throw away all higher photon number events,  $\lambda$  should be much smaller than one. However, for moderate values, we can obtain the true number of detected photons,  $\lambda N_{\text{acc}}$  from the measured number  $N_{\text{det}}$  by applying the correction formula

$$\lambda N_{\text{acc}} = -\ln \left( 1 - \frac{N_{\text{det}}}{N_{\text{acc}}} \right). \quad (14)$$



For the measurements of the  $z$ -resolved luminescence spectra shown in figure 7 we have  $T_1 = 0.5$  s and  $N_{\text{acc}} = 400$ . In order to keep the maximum number of detected photons well below  $N_{\text{acc}}$ , we inserted neutral density filters before the entrance slit of the monochromator. Their transmission factors have been determined by direct intensity calibration as  $D1 = 0.314$  and  $D2 = 0.0333$ .

In figure 7, each measurement is numbered according to its position in time given in figure 6. For each image we specify the laser power, the maximum number of counted photons (which allows us to judge the signal-to-noise ratio) and the totally integrated intensity. At first sight, all the images look very much the same, despite the three orders of magnitude increase in laser power. In particular, we observe neither the sharp spatial and spectral peak at the bottom of the trap, which is expected as a signature for BEC in case of an ideal Bose gas, nor the predicted flattening of the emission along the  $z$ -direction in case of an interacting Bose gas [31]. In this respect, the measurements shown are similar to those reported in all earlier work [11, 15]. A closer look, however, reveals subtle changes of the shape of the spectra depending on the laser power. For power levels below  $30 \mu\text{W}$ , the  $z$ -resolved spectrum of the exciton cloud shows no significant changes—here note especially measurements 9 and 21, which were taken under very different He bath temperatures (see figure 6). For power levels above  $30 \mu\text{W}$ , the images change gradually by showing a spectral narrowing and a slight blue shift. These changes suddenly come to a stop between measurements 17 and 18, with the images from now on both spatially and spectrally much broader and resembling those taken at low powers. The latter data have been taken at almost the same laser power of  $300 \mu\text{W}$ , but the He bath temperature was significantly different. Measurement 17 started at  $T_{\text{bath}} = 42$  mK. During the measurement, the laser power resulted in a heating up to  $T_{\text{bath}} = 49$  mK. In contrast, measurement 18 already started at  $T_{\text{bath}} = 45$  mK and stopped at  $T_{\text{bath}} = 50$  mK. This temperature variation of the mixing chamber should directly reflect the actual lattice temperature  $T_{\text{latt}}$  of the  $\text{Cu}_2\text{O}$  crystal. At the beginning of measurement 17,  $T_{\text{latt}}$  must have been quite close to that of the bath while at the start of measurement 18,  $T_{\text{latt}}$  has only cooled down to midway between start and end of measurement 17. This difference in lattice temperature is reflected in a concomitant difference in the spectral temperature which is  $T_s = 0.62$  K for measurement 17 and  $T_s = 0.72$  K for measurement 18. The totally integrated intensities of both measurements are expected to be similar due to the same laser power, however, that of measurement 18 is about 30% larger.

We can resolve this puzzle by assuming that the difference between both measurements comes from the existence of a Bose–Einstein condensate of excitons in measurement 17, while measurement 18 describes a normal exciton cloud at temperatures above the critical temperatures for BEC for the actual number of excitons in the trap, which is the same in both measurements. Then the lower intensity in 17 would be the result of the decreased number of thermalized excitons, since according to [31] and anticipating the discussion in section 3, excitons in the condensate are in the ground state ( $k = 0$ ), and, therefore, could not emit light with wave vector  $k_0$  at all (as in a homogeneous system), or is strongly suppressed (as would be the case in the trap).

Thus, we propose the following scenario for measurement 17: in the beginning, we have a system with a large fraction of the excitons in a condensate, with a reduced luminescence intensity. As time increases, the crystal heats up and the condensate fraction is reduced. When the lattice temperature reaches the critical temperature, we have a situation just like in measurement 18. Therefore, after being integrated over the exposure time  $T_1$ , the  $z$ -resolved spectra should look the same. In a first approximation, the image of 17 is a superposition of

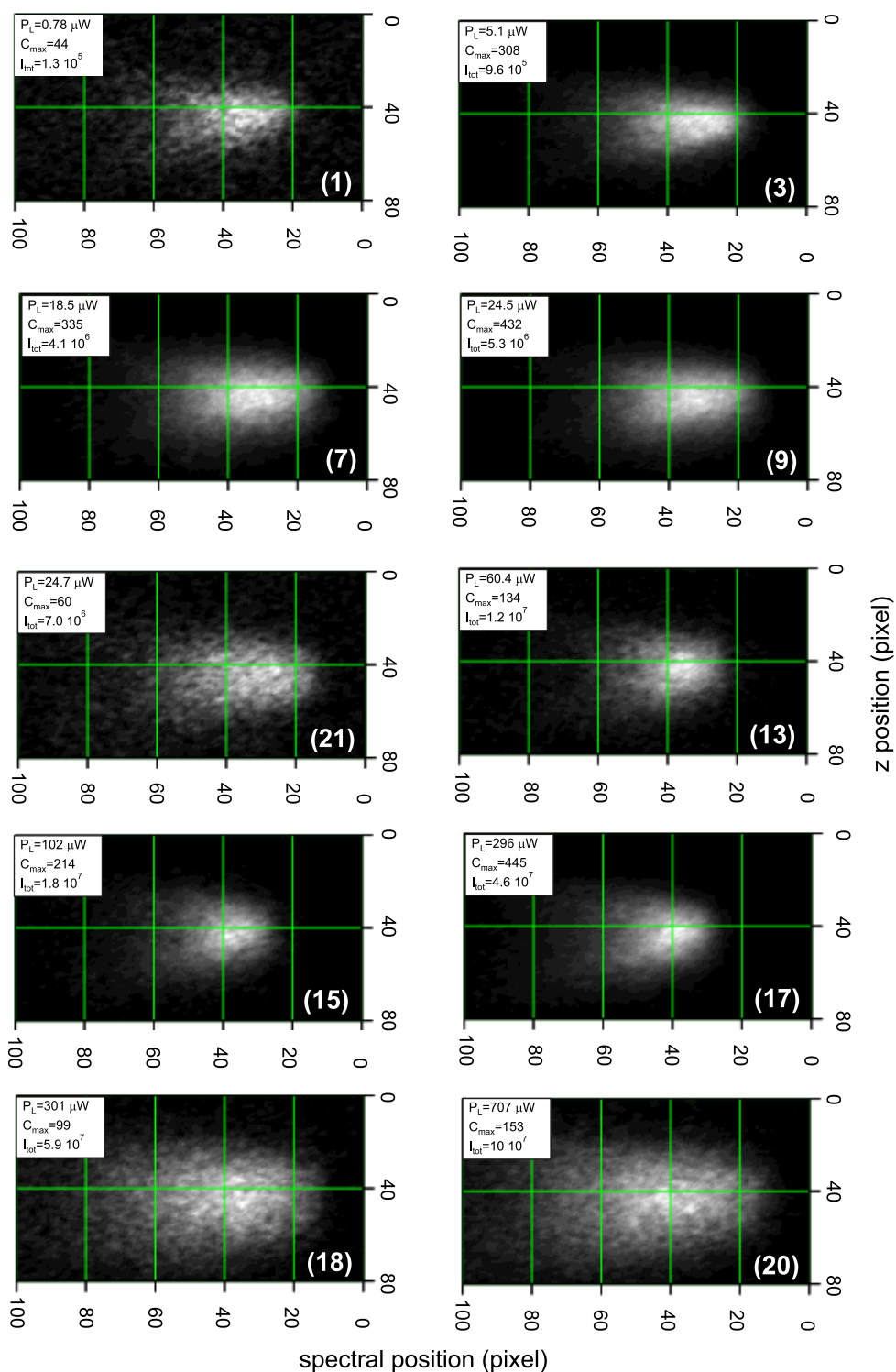


**Figure 7.** Series of  $z$ -resolved luminescence spectra for different excitation powers  $P_L$  and bath temperatures (see figure 6).  $C_{\text{max}}$  denotes the peak value and  $I_{\text{tot}}$  the totally integrated intensity. The numbers in parentheses denote the measurement numbers, cf figure 6.

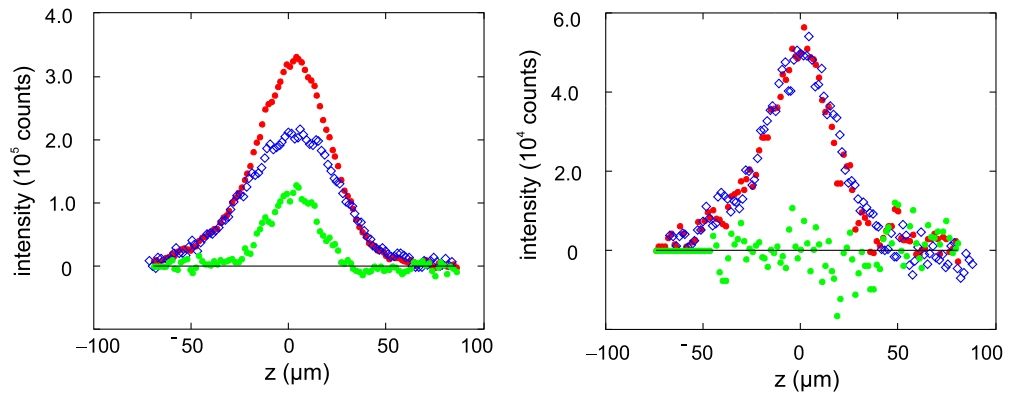


**Figure 8.** Comparison of the  $z$ -profiles of measurements 17 and 18 (left panel) and 9 and 21 (right panel). Each pair was taken at the same laser power, but at different bath temperatures. For details see text.

that of measurement 18 reduced by a factor  $\gamma$  and that of a system with a condensate. To demonstrate that this is indeed the case, we compare in figure 8 in the left panel the  $z$ -profiles for both measurements. By assuming  $\gamma = 0.6$ , the wings of both profiles do coincide exactly, which is clearly visible in the difference profile. The difference around the trap centre, however, has a characteristic, non-Gaussian line shape resembling that of a condensate (compare figure 9). A similar comparison of measurements 9 and 21, both taken at a laser power of  $25 \mu\text{W}$  (right panel of figure 8) shows no difference in the  $z$ -profiles within the statistical errors.

While such a comparison of different measurements seems to be intuitively correct, there are several objections against this procedure. First, the measurements we compare have quite different values for the spatial temperature and thus different spatial extensions in the trap. Second, we cannot exclude *a priori* that, e.g. measurement 18 also has a condensate. To overcome these difficulties, we have to look for a way to analyse each measurement for itself. Theoretical studies of the thermodynamics of an interacting Bose gas of excitons [31] have shown that even in the case of a BEC both the density of excitons and the spectrally integrated luminescence intensity outside the condensate region closely follow a Gaussian distribution reflecting the temperature of the exciton gas. Therefore, by fitting a Gaussian only to the wings at larger  $z$  of the intensity profile, we should have access to the distribution of thermal excitons only. If there is no condensate present, this Gaussian should also describe the intensity profile in the centre of the trap. On the other hand, any deviation of the measured profile from this curve is a clear indication of an additional luminescing component in the trap. If the line shape of this component is non-Gaussian, this would clearly indicate the existence of a condensate.

For the measurements shown in figure 7, the results of such a fitting procedure are shown in figure 9. The red and blue diamonds are the experimental points, whereby the blue diamonds mark those intensity points that have been used in the fitting. The blue line gives the shape of the Gaussian. In order to reproduce the obviously different line shapes for positive and negative  $z$  values due to the Morse-type potential of the trap in the  $z$ -direction, we used for the fit an asymmetric Gaussian function of the form

$$S(z) \propto \exp\left(-\frac{(z - z_0)^2}{(\Theta(z_0 - z)\sigma_- + \Theta(z - z_0)\sigma_+)^2}\right). \quad (15)$$

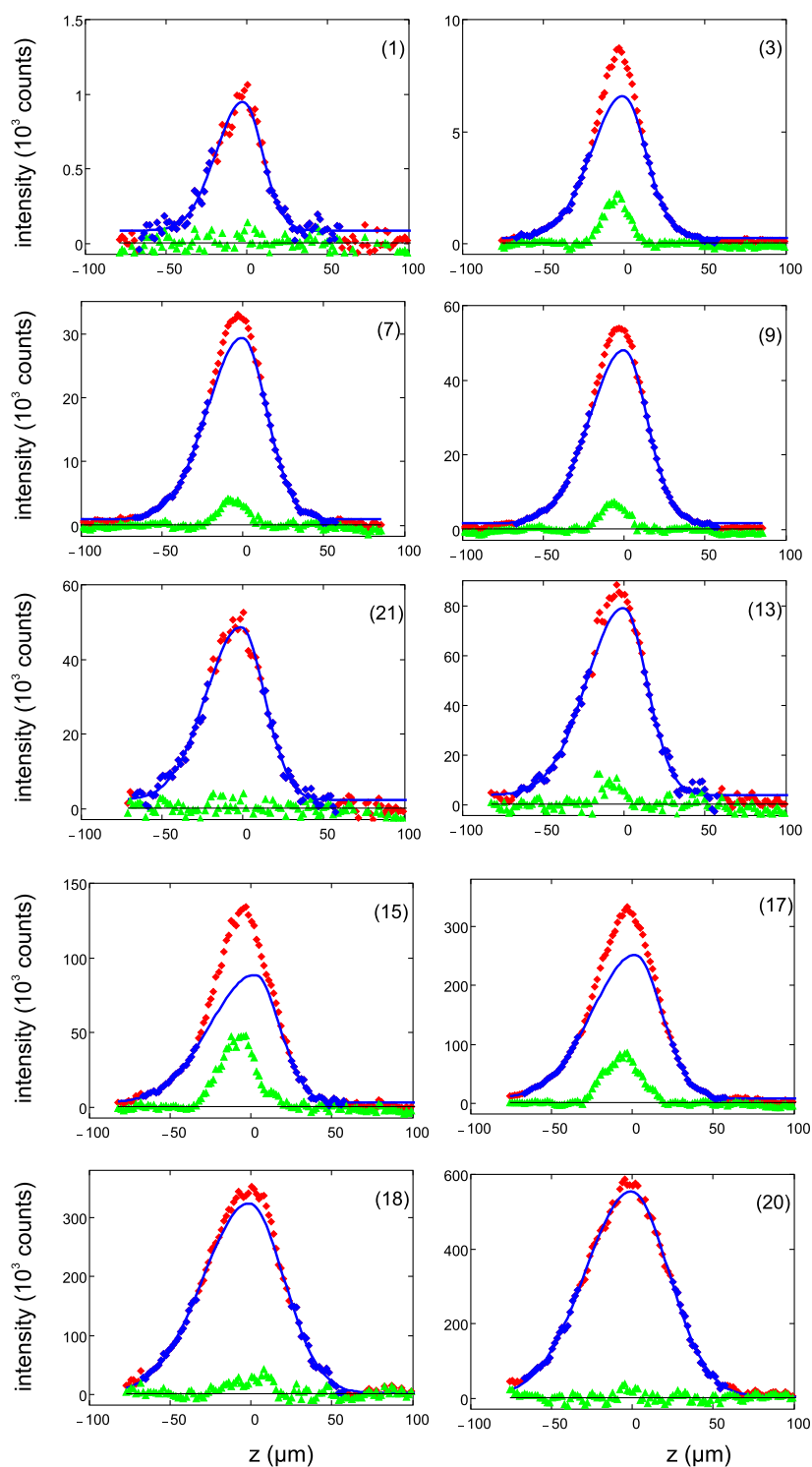


**Figure 9.** Comparison of  $z$ -profiles with fits by a Gaussian. Red and blue diamonds: total measured profiles, solid blue lines: Gaussian fit of the total profiles, blue diamonds: data points used for the fit, green triangles: the difference between total profile and fit. The numbers in parentheses denote the measurement numbers, cf figure 6.

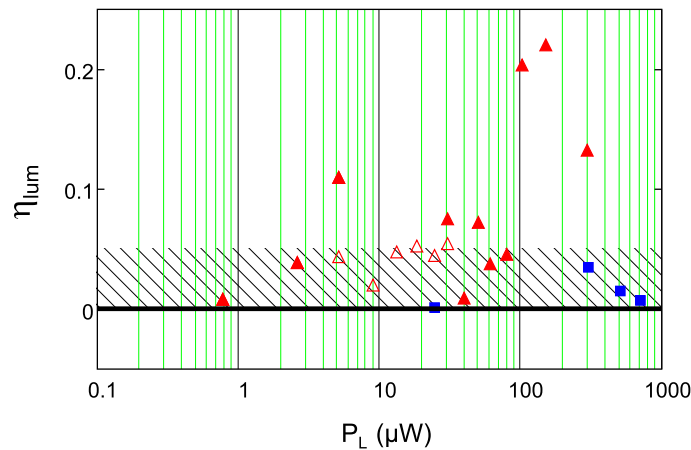


**Figure 10.** Power dependence of the ratio between integrated intensities of the condensate and of the total band. Filled red triangles: measurements 1–3 and 10–17, open red triangles: measurements 4–9, blue squares: measurements 18–21. Between measurements 3 and 4, and between measurements 9 and 10, there was a change of the neutral density filter, cf figure 6. The shaded band denotes an area where the contribution is too small for a significant proof of a condensate.

For all measurements, the ratio of  $\sigma_+/\sigma_-$  is obtained as 1.5, in consistence with the shape of the potential. The number of data points for the fitting was chosen for each set of data such that the average error per point becomes minimal. If we choose less points, the statistical error due to noise will increase; if we choose more points, the systematic error increases if the profiles contain an additional contribution. The green triangles show the difference between the experimental points and the Gaussian fits. In total, the results of the procedure substantiate our previous analysis. The measurements at very low power (1) and at high bath temperature (20, 21), where we expect no condensate, indeed can be fitted completely by a single Gaussian. Measurements 15 and 17 show clearly a bimodal distribution and thus a strong condensate component. However, in measurement 18 a small additional contribution remains. To show systematically the results of the fit, we have plotted in figure 10 the ratio of the green component to that of the overall intensity. Looking more closely at the results shown in figure 10, we can identify at least four sets of data with a strong condensate contribution, while most of the other measurements show a contribution below 0.05, which we will consider as not significant. The occurrence of a condensate in the power range between 60 and 300  $\mu\text{W}$  is understandable in view of the rather high number of paraexcitons in the trap which, according to the rate model (figure 2) is about  $4 \times 10^7$  at 100  $\mu\text{W}$ . The appearance of a condensate at the low power of 5  $\mu\text{W}$  is rather surprising and requires further consideration. Indeed, the theory presented in the next section will show that, under the conditions of our experiments (a bath temperature of 38 mK and no heating of the sample), condensation will take place at exciton numbers as low as  $4 \times 10^6$  (see figure 19).

Here we stress that the luminescence fraction  $\eta_{\text{lum}}$  shown in figure 10 is different from the fraction of particles in the condensate  $\eta_c = N_c/N_{\text{tot}}$ . If  $f_{\text{lum}}$  denotes the ratio of the luminescence efficiency of excitons in the condensate to that of excitons in the thermal cloud (see section 3.2),

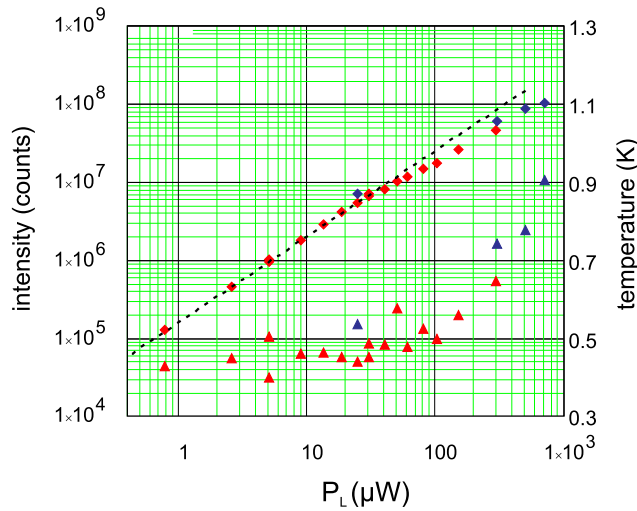


**Figure 11.** Dependence of the totally integrated intensity (squares) and spatial temperature (triangles) on the laser power. The blue points mark measurements 18–21. The dashed line gives a power dependence according to  $P_L^b$  with  $b = 1.1$  which describes the low power regime quite accurately.

the relation is given by

$$\eta_{\text{lum}} = \frac{f_{\text{lum}}\eta_c}{1 - \eta_c + f_{\text{lum}}\eta_c}. \quad (16)$$

At present,  $f_{\text{lum}}$  is neither known experimentally nor theoretically (see section 3.2), however, it must be smaller than one because otherwise we would not observe a kink in the luminescence dependence on laser power (see figures 11 and 12) so that  $\eta_c > \eta_{\text{lum}}$ .

Our interpretation is further substantiated by the dependence of the totally integrated intensity on the excitation laser power which is shown in figure 11.

At low power, the dependence is almost linear, indicating that decay processes by exciton–exciton collisions are not important. Actually, the dependence is even slightly superlinear which might be due to the effect of increasing homogeneous broadening at higher exciton numbers. At power levels of about  $60 \mu\text{W}$ , we clearly observe a kink resulting in a weaker slope at higher power levels. This is just the behaviour predicted by the theory in section 3.3.3. The critical power at the kink is in full agreement with the conclusion drawn from figure 10, where we observed the onset of condensation at powers above  $60 \mu\text{W}$ . This dependence is abruptly changed for the measurements 18–21 in agreement with the vanishing of the condensate. At high exciton numbers (under these conditions, we expect  $N \simeq 1 \times 10^8$  according to figure 2) we have a substantial effect of the two-body decay resulting in sublinear behaviour, see the data marked by blue symbols.

We note that the theory presented in the next section attributes such a kink in the power dependence of the total intensity of an exciton gas in a trap to the occurrence of condensation. Actually, in all of our measurements using different potential traps and under different excitation conditions such a kink shows up, provided that the He bath temperature is below 400 mK. Exemplarily this is shown in figures 12 and 13 for three different sets of data. In figure 12 we compare two measurements which have the same dependence of the He bath temperature

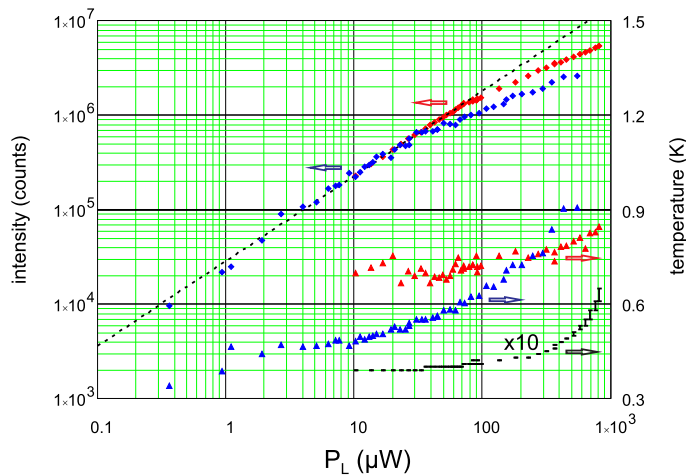


**Figure 12.** Dependence of the totally integrated intensity (squares), spatial temperature (triangles) and start and final bath temperature during the measurement (black bars) on the laser power for two different sets of data.

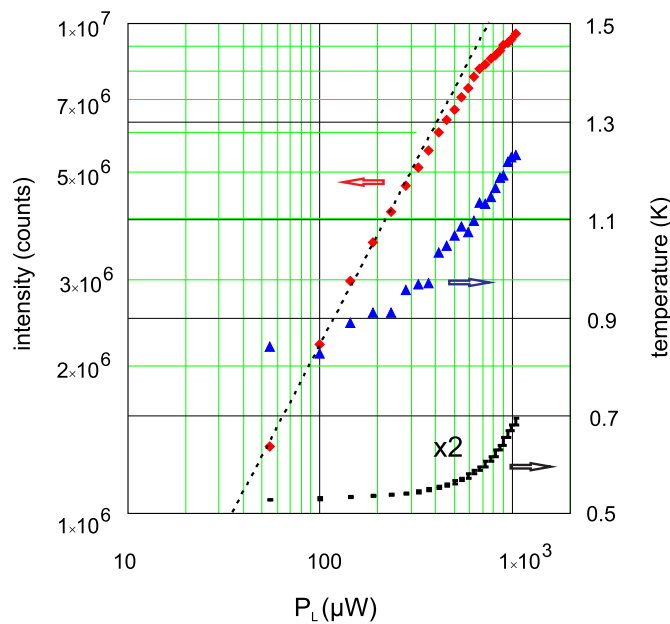


**Figure 13.** Dependence of the totally integrated intensity (squares), spatial temperature (triangles), and start and final bath temperature during the measurement (black bars) on the laser power.

but differ in their spatial temperatures. While at low powers both curves coincide, the curve corresponding to lower spatial temperature shows the kink at lower powers. In figure 13 we display the power dependence for the case where both the He bath temperature and the spatial temperature are much higher and the kink occurs at powers one order of magnitude larger than in the measurements of figure 12. This dependence of the onset of BEC on both the bath temperature and the spatial temperature will be explained by the theory presented in the next

section. The data in figure 13 furthermore demonstrate that the origin of the kink cannot be the Auger like decay of excitons at high densities, as one might suspect. This deviation from linearity in the power dependence already shows up below the kink.

### 3. Theory

After presenting the experimental results, in this section we will provide the theoretical description, attempting to explain the main effects found in the luminescence spectra.

So far, excitons in potential traps have been described mostly by theoretical models of non-interacting bosons. Concepts, to include e.g. interaction effects, have been worked out for atomic condensates. Along this line, the thermodynamics of a one-component Bose gas has been investigated extensively, see, e.g., [32–35]. First applications of excitons exist too [36]. Recently, distinct signatures of a condensate in the decay luminescence spectrum of the non-condensed excitons have been predicted using a mean-field formalism in local density approximation [31]. In analogy to generalizations for multi-component atomic gases [37–41] and spinor polaritons [42, 43], a generalization to a multi-component gas of interacting paraexcitons and orthoexcitons has been given in [44].

Here, we focus on the thermodynamics of weakly interacting excitons in a trap and assume the whole exciton gas to be in thermodynamic equilibrium. This allows us to apply the theory developed in [31, 44].

#### 3.1. Thermodynamics of trapped excitons

In order to write down the Hamiltonian of the exciton system, the interaction potential between excitons has to be modelled. The description of exciton–exciton interaction is a long-standing problem (see, e.g., [45–50]), and so far no satisfying solution for the general case has been obtained. For our calculations, we assume a contact potential interaction  $V(\mathbf{r} - \mathbf{r}') = U_0 \delta(\mathbf{r} - \mathbf{r}')$ , where the interaction strength  $U_0$  is given by the  $s$ -wave scattering length  $a_s$  via  $U_0 = 4\pi a_s/M$ .  $M$  is the exciton mass  $M = 2.6m_e$  in units of the free electron mass  $m_e$  [22]. This leads to the Hamiltonian in second quantization for the grand canonical ensemble:

$$\mathcal{H} = \int d^3\mathbf{r} \psi^\dagger(\mathbf{r}, t) \left( -\frac{\hbar^2 \nabla^2}{2M} + V_{\text{ext}}(\mathbf{r}) - \mu \right) \psi(\mathbf{r}, t) + \frac{1}{2} \int d^3\mathbf{r} U_0 \psi^\dagger(\mathbf{r}, t) \psi^\dagger(\mathbf{r}, t) \psi(\mathbf{r}, t) \psi(\mathbf{r}, t), \quad (17)$$

with the trap potential  $V_{\text{ext}}(\mathbf{r})$  and the chemical potential  $\mu$ . Decomposing the field operators in the usual fashion  $\psi(\mathbf{r}, t) = \Phi(\mathbf{r}) + \tilde{\psi}(\mathbf{r}, t)$ , with the condensate wave function  $\Phi(\mathbf{r}) = \langle \psi(\mathbf{r}, t) \rangle = \langle \psi(\mathbf{r}) \rangle$  and the operator of the thermal excitons  $\tilde{\psi}(\mathbf{r}, t)$ , one arrives at the Gross–Pitaevskii equation (GPE)

$$0 = \left( -\frac{\hbar^2 \nabla^2}{2M} + V_{\text{ext}}(\mathbf{r}) - \mu + U_0 [n(\mathbf{r}) + n^T(\mathbf{r})] \right) \Phi(\mathbf{r}) + U_0 \tilde{m}(\mathbf{r}) \Phi^*(\mathbf{r}), \quad (18)$$

and the equations of motion for the thermal excitons

$$i\hbar \frac{\partial \tilde{\psi}(\mathbf{r}, t)}{\partial t} = \left( -\frac{\hbar^2 \nabla^2}{2M} + V_{\text{ext}}(\mathbf{r}) - \mu + 2U_0 n(\mathbf{r}) \right) \tilde{\psi}(\mathbf{r}, t) + U_0 [\Phi^2(\mathbf{r}) + \tilde{m}(\mathbf{r})] \tilde{\psi}^\dagger(\mathbf{r}, t), \quad (19)$$



with the normal and anormal averages  $n^T = \langle \tilde{\psi}^\dagger \tilde{\psi} \rangle$  and  $\tilde{m} = \langle \tilde{\psi} \tilde{\psi} \rangle$ , the condensate density  $n^c = |\Phi|^2$  and the total density  $n = n^c + n^T$ .

Since the spatial extension of the potential trap is large compared to the typical length scales of the interacting exciton gas (in particular with respect to the thermal deBroglie wavelength of the excitons), we can use the local density approximation, thus treating the excitons as a locally homogeneous system. The equation of motion (19) is solved by a Bogoliubov transformation. In the so-called Hartree–Fock–Bogoliubov–Popov limit ( $\tilde{m} \rightarrow 0$ ), the quasiparticle energy reads

$$E(\mathbf{k}, \mathbf{r}) = \sqrt{\mathcal{L}(\mathbf{k}, \mathbf{r})^2 - (U_0 n^c(\mathbf{r}))^2}, \quad (20)$$

with

$$\mathcal{L}(\mathbf{k}, \mathbf{r}) = \hbar^2 k^2 / 2M + V_{\text{ext}}(\mathbf{r}) - \mu + 2U_0 n(\mathbf{r}). \quad (21)$$

Within these approximations, the non-condensate density  $n^T$  is given by

$$n^T(\mathbf{r}) = \int \frac{d^3 \mathbf{k}}{(2\pi)^3} \left[ \frac{\mathcal{L}(\mathbf{k}, \mathbf{r})}{E(\mathbf{k}, \mathbf{r})} \left( n_B(E(\mathbf{k}, \mathbf{r})) + \frac{1}{2} \right) - \frac{1}{2} \right] \Theta(E^2(\mathbf{k}, \mathbf{r})). \quad (22)$$

Applying the Thomas–Fermi approximation to the GPE (18), i.e. neglecting the kinetic energy term, yields the condensate density as

$$n^c(\mathbf{r}) = \frac{1}{U_0} \left[ \mu - V_{\text{ext}}(\mathbf{r}) - 2U_0 n^T(\mathbf{r}) \right] \Theta\left( \mu - V_{\text{ext}}(\mathbf{r}) - 2U_0 n^T(\mathbf{r}) \right). \quad (23)$$

Evaluating equations (22) and (23),  $n^T$  and  $n^c$  have to be determined self-consistently.

### 3.2. Theory of decay luminescence

Since the optical wavelength of the emission is much smaller than the trapped exciton cloud, we apply a local approximation to the emission spectrum [51, 52] as well, which is determined by the excitonic spectral function  $A(\mathbf{r}, \mathbf{k}, \omega)$ ,

$$I(\mathbf{r}, \omega) \propto 2\pi \hbar |S(\mathbf{k} = 0)|^2 \delta(\hbar\omega' - \mu) n^c(\mathbf{r}) + \sum_{\mathbf{k} \neq 0} |S(\mathbf{k})|^2 n_B(\hbar\omega' - \mu) A(\mathbf{r}, \mathbf{k}, \hbar\omega' - \mu), \quad (24)$$

with  $S(\mathbf{k})$  representing the exciton–photon coupling. The spectral function is given by the quasiparticle spectrum in (20):

$$A(\mathbf{r}, \mathbf{k}, \omega) = 2\pi \hbar \left[ u^2(\mathbf{k}, \mathbf{r}) \delta(\hbar\omega - E(\mathbf{k}, \mathbf{r})) - v^2(\mathbf{k}, \mathbf{r}) \delta(\hbar\omega + E(\mathbf{k}, \mathbf{r})) \right], \quad (25)$$

where  $u(\mathbf{k}, \mathbf{r})$  and  $v(\mathbf{k}, \mathbf{r})$  are the Bogoliubov amplitudes,

$$\begin{aligned} u(\mathbf{k}, \mathbf{r})^2 &= \frac{1}{2} (\mathcal{L}(\mathbf{k}, \mathbf{r}) / E(\mathbf{k}, \mathbf{r}) + 1), \\ v(\mathbf{k}, \mathbf{r})^2 &= \frac{1}{2} (\mathcal{L}(\mathbf{k}, \mathbf{r}) / E(\mathbf{k}, \mathbf{r}) - 1). \end{aligned} \quad (26)$$

In  $\text{Cu}_2\text{O}$ , the decay of ground-state paraexcitons in the yellow series is optically forbidden. However, due to the applied strain, a mixing with the green series takes place and the decay becomes weakly allowed [53]. The paraexcitons decay directly, whereby momentum conservation requires that only excitons with the same momentum as the emitted photons are involved. This zero-phonon decay can be treated by setting  $\omega' = \omega - E_{\text{gX}}/\hbar$  with the excitonic band gap  $E_{\text{gX}}$  and  $|S(\mathbf{k})|^2 = S_0^2 \delta(\mathbf{k} - \mathbf{k}_0)$  with  $\mathbf{k}_0$  being the wave vector of the intersection of the photon and exciton dispersions.

Due to the form of  $S(\mathbf{k})$ , a condensate of paraexcitons in  $\text{Cu}_2\text{O}$  (energetically in the ground state, i.e.  $k = 0$ ) should not contribute to the luminescence spectrum. However, this statement holds rigorous only for homogeneous, infinitely extended systems. Due to the finite size of the condensate, it is spread out in  $\mathbf{k}$ -space, and a weak contribution to the luminescence should be expected. Taking the condensate as a classical coherent emitter, the radiation follows from classical Maxwell equations as the Fourier transform of the polarization [54] at the wave vector of the emitted photon  $\mathbf{k}_0$ . Since the polarization is proportional to the condensate wave function, the (dimensionless) strength of the contribution  $S_c$  ( $|S(\mathbf{k} = 0)|^2 = S_c S_0^2$ ) should be proportional to the components of the Fourier transform of the ground-state wave function at  $\mathbf{k} = \mathbf{k}_0$ . Our calculations show that  $S_c$  is of the order of  $10^{-6}$  to  $10^{-7}$ . Therefore, we will discuss possible effects of a BEC in the spectrum considering a weakly luminescing as well as a completely dark condensate.

Furthermore, to account for the finite spectral resolution in experiments, we convolve the spectral intensity (24) with a spectral response function of the shape  $\exp[-(\omega/\Delta)^2]$ . Here,  $\Delta$  is a measure for the spectral resolution. Using these assumptions, the spectrum reads:

$$I(\mathbf{r}, \omega) \propto S_c (2\pi)^3 \exp \left[ - \left( \frac{\hbar\omega' - \mu}{\Delta} \right)^2 \right] n^c(\mathbf{r}) + u^2(\mathbf{k}_0, \mathbf{r}) n_B(E(\mathbf{k}_0, \mathbf{r})) \exp[-\varepsilon_-^2(\omega', \mathbf{k}_0, \mathbf{r})] - v^2(\mathbf{k}_0, \mathbf{r}) n_B(-E(\mathbf{k}_0, \mathbf{r})) \exp[-\varepsilon_+^2(\omega', \mathbf{k}_0, \mathbf{r})], \quad (27)$$

with  $\varepsilon_{\pm}(\omega', \mathbf{k}, \mathbf{r}) \equiv (\hbar\omega' - \mu \pm E(\mathbf{k}, \mathbf{r}))/\Delta$ . As explained in section 2, in the experiment, a spectrograph is used to obtain different spectra by integrating over either one or more spatial coordinates and/or  $\omega$ . Here, we consider the  $z$ -resolved luminescence spectrum  $I(z, \omega)$ , the  $z$ -profiles of the luminescence  $I(z)$ , the spatially integrated luminescence  $I(\omega)$ , and the totally integrated luminescence  $I_{\text{tot}}$ . The  $z$ -resolved luminescence spectrum is obtained by imaging a small strip of width  $2\Delta y$  elongated along the  $z$ -direction onto the entrance slit of the spectrograph, hence integrating over the  $x$ - and  $y$ -direction. The  $z$ -profiles are generated by integrating  $I(z, \omega)$  over the energy ( $\omega$ ). Integrating over all spatial dimensions yields the spatially integrated luminescence  $I(\omega)$ . As a fourth option, one can also integrate over  $\mathbf{r}$  and  $\omega$ , arriving at the totally integrated luminescence  $I_{\text{tot}}$ , which only depends on the exciton number  $N$  and the temperature  $T$ .

### 3.3. Results

**3.3.1. Luminescence spectrum.** For the calculations, we used an anharmonic potential trap fitted to the experimental of section 2 but with a trap minimum of  $V_0 = 1.04$  meV. The  $s$ -wave scattering length was chosen to be  $a_s = 2.18a_B$  (taken from [55], see also [56–58]) with the excitonic Bohr radius  $a_B = 0.7$  nm.

First, we revisit the flat bottomed shape of the spectrum discussed in [31]. In figure 14, we plot the luminescence spectrum for a constant temperature  $T = 0.6$  K and three different exciton numbers (left column:  $N = 2.5 \times 10^7$ , middle column:  $N = 2.5 \times 10^8$ , right column:  $N = 8.0 \times 10^8$ ). The condensate is expected to remain completely dark. The left image of figure 14 shows a thermal spectrum exhibiting the typical nearly parabolic shape that was also found in the experimental results presented in figures 3 and 7. Increasing the exciton number by a factor of 10 while keeping the temperature constant results in the onset of a BEC with a condensate fraction of  $N_c/N = 0.05$ . The shape of the spectrum is altered and develops a flat bottom at the chemical potential as reported in [31]. Further increasing the exciton number

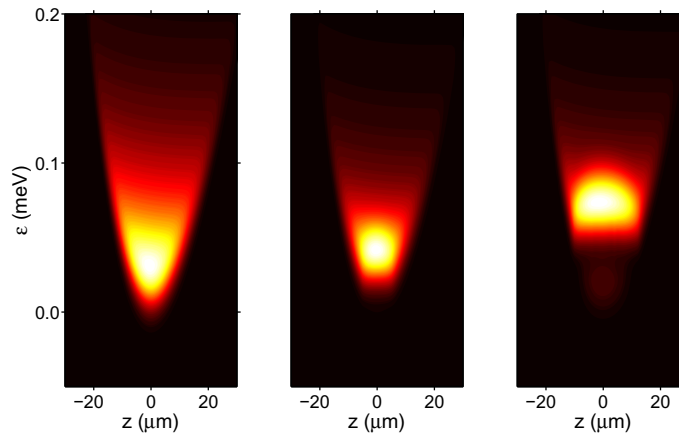


**Figure 14.**  $z$ -resolved luminescence spectra  $I(z, \omega)$  at  $T = 0.6$  K with dark condensate. The exciton numbers are  $N = 2.5 \times 10^7$  (left),  $N = 2.5 \times 10^8$  (middle) and  $N = 8.0 \times 10^8$  (right). Condensate fractions are  $N_c/N = 0$  (left),  $N_c/N = 0.05$  (middle) and  $N_c/N = 0.50$  (right). Trap minimum is at  $V_0 = 1.04$  meV and  $\varepsilon = \hbar\omega - E_{gX} - V_0$ .

leads to a more pronounced flat bottom and an energetic shift of the spectrum with the chemical potential. Additionally, a new contribution to the thermal spectrum below the chemical potential, arising from the  $v^2$ -term in equation (25), becomes faintly visible. These effects are linked to the occurrence of a BEC and would indicate its existence even without direct emission from the condensate.

Comparing these predictions with the experimental findings, e.g. figures 3 and 7, one has to conclude that the signatures were not observed in the experiment. However, if the condensate exhibits a very weak luminescence, the changes in the spectrum predicted from theory are much more subtle. This can be seen in the left column of figure 15 ( $S_c = 10^{-6}/3$ ), cf again figures 3 and 7. In contrast to the case of a dark condensate, there is no drastic qualitative change in the spectra from top to bottom. Also, the shift on the energy axis appears to be smaller and could well be an interaction effect of thermal excitons. Therefore, the contribution from the condensate hides the flat bottom as well as the shift on the energy axis, without being a clearly visible delta-shaped peak, as expected for a fully contributing condensate. This explains why a conclusive detection of a condensate via spectral signatures requires a very careful analysis of the experiments.

The spectra in the left column of figure 15 consist of different contributions. To illustrate this, we plot the results for the spatially integrated luminescence  $I(\omega)$  in the middle column of figure 15, cf the measurements shown in figures 3 and 5. The upper panel shows a spectrum in the non-condensed case at low densities. Its shape is given by a Bose distribution convolved with the spectral resolution of the spectrometer. The middle panel shows a spectrum at higher densities, where interaction effects are already important and a very small condensate contribution already occurs, nearly invisible in the total curve. Compared to the previous case, the peak becomes narrower and shifts to higher energies, while the tail remains qualitatively the same. The bottom graph shows the case with a condensate fraction of 0.5 including a distinct condensate contribution (dashed-dotted blue) which has a Gaussian shape and is centred at

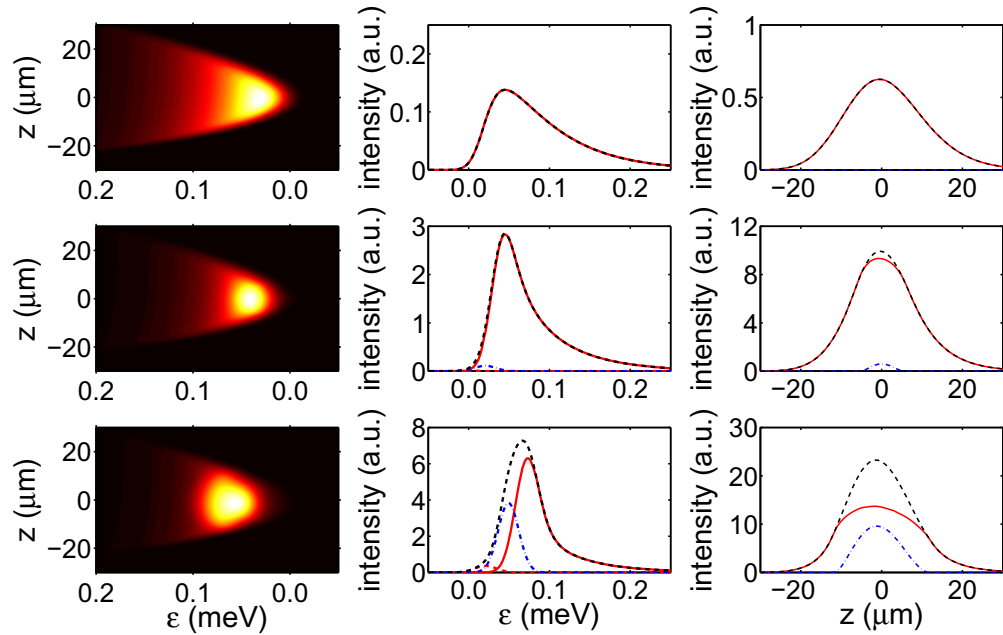


**Figure 15.**  $z$ -resolved luminescence spectra,  $z$ -integrated luminescence and  $z$ -profiles of the luminescence with weakly luminescing condensate ( $S_c = 10^{-6}/3$ ) for the same parameters as in figure 14. Left column: luminescence spectra  $I(z, \omega)$ . Middle column:  $z$ -integrated luminescence  $I(\omega)$ . Right column:  $z$ -profiles  $I(z)$ . Red curves (full and dashed) denote the contributions from thermal excitons, the blue dash-dotted curve gives the condensate contribution, and the total emission is shown as a dashed black line.

the chemical potential. The contribution from the thermal excitons consists of the  $u^2$  part of the spectral function (solid red) and the  $v^2$  part of the spectral function (dashed red), compare with equation (27). The black line represents the sum over all contributions. In contrast to the very weakly condensed case (middle), the contribution related to the  $v^2$  term appears below the chemical potential (dashed red). Except for this additional contribution, the total emission is only slightly shifted towards higher energies and has a higher maximum compared to the middle graph in figure 15. The width of all the Gaussian-like peaks in figure 15 is directly given by the spectral resolution  $\Delta = 18 \mu\text{eV}$ .

**3.3.2. Spatially resolved luminescence.** The results for the spatially resolved luminescence  $I(z)$  are presented in the right column of figure 15 and should be compared to the experimental results shown in figures 3, 4, 8 and 9.

Without any contribution from the condensate, one would expect the solid red line. The non-condensed case follows a Gaussian shape (top graph), while the onset of the BEC leads to a deformation in the form of a plateau (middle and bottom graphs). However, taking a weakly luminescing condensate (dashed blue) into account, the total emission (black dashed) looks Gaussian-like again, masking the signature of the condensate (middle and bottom graphs).

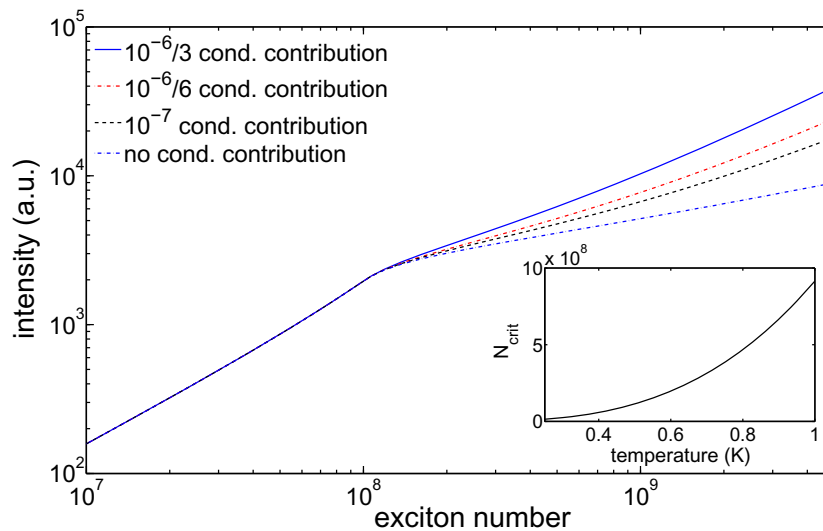


**Figure 16.** Totally integrated luminescence  $I_{\text{tot}}$  for  $T = 0.5$  K and different fractions of condensate contribution. Change of  $N_{\text{crit}}$  (position of kink) with temperature is shown in the inset.

*3.3.3. Totally integrated luminescence.* Integrating over all variables ( $\mathbf{r}$  and  $\omega$ ) yields the totally integrated luminescence  $I_{\text{tot}}$ , which had been considered in the experiments in figures 11–13. In figure 16, we show the numerical results for  $I_{\text{tot}}$  as a function of the exciton number  $N$  for a fixed temperature of  $T = 0.5$  K. Remember that  $N$  is connected to the excitation laser power  $P_L$ , cf. the results of the rate model, figure 2. For small  $N$ , the totally integrated luminescence increases linearly with the exciton number until a critical value is reached. At the critical exciton number, the curve has a kink and continues with a weaker slope afterwards. The additional contribution from a weakly luminescing condensate does not alter the behaviour qualitatively in this case, as can be seen from the other curves in figure 16. As shown in the inset of figure 16, the critical exciton number shifts with the temperature approximately as expected with  $T^3$ , equation (1). Obviously, here the interaction has no drastic effect on the behaviour known for an ideal gas.

However, in the experimental situation, it is merely impossible to measure over orders of magnitude of particle number without changing the exciton temperature. The temperature will rise as a result of the energy introduced into the system by the laser. Therefore, experimental points may lie anywhere in the  $N$ – $T$  plane. The theoretical results for the totally integrated luminescence as a function of exciton number and temperature are shown in figure 17. Depending on how fast the temperature increases with exciton number, it is very well possible to never cross the phase boundary and observe the kink in the totally integrated luminescence.

### 3.4. Discussion

In the previous section, we presented the different spectral signatures of a non-emitting condensate in the thermal emission of excitons in global thermal equilibrium. The five main signatures are: (i) the formation of a flat bottom in the luminescence spectrum  $I(z, \omega)$ , (ii) the

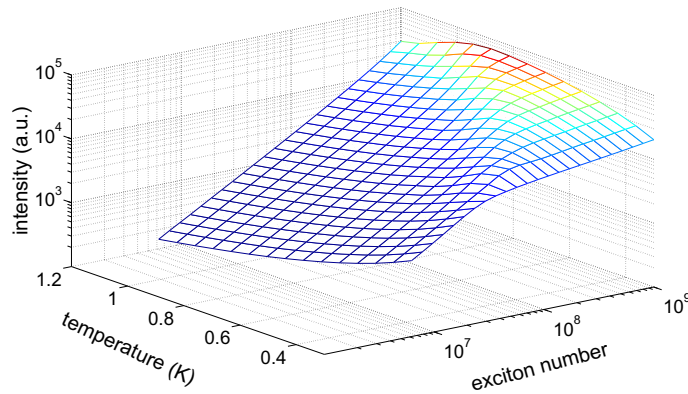


**Figure 17.** Totally integrated luminescence  $I$  for a range of different temperatures and exciton numbers in the same potential trap as in figure 14.

shift on the energy axis of the spectrum  $I(z, \omega)$ , (iii) a deviation of the  $z$ -profiles  $I(z)$  from the Gaussian shape, (iv) the appearance of the  $v^2$  term in the spatially integrated luminescence  $I(\omega)$  and (v) the kink in the totally integrated luminescence  $I_{\text{tot}}$  at  $N_{\text{crit}}$ .

If the contribution from the condensate is much weaker than that which we estimated (i.e.  $S_c$  of the order of  $10^{-6}$ – $10^{-7}$ ), signature (i) should be experimentally visible. This is neither the case in the current experiment nor any others previously. If the contribution is much stronger though, one should expect the delta-shaped peak as predicted by the standard theory [1, 51, 52]. This substantiates our estimation for  $S_c$ .

However, if the condensate contribution is comparable to that of the thermal excitons, the flat bottom in (i) can be masked as shown in figure 15. The changes in the shape are very subtle and probably not detectable in an actual experiment. The shift on the energy axis (ii) is also altered by the condensate contribution. Additionally, there are numerous other effects that can change the energetic position of the spectrum, e.g. a background plasma of electrons and holes [6, 7]. Therefore, this shift might not be a good indicator for the onset of the BEC. The deformation of the  $z$ -profiles (iii) would also be masked by the condensate contribution. Here, the latter one complements the thermal luminescence, again resulting in a Gaussian profile. Contrarily, in the measured profiles (figure 9), the condensate adds a contribution to the thermal Gaussian profile. We will revisit this point later.

Without a condensate, the spectra can be fitted with a renormalized Bose distribution convolved with the spectral resolution of the spectrometer. With a condensate, the  $v^2$  peak (iv) causes a characteristic deformation of the low energy flank of the spatially integrated luminescence. For a dark condensate, however, it would be a free standing peak separated from the rest of the spectrum. Both cases should be detectable in an experiment though. However, this signature (iv) as well as the energetic shift (ii) are very subtle and are probably masked by noise, compare figures 3 and 7.

The most promising signature of condensation would be the kink in the totally integrated luminescence (v), as it is not altered qualitatively by the condensate contribution. In this case it only changes the slope after the kink, but does not hide the kink itself. Although in figures 11–13 no isotherms are plotted—the exciton temperature rises with excitation power—there is obviously a kink in the measured integrated intensity. Looking at figure 17, a path on the surface will exhibit a kink even with increasing temperature, if the ridge is

crossed. Therefore, we can relate the kink in the experimental figures, at least qualitatively, to the occurrence of a condensate.

### 3.5. Excitons in local equilibrium

As stated above, the theory derived in section 3 assumes that the exciton gas in the trap is in global thermodynamic equilibrium. The experimental results presented in the previous section show, however, that this is obviously not the case and that the exciton temperature is the key quantity to detect deviations from global equilibrium. The conclusions are that (i) the *spectral* (or *spatial*) temperature is not equal to the exciton temperature and (ii) the assumption of global equilibrium, therefore, must be wrong, cf the discussion in section 2.3.1.

In contrast to the latter statement, the luminescence spectra calculated by the equilibrium theory reproduce the measured spectra qualitatively quite well, cf figures 3 and 15. Thus it seems to be reasonable to abandon the global equilibrium assumption, but to keep the local equilibrium assumption. In this case, the thermally excited excitons still have an equilibrium (Bose) distribution, but with spatially varying temperature and chemical potential. The space dependence of the latter quantities is in principle unknown, but from the experiment we can conclude that the temperature should not vary over the dimension of the trap, see section 2.3.1. The only criterion for the spatial dependence  $\mu(\mathbf{r})$  is that the spectra must be reproduced. Therefore, we demand that the spatially integrated spectrum  $I(\omega)$  (at least its high-energy tail) follows a Bose distribution with the spatial temperature and some formal constant chemical potential  $\tilde{\mu}$  which is used to fix the particle number. This leads to

$$\mu(\mathbf{r}) = \left(1 - \frac{T_X}{T_s}\right) (V_{\text{ext}}(\mathbf{r}) + E_0 + 2U_0 n^T(\mathbf{r})) + \frac{T_X}{T_s} \tilde{\mu}, \quad (28)$$

which allows direct use of the theory of section 3.1 in this non-equilibrium situation also.

In what follows, we apply the local equilibrium theory to two typical experimental situations. Thereby we fix the total particle number  $N = 10^8$  and the spatial temperature  $T_s = 0.6$  K and vary the exciton temperature. The condensate contributes to the luminescence with  $S_c = 4 \times 10^{-7}$ . The spatially resolved spectra for both cases are displayed in figure 18, left column. As expected, in the uncondensed case ( $T_X = 0.25$  K, upper row), the spectrum just follows the external potential. The condensed case ( $T_X = 0.15$  K, lower row) with a condensate fraction  $\eta_c = 0.2$  looks qualitatively not very different. In particular, due to the spatial variation of the chemical potential according to equation (28), the flat bottom of the spectrum (cf figure 14) disappears.

In the condensed case ( $T_X = 0.15$  K), the  $z$ -profile of the luminescence exhibits a clearly non-Gaussian shape (figure 18, right column, lower panel, red line). For the slightly higher temperature of  $T_X = 0.25$  K (upper panel), the shape is approximately Gaussian. Therefore, we fit the thermal component of the  $z$ -profile for the condensed case by an asymmetric (due to the potential asymmetry) Gaussian. In order to exclude the condensate contribution, we omit in the fitting procedure the data points in the centre of the trap where the condensate is situated. The size of the excluded area is determined by minimizing the error of the fit. The fitting result is given by the dash-dotted blue line in the lower right figure. It basically follows the thermal profile component. The small deviations from the Gaussian shape are caused by the potential anharmonicity and by the renormalization of the potential due to the interparticle interaction. Thus, the procedure to extract the thermal component from the experimental  $z$ -profiles shown in figure 9, where a Gaussian fit has been applied, too, seems to be justified.

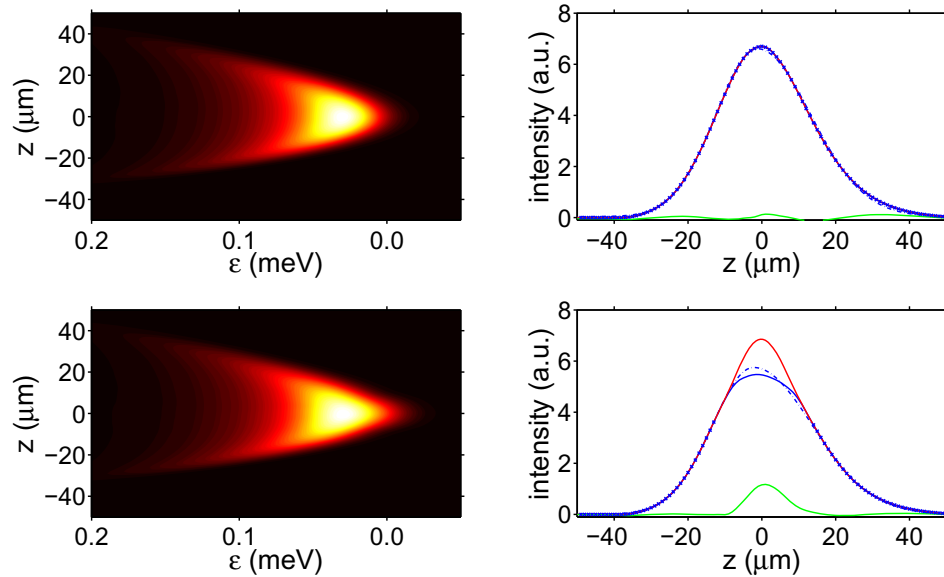


**Figure 18.** Spatially resolved luminescence spectra (left) and  $z$ -profiles of the intensity (right) for  $N = 10^8$  and  $T_s = 0.6$  K. Upper row: exciton temperature  $T_X = 0.25$  K (uncondensed case), lower row:  $T_X = 0.15$  K (condensed case,  $\eta_c = 0.2$ ). Solid red lines: total profiles (thermal + condensate), solid blue: only thermal contribution, dash-dotted blue: Gaussian fit of the total profiles, blue crosses: data points used for the fit, solid green: the difference between the total profile and the fit. The ratio between the integrated intensities of the condensate and of the total band is  $\eta_{\text{lum}} = 0.07$ .

The difference between the total  $z$ -profiles and the Gaussian fits is given by the green lines. It basically reflects the condensate contribution. For the condensed case we obtain a luminescence fraction  $\eta_{\text{lum}} = 0.07$  which would set  $f_{\text{lum}} = 0.25$ .

The two cases depicted in figure 18 can be compared to the measured  $z$ -profiles shown in figure 9. The ‘uncondensed case’ (upper row in figure 18) obviously corresponds, e.g. to measurements 1 and 21, where the difference between data and fit is just noise. On the other hand, the ‘condensed case’ (lower row in figure 18) finds its counterparts, e.g. in measurements 3 and 17. In each case, a striking qualitative agreement is found. This substantially corroborates our explanation of the experimental findings with the occurrence of an excitonic BEC.

Figure 19 shows the critical particle number for BEC dependent on exciton temperature  $T_X$  and spatial temperature  $T_s$ . The global equilibrium case is represented by the diagonal  $T_X = T_s$ . If the excitons are excited outside the trap, their spatial profile will be at first always broader than when in equilibrium. Therefore,  $T_s < T_X$  can be ruled out in the current experiment. Obviously, for a given exciton temperature, the critical number is smallest for global thermal equilibrium and increases with increasing spectral temperature. Even at low powers, i.e. for quite low exciton numbers, a condensate is possible if the exciton temperature is close to the He bath temperature, cf. the situation shown in figure 9, measurement 3, where the spatial temperature is 0.35 K and the exciton number is  $4 \times 10^6$  which just corresponds to the critical number at  $T_X = 0.04$  K.

With the help of this figure, we can systemize the experimentally observed power dependence of the totally integrated intensity shown in figures 11–13. This is done by examining



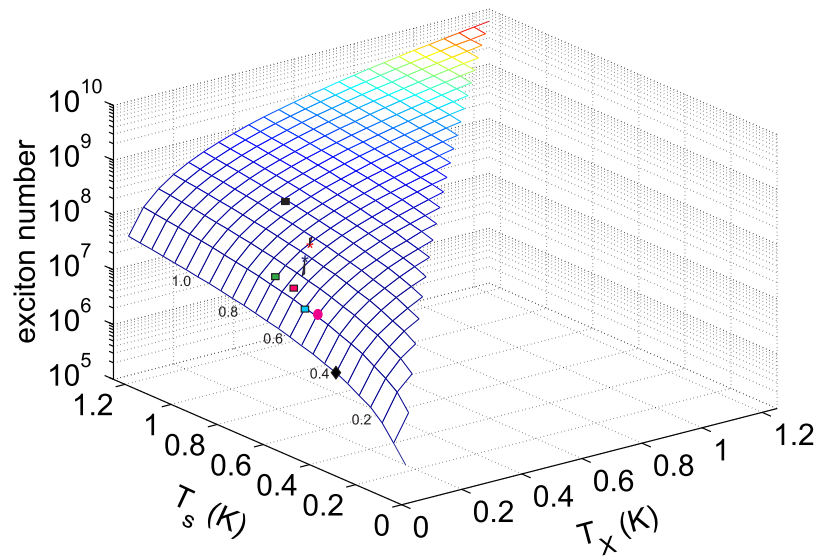


**Figure 19.** Critical particle number  $N_{\text{crit}}$  for BEC versus exciton temperature  $T_X$  and spatial temperature  $T_s$ . The diagonal  $T_X = T_s$  corresponds to global equilibrium;  $T_X > T_s$  is, for excitation outside the trap, physically meaningless. The blue coloured rectangle corresponds to the critical power of  $30 \mu\text{W}$  for the data shown in figure 12 (blue symbols), the red coloured rectangle corresponds to the critical power of  $60 \mu\text{W}$  for the data shown in figure 12 (red symbols), the black coloured rectangle corresponds to the critical power of  $600 \mu\text{W}$  for the data shown in figure 13, and the green coloured rectangle corresponds to the critical power of  $78 \mu\text{W}$  (data not shown). The magenta coloured dot corresponds to the critical power of  $40 \mu\text{W}$  from the measurements shown in figure 11. The stars denote the conditions of measurements 17 (blue) and 18 (red), and the black diamond denotes the critical number for measurement 3, all from figure 7.

the exciton temperature  $T_X$  as the critical number (corresponding to the critical power and the respective spatial temperature) crosses the critical surface. These points are plotted as coloured rectangles in figure 19. The values for  $T_X$  give a very systematic picture. With increasing critical power, both the spatial and the exciton temperature rise. Thereby,  $T_X$  is always larger than the bath temperature, which is consistent with the expected crystal heating, compare appendix C.

Figure 19 also compares the data for the measurements 17 (blue star) and 18 (red star) of figures 7 and 9 showing that the conditions in measurement 17 are such that we are well above  $N_{\text{crate}}$ , while for measurement 18 we are just touching the critical surface.

#### 4. Conclusions and outlook

We have presented a series of experiments that investigate the luminescence from paraexcitons in cuprous oxide after cw-excitation. The excitons have been confined in a potential trap with the host crystal immersed in liquid helium at temperatures down to 38 mK. The spatially resolved luminescence spectra do not show notable variations when varying the laser excitation power from below  $1 \mu\text{W}$  to above 1 mW. However, we observed a number of characteristic changes

in the spatial profiles of the luminescence and in the totally integrated intensity: In the spatial profiles, a new component in the centre of the trap occurs at intermediate laser powers which cannot be fitted by a thermal Gaussian distribution. This component vanishes at very low power and at very high power levels. At the mentioned intermediate power levels, we see deviations from the linear dependence of the totally integrated intensity on the laser power: most notably a well defined kink appears in the slope of the curves. From the linear dependence of the total intensity on laser power, we conclude that two-body decay processes of the excitons do not play any significant role. This is in agreement with previous measurements under pulsed excitation in the same samples [17].

With increasing laser power, we observe a slight increase in the effective temperature that is inferred from the high-energy tail of the luminescence spectra from 0.35 K up to a maximum of 1 K. This spectral temperature does only reflect the spatial distribution of excitons in the trap and is not identical to the local temperature which determines the energy distribution of the excitons at each point in the trap. The local temperature will be determined by exciton relaxation processes and is expected to go down almost to the bath temperature at low excitation power.

Recently, [15] reported a strong heating of the exciton gas at high pump powers and claimed that this effect originates from a relaxation explosion of excitons when a transition into a Bose–Einstein condensate takes place. We observe a similar heating under high excitation powers but can definitely rule out the existence of a BEC in this high power range.

In order to understand the observed features of the luminescence spectra, we theoretically analysed the thermodynamics and the luminescence properties of excitons in a potential trap. Thereby the excitons are described as an interacting Bose gas in the framework of a Hartree–Fock–Bogoliubov–Popov approach. Already under the assumption of global thermal equilibrium, this theoretical approach suggests that the observed kink in the totally integrated intensity signals the transition into a Bose–Einstein condensate of trapped paraexcitons. Taking into account the specific non-equilibrium situation in the trap, the theory also consistently describes the characteristic changes in the spatial profiles of the luminescence: while the theory predicts almost no changes in the spatially resolved spectra, it allows us to identify the additional component in the spatial profiles as due to a weakly luminescing condensate.

To conclude, we have presented strong evidence, both from experiment and theory, that at ultracold temperatures in the range of 100 mK, paraexcitons in  $\text{Cu}_2\text{O}$  undergo a transition into a Bose–Einstein condensate.

Nevertheless, further experimental investigations are necessary to prove the existence of a BEC of excitons in cuprous oxide beyond any doubt. For example, direct measurements of the lattice temperature and of the local exciton temperature will provide a better understanding of the thermodynamics. Thereby, it might be intriguing to apply spatially resolved Brillouin scattering since the energies of the phonons involved are comparable to the thermal energy. The local exciton temperature would be detectable via infrared absorption of the 1S–2P transition [29, 30]. The most important aspect, however, must be the direct proof of the macroscopic coherence of the condensate by interferometric methods or by means of intensity correlation measurements, both currently under way.

Theoretically, one can try to improve the exciton density calculations by using more advanced approximations, e.g. by solving the Gross–Pitaevskii equation exactly instead of using the Thomas–Fermi approximation. It also seems to be necessary to improve the luminescence theory in order to account, more rigorously, for the inhomogeneity of the system,

e.g. following the ideas of [59]. Moreover, one should also include the spectral broadening due to exciton–exciton interaction. This would require the inclusion of higher order correlations beyond the Hartree–Fock–Bogoliubov–Popov approximation by calculating the densities and the spectral function on the level of the Beliaev approximation [60]. Recently, we have shown that, already for the thermal excitons, a more realistic description requires us to take the lifetime broadening of the exciton states into account [17], which relaxes the strict wave vector conservation in (24).

Quite recent results by Naka *et al* [25] show that the Auger-decay produces a significant number of free electrons and holes which are also captured by the trap (see figure 2). This should lead to a shift and a broadening of the exciton states by the surrounding electron–hole plasma [6, 7, 61, 62]. An inclusion of this ‘plasma damping’ in the theory requires taking into account collisions of the excitons with charged fermions. This is clearly beyond the scope of the theory of weakly interacting bosons.

### Acknowledgments

We thank Dietmar Fröhlich (Dortmund) for supplying the sample. Furthermore, we thank him, Günter Manzke and Wolf-Dietrich Kraeft (Rostock), Manfred Bayer, Jan Brandt, and Christian Sandfort (Dortmund), and Andreas Alvermann (Greifswald) for many helpful discussions and critical comments. Our special thanks go to Herwig Ott (Kaiserslautern) for lending us the CR599 laser system. We acknowledge the support by the Deutsche Forschungsgemeinschaft (Collaborative Research Center SFB 652 ‘Starke Korrelationen im Strahlungsfeld’) and by JSPS KAKENHI (grant no. 21740227).

### Appendix A. Strain Hamiltonian for electron–hole states

For the derivation of the energy shifts of electron–hole pairs we consider that the top  $\Gamma_7^+$  valence band states can be written as [9]

$$\Psi_{+1/2}^7 = -\frac{1}{\sqrt{6}} [(Y_2^{-2} - Y_2^2)\alpha_v + 2Y_2^{-1}\beta_v], \quad (\text{A.1})$$

$$\Psi_{-1/2}^7 = +\frac{1}{\sqrt{6}} [(Y_2^{-2} - Y_2^2)\beta_v - 2Y_2^1\alpha_v]. \quad (\text{A.2})$$

Here  $Y_2^m$  denotes the spherical harmonics and  $\alpha_{c,v}$ ,  $\beta_{c,v}$  the electron spin functions of the valence and conduction bands. By inspection of table VI of [9] we immediately see the paraexciton state

$$\Phi_{12} = \Phi_{\text{YS}} \frac{1}{\sqrt{2}} (\Psi_{-1/2}^7\alpha_c + \Psi_{+1/2}^7\beta_c) \quad (\text{A.3})$$

with  $\Phi_{\text{YS}}$  being the envelope function of the yellow 1S state. We immediately see that the paraexciton state has the same behaviour as the  $\Gamma_7^+$  band states. In all matrix elements of the strain Hamiltonian, all terms containing the electron–hole exchange are missing. Since the interaction with the  $\Gamma_8^+$  states does not change, the electron–hole pairs show the same behaviour under strain, i.e. they experience an effective trapping potential similar to the paraexcitons.

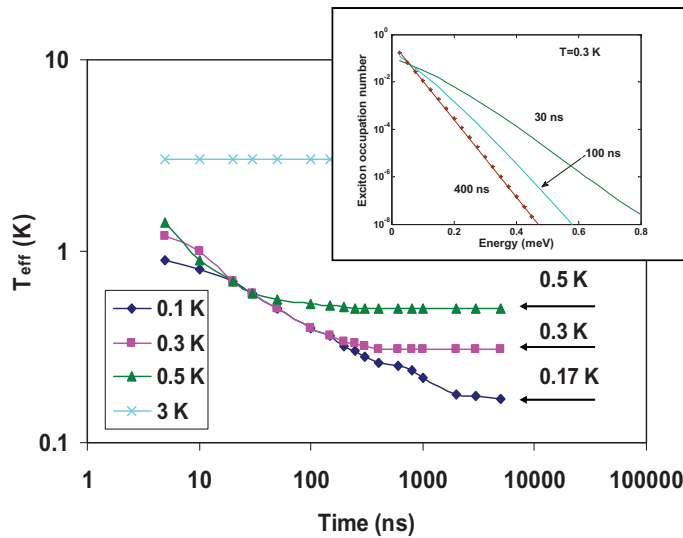


**Figure B.1.** Cooling behaviour of laser excited paraexcitons for different bath temperatures. Plotted are the effective temperatures of the distribution function obtained by fitting with a Bose distribution. The cooling curve for a lattice temperature of 0.05 K is identical to that of 0.1 K. The inset shows as an example the distribution for a lattice temperature of 0.3 K, an exciton density of  $n = 1 \times 10^{15} \text{ cm}^{-3}$  at  $t = 100 \text{ ns}$  from which a temperature of  $T_{\text{eff}} = 0.33 \text{ K}$  is derived.

## Appendix B. Exciton relaxation

A central problem in the dynamics of excitons at milli-Kelvin temperatures is the relaxation and thermalization by contact to a bath of thermal phonons, as the acoustical modes will freeze out [63]. Therefore, we have simulated the relaxation of hot, laser excited excitons by assuming interactions with longitudinal acoustic phonons and Auger-like two-particle decay in a potential trap by integrating the Boltzmann equation [28]. Here we present additional results for the homogeneous situation including elastic exciton–exciton scattering, where the model follows closely that described in [64–66]. The resulting system of differential equations was integrated using as an initial distribution a Gaussian of width 0.1 meV centred at  $e_L = 5 \text{ meV}$ . The initial exciton density was assumed to be  $n_0 = 1 \times 10^{15} \text{ cm}^{-3}$ . For the elastic exciton–exciton scattering cross section  $\sigma = 50 \text{ nm}^2$  [66] was taken. The main results are shown in figure B.1, where the effective temperature of the exciton gas obtained by fitting the distribution function by a Bose distribution (see inset) is plotted for different lattice temperatures as a function of time.

## Appendix C. Thermal behaviour of the dilution refrigerator and the sample

The  $^3\text{He}/^4\text{He}$  dilution cryostat uses a mixture of  $^3\text{He}$  and  $^4\text{He}$  for the cooling process. The coldest region is inside the mixing chamber, consisting of a  $^3\text{He}$ -rich (100%  $^3\text{He}$ ) and a  $^3\text{He}$ -poor (6.4%  $^3\text{He}$ ) phase separated by a phase boundary, the basic thermodynamics of which is well known [67]. In the following analysis, we assume that the sample is immersed inside

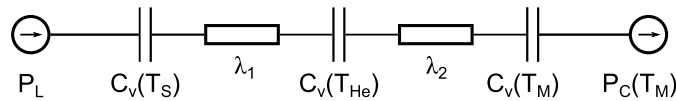


**Figure C.1.** A thermal network describing the sample and mixing chamber in the  $^3\text{He}/^4\text{He}$  dilution cryostat. For an explanation, see text.

the dilute  $^3\text{He}/^4\text{He}$  mixture and that the resistor measuring the bath temperature is placed in between the sample and the phase boundary in the mixing chamber.

To derive a connection between the sample temperature and the measured bath temperature we have to consider the whole system as a thermal network as shown in figure C.1. The incoming laser beam with power  $P_L$  hits the sample which is at a temperature  $T_S$  and has a heat capacity  $C_v(T_S)$ . It is surrounded by the dilute  $^3\text{He}/^4\text{He}$  mixture (temperature  $T_{\text{He}}$ ), which itself is connected to the mixing chamber at a temperature  $T_M$  with heat capacities  $C_v(T_{\text{He}})$  and  $C_v(T_M)$ , respectively. The mixing chamber is cooled with a power  $P_C(T_M)$  depending on its temperature. The heat conduction between the different compartments is represented by the heat conductivities  $\lambda_1$  and  $\lambda_2$ . Applying the continuity equation for the energy flow, the network is described by the following system of equations:

$$C_v(T_S) \frac{dT_S}{dt} = F_{\text{heat}}(P_L) - \lambda_1(T_S - T_{\text{He}}), \quad (\text{C.1})$$

$$C_v(T_{\text{He}}) \frac{dT_{\text{He}}}{dt} = \lambda_1(T_S - T_{\text{He}}) - \lambda_2(T_{\text{He}} - T_M), \quad (\text{C.2})$$

$$C_v(T_M) \frac{dT_M}{dt} = \lambda_2(T_{\text{He}} - T_M) - P_C(T_M). \quad (\text{C.3})$$

Here  $F_{\text{heat}}$  gives the connection between the laser input power and the heat generated in the sample due to the excitonic relaxation and decay processes (compare section 2.2). For the parameters given in table 1, the results are shown in figure C.2. We can approximate the dependence with a function of the form

$$F_{\text{heat}} = \alpha P_L + \beta \left[ P_{\text{XX}} \left( \sqrt{1 + P_L/P_{\text{XX}}} - 1 \right) \right]^2 \quad (\text{C.4})$$

with the fit parameters  $\alpha = 0.045$ ,  $\beta = 0.014 \mu\text{m}^{-1}$  and  $P_{\text{XX}} = 16.67 \mu\text{W}$ .

### C.1. Heat capacities

Regarding the heat capacity of the *sample*, it is necessary to take into consideration that not only the crystal is heated by the laser, but, due to the good thermal contact supplied by the pressure on the sample, also the sample holder, which consisted of pure titanium. Therefore, we assumed the temperatures of sample and sample holder to be the same. The variation of the heat capacity of the sample  $\text{Cu}_2\text{O}$  with temperature is well approximated by the Debye model as a  $T^3$  temperature dependence. A fit of measured data [68] by

$$C_{v\text{Cu}_2\text{O}} = AT^B, \quad (\text{C.5})$$

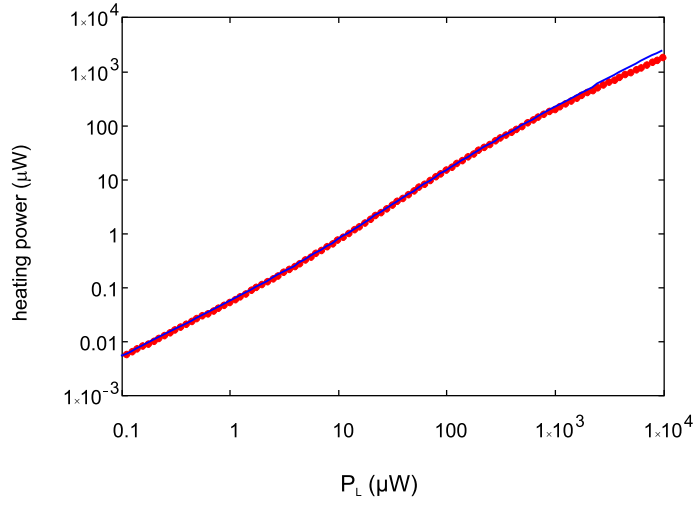


**Figure C.2.** Comparison of the amount of heating as a function of laser power. The full red dots are obtained from the rate model of section 2.2, the full line is the fit according to equation (C.4).

results in the parameters  $A = 8.06 \pm 0.05 \text{ J mol}^{-1} \text{ K}^{-4}$  and  $B = 3.0 \pm 0.05$ . For the specimen holder, we consider only the superconducting state below the critical temperature ( $T_{\text{cTi}} = 0.4 \text{ K}$  [69]), restricting the following analysis to the interesting case of  $T_{\text{S}} < 0.4 \text{ K}$ . Here, the heat capacity is composed of an electron and a phonon part,  $C_{\text{vTi}} = C_{\text{ve}} + C_{\text{vph}}$ . While the phonon part is negligible, the electron part is given by

$$C_{\text{vTi}} = C_{\text{ve}} = C_{\text{Ti}} \gamma_{\text{Ti}} T_{\text{c}} \exp\left(\frac{-1.5T_{\text{c}}}{T}\right), \quad (\text{C.6})$$

with  $C_{\text{Ti}} = 9.17$  and the Sommerfeld constant  $\gamma_{\text{Ti}} = 3.3 \text{ mJ mol}^{-1} \text{ K}^{-2}$  [69].

Experimental data for the *heat capacity of the helium mixture* [70] for different concentrations of  $^3\text{He}$  in  $^4\text{He}$  were interpolated to a concentration of  $x_{^3\text{He}} = 6.4\%$  and fitted resulting in a dependence

$$C_{\text{v}}(T_{\text{He,M}}) = D \left(\frac{T_{\text{He,M}}}{\text{K}}\right)^E + F, \quad (\text{C.7})$$

with  $D = 0.417 \text{ J mol}^{-1} \text{ K}^{-1}$ ,  $E = 6.117$  and  $F = 0.7 \text{ J mol}^{-1} \text{ K}^{-1}$ .

## C.2. Cooling power

For the description of the cooling power  $P_{\text{C}}$  of the dilution process, where the  $^3\text{He}$ -atoms flow from the  $^3\text{He}$ -rich (concentrated) to the -poor (dilute) phase, we consider the enthalpy of the system. By assuming that pure  $^3\text{He}$  flows through the heat exchangers into the mixing chamber with the dilute phase, the cooling power is given in accordance with [67] by

$$P_{\text{C}} = \dot{n}_3 [H_{\text{d}}(T) - H_{\text{c}}(T)] \quad (\text{C.8})$$

$$= \dot{n}_3 [95T_{\text{M}}^2 - 11T_{\text{W}}^2], \quad (\text{C.9})$$

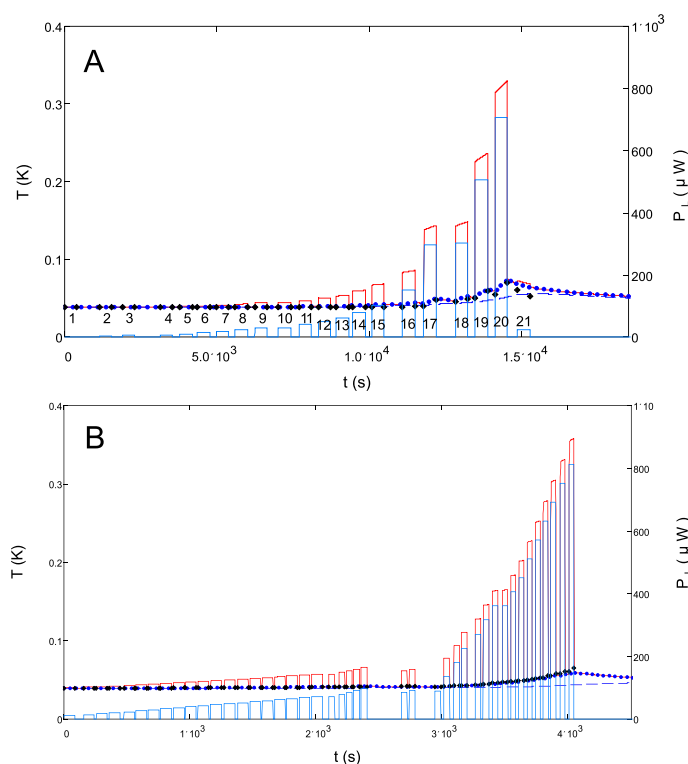


**Figure C.3.** The numerical solution of the system of differential equations expressed as the variation of temperature (cf equations (C.2) and (C.3)) with measurement time for  $\lambda_1 = 6 \times 10^{-4}$  and  $\lambda_2 = 27 \times 10^{-4} \text{ W K}^{-1}$ . The solid red framed bars represent the temperature of the sample  $T_S$ , the blue dotted curve shows the temperature of the surrounding helium bath  $T_{\text{He}}$  and the blue dashed line describes the temperature in the mixing chamber  $T_M$ . The solid blue framed bars are the representation of the measured incoming laser power  $P_L$ . The measured helium temperatures are shown as black diamonds.

with the molar flow rate  $\dot{n}_3$ , the temperature in the mixing chamber  $T_M$  and the temperature behind the heat exchanger  $T_W$ . To obtain the unknown parameters of equation (C.9), we take as calibration points the lowest temperature reached without any heat load  $T_M = 20 \text{ mK}$  and  $P_C = 100 \mu\text{W}$  at  $T_M = 100 \text{ mK}$ . From these data we obtain  $\dot{n}_3 = 1.25 \times 10^{-4} \text{ mol s}^{-1}$  and  $T_W = 0.115 \text{ K}$ . From this cooling power we have to subtract the heat load  $P_0$  due to the cryostat windows, which leads to a minimum temperature of  $T_M = 38 \text{ mK}$  corresponding to a power of  $P_0 = 13.4 \mu\text{W}$ .

### C.3. Determination of the temperatures in the cryostat system

To obtain the temperatures of the different parts of the thermal network from the system of coupled differential equations, it is necessary to specify the amount of substance in the system.

The  $\text{Cu}_2\text{O}$  specimen is a cube with an edge length of 3 mm, a molar mass of  $M = 143.09 \text{ g mol}^{-1}$  and a density of  $\rho = 6.48 \text{ g cm}^{-3}$ . Hence, the amount of substance inside the cube is  $n_{\text{Cu}_2\text{O}} = 1.398 \times 10^{-3} \text{ mol}$ . From the measured weight of the titanium sample holder

of  $m = 26$  g and a molar mass of  $M = 47.9$  g mol<sup>-1</sup>, we obtain  $n_{\text{Ti}} = 0.5$  mol. The amount of substance in the helium mixture can only be estimated. In our system, a 15% helium <sup>3</sup>He/<sup>4</sup>He mixture of approximately  $V = 400$  l circulates under a pressure of  $p = 0.8$  bar. That leads to an amount of  $n_{\text{He}/^4\text{He}}$  mixture = 14.3 mol from which only about two thirds are in the mixing chamber. For our calculations, we assume that 1 mol is in the bath and 2.75 mol is in the mixing chamber. Then the only quantities which have still to be specified are the heat conductivities  $\lambda_{1,2}$ . This was done by adjusting the solutions of the coupled differential equations to different measurements until all the data could be described by the same set of parameters. As examples we show in figure C.3 the results for the series of measurements from figures 5 and 6.

The calculations were done with  $\lambda_1 = 6 \times 10^{-4}$  and  $\lambda_2 = 27 \times 10^{-4}$  W K<sup>-1</sup> and show an almost quantitative agreement with the experimental data, despite very large changes in laser power (solid blue framed bars) during the measurements, which indicates the correctness of our model.

## References

- [1] Blatt J M, Böer K W and Brandt W 1962 *Phys. Rev.* **126** 1691
- [2] Moskalenko S A 1962 *Fiz. Tverd. Tela* **4** 276  
Moskalenko S A 1962 *Sov. Phys. Solid State* **4** 276 (Engl. transl.)
- [3] Fröhlich D, Kenkies R, Uihlein C and Schwab C 1979 *Phys. Rev. Lett.* **43** 1260
- [4] Snoke D W 2002 *Science* **298** 1368
- [5] Alvermann A, Littlewood P B and Fehske H 2011 *Phys. Rev. B* **84** 035126
- [6] Semkat D, Richter F, Kremp D, Manzke G, Kraeft W-D and Henneberger K 2009 *Phys. Rev. B* **80** 155201
- [7] Manzke G, Semkat D, Richter F, Kremp D and Henneberger K 2010 *J. Phys.: Conf. Ser.* **210** 012020
- [8] Fröhlich D, Kulik A, Uebbing B, Mysyrowicz A, Langer V, Stolz H and von der Osten W 1991 *Phys. Rev. Lett.* **67** 2343
- [9] Waters R G, Pollak F H, Bruce R H and Cummins H Z 1980 *Phys. Rev. B* **21** 1665
- [10] Pethick C J and Smith H 2002 *Bose–Einstein Condensation in Dilute Gases* (Cambridge: Cambridge University Press)
- [11] Trauernicht D P, Wolfe J P and Mysyrowicz A 1986 *Phys. Rev. B* **34** 2561
- [12] Snoke D W, Wolfe J P and Mysyrowicz A 1990 *Phys. Rev. Lett.* **64** 2543
- [13] Lin J-L and Wolfe J P 1993 *Phys. Rev. Lett.* **71** 1222
- [14] Snoke D W and Negoita V 2000 *Phys. Rev. B* **61** 2904
- [15] Yoshioka K, Chae E and Kuwata-Gonokami M 2011 *Nature Commun.* **2** 328
- [16] Denev S and Snoke D W 2002 *Phys. Rev. B* **65** 085211
- [17] Schwartz R, Naka N, Kieseling F and Stolz H 2012 *New J. Phys.* **14** 023054
- [18] Sandfort Ch, Brandt J, Finke Ch, Fröhlich D, Bayer M, Stolz H and Naka N 2011 *Phys. Rev. B* **84** 165215
- [19] Deng H, Haug H and Yamamoto Y 2010 *Rev. Mod. Phys.* **82** 1489
- [20] Szymańska M H, Keeling J and Littlewood P B 2007 *Phys. Rev. B* **75** 195331
- [21] Aßmann M, Tempel J-S, Veita F, Bayer M, Rahimi-Iman A, Löffler A, Höfling S, Reitzenstein S, Worschech L and Forchel A 2011 *Proc. Natl Acad. Sci. USA* **108** 1804
- [22] Brandt J, Fröhlich D, Sandfort Ch, Bayer M, Stolz H and Naka N 2007 *Phys. Rev. Lett.* **99** 217403
- [23] Wolfe J P, Markiewicz R S, Kittel C and Jeffries C D 1977 *Phys. Rev. B* **15** 1988
- [24] Naka N and Nagasawa N 2002 *Phys. Rev. B* **65** 075209
- [25] Naka N, Akimoto I, Shirai M and Kan’no K 2012 *Phys. Rev. B* **85** 035209
- [26] Kavoulakis G M, Baym G and Wolfe J P 1996 *Phys. Rev. B* **53** 7227
- [27] Ashcroft N W and Mermin N D 1976 *Solid State Physics* (Fort Worth, TX: Harcourt Brace College Publishers)
- [28] Som S, Kieseling F and Stolz H 2012 *J. Phys.: Condens. Matter* **24** 335803



- [29] Jörger M, Fleck T, Klingshirn C and von Baltz R 2005 *Phys. Rev. B* **71** 235210
- [30] Kubouchi M, Yoshioka K, Shimano R, Mysyrowicz A and Kuwata-Gonokami M 2005 *Phys. Rev. Lett.* **94** 016403
- [31] Stolz H and Semkat D 2010 *Phys. Rev. B* **81** 081302
- [32] Griffin A 1996 *Phys. Rev. B* **53** 9341
- [33] Dalfovo F, Giorgini S, Pitaevskii L P and Stringari S 1999 *Rev. Mod. Phys.* **71** 463
- [34] Bergeman T, Feder D L, Balazs N L and Schneider B I 2000 *Phys. Rev. A* **61** 063605
- [35] Proukakis N P and Jackson B 2008 *J. Phys. B: At. Mol. Opt. Phys.* **41** 203002
- [36] Bányai L A, Bundaru A M and Haug H 2004 *Phys. Rev. B* **70** 045201
- [37] Ho T L and Shenoy V B 1996 *Phys. Rev. Lett.* **77** 3276
- [38] Bashkin E P and Vagov A V 1997 *Phys. Rev. B* **56** 6207
- [39] Shi H, Zheng W M and Chui S T 2000 *Phys. Rev. A* **61** 063613
- [40] Zhang W, Yi S and You L 2004 *Phys. Rev. A* **70** 043611
- [41] Chang M-S, Qin Q, Zhang W, You L and Chapman M S 2005 *Nature Phys.* **1** 111
- [42] Shelykh I A, Malpuech G and Kavokin A V 2005 *Phys. Status Solidi a* **202** 2614
- [43] Kasprzak J, André R, Dang L S, Shelykh I A, Kavokin A V, Rubo Yu G, Kavokin K V and Malpuech G 2007 *Phys. Rev. B* **75** 045326
- [44] Sobkowiak S, Semkat D, Stolz H, Koch Th and Fehske H 2010 *Phys. Rev. B* **82** 064505
- [45] Sheboul M I and Ekardt W 1976 *Phys. Status Solidi b* **73** 165
- [46] Ciuti C, Savona V, Piermarocchi C, Quattropani A and Schwendimann P 1998 *Phys. Rev. B* **58** 7926
- [47] Okumura S and Ogawa T 2001 *Phys. Rev. B* **65** 035105
- [48] Zimmermann R and Schindler Ch 2007 *Solid State Commun.* **144** 395
- [49] Schindler Ch and Zimmermann R 2008 *Phys. Rev. B* **78** 045313
- [50] Combescot M, Betbeder-Matibet O and Dubin F 2008 *Phys. Rep.* **463** 215
- [51] Shi H, Verechaka G and Griffin A 1994 *Phys. Rev. B* **50** 1119
- [52] Haug H and Kranz H 1983 *Z. Phys. B* **53** 151
- [53] Kreingold F I and Makarov V L 1975 *Sov. Phys. Semicond.* **8** 962
- [54] Born M and Wolf E 1999 *Principles of Optics* 7th edn (Cambridge: Cambridge University Press)
- [55] Shumway J and Ceperley D M 2001 *Phys. Rev. B* **63** 165209
- [56] Ivanov I A, Mitroy J and Varga K 2002 *Phys. Rev. A* **65** 022704
- [57] Shumway J and Ceperley D M 2005 *Solid State Commun.* **134** 19
- [58] Sharma H, Kumari K and Chakraborty S 2009 *Eur. Phys. J. D* **53** 189
- [59] Richter F, Florian M and Henneberger K 2008 *Phys. Rev. B* **78** 205114
- [60] Hohenberg P C and Martin P C 1965 *Ann. Phys., NY* **34** 291
- [61] Nägerl J S, Stabenau B, Böhne G, Dreher S, Ulbrich R G, Manzke G and Henneberger K 2001 *Phys. Rev. B* **63** 235202
- [62] Semkat D, Richter F, Kremp D, Manzke G, Kraeft W-D and Henneberger K 2010 *J. Phys.: Conf. Ser.* **220** 012005
- [63] Brandt J, Felbier P, Fröhlich D, Sandfort Ch, Bayer M and Stolz H 2010 *Phys. Rev. B* **81** 155214
- [64] Ell C, Ivanov A L and Haug H 1998 *Phys. Rev. B* **57** 9663
- [65] Snoke D W, Braun D and Cardona M 1991 *Phys. Rev. B* **44** 2991
- [66] O'Hara K E and Wolfe J P 2000 *Phys. Rev. B* **62** 12909
- [67] Enss Ch and Hunklinger S 2000 *Tiefemperaturphysik* (Berlin: Springer)
- [68] Gregor L V 1962 *J. Phys. Chem.* **66** 1645
- [69] Martienssen W and Warlimont H 2005 *Springer Handbook of Condensed Matter and Materials Data* (Berlin: Springer)
- [70] De Bruyn Ouboter R, Taconis K W, Le Pair C and Beenakker J J M 1960 *Physica* **26** 853



# Theory of zero-phonon decay luminescence of semiconductor excitons

Thomas Koch<sup>1,\*</sup>, Dirk Semkat<sup>2</sup>, Heinrich Stolz<sup>2</sup>, and Holger Fehske<sup>1</sup>

Received 6 June 2016, revised 11 August 2016, accepted 12 August 2016

Published online 26 September 2016

We present a theoretical approach to the zero-phonon decay luminescence of excitons. In a two-step approach, the weakly interacting condensed exciton gas is Bogolyubov transformed before the resulting quasiparticles are coupled to the photon field. The field–field correlation function, which gives the luminescence intensity and first-order coherence, is calculated in the framework of real-time Green's functions of the photons. The resulting spectrum of the new, so-called bogolariton, quasiparticles is discussed.

## 1 Introduction

Excitons in excited semiconductors have been suggested as promising candidates for the observation of Bose–Einstein condensation (BEC) more than five decades ago [1, 2]. Due to their rather small mass comparable to the free electron mass, the conditions for densities and temperatures should be easily achievable in the experiment. However, despite many efforts creating a dense gas of excitons either in a bulk crystal or in a potential trap, a conclusive demonstration of excitonic BEC is still missing.

At present, cuprous oxide (Cu<sub>2</sub>O) is in the focus of both experimental and theoretical efforts (for a recent overview see Ref. [3]), namely because of the large binding energy and the long lifetime of the exciton states in this material [4, 5]. In current experiments, entrapment of the excitons in a strain induced external potential is used to obtain sufficiently high particle densities. Due to the strain, the usually forbidden direct (zero-phonon) decay of lowest paraexciton state becomes weakly allowed. As a consequence, the excitonic system is accessible by the exciton decay luminescence, which should feature signatures of exciton condensation. The most obvious evidence, of course, would be the detection of coherence. On the other hand, an exciton condensate is also reflected in the luminescence and photon spectra [6, 7]. Theory must provide, therefore,

an approach both to coherence as well as spectral properties of the luminescence signal.

Previous theoretical approaches to the excitonic decay luminescence [8, 9] were based on an exciton-photon coupling Hamiltonian containing only “normal” terms, i.e., the creation of a photon and simultaneous destruction of an exciton. However, since the Bogolyubov picture of exciton condensation accounts for anomalous exciton-exciton interaction terms, anomalous exciton-photon coupling terms should also be included when deriving the luminescence. This allows to account for the polariton effect in a very general manner. In contrast to microcavity systems, the trapped excitons couple to free photon modes. Then the exciton–photon interaction is inherently a quasi-equilibrium problem, where the luminescence should take place via transient polariton-like states.

In the following, we start with a brief summary of the thermodynamics of excitons in a potential trap, where the exciton Hamiltonian is diagonalised by a Bogolyubov transformation. Then we elaborate in detail the coupling of the Bogolyubov quasiparticles to the photon field. Within a Green's functions framework, we analyse the resulting new quasiparticle dispersion and discuss its consequences for the field–field correlation function and the decay luminescence intensity.

## 2 Trapped exciton gas

Since in Cu<sub>2</sub>O the paraexciton lifetime far exceeds the time to reach thermal (quasi-)equilibrium [10, 11], for the moment we do not consider recombination and

<sup>1</sup> Institut für Physik, Ernst–Moritz–Arndt–Universität Greifswald, 17489 Greifswald, Germany

<sup>2</sup> Institut für Physik, Universität Rostock, 18051 Rostock, Germany

\* Corresponding author E-mail: thomas.koch@physik.uni-greifswald.de

neglect the coupling to the light field. Consequently, we model the trapped excitons as a gas of structureless, interacting bosons in an external potential. Furthermore, the extension of the potential trap is considered to be large compared to the thermal de Broglie wavelength of the excitons. That is why we apply the local density approximation, i.e., we treat the excitons as a locally homogeneous system where the spatial dependence enters only via  $V_{\text{ext}}(\mathbf{r})$ . With the  $\mathbf{r}$  argument omitted for brevity, the corresponding Hamiltonian in the grand canonical ensemble reads

$$\hat{H}_x = \sum_{\mathbf{q}} \left( \frac{\hbar^2 q^2}{2m} + E_g + V_{\text{ext}} - \mu \right) \hat{B}_{\mathbf{q}}^\dagger \hat{B}_{\mathbf{q}} + \frac{U}{2V} \sum_{\mathbf{q}, \mathbf{p}, \mathbf{k}} \hat{B}_{\mathbf{p}+\mathbf{q}}^\dagger \hat{B}_{\mathbf{k}-\mathbf{q}}^\dagger \hat{B}_{\mathbf{p}} \hat{B}_{\mathbf{k}}, \quad (1)$$

with the creation (annihilation) operators  $\hat{B}_{\mathbf{q}}^\dagger$  ( $\hat{B}_{\mathbf{q}}$ ) of excitons with wave vector  $\mathbf{q}$ , the effective exciton mass  $m$ , the excitonic gap energy  $E_g$  (i.e., the band gap minus the exciton binding energy), the trapping potential  $V_{\text{ext}}$  and the equilibrium chemical potential  $\mu$ . We assume solely contact interaction whose strength is given by the s-wave scattering length  $a_s$ :

$$U = \frac{4\pi \hbar^2 a_s}{m}. \quad (2)$$

To account for a possible exciton condensate, we apply to Eq. (1) the Bogolyubov prescription, i.e., we replace the operators  $\hat{B}_0^{(\dagger)}$  by  $\sqrt{N_c}$ , where  $N_c$  is the number of condensed particles. Accordingly, from now on the operators  $\hat{B}_{\mathbf{q}}$  refer to the non-condensed particles with  $\mathbf{q} \neq 0$ . Retaining only those parts of the Hamiltonian that are quadratic in  $\hat{B}_{\mathbf{q}}$ , we have

$$\hat{H}_x \approx E_c + \sum_{\mathbf{q}} \left( \frac{\hbar^2 q^2}{2m} + E_g + V_{\text{ext}} - \mu \right) \hat{B}_{\mathbf{q}}^\dagger \hat{B}_{\mathbf{q}} + \frac{Un_c}{2} \sum_{\mathbf{q} \neq 0} \left( 2\hat{B}_{\mathbf{q}}^\dagger \hat{B}_{\mathbf{q}} + \hat{B}_{\mathbf{q}}^\dagger \hat{B}_{-\mathbf{q}}^\dagger + \hat{B}_{\mathbf{q}} \hat{B}_{-\mathbf{q}} \right), \quad (3)$$

with the energy  $E_c$  of the condensate.

The quadratic Hamiltonian in Eq. (3) may be diagonalised by the Bogolyubov transformation

$$\hat{B}_{\mathbf{q}} = u_{\mathbf{q}} \hat{b}_{\mathbf{q}} - v_{-\mathbf{q}}^* \hat{b}_{-\mathbf{q}}^\dagger. \quad (4)$$

The new operators  $\hat{b}_{\mathbf{q}}^{(\dagger)}$  obey the bosonic commutation relations  $[\hat{b}_{\mathbf{q}}, \hat{b}_{\mathbf{q}'}^\dagger] = \delta_{\mathbf{q}, \mathbf{q}'}$ , provided the Bogolyubov amplitudes  $u_{\mathbf{q}}$  and  $v_{\mathbf{q}}$  satisfy the relation  $|u_{\mathbf{q}}|^2 - |v_{-\mathbf{q}}|^2 = 1$ . Under this condition, the anomalous terms in the Hamil-

tonian vanish for

$$u_{\mathbf{q}}^2(\mathbf{r}) = \frac{1}{2} \left( \frac{L_{\mathbf{q}}(\mathbf{r})}{E_{\mathbf{q}}(\mathbf{r})} + 1 \right), \quad (5)$$

$$v_{\mathbf{q}}^2(\mathbf{r}) = \frac{1}{2} \left( \frac{L_{\mathbf{q}}(\mathbf{r})}{E_{\mathbf{q}}(\mathbf{r})} - 1 \right). \quad (6)$$

Here,  $E_{\mathbf{q}}$  is the Bogolyubov dispersion

$$E_{\mathbf{q}}(\mathbf{r}) = \sqrt{L_{\mathbf{q}}^2(\mathbf{r}) - U^2 n_c^2(\mathbf{r})}, \quad (7)$$

$$L_{\mathbf{q}}(\mathbf{r}) = \frac{\hbar^2 q^2}{2m} - \mu + E_g + V_{\text{ext}}(\mathbf{r}) + 2Un(\mathbf{r}), \quad (8)$$

and  $n = n_c + n_T$  is the total particle density. The density of thermal excitations follows as

$$n_T(\mathbf{r}) = \int \frac{d^3 q}{8\pi^3} \left[ \frac{L_{\mathbf{q}}(\mathbf{r})}{E_{\mathbf{q}}(\mathbf{r})} \left( n_B(E_{\mathbf{q}}(\mathbf{r})) + \frac{1}{2} \right) - \frac{1}{2} \right] \Theta(E_{\mathbf{q}}(\mathbf{r})^2), \quad (9)$$

with  $n_B(E) = [\exp(E/k_B T) - 1]^{-1}$ , while the Thomas-Fermi result for the density of trapped condensate particles reads [12]

$$n_c(\mathbf{r}) = \max\{0, \frac{1}{U} (\mu - V_{\text{ext}}(\mathbf{r}) - E_g - 2Un_T(\mathbf{r}))\}. \quad (10)$$

As is well known, the Bogolyubov quasiparticles, the so-called bogolons, represent phonon like excitations in the long wavelength limit and free excitons in the limit of large  $\mathbf{q}$ . The excitonic spectral function  $A_{BB}(\mathbf{q}, \omega, \mathbf{r})$  features two branches at  $\hbar\omega = \pm E_{\mathbf{q}}$ , weighted by the Bogolyubov amplitudes:

$$A_{BB}(\mathbf{q}, \omega, \mathbf{r}) = 2\pi \hbar [u_{\mathbf{q}}^2(\mathbf{r}) \delta(\hbar\omega - E_{\mathbf{q}}(\mathbf{r})) - v_{\mathbf{q}}^2(\mathbf{r}) \delta(\hbar\omega + E_{\mathbf{q}}(\mathbf{r}))]. \quad (11)$$

In the non-condensed situation, i.e. for  $n_c = 0$  and  $E_{\mathbf{q}} = L_{\mathbf{q}}$ , we have  $v_{\mathbf{q}} = 0$  and  $u_{\mathbf{q}} = 1$ , so that only one spectral branch remains and the Bogolyubov quasiparticles become free excitons in a Hartree-Fock mean field.

### 3 Bogolon-photon coupling

Excitons decay by emitting photons. In cuprous oxide, direct (i.e. zero-phonon) paraexciton decay becomes weakly allowed when strain is applied. In the following, we aim on describing this zero-phonon decay process.

Thanks to the Bogolyubov transformation outlined above, the system of interacting excitons is transformed to a system of non-interacting quasiparticles with the

Hamiltonian

$$\hat{H}_x = \sum_{\mathbf{q}} E_{\mathbf{q}} \hat{b}_{\mathbf{q}}^{\dagger} \hat{b}_{\mathbf{q}} \quad (12)$$

Accordingly, we write the Hamiltonian of the free photon field as a sum of oscillator modes,

$$\hat{H}_p = \sum_{\mathbf{q}} \hbar \omega_{\mathbf{q}} \hat{a}_{\mathbf{q}}^{\dagger} \hat{a}_{\mathbf{q}}, \quad (13)$$

with the photonic operators  $a_{\mathbf{q}}^{(\dagger)}$  and the dispersion  $\omega_{\mathbf{q}} = cq$ . Here,  $c = c_0/\sqrt{\varepsilon_b}$  is the velocity of light in the medium, where  $c_0$  is the vacuum velocity of light and  $\varepsilon_b$  is the background dielectric constant.

To model the bogolon-photon interaction, we start from the minimal coupling Hamiltonian [13],

$$\hat{H}_{\text{xp}} = -\frac{e}{m_0} \sum_j \hat{\mathbf{A}}(\hat{\mathbf{r}}_j) \cdot \hat{\mathbf{p}}_j + \frac{e^2}{2m_0} \sum_j |\hat{\mathbf{A}}(\hat{\mathbf{r}}_j)|^2, \quad (14)$$

where  $m_0$  is the free electron mass and  $\hat{\mathbf{r}}_j$  and  $\hat{\mathbf{p}}_j$  are the position and momentum of the  $j$ -th electron. We now insert into Eq. (14) the Heisenberg equation of motion  $i\hbar \dot{\hat{\mathbf{p}}}_j = m_0 [\hat{\mathbf{r}}_j, \hat{H}_x]$ . Thereby we expand the position operator in terms of the many-body wave functions of the bogolons,  $\Psi_{\mathbf{q}}^B$ , as follows [13]:

$$\begin{aligned} \hat{\mathbf{r}}_j = & \sum_{\mathbf{q}} \langle 0 | \hat{\mathbf{r}}_j | \Psi_{\mathbf{q}}^B \rangle \hat{b}_{\mathbf{q}} + \sum_{\mathbf{q}} \langle \Psi_{\mathbf{q}}^B | \hat{\mathbf{r}}_j | 0 \rangle \hat{b}_{\mathbf{q}}^{\dagger} \\ & + \sum_{\substack{\mathbf{q}, \mathbf{q}' \\ \mathbf{q} \neq \mathbf{q}'}} \langle \Psi_{\mathbf{q}}^B | \hat{\mathbf{r}}_j | \Psi_{\mathbf{q}'}^B \rangle \hat{b}_{\mathbf{q}}^{\dagger} \hat{b}_{\mathbf{q}}. \end{aligned} \quad (15)$$

In the following, we neglect the last term on the r.h.s. of Eq. (15), i.e., we take into account only transitions from the Bogolyubov ground state, i.e., the condensate, to the excited states and vice versa. After evaluating the commutator  $[\hat{\mathbf{r}}_j, \hat{H}_x]$  and expanding the vector potential operator  $\hat{\mathbf{A}}$  into the set of normal modes,

$$\hat{\mathbf{A}}(\mathbf{r}) = \sum_{\mathbf{q}\lambda} \sqrt{\frac{\hbar}{2\varepsilon_0 V \omega_{\mathbf{q}}}} \mathbf{e}_{\mathbf{q}\lambda} (\hat{a}_{\mathbf{q}} + \hat{a}_{-\mathbf{q}}^{\dagger}) e^{i\mathbf{q}\cdot\mathbf{r}}, \quad (16)$$

the total Hamiltonian  $\hat{H} = \hat{H}_x + \hat{H}_p + \hat{H}_{\text{xp}}$  takes the form:

$$\begin{aligned} \hat{H} = & \sum_{\mathbf{q}} E_{\mathbf{q}} \hat{b}_{\mathbf{q}}^{\dagger} \hat{b}_{\mathbf{q}} + \sum_{\mathbf{q}} \hbar \omega_{\mathbf{q}} \hat{a}_{\mathbf{q}}^{\dagger} \hat{a}_{\mathbf{q}} \\ & + i \sum_{\mathbf{q}} C_{\mathbf{q}} (\hat{a}_{\mathbf{q}} + \hat{a}_{-\mathbf{q}}^{\dagger}) (\hat{b}_{-\mathbf{q}} - \hat{b}_{\mathbf{q}}^{\dagger}) \\ & + \sum_{\mathbf{q}} D_{\mathbf{q}} (\hat{a}_{-\mathbf{q}} + \hat{a}_{\mathbf{q}}^{\dagger}) (\hat{a}_{\mathbf{q}} + \hat{a}_{-\mathbf{q}}^{\dagger}), \end{aligned} \quad (17)$$

with the coupling strength parameters

$$C_{\mathbf{q}} = E_{\mathbf{q}} \sqrt{\frac{2\pi e^2}{4\pi \varepsilon_0 \varepsilon_r V \hbar \omega_{\mathbf{q}}}} \left\langle \Psi_{\mathbf{q}}^B \left| \mathbf{e}_{\mathbf{q}\lambda} \cdot \sum_j \mathbf{r}_j e^{i\mathbf{q}\cdot\mathbf{r}_j} \right| 0 \right\rangle, \quad (18)$$

and  $D_{\mathbf{q}} = |C_{\mathbf{q}}|^2 / E_{\mathbf{q}}$ . Using the dipole approximation  $\exp(i\mathbf{q} \cdot \mathbf{r}_j) \approx 1$  and the definition of the oscillator strength

$$f = \frac{2m_0 E_{\mathbf{q}}}{\hbar^2} \left| \left\langle \Psi_{\mathbf{q}}^B \left| \mathbf{e}_{\mathbf{q}\lambda} \cdot \sum_j \mathbf{r}_j \right| 0 \right\rangle \right|^2, \quad (19)$$

we obtain the coupling strength as [14]

$$C_{\mathbf{q}} = \sqrt{\frac{\hbar^2 e^2 f}{4\varepsilon_0 \varepsilon_r m_0 V}} \sqrt{\frac{E_{\mathbf{q}}}{\hbar \omega_{\mathbf{q}}}}. \quad (20)$$

Note that definition (19) originally involves the exciton state  $\langle \Psi_{\mathbf{q}}^X |$ . However, we will not derive  $f$  microscopically, but use an experimentally obtained value for our calculations. Exciton states in the experiment are by nature “dressed”, i.e. bogolon, states.

For later use, we note the Heisenberg equations of motions of the photon and bogolon operators, which follow from Eq. (17) as

$$\begin{aligned} i\hbar \dot{\hat{a}}_{\mathbf{q}}(t) = & \hbar \omega_{\mathbf{q}} \hat{a}_{\mathbf{q}}(t) + iC_{\mathbf{q}} (\hat{b}_{\mathbf{q}}(t) - \hat{b}_{-\mathbf{q}}^{\dagger}(t)) \\ & + 2D_{\mathbf{q}} (\hat{a}_{\mathbf{q}}(t) + \hat{a}_{-\mathbf{q}}^{\dagger}(t)), \end{aligned} \quad (21)$$

$$i\hbar \dot{\hat{b}}_{\mathbf{q}}(t) = E_{\mathbf{q}} \hat{b}_{\mathbf{q}}(t) - iC_{\mathbf{q}} (\hat{a}_{\mathbf{q}}(t) + \hat{a}_{-\mathbf{q}}^{\dagger}(t)). \quad (22)$$

## 4 Luminescence spectrum

In experiments, the photoelectric effect is used for luminescence measurements. That is why only normal-ordered components of the field-field correlation functions are considered, e.g.,

$$g_{EE}^{(1)}(\mathbf{r}_1, t_1; \mathbf{r}_2, t_2) = \left\langle \hat{\mathbf{E}}^{(-)}(\mathbf{r}_2, t_2) \hat{\mathbf{E}}^{(+)}(\mathbf{r}_1, t_1) \right\rangle. \quad (23)$$

The field components of positive and negative frequencies are [15]:

$$\hat{\mathbf{E}}^{(-)}(\mathbf{r}, t) = \sum_{\mathbf{q}\lambda} \sqrt{\frac{\hbar \omega_{\mathbf{q}}}{2\varepsilon_0 V}} \mathbf{e}_{\mathbf{q}\lambda} e^{-i\mathbf{q}\cdot\mathbf{r}} \hat{a}_{\mathbf{q}}^{\dagger}(t), \quad (24)$$

$$\hat{\mathbf{E}}^{(+)}(\mathbf{r}, t) = \sum_{\mathbf{q}\lambda} \sqrt{\frac{\hbar \omega_{\mathbf{q}}}{2\varepsilon_0 V}} \mathbf{e}_{\mathbf{q}\lambda} e^{i\mathbf{q}\cdot\mathbf{r}} \hat{a}_{\mathbf{q}}(t). \quad (25)$$

Inserting these into Eq. (23) and evaluating the sum over polarisation vectors, the field–field correlation function reads

$$g_{EE}^{(1)}(\mathbf{r}_1, \mathbf{r}_2, t_1, t_2) = \frac{\hbar}{2V\epsilon_0} \sum_{\mathbf{q}\mathbf{q}'} (1 + \cos \Theta) \sqrt{\omega_{\mathbf{q}}\omega_{\mathbf{q}'}} \\ \times i\hbar g_{aa}^{<}(\mathbf{q}, \mathbf{q}', t_1, t_2) e^{i(\mathbf{q}\cdot\mathbf{r}_1 - \mathbf{q}'\cdot\mathbf{r}_2)}, \quad (26)$$

where  $\Theta$  is the angle between the wave vectors  $\mathbf{q}$  and  $\mathbf{q}'$  and we have defined the photonic correlation function

$$i\hbar g_{aa}^{<}(\mathbf{q}, \mathbf{q}', t_1, t_2) \equiv \langle \hat{a}_{\mathbf{q}'}^\dagger(t_2) \hat{a}_{\mathbf{q}}(t_1) \rangle. \quad (27)$$

To calculate  $g_{aa}^{<}$  we have to evaluate a number of similar real-time correlation functions of (mixed) photon and bogolon operators, which may be represented by the matrix

$$i\hbar g_{XY}^{\alpha\beta<}(\mathbf{q}, \mathbf{q}', t_1, t_2) \\ = \begin{pmatrix} \langle Y_{\mathbf{q}'}^\dagger(t_2) X_{\mathbf{q}}(t_1) \rangle & \langle Y_{\mathbf{q}'}(t_2) X_{\mathbf{q}}(t_1) \rangle \\ \langle Y_{\mathbf{q}'}^\dagger(t_2) X_{\mathbf{q}'}^\dagger(t_1) \rangle & \langle Y_{\mathbf{q}'}(t_2) X_{\mathbf{q}'}^\dagger(t_1) \rangle \end{pmatrix}, \quad (28)$$

where  $X$  and  $Y$  represent the operators  $\hat{a}$  and/or  $\hat{b}$ , while  $\alpha$  and  $\beta$  are the matrix indices. Specifically, we have  $g_{aa}^{11<} = g_{aa}^{11<}$ . The correlation functions in Eq. (28) can be determined from the more general Keldysh Green functions defined as [16–18]

$$i\hbar G_{XY}^{\alpha\beta}(\mathbf{q}, \mathbf{q}', t_1, t_2) \\ = \begin{pmatrix} \langle T_{\mathcal{C}} X_{\mathbf{q}}(t_1) Y_{\mathbf{q}'}^\dagger(t_2) \rangle & \langle T_{\mathcal{C}} X_{\mathbf{q}}(t_1) Y_{\mathbf{q}'}(t_2) \rangle \\ \langle T_{\mathcal{C}} X_{\mathbf{q}}^\dagger(t_1) Y_{\mathbf{q}'}^\dagger(t_2) \rangle & \langle T_{\mathcal{C}} X_{\mathbf{q}}^\dagger(t_1) Y_{\mathbf{q}'}(t_2) \rangle \end{pmatrix}, \quad (29)$$

with the time ordering operator  $T_{\mathcal{C}}$  defined on the two-branch time contour (chronological/antichronological ordering when both times are on the upper/lower branch; otherwise ordering of operators with times on the upper branch right from those on the lower one). The functions  $G$  may be calculated by using Eqs. (21) and (22). Then, using the free Green functions of photons and bogolons,

$$\left( i\hbar \frac{\partial}{\partial t_1} - \hbar\omega_{\mathbf{q}} \right) G_{aa}^{(0)}(\mathbf{q}, \mathbf{q}', t_1, t_2) = \delta(\mathbf{q} - \mathbf{q}') \delta(t_1 - t_2), \quad (30)$$

$$\left( i\hbar \frac{\partial}{\partial t_1} - E_{\mathbf{q}} \right) G_{bb}^{(0)}(\mathbf{q}, \mathbf{q}', t_1, t_2) = \delta(\mathbf{q} - \mathbf{q}') \delta(t_1 - t_2), \quad (31)$$

and defining the matrix multiplication  $f_1(\mathbf{q}, t) \bullet f_2(\mathbf{q}, t) \equiv \sum_{\mathbf{q}'} \int_{\mathcal{C}} dt' f_1(\mathbf{q}, t) f_2(\mathbf{q}', t')$ , the coupled selfconsistent Dyson

equations can be written as:

$$G_{aa}^{11}(\mathbf{q}, \mathbf{q}', t_1, t_2) \\ = G_{aa}^{(0)}(\mathbf{q}, \mathbf{q}', t_1, t_2) + G_{aa}^{(0)}(\mathbf{q}, \bar{\mathbf{q}}, t_1, \bar{t}) \bullet \\ \bullet \tilde{C}_{\bar{\mathbf{q}}} \left[ G_{bb}^{(0)}(\bar{\mathbf{q}}, \bar{\mathbf{q}}, \bar{t}, \bar{t}) + G_{bb}^{(0)}(-\bar{\mathbf{q}}, -\bar{\mathbf{q}}, -\bar{t}, -\bar{t}) \right] \bullet \\ \bullet \tilde{C}_{\bar{\mathbf{q}}} \left[ G_{aa}^{11}(\bar{\mathbf{q}}, \mathbf{q}', \bar{t}, t_2) + G_{aa}^{21}(-\bar{\mathbf{q}}, \mathbf{q}', \bar{t}, t_2) \right] \\ + 2G_{aa}^{(0)}(\mathbf{q}, \bar{\mathbf{q}}, t_1, \bar{t}) \bullet \\ \bullet D_{\bar{\mathbf{q}}} \left[ G_{aa}^{11}(\bar{\mathbf{q}}, \mathbf{q}', \bar{t}, t_2) + G_{aa}^{21}(-\bar{\mathbf{q}}, \mathbf{q}', \bar{t}, t_2) \right], \quad (32)$$

$$G_{aa}^{21}(\mathbf{q}, \mathbf{q}', t_1, t_2) \\ = G_{aa}^{(0)}(\mathbf{q}, \bar{\mathbf{q}}, -t_1, -\bar{t}) \bullet \\ \bullet \tilde{C}_{\bar{\mathbf{q}}} \left[ G_{bb}^{(0)}(\bar{\mathbf{q}}, \bar{\mathbf{q}}, -\bar{t}, -\bar{t}) + G_{bb}^{(0)}(-\bar{\mathbf{q}}, -\bar{\mathbf{q}}, \bar{t}, \bar{t}) \right] \\ \bullet \tilde{C}_{\bar{\mathbf{q}}} \left[ G_{aa}^{21}(\bar{\mathbf{q}}, \mathbf{q}', \bar{t}, t_2) + G_{aa}^{11}(-\bar{\mathbf{q}}, \mathbf{q}', \bar{t}, t_2) \right] \\ - 2G_{aa}^{(0)}(\mathbf{q}, \bar{\mathbf{q}}, -t_1, -\bar{t}) \bullet \\ \bullet D_{\bar{\mathbf{q}}} \left[ G_{aa}^{21}(\bar{\mathbf{q}}, \mathbf{q}', \bar{t}, t_2) + G_{aa}^{11}(-\bar{\mathbf{q}}, \mathbf{q}', \bar{t}, t_2) \right]. \quad (33)$$

To get the frequency-dependent intensity signal  $I(\mathbf{r}, \omega)$  we consider the Fourier transform of the correlation function in Eq. (26) for  $\mathbf{r}_1 = \mathbf{r}_2 = \mathbf{r}$ , i.e.,

$$I(\mathbf{r}, \omega) \propto g_{EE}^{(1)}(\mathbf{r}, \mathbf{r}, \omega) \\ = \frac{\hbar}{2V\epsilon_0} \sum_{\mathbf{q}\mathbf{q}'} (1 + \cos \Theta) \sqrt{\omega_{\mathbf{q}}\omega_{\mathbf{q}'}} \\ \times i\hbar g_{aa}^{11<}(\mathbf{q}, \mathbf{q}', \omega) e^{i(\mathbf{q}-\mathbf{q}')\cdot\mathbf{r}}. \quad (34)$$

In order to obtain the correlation function  $g_{aa}^{11<}$ , we use  $G^{(0)} \propto \delta(\mathbf{q} - \mathbf{q}')$  and apply the usual Langreth rules [19]. That results in a system of four coupled equations for  $g_{aa}^{11<}$ ,  $g_{aa}^{21<}$ , and the two respective retarded or advanced functions, a closed solution of which is still pending. However, the solution of the subsystem of retarded and advanced functions can be given straightforwardly,

$$g_{aa}^{11r/a}(\mathbf{q}, \mathbf{q}', \omega) = \delta(\mathbf{q} - \mathbf{q}') \\ \times \frac{1}{\hbar} \frac{((\omega \pm i\epsilon) + \omega_{\mathbf{q}} + 2d_{\mathbf{q}})((\omega \pm i\epsilon)^2 - e_{\mathbf{q}}^2) + 2c_{\mathbf{q}}^2 e_{\mathbf{q}}}{((\omega \pm i\epsilon)^2 - \omega_{\mathbf{q}}^2 - 4d_{\mathbf{q}}\omega_{\mathbf{q}})((\omega \pm i\epsilon)^2 - e_{\mathbf{q}}^2) - 4c_{\mathbf{q}}^2 e_{\mathbf{q}}\omega_{\mathbf{q}}}. \quad (35)$$

with  $E_{\mathbf{q}} = \hbar e_{\mathbf{q}}$ ,  $C_{\mathbf{q}} = \hbar c_{\mathbf{q}}$ , and  $D_{\mathbf{q}} = \hbar d_{\mathbf{q}}$ . The poles of these functions give the excitation spectrum. We find four

solutions  $(\omega \pm i\epsilon) = \pm\Omega_{\mathbf{q}}^{\pm}$ , with

$$\Omega_{\mathbf{q}}^{\pm 2} = \frac{1}{2}(e_{\mathbf{q}}^2 + \omega_{\mathbf{q}}^2 + 4d_{\mathbf{q}}\omega_{\mathbf{q}}) \pm \frac{1}{2}\sqrt{(e_{\mathbf{q}}^2 - \omega_{\mathbf{q}}^2 - 4d_{\mathbf{q}}\omega_{\mathbf{q}})^2 + 16c_{\mathbf{q}}^2 e_{\mathbf{q}}\omega_{\mathbf{q}}}. \quad (36)$$

This result is analogous to the Hopfield polariton spectrum [20] with its non-crossing upper and lower polariton branches. Note however, that the energy  $E_{\mathbf{q}}$  is now the Bogolyubov dispersion of the interacting, condensed exciton system. Therefore, the new quasiparticles will be called “bogolaritons” in the following.

The retarded and advanced Green functions give the photonic spectral function  $A_{aa}(\omega)$ , which follows from Eq. (35) as

$$\begin{aligned} A_{aa}(\mathbf{q}, \mathbf{q}', \omega) &= i\hbar \left[ g_{aa}^{11r}(\mathbf{q}, \mathbf{q}', \omega) - g_{aa}^{11a}(\mathbf{q}, \mathbf{q}', \omega) \right] \\ &= 2\pi\delta(\mathbf{q} - \mathbf{q}') \\ &\quad \times \left[ U_{\mathbf{q}}^{+2}\delta(\omega - \Omega_{\mathbf{q}}^+) + V_{\mathbf{q}}^{+2}\delta(\omega + \Omega_{\mathbf{q}}^+) \right. \\ &\quad \left. + U_{\mathbf{q}}^{-2}\delta(\omega - \Omega_{\mathbf{q}}^-) + V_{\mathbf{q}}^{-2}\delta(\omega + \Omega_{\mathbf{q}}^-) \right]. \quad (37) \end{aligned}$$

The weights of the positive and negative upper and lower bogolariton branches in the photon spectral function are

$$U_{\mathbf{q}}^{+2} = \frac{(\Omega_{\mathbf{q}}^+ + \omega_{\mathbf{q}} + 2d_{\mathbf{q}})(\Omega_{\mathbf{q}}^{+2} - e_{\mathbf{q}}^2) + 2c_{\mathbf{q}}^2 e_{\mathbf{q}}}{2\Omega_{\mathbf{q}}^+(\Omega_{\mathbf{q}}^{+2} - \Omega_{\mathbf{q}}^{-2})}, \quad (38)$$

$$V_{\mathbf{q}}^{+2} = \frac{(\Omega_{\mathbf{q}}^+ - \omega_{\mathbf{q}} - 2d_{\mathbf{q}})(\Omega_{\mathbf{q}}^{+2} - e_{\mathbf{q}}^2) - 2c_{\mathbf{q}}^2 e_{\mathbf{q}}}{2\Omega_{\mathbf{q}}^+(\Omega_{\mathbf{q}}^{+2} - \Omega_{\mathbf{q}}^{-2})}, \quad (39)$$

$$U_{\mathbf{q}}^{-2} = \frac{(\Omega_{\mathbf{q}}^- + \omega_{\mathbf{q}} + 2d_{\mathbf{q}})(\Omega_{\mathbf{q}}^{-2} - e_{\mathbf{q}}^2) + 2c_{\mathbf{q}}^2 e_{\mathbf{q}}}{2\Omega_{\mathbf{q}}^-(\Omega_{\mathbf{q}}^{-2} - \Omega_{\mathbf{q}}^{+2})}, \quad (40)$$

$$V_{\mathbf{q}}^{-2} = \frac{(\Omega_{\mathbf{q}}^- - \omega_{\mathbf{q}} - 2d_{\mathbf{q}})(\Omega_{\mathbf{q}}^{-2} - e_{\mathbf{q}}^2) - 2c_{\mathbf{q}}^2 e_{\mathbf{q}}}{2\Omega_{\mathbf{q}}^-(\Omega_{\mathbf{q}}^{-2} - \Omega_{\mathbf{q}}^{+2})}. \quad (41)$$

We note that for vanishing exciton-photon coupling, i.e. for  $c_{\mathbf{q}} = d_{\mathbf{q}} = 0$ , we have  $\Omega_{\mathbf{q}}^+ = \max\{e_{\mathbf{q}}, \omega_{\mathbf{q}}\}$  and  $\Omega_{\mathbf{q}}^- = \min\{e_{\mathbf{q}}, \omega_{\mathbf{q}}\}$ . Accordingly we find  $U_{\mathbf{q}}^{\pm 2} = 1$  for  $e_{\mathbf{q}} \leq \omega_{\mathbf{q}}$  and  $U_{\mathbf{q}}^{\pm 2} = 0$  for  $e_{\mathbf{q}} \geq \omega_{\mathbf{q}}$ , so that the spectral function in Eq. (37) reduces to that of the free photons:  $A_{aa}(\mathbf{q}, \mathbf{q}', \omega) = 2\pi\delta(\mathbf{q} - \mathbf{q}')\delta(\omega - \omega_{\mathbf{q}})$ .

## 5 Results

As with the theoretical description, our numerical evaluation takes two steps: First, we calculate self-consistently the paraexciton density distribution in the trap and the

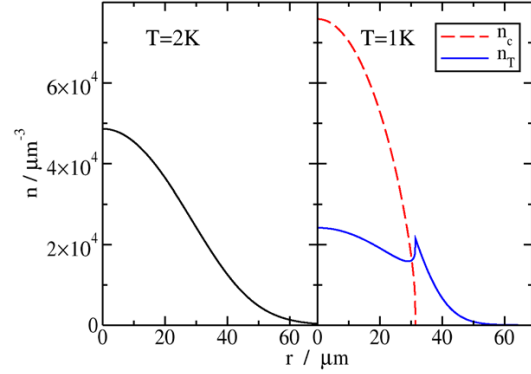


**Figure 1** Exciton density ( $n$ ) as a function of the trap radius ( $r$ ) for a total number of excitons  $N = 10^{10}$ . Left panel: non-condensed situation with  $T = 2$  K and  $\mu - E_g = 231$   $\mu\text{eV}$ . Right panel: condensed situation with  $T = 1$  K,  $\mu - E_g = 314$   $\mu\text{eV}$ , and  $N_c = N_T = 5 \times 10^9$ .

corresponding bogolon spectrum. Second, we keep the exciton distribution fixed and insert  $E_{\mathbf{q}}$ , as well as the free photon dispersion  $\omega_{\mathbf{q}}$  into the combined “bogolariton” spectrum  $\Omega_{\mathbf{q}}^{\pm}$ .

Although the typical experimental situation features a trap with cylindrical symmetry [4, 5], for simplicity we will consider a spherical harmonic trap,  $V_{\text{ext}}(r) = V_0 + \alpha r^2$ , with  $V_0 = -2$  meV and  $\alpha = 0.21$   $\mu\text{eV}/\mu\text{m}^2$  fitted to the bottom of the experimentally observed strain trap potentials. The paraexciton interaction strength is given by the corresponding s-wave scattering length (cf. Eq. 2). The latter follows, in principle, from a four-particle scattering problem (two electrons and two holes), which has no satisfying solution for excitons, so far. That is why in our calculations we use a representative value of  $a_s = 2.18 a_B$  (with the excitonic Bohr radius  $a_B = 0.7$  nm) deduced from the scattering lengths of the positronium problem given in Ref. [21]. With the effective exciton mass  $m = 2.6m_e$ , we then have  $U = 2.53 \times 10^{-3}$   $\mu\text{eV}\mu\text{m}^3$ . The exciton-bogolon interaction is determined by the oscillator strength per unit cell,  $f/V$ , where we use the experimental value  $f = 4.7 \times 10^{-10}$  for the quadrupole transition and  $V = (4.48\text{\AA})^3$ , so that  $C_{\mathbf{q}} = 42.45$   $\mu\text{eV}\sqrt{E_{\mathbf{q}}/\hbar\omega_{\mathbf{q}}}$ . In what follows, we fix the total exciton number as  $N = 10^{10}$ , which gives a critical temperature of  $T_c \approx 1.5$  K.

Figure 1 compares our results for the density distribution of the non-condensed ( $T = 2$  K,  $\mu - E_g = 231$   $\mu\text{eV}$ ) and condensed systems ( $T = 1$  K,  $\mu - E_g = 314$   $\mu\text{eV}$ ), with the latter exhibiting a condensate fraction of  $N_c/N = 0.5$ .

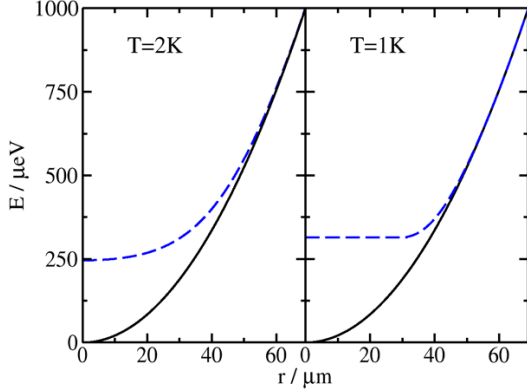


**Figure 2** Minimal excitation energy  $E = E_0(r) - E_g - V_0 + \mu$  of bogolons (blue dashed lines), compared to the external potential  $V_{\text{ext}}(r) - V_0 - E_g$  (black lines). Left panel: non-condensed situation with  $T = 2$  K and  $\mu - E_g = 231$   $\mu\text{eV}$ . Right panel: condensed situation with  $T = 1$  K,  $\mu - E_g = 314$   $\mu\text{eV}$  and  $N_c = N_T = 5 \times 10^9$ .

Figure 2 displays the corresponding minimal excitation energies  $E_0(r)$ , compared to the external potential  $V_{\text{ext}}(r)$ . In the non-condensed case, the thermal exciton cloud has an extension of about  $70\mu\text{m}$ . The mean-field interaction causes a considerable flattening of the dispersion curve when compared to the external potential. In the condensed system, the thermal excitons get pushed aside by the condensed exciton cloud. The two phases still mix, however, since the paraexciton interaction is too weak for a complete phase separation [23]. The cusp in the thermal density profile is an artefact of the Thomas–Fermi approximation for the condensate density which becomes invalid near the edge of the condensate cloud. The solution of the full Gross–Pitaevskii equation would yield a smooth course of the condensate and thermal density curves. Note that the quasiparticle spectrum exhibits a flat bottom wherever  $n_c > 0$ .

Now we switch on the bogolon-photon interaction. Figure 3 shows the resulting positive upper and lower branches of the new quasiparticle spectrum  $\hbar\Omega_q^\pm$  as a function of  $q$  for  $r = 0$ . Here,  $\hbar\Omega_0^+$  corresponds to the minimal bogolon energy  $E_0(r = 0)$  in Fig. 2. Varying  $r$  will simply shift the minimum  $\hbar\Omega_0^+$  according to Fig. 2, so that in the following, we will keep  $r = 0$  fixed. The inset of Fig. 3 shows a zoom in on the crossing point of the uncoupled photon and bogolon dispersions. As expected, we find a gap with a width of  $2C_q \approx 90$   $\mu\text{eV}$ .

Figure 4 gives the  $q$ -dependence of the spectral weights  $U_q^{\pm 2}$  and  $V_q^{\pm 2}$  contributing to the photonic spectral function in Eq. (37). As a matter of course, far from

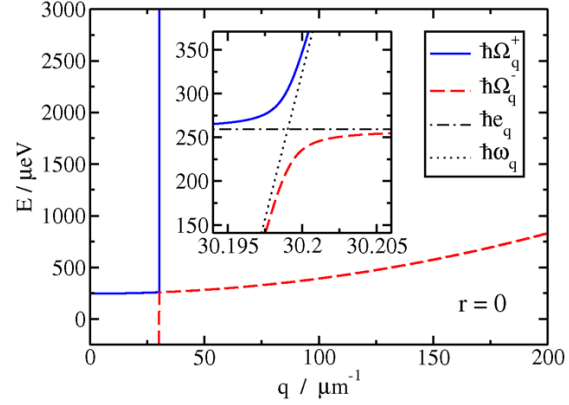


**Figure 3** Upper and lower bogolariton spectrum  $E = \hbar\Omega_q^\pm - E_g - V_0 + \mu$  as a function of  $q$ , for  $r = 0$  and  $T = 2$  K. The inset magnifies the (avoided) crossing region of the free photon and bogolon dispersions.

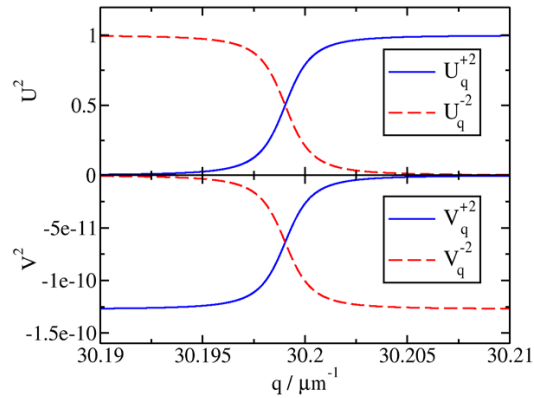


**Figure 4** Spectral weights of the upper and lower bogolariton spectrum, in dependence on  $q$ , for  $r = 0$  and  $T = 2$  K.

the gap, the weights  $U_q^{\pm 2}$  equal one or zero, representing the undisturbed photon states. Near the gap, they smoothly switch roles, whereby their sum remains constant. The weights of the mirror branches are smaller by ten orders of magnitude, and they will be ignored in the following. We note, however, that the  $V_q^\pm$  are finite even for  $n_c = 0$ . In contrast, the bogolon mirror branch in Eq. (11) only exists in the presence of a condensate ( $\nu_q = 0$  for  $n_c = 0$ ); a result which has formerly been declared a footprint of exciton condensation [22, 23].

Combining our results for the dispersions and weights, Fig. 5 presents the photon spectral function  $A_{aa}(q, E)$  in the vicinity of the gap (with a slight broadening of the delta peaks, for visibility). The photon



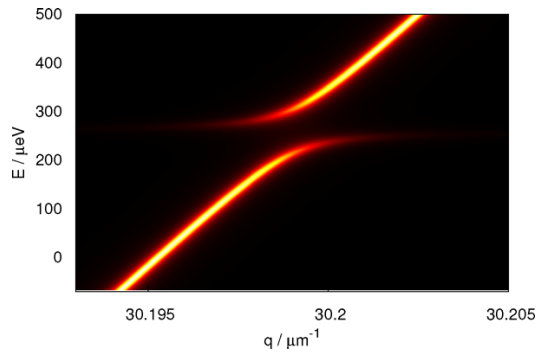


**Figure 5** Photonic spectral function  $A_{aa}$  as a function of  $q$  and  $E = \hbar\omega - E_g - V_0 + \mu$  in the avoided crossing region, for  $r = 0$  and  $T = 2$  K.

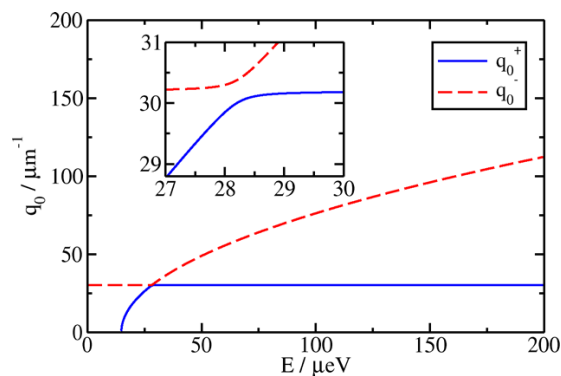


**Figure 6** Critical wave vectors  $q_0^\pm$  as a function of  $E = \hbar\omega - E_g - V_0 + \mu$ , for  $r = 0$  and  $T = 2$  K.

dispersion is considerably renormalised, with a hockey stick like structure at the gap.

As a consequence, the luminescence at a given energy will now depend on the bogolariton density of states at two critical wave numbers  $q_0^\pm$ . This is in contrast to earlier works [8, 9, 22, 23], where the intensity signal was given by the coupling strength and bogolon density of states at the fixed value  $q_0 = 30.2 \mu\text{m}^{-1}$  at the intersection of the free bogolon and photon dispersions (cf. inset of Fig. 3). We numerically determine the wave numbers  $q_0^\pm$  so that  $E = \hbar\Omega_q^\pm$  for fixed  $r$ . Figure 6 presents  $q_0^\pm$  as a function of  $E$  at  $r = 0$ . For small  $E$ , we find  $q_0^- \sim q_0$ , and the wave number  $q_0^+$  is undetermined as long as  $E < \hbar\Omega_q^+$ . After  $E$  crosses the gap position, we find  $q_0^+ \sim q_0$ , while  $q_0^-$  grows due to the  $q^2$ -dependence of the bogolon dispersion. We note that the smallest difference between  $q_0^+$  and  $q_0^-$  is found at the gap:  $q_0^- - q_0^+ = 0.38 \mu\text{m}^{-1}$ .

## 6 Conclusion and outlook

To summarise, this work presents the first results of a real-time Green's function based theory for the luminescent zero-phonon decay of condensed semiconductor excitons. Motivated by the long lifetime of the paraexcitons in cuprous oxide, our approach adopts a two-step picture: the excitons reach their own thermodynamic quasi-equilibrium (and possibly a condensate) before any interaction with the photonic states takes place. The exciton luminescence is then understood as a steady-state decay of bogolon quasiparticles via polariton-like transient states, while the corresponding photon correlation function determines the luminescence intensity.

We find that the photonic spectrum shows a characteristic gap around the former crossing point of free photons and bogolons. The gap's position is dependent on the spatial profile of the bogolon dispersion within the trap. Due to the anomalous terms in the coupling Hamiltonian, mirror branches contribute to the luminescence even without a condensate. Their weight, however, is extremely small.

The present theory can be extended in several directions. The most pressing task is the calculation of the photonic correlation function which not only contains the spectrum but also the steady-state occupation of the bogolariton states. Of course, the most striking signature for BEC would be the coherence of the emitted light. Therefore, the first and second order coherence functions (the former also contained in the field-field correlation function) would be highly desirable to calculate. Moreover, the phonon-assisted decay of orthoexcitons, in principle, can be accounted for in our scheme by introducing a corresponding self-energy term in the Keldysh formalism.

**Acknowledgements.** We would like to thank P. Grünwald (Rostock) and K. W. Becker (Dresden) for many fruitful discussions. This work was supported by the Deutsche Forschungsgemeinschaft via Collaborative Research Center SFB 652, project B14.

**Key words.** Excitons, Bose-Einstein condensation, luminescence spectra, cuprous oxide.

## References

- [1] J. M. Blatt, K. W. Böer, and W. Brandt, *Phys. Rev.* **126**, 1691 (1962).
- [2] S. A. Moskalenko, *Fiz. Tverd. Tela* **4**, 276 (1962).
- [3] D. Snoko and G. M. Kavoulakis, *Rep. Prog. Phys.* **77**, 116501 (2014).

- [4] R. Schwartz, N. Naka, F. Kieselung, and H. Stolz, *New J. Phys.* **14**, 023054 (2012).
- [5] H. Stolz, R. Schwartz, F. Kieselung, S. Som, M. Kaupisch, S. Sobkowiak, D. Semkat, N. Naka, Th. Koch, and H. Fehske, *New J. Phys.* **14**, 105007 (2012).
- [6] K. Kamida and T. Ogawa, *Phys. Rev. B* **83**, 165319 (2011).
- [7] V.-N. Phan, K. W. Becker, and H. Fehske, *Phys. Rev. B* **93**, 075138 (2016).
- [8] H. Haug and H. Kranz, *Z. Phys. B* **53**, 151 (1983).
- [9] H. Shi, G. Verechaka, and A. Griffin, *Phys. Rev. B* **50**, 1119 (1994).
- [10] S. Sobkowiak, D. Semkat, and H. Stolz, *Phys. Rev. B* **90**, 075206 (2014).
- [11] S. Sobkowiak, D. Semkat, and H. Stolz, *Phys. Rev. B* **91**, 075209 (2015).
- [12] T. Bergeman, D. L. Feder, N. L. Balazs, and B. I. Schneider, *Phys. Rev. A* **61**, 063605 (2000).
- [13] D. Gerace and L. C. Andreani, *Phys. Rev. B* **75**, 235325 (2007).
- [14] L. C. Andreani, in: *Strong Light-Matter Coupling, From Atoms to Solid-State Systems*, edited by A. Auffèves, D. Gerace, M. Richard, S. Portolan, M. F. Santos, L. C. Kwek, and C. Miniatura (World Scientific, Singapore, 2014).
- [15] R. J. Glauber, *Phys. Rev.* **130**, 2529 (1963).
- [16] L. V. Keldysh, *Zh. Eksp. Teor. Fiz.* **47**, 1515 (1964).
- [17] A. L. Fetter and J. D. Walecka, *Quantum Theory of Many-Particle Systems* (McGraw-Hill, New York, 1971).
- [18] D. Kremp, M. Schlanges, and W.-D. Kraeft, *Quantum Statistics of Nonideal Plasmas* (Springer, Berlin, 2005).
- [19] D. C. Langreth, in: *Linear and Nonlinear Electron Transport in Solids*, edited by J. T. Devreese and E. Dorenvan (Plenum, New York, 1976).
- [20] J. J. Hopfield, *Phys. Rev.* **112**, 1555 (1958).
- [21] J. Shumway and D. M. Ceperley, *Phys. Rev. B* **63**, 165209 (2001).
- [22] H. Stolz and D. Semkat, *Phys. Rev. B* **81**, 081302(R) (2010).
- [23] S. Sobkowiak, D. Semkat, H. Stolz, Th. Koch, and H. Fehske, *Phys. Rev. B* **82**, 064505 (2010).

# Bibliography

- [1] D. Segal and B. K. Agarwalla, “Vibrational heat transport in molecular junctions,” *Annual Review of Physical Chemistry*, vol. 67, no. 1, p. 185, 2016.
- [2] J. A. del Alamo, “Nanometre-scale electronics with III–V compound semiconductors,” *Nature*, vol. 479, p. 317, 2011.
- [3] I. Bloch, “Ultracold quantum gases in optical lattices,” *Nature Physics*, vol. 1, p. 23, 2005.
- [4] R. Peierls, *Quantum Theory of Solids*. Oxford: Oxford University Press, 1955.
- [5] K. W. Hipps and U. Mazur, “Inelastic electron tunneling: an alternative molecular spectroscopy,” *J. Phys. Chem.*, vol. 97, p. 7803, 1993.
- [6] M. A. Reed, C. Zhou, C. J. Muller, T. P. Burgin, and J. M. Tour, “Conductance of a molecular junction,” *Science*, vol. 278, p. 252, 1997.
- [7] H. Park, J. Park, A. K. L. Lim, E. H. Anderson, A. P. Alivisatos, and P. L. McEuen, “Nanomechanical oscillations in a single  $c_{60}$  molecule,” *Nature*, vol. 407, p. 57, 2000.
- [8] K. J. Franke and J. I. Pascual, “Effects of electron-vibration coupling in transport through single molecules,” *J. Phys. Condens. Matter*, vol. 24, no. 39, p. 394002, 2012.
- [9] T. Holstein, “Studies of polaron motion. Part I. The molecular-crystal model,” *Ann. Phys. (N.Y.)*, vol. 8, p. 325, 1959.
- [10] T. Holstein, “Studies of polaron motion. part II. the “small” polaron,” *Ann. Phys. (N.Y.)*, vol. 8, p. 343, 1959.
- [11] H. Fehske and S. A. Trugman, “Numerical solution of the holstein polaron problem,” in *Polarons in Advanced Materials* (A. S. Alexandrov, ed.), vol. 103 of *Springer Series in Material Sciences*, pp. 393–461, Dordrecht: Canopus/Springer Publishing, 2007.
- [12] I. G. Lang and Y. A. Firsov, “Kinetic theory of semiconductors with low mobility,” *Zh. Eksp. Teor. Fiz.*, vol. 43, p. 1843, 1962. [Sov. Phys. JETP **16**, 1301 (1963)].
- [13] A. Weiße and H. Fehske, “Peierls instability and optical response in the one-dimensional half-filled Holstein model of spinless fermions,” *Phys. Rev. B*, vol. 58, p. 13526, 1998.

- [14] K. Flensberg, “Tunneling broadening of vibrational sidebands in molecular transistors,” *Phys. Rev. B*, vol. 68, p. 205323, 2003.
- [15] A. Zazunov and T. Martin, “Transport through a molecular quantum dot in the polaron crossover regime,” *Phys. Rev. B*, vol. 76, p. 033417, 2007.
- [16] A. Mitra, I. Aleiner, and A. J. Mills, “Phonon effects in molecular transistor: Quantal and classical treatment,” *Phys. Rev. B*, vol. 69, p. 245302, 2004.
- [17] S. Takei, Y. B. Kim, and A. Mitra, “Enhanced Fano factor in a molecular transistor coupled to phonons and Luttinger-liquid leads,” *Phys. Rev. B*, vol. 72, p. 075337, 2005.
- [18] M. Hohenadler and H. Fehske, “Bipolaron formation in 1D-3D quantum dots: a lattice quantum Monte Carlo approach,” *J. Phys.: Condens. Matter*, vol. 19, p. 255210, 2007.
- [19] A. L. Magna and I. Deretzis, “Phonon driven nonlinear electrical behavior in molecular devices,” *Phys. Rev. Lett.*, vol. 99, p. 136404, 2007.
- [20] Y. Meir and N. S. Wingreen, “Landauer formula for the current through an interacting electron region,” *Phys. Rev. Lett.*, vol. 68, no. 16, pp. 2512–2515, 1992.
- [21] N. S. Wingreen, K. W. Jacobsen, and J. W. Wilkins, “Inelastic scattering in resonant tunnelling,” *Phys. Rev. B*, vol. 40, p. 11834, 1989.
- [22] U. Lundin and R. H. McKenzie, “Temperature dependence of polaronic transport through single molecules and quantum dots,” *Phys. Rev. B*, vol. 66, p. 075303, 2002.
- [23] J. Zhu and A. V. Balatsky, “Theory of current and shot noise spectroscopy in single-molecular quantum dots with a phonon mode,” *Phys. Rev. B*, vol. 67, p. 165326, 2003.
- [24] M. Galperin, A. Nitzan, and M. A. Ratner, “Resonant inelastic tunnelling in molecular junctions,” *Phys. Rev. B*, vol. 73, p. 045314, 2006.
- [25] J. M. Blatt, K. Böer, and W. Brandt, “Bose-Einstein condensation of excitons,” *Phys. Rev.*, vol. 126, p. 1691, 1962.
- [26] S. A. Moskalenko *Fiz. Tverd. Tela (Sov. Phys. Solid State)*, vol. 4, p. 276, 1962.
- [27] D. Fröhlich, R. Kenkies, C. Uihlein, and C. Schwab, “Assignment of the even-parity excitons in  $\text{Cu}_2\text{O}$ ,” *Phys. Rev. Lett.*, vol. 43, p. 1260, 1979.
- [28] D. W. Snoke, “Spontaneous Bose coherence of excitons and polaritons,” *Science*, vol. 298, p. 1368, 2002.

- 
- [29] A. Alvermann, P. B. Littlewood, and H. Fehske, “Variational discrete variable representation for excitons on a lattice,” *Phys. Rev. B*, vol. 84, p. 035126, 2011.
- [30] R. Schwartz, N. Naka, F. Kieseling, and H. Stolz, “Dynamics of excitons in a potential trap at ultra-low temperatures: paraexcitons in  $\text{Cu}_2\text{O}$ ,” *New J. Phys.*, vol. 14, p. 023054, 2012.
- [31] A. Griffin, “Conserving and gapless approximations for an inhomogeneous Bose gas at finite temperatures,” *Phys. Rev. B*, vol. 53, p. 9341, 1996.
- [32] F. Dalfovo, S. Giorgini, L. P. Pitaevskii, and S. Stringari, “Theory of Bose-Einstein condensation in trapped gases,” *Rev. Mod. Phys.*, vol. 71, p. 463, 1999.
- [33] T. Bergeman, D. L. Feder, N. L. Balazs, and B. I. Schneider, “Bose condensates in a harmonic trap near the critical temperature,” *Phys. Rev. A*, vol. 61, p. 063605, 2000.
- [34] N. P. Proukakis and B. Jackson, “Finite-temperature models of Bose-Einstein condensation,” *J. Phys. B*, vol. 41, p. 203002, 2008.
- [35] L. A. Bányai, A. M. Bundaru, and H. Haug, “Quasiclassical approach to Bose condensation in a finite potential well,” *Phys. Rev. B*, vol. 70, p. 045201, 2004.
- [36] H. Stolz and D. Semkat, “Unique signatures for Bose-Einstein condensation in the decay luminescence lineshape of weakly interacting excitons in a potential trap,” *Phys. Rev. B*, vol. 81, p. 081302, 2010.
- [37] T. L. Ho and V. B. Shenoy, “Binary mixtures of Bose condensates of alkali atoms,” *Phys. Rev. Lett.*, vol. 77, p. 3276, 1996.
- [38] E. P. Bashkin and A. V. Vagov, “Instability and stratification of a two-component Bose-Einstein condensate in a trapped ultracold gas,” *Phys. Rev. B*, vol. 56, p. 6207, 1997.
- [39] H. Shi, W. M. Zheng, and S. T. Chui, “Phase separation of Bose gases at finite temperature,” *Phys. Rev. A*, vol. 61, p. 063613, 2000.
- [40] W. Zhang, S. Yi, and L. You, “Bose-Einstein condensation of trapped interacting spin-1 atoms,” *Phys. Rev. A*, vol. 70, p. 043611, 2004.
- [41] M.-S. Chang, Q. Qin, W. Zhang, L. You, and M. S. Chapman, “Coherent spinor dynamics in a spin-1 Bose condensate,” *Nature Physics*, vol. 1, p. 111, 2005.
- [42] I. A. Shelykh, G. Malpuech, and A. V. Kavokin, “Bogoliubov theory of Bose-condensates of spinor exciton-polaritons,” *Phys. Status Solidi A*, vol. 202, p. 2614, 2005.

- [43] J. Kasprzak, R. André, L. S. Dang, I. A. Shelykh, A. V. Kavokin, Y. G. Rubo, K. V. Kavokin, and G. Malpuech, “Build up and pinning of linear polarization in the Bose condensates of exciton polaritons,” *Phys. Rev. B*, vol. 75, p. 045326, 2007.
- [44] H. Shi, G. Verechaka, and A. Griffin, “Theory of the decay luminescence spectrum of a Bose-condensed interacting exciton gas,” *Phys. Rev. B*, vol. 50, p. 1119, 1994.
- [45] L. P. Kadanoff and G. Baym, *Quantum Statistical Mechanics*. Reading, Massachusetts: Benjamin/Cumming Publishing Company, 1962.
- [46] L. V. Keldysh, “Diagram technique for nonequilibrium processes,” *Zh. Eksp. Teor. Fiz.*, vol. 47, p. 1515, 1964.
- [47] J. A. Malen, P. Doak, K. Baheti, T. D. Tilley, R. A. Segalman, and A. Majumdar, “Identifying the length dependence of orbital alignment and contact coupling in molecular heterojunctions.,” *Nano Lett.*, vol. 9, no. 3, pp. 1164–9, 2009.
- [48] C. Evangeli, K. Gillemot, E. Leary, M. T. González, G. Rubio-Bollinger, C. J. Lambert, and N. Agrait, “Engineering the thermopower of C60 molecular junctions.,” *Nano Lett.*, vol. 13, no. 5, pp. 2141–5, 2013.
- [49] E. Pop, D. Mann, J. Cao, Q. Wang, K. Goodson, and H. Dai, “Negative Differential Conductance and Hot Phonons in Suspended Nanotube Molecular Wires,” *Phys. Rev. Lett.*, vol. 95, no. 15, p. 155505, 2005.
- [50] R. Leturcq, C. Stampfer, K. Inderbitzin, L. Durrer, C. Hierold, E. Mariani, M. G. Schultz, F. von Oppen, and K. Ensslin, “Franck–Condon blockade in suspended carbon nanotube quantum dots,” *Nat. Phys.*, vol. 5, no. 5, pp. 327–331, 2009.
- [51] R. Scheibner, M. Knig, D. Reuter, A. D. Wieck, C. Gould, H. Buhmann, and L. W. Molenkamp, “Quantum dot as thermal rectifier,” *New J. Phys.*, vol. 10, no. 8, p. 083016, 2008.
- [52] H. Song, Y. Kim, Y. H. Jang, H. Jeong, M. A. Reed, and T. Lee, “Observation of molecular orbital gating.,” *Nature*, vol. 462, no. 7276, pp. 1039–43, 2009.
- [53] Z.-L. Cheng, R. Skouta, H. Vazquez, J. R. Widawsky, S. Schneebeli, W. Chen, M. S. Hybertsen, R. Breslow, and L. Venkataraman, “In situ formation of highly conducting covalent Au-C contacts for single-molecule junctions.,” *Nat. Nanotechnol.*, vol. 6, no. 6, pp. 353–7, 2011.
- [54] T. E. Humphrey, R. Newbury, R. P. Taylor, and H. Linke, “Reversible quantum Brownian heat engines for electrons,” *Phys. Rev. Lett.*, vol. 89, p. 116801, 2002.

- 
- [55] O. Entin-Wohlman, Y. Imry, and A. Aharony, “Three-terminal thermoelectric transport through a molecular junction,” *Phys. Rev. B*, vol. 82, p. 115314, 2010.
- [56] H. J. W. Haug and A. Jauho, *Quantum Kinetics in Transport and Optics of Semiconductors*. Berlin Heidelberg: Springer, 2008.
- [57] H. Fehske, D. Ihle, J. Loos, U. Trapper, and H. Büttner, “Polaron formation and hopping conductivity in the holstein-hubbard model,” *Z. Phys. B*, vol. 94, p. 91, 1994.
- [58] J. Loos, T. Koch, A. Alvermann, A. R. Bishop, and H. Fehske, “Phonon affected transport through molecular quantum dots,” *J. Phys. Condens. Matter*, vol. 21, p. 395601, 2009.
- [59] T. Koch, J. Loos, A. Alvermann, A. R. Bishop, and H. Fehske, “Transport through a vibrating quantum dot: Polaronic effects,” *J. Phys. Conf. Ser.*, vol. 220, p. 012014, 2010.
- [60] E. Eidelstein, D. Goberman, and A. Schiller, “Crossover from adiabatic to antiadiabatic phonon-assisted tunneling in single-molecule transistors,” *Phys. Rev. B*, vol. 87, no. 7, p. 075319, 2013.
- [61] A. L. Fetter and J. D. Walecka, *Quantum theory of many-particle systems*. Berlin Heidelberg: McGraw-Hill Publishing Company, 1971.
- [62] O. Entin-Wohlman, Y. Imry, and A. Aharony, “Voltage-induced singularities in transport through molecular junctions,” *Phys. Rev. B*, vol. 80, p. 035417, 2009.
- [63] A. Jovchev and F. B. Anders, “Influence of vibrational modes on quantum transport through a nanodevice,” *Phys. Rev. B*, vol. 87, no. 19, p. 195112, 2013.
- [64] C. W. J. Beenakker and A. A. M. Staring, “Theory of the thermopower of a quantum dot,” *Phys. Rev. B*, vol. 46, no. 15, p. 9667, 1992.
- [65] P. S. Cornaglia, H. Ness, and D. R. Grempel, “Many-body effects on the transport properties of single-molecule devices,” *Phys. Rev. Lett.*, vol. 93, p. 147201, 2004.
- [66] S. Andergassen, T. A. Costi, and V. Zlatić, “Mechanism for large thermoelectric power in molecular quantum dots described by the negative- $U$  Anderson model,” *Phys. Rev. B*, vol. 84, p. 241107, 2011.
- [67] M. Galperin, A. Nitzan, and M. Ratner, “Heat conduction in molecular transport junctions,” *Phys. Rev. B*, vol. 75, no. 15, p. 155312, 2007.
- [68] A. Alvermann, D. M. Edwards, and H. Fehske, “Boson-controlled quantum transport,” *Phys. Rev. Lett.*, vol. 98, p. 056602, 2007.

- [69] A. Alvermann, D. M. Edwards, and H. Fehske, “Analytical calculation of the Green’s function and Drude weight for a correlated fermion-boson system,” *Journal of Physics: Conference Series*, vol. 220, p. 012023, 2010.
- [70] S. Ejima and H. Fehske, “Charge-density-wave formation in the Edwards fermion-boson model at one-third band filling,” *JPS Conf. Proc.*, vol. 3, p. 013006, 2014.
- [71] M. Chakraborty, N. Mohanta, A. Taraphder, B. I. Min, and H. Fehske, “Edwards polaron formation : From one to three dimensions,” *Phys. Rev. B*, vol. 93, p. 155130, Apr 2016.
- [72] D. Semkat, F. Richter, D. Kremp, G. Manzke, W.-D. Kraeft, and K. Henneberger, “Ionization equilibrium in an excited semiconductor: Mott transition versus Bose-Einstein condensation,” *Phys. Rev. B*, vol. 80, p. 155201, 2009.
- [73] G. Manzke, D. Semkat, F. Richter, D. Kremp, and K. Henneberger, “Mott transition versus Bose-Einstein condensation of excitons,” *J. Phys.: Conf. Ser.*, vol. 210, p. 012020, 2010.
- [74] H. Haug and H. Kranz, “Bose-Einstein condensation in nonequilibrium systems,” *Z. Phys. B*, vol. 53, p. 151, 1983.
- [75] J. Shumway and D. M. Ceperley, “Quantum Monte Carlo treatment of elastic exciton-exciton scattering,” *Phys. Rev. B*, vol. 63, p. 165209, 2001.
- [76] D. Gerace and L. C. Andreani, “Quantum theory of exciton-photon coupling in photonic crystal slabs with embedded quantum wells,” *Phys. Rev. B*, vol. 75, p. 235325, 2007.
- [77] L. C. Andreani in *Strong Light-Matter Coupling, From Atoms to Solid-State Systems* (A. Auffèves, D. Gerace, M. Richard, S. Portolan, M. F. Santos, L. C. Kwek, and C. Miniatura, eds.), Singapore: World Scientific, 2014.
- [78] R. J. Glauber, “The quantum theory of optical coherence,” *Phys. Rev.*, vol. 130, p. 2529, 1963.
- [79] D. Kremp, M. Schlanges, and W.-D. Kraeft, *Quantum Statistics of Nonideal Plasmas*. Berlin: Springer, 2005.
- [80] D. C. Langreth in *Linear and Nonlinear Electron Transport in Solids* (J. T. Devreese and E. van Doren, eds.), New York: Plenum, 1976.
- [81] J. J. Hopfield, “Theory of the contribution of excitons to the complex dielectric constant of crystals,” *Phys. Rev.*, vol. 112, p. 1555, 1958.
- [82] P. C. Hohenberg and P. C. Martin, “Microscopic theory of superfluid helium,” *Ann. Phys. (NY)*, vol. 34, p. 291, 1965.



# Scientific Contributions

## Publications

1. “Phonon affected transport through molecular quantum dots,” J. Loos, T. Koch, A. Alvermann, A. R. Bishop, and H. Fehske, *J. Phys.: Condens. Matter* **21**, 395601 (2009)
2. “Transport through a vibrating quantum dot: Polaronic effects,” T. Koch, J. Loos, A. Alvermann, A. R. Bishop, and H. Fehske, *J. Phys.: Conf. Ser.* **220**, 012014 (2010)
3. “Interacting multicomponent exciton gases in a potential trap: Phase separation and Bose-Einstein condensation,” S. Sobkowiak, D. Semkat, H. Stolz, T. Koch, and H. Fehske, *Phys. Rev. B* **82**, 064505 (2010)
4. “Phase separation of multicomponent excitonic Bose-Einstein condensates,” S. Sobkowiak, D. Semkat, H. Stolz, T. Koch, and H. Fehske, *Phys. Status Solidi C* **8**, 1178 (2011)
5. “Nonequilibrium transport through molecular junctions in the quantum regime,” T. Koch, J. Loos, A. Alvermann, and H. Fehske, *Phys. Rev. B* **84**, 125131 (2011)
6. “Phonon-affected steady-state transport through molecular quantum dots,” T. Koch, H. Fehske, and J. Loos, *Phys. Scr.* **T151**, 014039 (2012)
7. “Condensation of excitons in  $\text{Cu}_2\text{O}$  at ultracold temperatures: experiment and theory,” H. Stolz, R. Schwartz, F. Kieseling, S. Som, M. Kaupsch, S. Sobkowiak, D. Semkat, N. Naka, T. Koch and H. Fehske, *New. J. Phys.* **14**, 105007 (2012)
8. “Thermoelectric effects in molecular quantum dots with contacts,” T. Koch, J. Loos, and H. Fehske, *Phys. Rev. B* **89**, 155133 (2014)
9. “Theory of zero-phonon decay luminescence of semiconductor excitons,” Th. Koch, D. Semkat, H. Stolz, and H. Fehske, *Fortschritte der Physik*, DOI: 10.1002/prop.201600068 (2016)

## Posters

1. “Interacting multi-component exciton gases in a Hertzian potential trap,” S. Sobkowiak, D. Semkat, H. Stolz, T. Koch, and H. Fehske, *DPG Spring Meeting*, Regensburg, 2010
2. “Transport through a vibrating quantum dot: Polaronic effects,” T. Koch, J. Loos, A. Alvermann, A. R. Bishop, and H. Fehske, *DPG Spring Meeting*, Regensburg, 2010
3. “Phonon affected steady-state transport through molecular quantum dots,” T. Koch, H. Fehske, J. Loos, and A. Alvermann, *Frontiers of Quantum and Mesoscopic Thermodynamics*, Prague, 2011
4. “Spectral signatures of excitonic BEC in  $\text{Cu}_2\text{O}$ ,” R. Schwartz, S. Sobkowiak, D. Semkat, Th. Koch, H. Fehske, H. Stolz, *DPG Spring Meeting*, Berlin, 2012
5. “Theory of decay luminescence of excitons,” D. Semkat, Th. Koch, S. Sobkowiak, H. Stolz, and H. Fehske, *Correlation Effects and Radiation Fields (CERF2015)*, Rostock, 2015
6. “Theory of zero-phonon decay luminescence of semiconductor excitons,” D. Semkat, Th. Koch, S. Sobkowiak, G. Manzke, H. Stolz, and H. Fehske, *Eighth International Conference on Spontaneous Coherence in Excitonic Systems (ICSCE8)*, Edinburgh, 2016

## Talks

1. “Ultra low temperature thermodynamics and spectroscopy of excitons in cuprous oxide confined in potential traps,” *SFB 652 Workshop, Strong correlations and collective effects in radiation fields*, Plau am See, 2010
2. “Transport through molecular quantum dots: Vibrational signatures and negative differential conductance,” *SFB 652 Workshop, Strong correlations and collective effects in radiation fields*, Sievershagen, 2012





# Erklärung

Hiermit erkläre ich, dass diese Arbeit bisher von mir weder an der Mathematisch-Naturwissenschaftlichen Fakultät der Ernst-Moritz-Arndt-Universität Greifswald noch einer anderen wissenschaftlichen Einrichtung zum Zwecke der Promotion eingereicht wurde. Ferner erkläre ich, dass ich diese Arbeit selbständig verfasst und keine anderen als die darin angegebenen Hilfsmittel und Hilfen benutzt und keine Textabschnitte eines Dritten ohne Kennzeichnung übernommen habe.

---

(Thomas Koch)

Greifswald, September 30, 2016



# Curriculum Vitae

## Personal Data

Name: Thomas Koch  
Date of Birth: 06 April 1984  
Place of Birth: Stralsund  
Family status: single

## Work Experience

May 2009 - Jun 2014,  
& Jul 2015 - Dec 2015      Scientific employee at the Institute of Physics of the  
Ernst-Moritz-Arndt Universität, Greifswald, Germany

## Training

since May 2009      PhD student in physics,  
Chair of Prof. Dr. Holger Fehske,  
Ernst-Moritz-Arndt Universität, Greifswald, Germany

Apr 2009      Diploma degree, Ernst-Moritz-Arndt Universität  
Diploma thesis: "Transport durch molekulare  
Quanten-Punkte: polaronische Effekte"

Okt 2003 - Apr 2009      Study of physics at the Ernst-Moritz-Arndt  
Universität, Greifswald, Germany

## School Education

Jun 2003      Abitur, Hansa-Gymnasium, Stralsund

1994 - 2003      Hansa-Gymnasium, Stralsund

1990 - 1994      Juri-Gagarin-Grundschule, Stralsund

---

(Thomas Koch)

Greifswald, September 30, 2016





# Acknowledgement

I want to express my deepest gratitude to Prof. Dr. Holger Fehske for his guidance and support over the past years. My special appreciation belongs to Dr. Jan Loos and Dr. Dirk Semkat for the long lasting successful cooperation and, of course, for their hospitality. I wish to express my sincere thanks to all of the work group members for their help and amicability. Finally, I wish to thank my family for the unceasing encouragement and continuous support.